"Il numero di Realtà é infinito. Il numero di ogni sottoclasse di Realtà é infinito. Ad esempio, il numero di Realtà che contengono l'Eternità é infinito, il numero di Realtà che non la contengono é infinito, il numero di Realtà in cui l'Eternità esiste ma viene abolita é infinito" — Isaac Asimov (La Fine dell'Eternità)

Chemoresistive gas sensors for cancer prevention

Giulia Zonta

Contents

Introduction **14**

Publications **17**

1 Chemoresistive gas sensors **21**
1.1 *Bulk* and Fermi distribution . . . 21
1.2 Intrinsic and extrinsic semiconductors . . . 22
1.3 Surface states . . . 23
1.4 Double layer . . . 25
1.5 Poisson equation and Depletion Approximation . . . 28
1.6 Limits of planar geometry . . . 29
1.7 Surface reactions . . . 34

2 Thick film sensors: production process **36**
2.1 Substrate . . . 37
2.2 Screen printing . . . 38
2.3 Drying and Firing . . . 40
2.4 Assembly . . . 40
2.5 Powder synthesis: *sol-gel* technique . . . 42
2.6 Humidity effects . . . 42
2.7 In-diffusion effects . . . 44
2.8 Sensor types . . . 49
2.8.1 Metal-oxides . . . 49
2.8.2 Metal-sulfides . . . 51

3 Towards medical applications **68**
3.1 Colorectal cancer (CRC) . . . 68
3.1.1 Symptoms . . . 69
3.1.2 The management . . . 70
3.1.3 Tumor biomarkers: VOCs . . . 72
3.1.4 Sampling . . . 76

3.2 Experimental setup . . . 78
3.2.1 Measurement apparatus. . . . 78
3.2.2 Data acquisition system . . . 82
3.3 Sensors responses to VOCs . . . 84
3.4 Working temperatures choice . . . 90
3.5 Sensors response . . . 91
3.6 Principal component analysis . . . 110
3.6.1 Example of PCA treatment . . . 111
3.6.2 CRC biomarkers analyzed with PCA . . . 115

4 Prototype for colorectal cancer pre-screening: SCENT A1 122
4.1 The device . . . 123
4.1.1 Structure of the device . . . 124
4.1.2 Sample treatment . . . 126
4.1.3 The sensing core . . . 128
4.2 SCENT A1 results . . . 135
4.2.1 Preliminary tests . . . 135
4.2.2 SCENT A1 results with PCA analysis . . . 145
4.2.3 QDA analysis . . . 150
4.2.4 ROC curve . . . 150
4.3 Clinical validation protocol . . . 154
4.3.1 Results of May-June 2016 . . . 157
4.3.2 Results of September-December 2016 . . . 159

5 The potential power of Gas Chromatography 169
5.1 GC main components . . . 170
5.2 Analysis with a GC . . . 172
5.3 GC applications . . . 174
5.4 Micro GC Agilent description . . . 175
5.5 Instrument calibration . . . 178
5.5.1 First calibration attempt . . . 178
5.5.2 Propane calibration . . . 179
5.5.3 Carbon dioxide (CO_2) calibration . . . 182
5.5.4 Ethene calibration . . . 186

Conclusions 190

Acknowledgements 203

List of Figures

1.1 Fermi function and band diagram for an intrinsic (a) and an extrinsic (b) semiconductor [1]. 24
1.2 Example of surface defects for a surface of TiO_2. 25
1.3 Neutral surface states in an n-type semiconductor: donors are occupied while acceptors are not. In the schematic representation, energy bands are represented for simplicity as a single level [1]. 26
1.4 *Double layer*. Electrons in the conduction band are captured by surface states, creating a negative surface which contrasts the presence of positive charged donors just below it [1]. 26
1.5 On the top grains are schematically represented with their structure composed by a bulk at the center, the depletion layer and the surface occupied by oxygen ions; on the bottom a schematic representation of the potential barriers between grains [1]. 27
1.6 Semiconductor grain. N_a is the acceptor density on the surface and N_d donor density in the depletion layer. 30
1.7 Representation of the band bending in the case in which $R > \Lambda$. 33
1.8 Representation of the band bending in the case in which $R < \Lambda$. It is possible to notice from the figure that, after the formation of the surface charge N_s, it follows a substantial flattening of the band bending between the surface and the center of the grain, smaller than the barrier eV_s. 34
1.9 Functional form of the potential $\phi(r)$ for $R = 100$ nm (a) and $R = 30$ nm (b). In both the situations the potential becomes zero at a distance $\Xi = 22$ nm from the surface. 34
1.10 Functional form of the potential $\phi(r)$ for $R = 10$ nm. The potential does not vanish even in the center of the grain and the behavior is quite constant, differing from that predicted by DA. 35

2.1 Production process scheme for thick film gas sensors. 37
2.2 Screen printing, lateral simplified section of the machine. 39

2.3 Illustration of the squeegee passage on the screen after the application of the photosensitive emulsion and of the paste. 40
2.4 Bonded sensors open (up) and closed (down) compared to a five-cent money. 41
2.5 Instrument for the assembly (bonder). 41
2.6 Analytic 3D surface that fits the concentration of H_2O and CO [3]. 43
2.7 Basic mechanism in n-type metal-oxides. 45
2.8 Dependence of the defect formation enthalpy ΔH_d on the Fermi energy. . . 46
2.9 Profile of the potential near the surface due to the band bending [8]. 48
2.10 Schottky barrier height versus relative oxygen pressure before and after in-diffusion [8]. 49
2.11 SEM micrograph of ZnO thick-film fired at 650°C [11]. 50
2.12 Electrical response to benzene (10 ppm) in dry air for four TiTaV samples: (1) Ti:Ta:V=100:5:5, (2) Ti:Ta:V=100:8:2, (3) Ti:Ta:V=100:15:5 and (4) Ti:Ta:V=100:2:8, measured at 300, 350, 400 and 450°C [2]. 52
2.13 Electrical response to 100 ppm of CO, to benzene (10 ppm) and to mixtures of the two gases in dry air for TiTaV (2) and TiTaV (3) fired at 650 and 850°C at the working temperature of 380°C [2]. 52
2.14 Molecular structure of CdS [31]. 54
2.15 Obtained powder for CdS. 54
2.16 SEM-EDX analysis of CdS [29]. 55
2.17 UV-vis analysis of CdS [29]. 56
2.18 XRD analysis of CdS [29]. 56
2.19 TG analysis of CdS [29]. 57
2.20 Comparison between responses of CdS to diverse gases. It results selective to alcohols [24]. 57
2.21 Mechanism of dehydrogenation of alcoholic chains [24]. 58
2.22 Response curve of CdS and CdO to ethanol at 300°C [24]. 58
2.23 Surface barrier height estimated for two CdS sensors [24]. 59
2.24 Mechanism of bandgap-resonant excitation [24]. 59
2.25 Response of CdS to diverse gases. The response peak is always at the excitation energy for green light. 60
2.26 Molecular structure of SnS_2. 61
2.27 Powder of SnS_2. 61
2.28 SEM-EDX analysis of SnS_2 [28]. 62
2.29 TEM analysis of SnS_2 [28]. 62
2.30 XRD analysis of SnS_2 [28]. 63
2.31 TG analysis of SnS_2 [28]. 63
2.32 Selectivity of SnS_2 thick films to carbonyl group [28]. 64
2.33 Response stability of SnS_2 with 10 ppm of acetone [24]. 65
2.34 Response of SnS_2 and of SnO_2 to 2500 ppm of methane [28]. 65
2.35 Surface barrier height found for SnS_2 and SnO_2 [30]. 66

2.36 Conductance of SnS_2 and SnO_2 in 500 sccm and 100 sccm of synthetic dry air. 66

3.1 Deaths for CRC every 100.000 subjects around the world, 2004 data [44]. . 69
3.2 Pre selection of the GC-MS input for PCA: the most suitable VOCs were selected for distinguishing between healthy subjects and patients suffering from a specific cancer: (A) 6 of 33 common VOCs for lung cancer; (B) 6 of 39 common VOCs for colon cancer; (C) 5 of 54 common VOCs for breast cancer; (D) 4 of 36 common VOCs for prostate cancer [37]. 74
3.3 Discriminating variable compounds considered in statistical analysis [63]. . 75
3.4 1-iodo-nonane chemical structure. 75
3.5 decanal chemical structure. 75
3.6 Individual values for the total volume of gas collected in 24 hours. Hatched bars indicate the total volume of hydrogen, spotted bars carbon dioxide, dark bars methane in three subjects (F3, F5, M5), and the remaining blank bar represents the volume of unidentified gas (probably nitrogen) [71]. . . . 77
3.7 Sensors responses (normalized to 1), as a function of time, to H_2S in dry conditions at 450°C. Humidity increases when H_2S is inflated, due to the reaction 3.1, shown in the text. The sensor codes are indicated in the graph for each response curve [2]. 79
3.8 Sensor inside the chamber (left) and chamber hermetically sealed (right). . 80
3.9 Circuit in which the sensor is inserted. 80
3.10 Heater circuit. 82
3.11 Data acquisition system: experimental setup [2]. 83
3.12 Sensor responses, as a function of time, to a drop of CH_2Cl_2 in dry conditions at the best detecting temperatures for C_6H_6 [2]. 86
3.13 Subtraction between successive plateaux of N_2 and dry synthetic air interferences, normalized over their baseline. The symbol Δ shows the difference of responses for that temperature to the variation, for addition, of 5 sccm of O_2 in the 500 sccm of the chamber [2]. 87
3.14 Subtraction between successive plateaux of N_2 and dry synthetic air interferences, normalized over their baseline. The symbol Δ shows the difference of responses for that temperature to the variation, for addition, of 5 sccm of O_2 in the 500 sccm of the chamber [2]. 88
3.15 Bottles containing decanal and 1-iodo-nonane in the liquid state. 89
3.16 Resistances associated to the working temperatures of sensors. R_h is the resistance at ambient temperature and R_0 is the resistance at a temperature of 0° 90
3.17 Sensor responses (R) as a function of time (t), to 2 ppm of C_6H_6 in dry conditions at 450°C [2]. 95

3.18 Sensor responses, as a function of time (t), to 20 ppm of H_2S in dry conditions at 450°C. Humidity increases when H_2S is inflated, due to the effect of the reaction 3.1 [2]. 96
3.19 Sensor responses (R), as a function of time (t), to SO_2 (1^{st} peak), $C_6H_6 + SO_2 + NO$ (2^{nd} peak), $C_6H_6 + SO_2 + NO$+wet air (3^{rd} peak), C_6H_6 (4^{th} peak) in dry conditions. The gas concentrations are of 2 ppm for all the gases. Temperature chosen are the ones at which the sensor responses to NO become negligible [2]. 97
3.20 Sensor responses (R), as a function of time (t), to H_2S (1^{st} peak), $C_6H_6 + H_2S + NO_2$ (2^{nd} peak), C_6H_6 (3^{rd} peak), in wet conditions. The gas concentrations are of 2 ppm for C_6H_6 and NO_2 and of 20 ppm for H_2S. Temperature chosen are the ones at which the sensor responses to NO_2 become negligible [2]. 98
3.21 Sensor responses (R), as a function of time (t), to $C_6H_6 + H_2 + CH_4$ (1^{st} peak), C_6H_6 (2^{nd} peak), $C_6H_6 + H_2 + CH_4$ with H_2 at a closer concentration to the one of C_6H_6 and the flow of C_6H_6 slightly delayed (3^{rd} peak), CH_4 (4^{th} peak, nearly null), H_2 (5^{th} peak), $H_2 + CH_4$ and delayed addition of C_6H_6 (6^{th} peak), $C_6H_6 + H_2 + CH4_+$ humidity as interferer (RH%: 23.01), in dry conditions (7th peak). Temperature chosen are the ones at which the sensor responses to H_2 are the lower as possible compared to C_6H_6 [2]. . . . 99
3.22 Sensor responses (R), as a function of time (t), to $C_9H_{19}I$ in dry conditions at 450°C [2]. 100
3.23 Sensor responses, as a function of time (t), to $C_{10}H_{10}O$ in dry conditions at 450°C [2]. 101
3.24 Sensor responses, normalized to 1, as a function of time (t), to $C_9H_{19}I + C_{10}H_{10}O$ in wet conditions (RH:32.0%) at 450°C [2]. 102
3.25 Histogram representing the responses of sensors to C_6H_6 as a function of temperature (T) in °C [2]. 103
3.26 Histogram representing the responses of sensors to $C_9H_{19}I$ as a function of the concentration (C) in moles [2]. 104
3.27 Histogram representing the responses of sensors to $C_{10}H_{20}O$ as a function of the concentration (C) in moles [2]. 105
3.28 Histogram representing the ratios regarding the interference $C_6H_6 + H_2 + CH_4$ (H_2 best rate, dry, 2ppm of C_6H_6 , chamber temperature: 34,8°C) [2]. 106
3.29 Histogram representing the ratios regarding the interference $C_6H_6 + SO_2 + NO$ (NO best rate, RH: 33.81%, 2ppm of C_6H_6 , chamber temperature: 36°C) [2]. 107
3.30 Histogram representing the ratios regarding the interference $C_6H_6 + H_2S + NO_2$ (NO_2 best rate, RH: 19.86%, 2ppm of C_6H_6 , chamber temperature: 34.6°C) [2]. 107

3.31 Sensor responses to $C_9H_{19}I$ and $C_{10}H_{20}O$ in combination, in wet conditions. The working temperature of all sensors is fixed at 450°C. Under parenthesis is shown the quantity of reagent (moles) taken for each measure [2]. 108
3.32 Zoom on the sensor response of $C_6H_6 + H_2S + NO_2$ interference, in wet conditions [2]. 109
3.33 Graphic representation of the data. 111
3.34 Graphic representation of the eigenvectors and of dispersions. 112
3.35 Plot of the variation from the mean value in the final form, by using the two eigenvectors. 114
3.36 The graph represents the superposition of the variations in Fig. 3.34 and new variations obtained via (13). 115
3.37 PC1 vs PC2 at 600°C, sensors as variables and gases as samples. 117
3.38 PC1 vs PC3 at 600°C, sensors as variables and gases as samples. 117
3.39 PC2 vs PC3 at 600°C, sensors as variables and gases as samples. 118
3.40 PC1 vs PC2 of TiTaV, temperatures (in the range 350-600°C) as variables and gases as samples. 118
3.41 PC1 vs PC2 of STN, temperatures (in the range 350-600°C) as variables and gases as samples. 119
3.42 PC1 vs PC2 of ST30 650, temperatures (in the range 350-600°C) as variables and gases as samples. 119
3.43 PC1 vs PC2 of ST25 650+Au, temperatures (in the range 350-600°C) as variables and gases as samples. 120
3.44 PC1 vs PC2 of ST25 650, temperatures (in the range 350-600°C) as variables and gases as samples. 120
3.45 PC1 vs PC2 of ST20 650, temperatures (in the range 350-600°C) as variables and gases as samples. 121

4.1 Schematic representation of SCENT A1 setup [85]. 124
4.2 The packaging of the device SCENT A1 [85]. 125
4.3 The sensor allocations of the sensing core of SCENT A1. 125
4.4 This image shows the saturated responses of a feces sample left under laboratory fume hood for one night, without any cooling treatment. It is not possible to get relevant data from this measurement [2]. 127
4.5 example of tumor affected feces, tested with a sensor array, the same day of the extraction from the intestine of the patient. The response of ZnO 850 is slightly oxidative. The first peaks are due to the effect of pressure, humidity and surface reactions. The final tiny peak is produced by the flow cleaning the sample chamber after the removal of the sample [2]. 128

4.6 example of tumor affected feces, tested with a sensor array, 23 days after the extraction from the intestine of the patient. The oxidative response of ZnO 850 turned into a strong reductive response, and all the responses are higher than the ones in Fig. 4.5. The first ZnO response saturated [2]. . . . 129
4.7 example of tumor affected feces, tested with a sensor array, the first day after the deposition. It is evident that all responses are reductive [2]. 130
4.8 Radar diagram of SA1 responses. Mature plum responses, tested in order to verify the functioning of the airflow system of SCENT A1 for the first time was included [2]. 135
4.9 Radar diagram of all SA1 responses, only feces included [2]. 136
4.10 Radar diagram of all SA2 responses [2]. 136
4.11 Radar diagram of all SA3 responses [2]. 137
4.12 Radar diagram of SA3 responses, all measures were made during the first two days after extraction/deposition [2]. 137
4.13 Radar diagram of SA3 responses, all measures were made during the first two days after extraction/deposition [2]. 138
4.14 Radar diagram of SA3 responses, all measures from the eighth to the fourteenth day after deposition/extraction [2]. 139
4.15 Radar diagram of SA3 responses, all measures from the fifteenth to the twenty-first day after deposition/extraction [2]. 139
4.16 Radar diagram of SA3 responses, all measures were made starting from the twenty-second day after deposition/extraction [2]. 140
4.17 Radar diagram of SA3 responses, all healthy subject feces responses [2]. . . 140
4.18 Radar diagram of SA3 responses, all tumor affected patient feces responses [2].141
4.19 Radar diagram of all SA4 responses. First responses of the new ZnO 850 are erratic, because the sensor was still stabilizing; after few days, his behavior followed that of the original Zno 850 (labeled with the word *same* under parenthesis) [2]. 142
4.20 Radar diagram of all SA5 responses. Some of the first responses are lower than the others due to the freezing of the samples and to drilled bottle cap tests [2]. 143
4.21 Radar diagram of SA5 responses, only one response for each sample (not frozen) [2]. 144
4.22 Radar diagram of all SA5 responses. Healthy and tumor affected subject feces responses are clearly distinguishable [2]. 144
4.23 Bulk drifting phenomenon, visible in the trend of ZnO 850 response [2]. . . 146
4.24 Double phase activation of the W11 sensor, compared to ST25 650+Au trend [2]. 146
4.25 Variation of the flux (and so of the responses) between drilled bottle cap tests (from first to third peak) and open bottle cap measures (fourth peak) [2].147

4.26 Single sensor responses of array SA9. On the vertical axis there is the value of response, indicated with R. R = Single sensor responses of array IX. On the vertical axis there is the value of response, indicated with R. $R = \frac{\Delta G}{G}$ (where ΔG is the change of the conductance in air contaminated by fecal exhalations and the conductance in environmental air and G is the conductance in air) for all sensors, except for $SmFeO_3$ for which R is the reciprocal negative of the previous quantity. Dark grey responses represent TA feces, while light grey ones represent CS feces [42]. 148

4.27 PCA analysis with array SA9. Green dots represent CS samples while blue dots represent TA samples, for a total of 13 tests. On the top there is the projection PC1 vs PC2, on the bottom the projection PC1 vs PC3. In both projections the green area represents the region identified by HS samples, while the blue area represents the region identified by TA samples. 149

4.28 PCA analysis with array SA11. Green dots represent CS samples while blue dots represent TA samples for a total of 16 tests. On the top there is the projection PC1 vs PC2, on the bottom the projection PC1 vs PC3. In both projections the green area represents the region identified by HS samples, while the blue area represents the region identified by TA samples. 151

4.29 Data used for QDA and their results. The error estimated starting from 16 (9 CS and 7 TA) samples is of about 5% [42]. 152

4.30 Gaussian curves obtained with QDA analysis. The *canonical variable* represents the only classification variable that results from the analysis starting from PCA data. The mean and the standard deviation has been obtained starting from the experimental data. The two Gaussian curves show very modest overlapping due to the fact that the classification algorithm calculates no false negatives and only one false positive [42]. 152

4.31 Single values of the *canonical variable* obtained by the QDA (S=CS and M=TA) [42]. 153

4.32 Confusion matrix that express all the parameters derived from the data of the eleven sensor arrays. 154

4.33 ROC curve. 155

4.34 The prototype SCENT A2, located at the Sensor Laboratory of UNIFE. . . 156

4.35 Graphical representation of the main steps of the protocol. 156

4.36 Explanatory drawing for the collection procedure of fecal material. 157

4.37 List of some of the main screening method proposed in the last years with the advantages and disadvantages with respect to our solution with SCENT A1. 158

4.38 Projection of two principal components obtained with PCA technique applied to healthy controls (green dots) and all FOBT positives (blue dots) tested in the first three weeks. The FOBT indicated with the number **1** has been removed due to an error in the sample preservation before the measurement 158

4.39 Preliminary results after about one month of tests. Projection of two principal components obtained with PCA technique applied to healthy controls and subjects resulted positive to FOBT and negative to colonoscopy (green dots) and subjects positive to both FOBT and colonoscopy (blue dots). White dots correspond to positives to FOBT with unknown colonoscopy result. (A) FOBT **6** and **25** fall in the common area of intersection between healthy and adenoma affected subjects; (B) FOBT **6** has been found as a positive subject by our prediction; (C) FOBT **23** and **28** fall in the healthy area; (D) FOBT **23** and **28** resulted negatives as in our previous prediction. 160

4.40 PC1 vs PC2 projection of all the tests with colonoscopy resultm upgraded to december 2016. The subjects resulted negative to colonoscopy are indicated as light blue dots, the ones with low/intermediate-risk adenomas are indicated as grey dots. The patients indicated with fuchsia and red filled squares are respectively a patient with diverse tumor formations and a patient with multiple polyposis. 161

4.41 PC1 vs PC3 projection of all the tests with colonoscopy resultm upgraded to december 2016. The subjects resulted negative to colonoscopy are indicated as light blue dots, the ones with low/intermediate-risk adenomas are indicated as grey dots. The patients indicated with fuchsia and red filled squares are respectively a patient with diverse tumor formations and a patient with multiple polyposis. 162

4.42 PC2 vs PC3 projection of all the tests with colonoscopy resultm upgraded to december 2016. The subjects resulted negative to colonoscopy are indicated as light blue dots, the ones with low/intermediate-risk adenomas are indicated as grey dots. The patients indicated with fuchsia and red filled squares are respectively a patient with diverse tumor formations and a patient with multiple polyposis. 163

4.43 PC1 vs PC2 projection of all the tests with colonoscopy resultm upgraded to december 2016. The subjects resulted negative to colonoscopy and low-risk adenomas are indicated as light blue dots. A subject with hyperplastic polyp and a subject with a low-risk plus an intermediate-risk polyp are indicated with gold filled squares. The patients indicated with fuchsia and red filled squares are respectively a patient with diverse tumor formations and a patient with multiple polyposis. 165

4.44 PC1 vs PC3 projection of all the tests with colonoscopy resultm upgraded to december 2016. The subjects resulted negative to colonoscopy and low-risk adenomas are indicated as light blue dots. A subject with hyperplastic polyp and a subject with a low-risk plus an intermediate-risk polyp are indicated with gold filled squares. The patients indicated with fuchsia and red filled squares are respectively a patient with diverse tumor formations and a patient with multiple polyposis. 166
4.45 PC2 vs PC3 projection of all the tests with colonoscopy resultm upgraded to december 2016. The subjects resulted negative to colonoscopy and low-risk adenomas are indicated as light blue dots. A subject with hyperplastic polyp and a subject with a low-risk plus an intermediate-risk polyp are indicated with gold filled squares. The patients indicated with fuchsia and red filled squares are respectively a patient with diverse tumor formations and a patient with multiple polyposis. 167

5.1 Schematic representation of a GC and its main constituents. 170
5.2 Schematic representation of a split/splitless injector [93]. 173
5.3 Photo of the Mirco GC Agilent 490. 176
5.4 Photo of the Micro GC connected to the computer in which the software Soprane 3.5.7 is installed. 176
5.5 Gas flow diagram of MicroGC 490 Agilent [94]. 177
5.6 Chemical structure of propane (C_3H_8). 180
5.7 Zoom of propane 500 (red), 200 (violet), 100 (green) and 50 (blue) ppm peaks. 181
5.8 Zoom of propane 500 (red), 200 (violet), 100 (green) and 50 (blue) ppm peaks. Here is noticeable the position of the peak at the right-hand side of N_2. 181
5.9 Calibration curve of propane (C3). The concentration employed are four: 500, 200, 100 and 50 ppm. 182
5.10 Correlation parameter of propane and detection time. 182
5.11 CO_2 molecular structure. 182
5.12 Typical CO_2 concentration (in ppm) and their effects on humans [101]. . . . 183
5.13 Zoom of carbon dioxide 500 (red), 200 (violet), 100 (green) and 50 (blue) ppm peaks. 184
5.14 Zoom of carbon dioxide 500 (red), 200 (violet), 100 (green) and 50 (blue) ppm peaks. Here is noticeable the position of the peak at the right-hand side of N_2. 185
5.15 Correlation parameter of carbon dioxide and detection time. 185
5.16 Calibration curve of CO_2. The concentration employed are four: 500, 200, 100 and 50 ppm. 185
5.17 Histogram of CO_2 concentration in the laboratory air during the day (24/10/2016). the separation line indicates the lunch time, when the laboratory is empty. . 187

5.18 Chemical formula of ethene. 187
5.19 Zoom of ethene 500 (blue), 200 (red), 100 (violet) and 50 (green) ppm peaks. 188
5.20 Zoom of ethene 500 (blue), 200 (red), 100 (violet) and 50 (green) ppm peaks. Here is noticeable the position of the peak at the right-hand side of N_2. . . 189
5.21 Correlation parameter of ethene and detection time. 189
5.22 Calibration curve of ethene. The concentration employed are four: 500, 200, 100 and 50 ppm. 189

Introduction

This thesis represents a review of my research activity during of my three years of Ph.D. in Physics, started in january 2014, which is also a continuation of the work that I began with my Master's thesis, entitled *Detection of low concentration of 1-iodo-nonane with nanostructured metal-oxide based sensors* (advisor: Prof. Cesare Malagù).
My research project focused on the application of nanostructured sensors based on semiconductor materials to medical applications, e.g., preventive screening and monitoring of tumors. Gas sensors employed for this study are completely realized at the Sensor and Semiconductor Laboratory at the Department of Physics and Earth Sciences of the University of Ferrara. They are thick film sensors of chemoresistive type, where chemoresistivity is the capability of modifying the electrical resistance as a function of surface chemical reactions.

Nowadays, nanostructured gas sensors are worldwide appreciated for their high sensitivity (tenths of part per billion, ppb) and for the fast outcome of the provided responses. Their selectivity is not high but it can be enhanced by combining sensors into arrays and through the study of new chemoresistive materials. These devices are small and quite inexpensive and useful for many medical applications, like breath analysis, increasing the interest of the scientific and medical communities. Other confirmed applications are in the environmental monitoring, in- and out-doors, and in the industrial field.

My thesis is divided into five chapters:

- in the **first** one it is reported a description of the main properties of semiconductors and the operating principle of sensors. In particular the sensing mechanism due to the surface reactions between the gas and the semicontuctor material (metal-oxide or metal-sulfide) in the shape of nanograins, which is the best configuration to increase the active surface;
- in the **second** chapter it is described the sensors production process, from the powder synthesis to the assembly. Then the focus is also on two main effects that influence the sensor response during the measurement due to humidity or in-diffusion of oxygen vacancies. Finally a brief description of the principal semiconductor material employed is shown, with a particular focus onto metal-sulfides as new materials for gas sensors. The study and the application of these new materials (e.g., cadmium

sulfide and tin sulfide) show interesting aspects regarding selectivity properties, stability and the potential employment of photo-illumination instead of high working temperatures. These materials, together with metal-oxides have been employed in all the research studies of my Ph.D. work;

- in the **third** chapter the focus is on medical applications, in particular colorectal cancer (CRC) screening and monitoring. This tumor is a major worldwide health problem, in fact the American Cancer Society classified it as the third most commonly diagnosed tumor in USA and the third leading cause of cancer death. However, due to its high curable rate (90%), the prevention is fundamental in order to avoid its degeneration. Due to the fact that each cancer produces its own gaseous biomarkers, which are volatile organic compounds (VOCs) emitted by cell membrane after a mechanism of peroxidation and due also to a change in metabolic activity with tumor, the first part of my research focused on the identification of CRC-VOCs inside the intestinal gas mixture. An artificial intestinal atmosphere has been reproduced in a laboratory setup and different sensing material have been tested to find the most selective ones to CRC-VOCs, e.g., 1-iodo-nonane, decanal and benzene. In this chapter is also introduced the principal component analyisis (PCA) technique, that can be employed to help in the discrimination of single compound into a gas mixture or in the discrimination of two specific gas mixtures;

- in the **fourth** chapter the approach has been changed in order to adapt the measurement processes to the needs of a real preventive screening procedure: non-invasivity, simplicity of sampling and measurements, low-costs. A device (SCENT A1) has been realized in order to analize not single biomarkers in intestinal gas mixtures but the difference between fecal exhalations of healthy subjects and of people affected by CRC (since the adenoma stage). This device has been patented thanks to the funds of the University of Ferrara and led to the establishment of the start-up SCENT S.r.l. and now the clinical validation is on-going thanks to the collaboration S. Anna Hospital of Ferrara and Unità Operativa Igiene Pubblica (AUSL). The protocol compares the SCENT A1 test (by the use of principal component analysis technique), with fecal occult blood test (FOBT) and colonoscopy (gold standard);

- in the **fifth** and last chapter it is introduced the micro-gaschromatographic technique. Thanks to the purchase of a micro-gaschromatograph, I have made the first attempt of calibration and measurements on some gases (i.e., carbon dioxide, propane and ethene) which are reported in the text. This will be only the beginning of a research line on the analysis of VOCs into gas mixtures and/or biologic samples.

The work of this three years of Ph.D. with the Sensors Laboratory team has led to eight publications on journals and a book (listed after Introduction) and to the participation as a speaker or with posters in various scientific conferences, both on sensors and medical.

Second, through the complementary reality of SCENT S.r.l. we won some awards that have allowed us to continue our research, as:

- recognition award of Start Cup Emilia Romagna 2013-Ferrara;
- UnifeCup 2013, Business Plan Competition with SCENT team (before enstablishment);
- selection for the participation at the PNI competition 2014;
- Premio Franci@INNOVazione 2015;
- INNOVAMI 2015, *Una nuova idea di impresa*;
- Premio Marzotto 2015;
- SCENT S.r.l., 5^{th} place in the biotech top 15 *StartupItalia*, july 2016;
- recognition for *Innovative thinking* of CNA 2016.

Publications

Articles

[1] G. Zonta, G. Anania, B. Fabbri, A. Gaiardo, S. Gherardi, A. Giberti, N. Landini, C. Malag*ù*, L. Scagliarini, V. Guidi, *Preventive screening of colorectal cancer with a device based on chemoresistive sensors*, Sensors and Actuators B: Chemical (2017), V. 238, pp. 1098-1101;

[2] A. Giberti, A. Gaiardo, B. Fabbri, S. Gherardi, V. Guidi, C. Malag*ù*, P. Bellutti, G. Zonta, D. Casotti, *Tin (IV) sulfide nanorods as a new gas sensing material*, Sensors and Actuators B: Chemical (2016), V. 223, pp. 827-833;

[3] B. Fabbri, A. Gaiardo, S. Gherardi, A. Giberti, V. Guidi, C. Malag*ù*, A. Martucci, M. Sturaro, G. Zonta, S. Gherardi, P. Bernardoni, *Chemoresistive properties of photo-activated thin and thick ZnO films*, Sensors and Actuators B: Chemical (2016), V. 222, pp.1251-1256;

[4] C. Malag*ù*, B. Fabbri, S. Gherardi, A. Giberti, V. Guidi, G. Zonta, *Chemoresistive gas sensors for detection of colorectal cancer biomarkers*, Sensors (2014), V. 4, N. 10, pp. 18982-18992;

[5] A. Giberti, D. Casotti, G. Cruciani, B. Fabbri, A. Gaiardo, V. Guidi, C. Malag*ù*, G. Zonta, *Electrical conductivity of CdS films for gas sensing: selectivity properties to alcoholic chains*, Sensors and Actuators B: Chemical (2014), V. 207, pp. 504-510;

[6] G. Zonta, G. Anania, B. Fabbri, A. Gaiardo, S. Gherardi, A. Giberti, V. Guidi, N. Landini, C. Malag*ù*, *Detection of colorectal cancer biomarkers in the presence of interfering gases*, Sensors and Actuators B: Chemical (2015), V. 218, pp. 289-295;

[7] A. Gaiardo, B. Fabbri, V. Guidi, P. Bellutti, A. Giberti, S. Gherardi, L. Vanzetti, C. Malag*ù*, G. Zonta, *Metal Sulfides as Sensing Materials for Chemoresistive Gas Sensors*,

Sensors (2016), V. 3, N. 3, pp. 296;

[8] A. Gaiardo, B. Fabbri, A. Giberti, V. Guidi, P. Bellutti, C. Malagù, M. Valt, G. Pepponi, S. Gherardi, G. Zonta, A. Martucci, M. Sturaro, N. Landini, *ZnO and Au/ZnO thin films: Room-temperature chemoresistive properties for gas sensing applications*, Sensors and Actuators B: Chemical (2016).

Books

[1] N. Landini, G. Zonta, C. Malagù, *Detection of tumor markers on feces with nanostructured sensors*, Scholars' Press (2015), ISBN-13: 978-3-639-76538-0.

Conference proceedings

[1] *Detection of colorectal biomarkers in the presence of interfering gases*, autori: G. Zonta, B. Fabbri, A. Giberti, V. Guidi, C. Malagù, presentato come poster e pubblicato in occasione di Eurosensors 2014, Brescia (Italia), tenutasi nel periodo 7-10 settembre 2014, Procedia Engineering DOI 10.1016/j.proeng.2014.11.559;

[2] *Mesoporous silicon gas sensor: design, fabrication and conduction model*, autori: B. Fabbri, V. Boldrini, G. Calabrese, A. Gaiardo, A. Giberti, V Guidi, C. Malagù, F. Spizzo, G. Zonta, S. Gherardi, presentato come poster ad AISEM 2015, Trento (Italia) tenutasi nel periodo 3-5 febbraio 2015, DOI 10.1109/AISEM.2015.7066860;

[3] *Tin (IV) sulfide chemoresistivity: a possible new gas sensing material*, autori: A. Gaiardo, A. Giberti, V Guidi, P. Bellutti, C. Malagù, B. Fabbri, G. Zonta, S. Gherardi, presentato come poster ad AISEM 2015, Trento (Italia) tenutasi nel periodo 3-5 febbraio 2015, DOI 10.1109/AISEM.2015.7066765;

[4] *Metal sulfides as a new class of sensing materials*, autori: V. Guidi, B. Fabbri, A. Gaiardo, S. Gherardi, A. Giberti, C. Malagù, G. Zonta, P. Bellutti, presentato come keynote presentation ad Eurosensors 2015, tenutasi a Freiburg (Germany) nel periodo 6-9 settembre 2015, Procedia Engineering DOI 10.1016/j.proeng.2015.08.586;

Abstracts

[1] *Chemoresistive gas sensors for detection of colorectal cancer biomarkers*, autori: B. Fabbri, S. Gherardi, A. Giberti, V. Guidi, C. Malagù, G. Zonta, presentato come poster e pubblicato in occasione di IMCS 2014 - The 15th International Meeting on Chemical Sensors, Buenos Aires (Argentina) tenutosi nel periodo 16-19 marzo 2014;

[2] *Thermo and photo-activation of metal sulfides for gas sensing*, autori: A. Gaiardo, A. Giberti, V. Guidi, P. Bellutti, C. Malagù, B. Fabbri, G. Zonta, S. Gherardi, presentato come discussione orale dal Prof. V. Guidi in occasione di 6th GOSPEL Workshop: Gas sensors based on semiconducting metal oxides - basic understanding & application fields, Tuebingen (Germany), tenutosi nel periodo 7-9 giugno 2015;

[3] *Hybrid technologies for chemoresistive gas sensors*, autori: V. Guidi, B. Fabbri, A. Gaiardo, A. Giberti, C. Malagù, G. Zonta, S. Gherardi, P. Bellutti, L. Lorenzelli, presentato come discussione orale dal Prof. V. Guidi in occasione di AIMETA2015, Genova (Italy), tenutosi nel periodo 14-17 settembre 2015;

[4] *ZnO vs ZnO/Au thin films: a comparison of sensing properties in photo-activation mode*, autori: V. Guidi, A. Gaiardo, P. Bellutti, C. Malagù, B. Fabbri, A. Giberti, G. Zonta, S. Gherardi, N. Landini, presentato come poster in occasione di Eurosensors 2015, Freiburg (Germany), tenutosi nel periodo 6-9 settembre 2015;

[5] *Silicon carbide: an high selectivity functional material for chemoresistive gas sensing field*, autori: Gaiardo, A. Giberti, V. Guidi, P. Bellutti, B. Fabbri, C. Malagù, G. Zonta, S. Gherardi, presentato come poster in occasione di Nanotechitaly 2015, Bologna (Italy), tenutosi nel periodo 25-27 novembre 2015;

[6] *Metal sulfides as novel class of sensing materials*, autori: B. Fabbri, A. Gaiardo, V. Guidi, P. Bellutti, A. Giberti, S. Gherardi, C. Malagù, G. Zonta, N. Landini, presentato come discussione orale dalla dott.ssa B. Fabbri in occasione di Convegno Nazionale Sensori 2016 (Roma), tenutosi nel periodo 23-25 febbraio 2016;

[7] *ZnO vs ZnO/Au thin films: gas sensing properties in photo-activation mode*, autori: A. Gaiardo, B. Fabbri, A. Giberti, G. Zonta, Gherardi, V. Guidi, P. Bellutti, A. Martucci, C. Malagù, M. Sturaro, M. Valt, N. Landini, presentato come discussione orale da A. Gaiardo Convegno Nazionale Sensori 2016 (Roma), tenutosi nel periodo 23-25 febbraio 2016;

[8] *Chemoresistive gas sensors for colorectal adenomas screening through faecal analysis*, autori: G. Zonta, C. Malagù, presentato come discussione orale da Giulia Zonta ad SGS 2015 - IX INTERNATIONAL WORKSHOP ON SEMICONDUCTOR GAS SEN-

SORS (Zakopane), 13-16/12/2015, SGS 2015 Book of Abstracts;

[9] *Screening per la prevenzione e la diagnosi precoce dei tumori al colon-retto mediante FOBT e sensori di gas*, autori: C. Palmonari, G. Anania, A. de Togni, N. Landini, C. Malagù, V. Matarese, P. Pazzi, L. Ricci, G. Zonta, inviata a CONGRESSO NAZIONALE GISCoR 2016, Firenze, 10 - 11 novembre 2016;

[10] *Devices for screening and monitoring of tumors based on chemoresistive sensors*, autori: G. Zonta, G. Anania, B. Fabbri, A. Gaiardo, S. Gherardi, A. Giberti, N. Landini, C. Malagù, V. Guidi, presentato come poster da Cesare Malagù ad EUROSENSORS 2016, Budapest, 4-9 Settembre 2016;

[11] *Chemoresistive sensors for colorectal cancer pre-screening*, autori: G. Zonta, G. Anania, B. Fabbri, A. Gaiardo, S. Gherardi, A. Giberti, N. Landini, C. Malagù, L. Scagliarini, V. Guidi, presentato da Giulia Zonta come discussione orale ad IMCS 2016, Jeju Island, 10-13 Luglio 2016;

[12] *Study of metal-sulfide chemoresistive properties for gas sensing*, autori: V. Guidi, B. Fabbri, A. Gaiardo, A. Giberti, C. Malagù, S. Gherardi, G. Zonta, N. Landini presentato da Giulia Zonta come poster ad IMCS 2016, Jeju Island, 10-13 Luglio 2016;

[13] *Organic-functionalized graphene oxide for room temperature chemoresistive gas sensing*, autori: V. Guidi, A. Gaiardo, M. Valt, B. Fabbri, C. Malagù, A. Giberti, G. Zonta, S. Gherardi, N. Landini, presentato come poster da Andrea Gaiardo ad IMCS 2016, Jeju Island, 10-13 Luglio 2016;

[14] *Silicon Carbide: a gas sensing material for selective detection of SO2*, autori: A. Gaiardo, A. Giberti, B. Fabbri, V. Guidi, C. Malagù, P. Bellutti, M. Valt, G. Pepponi, S. Gherardi, G. Zonta, N. Landini, presentato da Andrea Gaiardo come discussione orale ad IMCS 2016, Jeju Island, 10-13 Luglio 2016.

Patents

[1] C. Malagù, G. Zonta; S. Gherardi; A. Giberti; N. Landini; A. Gaiardo, *Dispositivo per lo screening preliminare di adenomi al colon-retto* (2014), RM2014A000595;

[2] C. Malagú, S. Gherardi, G. Zonta, N. Landini, A. Giberti, B. Fabbri, A. Gaiardo, G. Anania, G. Rispoli, L. Scagliarini, *Combinazione di materiali semiconduttori nanoparticolati per uso nel distinguere cellule normali da cellule tumorali* (2015), 102015000057717.

Chapter 1

Chemoresistive gas sensors

Chemoresistive solid state sensors are devices able to convert chemicophysical quantities (like gas concentration) into an electric signal.

The operating principle behind chemoresistive solid state sensors is based on two different phenomena: the change in the surface conductance and the variation of the bulk conductance, where the bulk is the internal volume of the sensing material. In the following chapters is presented an overview of the most relevant semiconductor properties, which must be taken into account for the realization of sensors [1] [2].

1.1 *Bulk* and Fermi distribution

Inside a crystal, electrons can assume only energy values within certain intervals, corresponding to the energy bands of the crystal itself. These energy bands are separated by forbidden bands (*band gap*).
In a semiconductor, the most energetic energy band, populated by electrons in their fundamental state, is the *Valence Band* (**VB**), separated by a *gap* (E_g) of the order of 1-3 eV from the *Conduction Band* (**CB**) formed by states at which electrons can be promoted if they are properly excited.

In a perfect crystal at absolute zero temperature, the conduction band is completely empty. Obviously, real crystals present in nature have some imperfections and the absolute zero cannot be reached, so in the conduction band we can still find some electrons, the same that are absent in the valence band.

In conditions of thermal equilibrium, electrons inside energy levels follow the **Fermi distribution**:

$$f = \frac{1}{1 + e^{\frac{E - E_F}{kT}}} \quad , \tag{1.1}$$

where k is the Boltzmann constant[1], T the absolute temperature and E_F the *Fermi level*[2] that determines the level with occupation probability equal to $\frac{1}{2}$. Therefore, the probability of finding a level occupied or not by an electron is the same at this energy. This distribution does not depend on the band structure of the crystal and, depending on the energy value, it is possible to make the following considerations:

- If $E \ll E_F$, the distribution $f \to 1$;
- The probability of finding an empty level becomes appreciable only if $E \simeq E_F$;
- If $E - E_F \ll kT$ the function assumes the form of the *Maxwell-Boltzmann distribution.*

If E_F is inside the forbidden bands, the Maxwell-Boltzmann approximation can be used to indicate the electron density in the CB or, analogously, the density of holes in the VB.

1.2 Intrinsic and extrinsic semiconductors

Semiconductors can be of two types, depending on the position of the E_F with respect to the forbidden band of the crystal. If E_F is located very close to the center of the gap, we have the same number of carriers in the VB and in the CB. In this case we can talk about *intrinsic semiconductor*. On the other hand, if we add some impurities or if the crystal has structural imperfections, the E_F can be shifted from the middle of the gap. The semiconductor is now called *extrinsic* and the number of holes and electrons is different. Sometimes the crystal should be so much doped that the Fermi level enters in the conduction (or in the valence) band. In this case the semiconductor is called *degenerate* and the Fermi level has almost the same meaning of the Fermi energy, because it well separates the empty zones from the filled ones and the semiconductor behaves like a metal.

Considering the extrinsic, non-degenerate case, we should have:

- **n-type** semiconductors if the number of holes in the valence band is less than the number of electrons in the conduction band and the Fermi level is shifted above the middle of the gap;
- **p-type** semiconductors if the number of holes in the valence band is bigger than the number of electrons in the conduction band and the Fermi level is moved below the middle of the gap.

[1] In statistical mechanics the Boltzmann constant is the ratio between the universal gas constant R and the Avogadro number N_A, $k = \frac{R}{N_A} = 1.3806488 \cdot 10^{-23} JK^{-1}$.

[2] It is a different concept than the Fermi energy, because the second one is defined as the energy that well separates empty levels from filled levels (useful concept for metals and degenerate semiconductors).

The creation of extrinsic semiconductors can take place via the *doping* technique, a method which consists in the introduction of foreign atoms (impurities) which replace the ones proper of the material. If they provide electrons to the material they are called *donors*. An example of donor is phosphorus (P), which has a valence electron more than silicon (Si). It creates a defect in the periodical structure of the silicon crystal, placing an electron next to the conduction band. It is sufficient a little thermal excitation (and so a small energy) to send the electron towards the CB ionizing the donor, which assumes a positive charge. On the other hand, if the foreign atoms introduced via the doping provide holes to the material, they are called *acceptors*. An example of acceptor is boron (B) which has only three valence electrons. In a silicon crystal, it creates a defect slightly above the VB and with a little thermal excitation an electron can jump from the valence band to the acceptor state, conferring it a negative charge. An illustration of the donor and acceptor levels position is shown in Fig. 1.1.

In a typical lattice, the number density of atoms is of the order of $10^{23} cm^{-3}$, while the density in volume of donors (or acceptors) is $N_d \sim 10^{16 \div 18} cm^{-3}$.
If we want to know the density of electrons in the conduction band, and the density of holes in the valence band, it is necessary to use, as stated above, the Maxwell-Boltzmann distribution. In fact:

- Assuming $E_C - E_F > 2kT$, we find that $n = N_C e^{[-\frac{(E_C - E_F)}{kT}]}$, where E_C is the energy of the edge of the conduction band and N_C is the effective density of states in a neighborhood of the CB bottom;

- Assuming $E_F - E_V > 2kT$, we find that $p = N_V e^{[-\frac{(E_F - E_V)}{kT}]}$, where E_V is the energy of the edge of the valence band and N_V is the effective density of states in a neighborhood of the VB top.

1.3 Surface states

At the external surface of a real crystal there is a sudden interruption of the regular reticular structure (Fig. 1.2). This gives birth to mechanisms of rearrangement in the crystal structure that produces an increasing reactivity of surface atoms or ions with respect to those of the *bulk*. There is essentially a perturbation which acts on the periodicity of the lattice on the surface. This perturbation is strong enough to create new localized electronic energy states, named *intrinsic*.

Most of the metal oxide semiconductors are ionic compounds. Surface ions are not coupled with the corresponding ions of opposite charge: metallic cations attract electrons acting as acceptors, while oxygen anions release electrons acting as donors. The unpaired electron represents an orbital, partially extended outside the surface of the semiconductor.

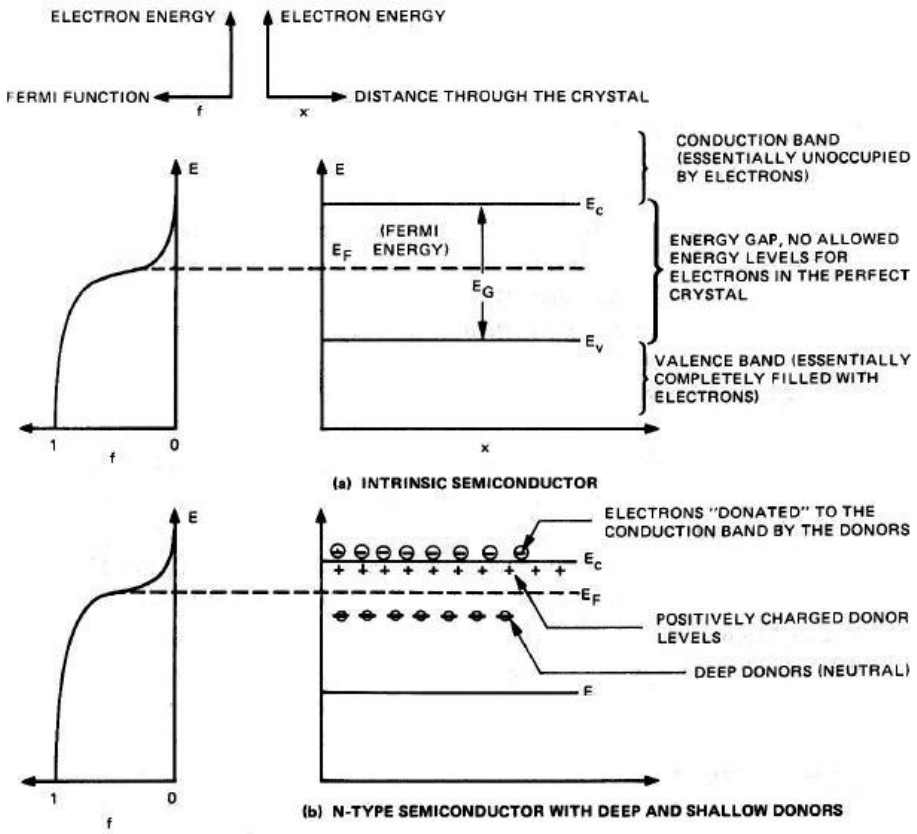

Figure 1.1: Fermi function and band diagram for an intrinsic (a) and an extrinsic (b) semiconductor [1].

In a similar situation the unpaired electron can capture another electron in order to form a pair, or it can enter the *bulk* of the crystal freeing a surface state. At this point it is easy to understand why at the surface there are both acceptors and donors, as in the band model of surface states in Fig. 1.3 (for simplicity here is illustrated the "flat band" case).

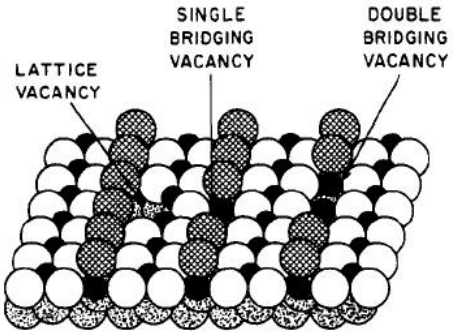

Figure 1.2: Example of surface defects for a surface of TiO_2.

1.4 Double layer

It is easy to guess that the "flat band" configuration is far from equilibrium. Electrons in the CB are characterized by an higher energy level than that of surface acceptors (Fig. 1.3). When acceptor states are totally empty, while donors totally filled, the E_F should necessary be in an intermediate position.

As a consequence, the electrochemical potential of electrons inside surface states is smaller than the electrochemical potential which characterizes the CB, and electrons here tend to migrate towards surfaces states, in order to minimize the energy of the system. This phenomenon leads to the formation of an accumulation layer of surface charge, balanced by the charge of donor ions located inside the *bulk*.

Fig. 1.4 represents schematically the migration of charge of donor ions towards a n-type semiconductor. There is the formation of the so called "double layer", consisting of positively charged donor ions which acts as a space charge, located at one side and, on the other side, of negatively charged states displaced on a plane. So the relative electric field arises in the external region.

Now it can be introduced the concept of **depletion layer**, a region in which the only uncompensated charges present are donors, with a intrinsic carrier density $N_i = N_d - N_a$ (where N_d and N_a are the density of donors and acceptors respectively). All mobile carriers inside the depletion layer are inevitably led to migrate towards the surface.

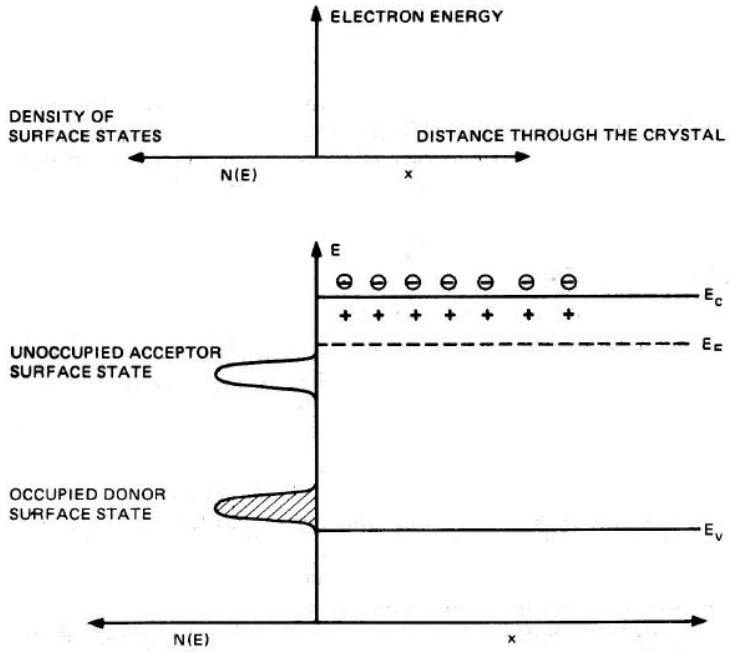

Figure 1.3: Neutral surface states in an n-type semiconductor: donors are occupied while acceptors are not. In the schematic representation, energy bands are represented for simplicity as a single level [1].

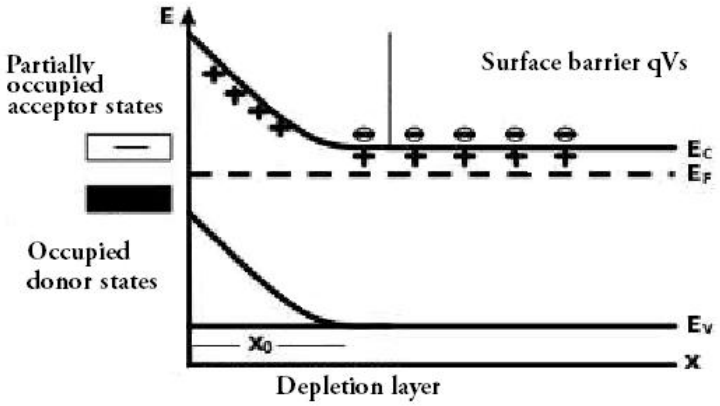

Figure 1.4: *Double layer*. Electrons in the conduction band are captured by surface states, creating a negative surface which contrasts the presence of positive charged donors just below it [1].

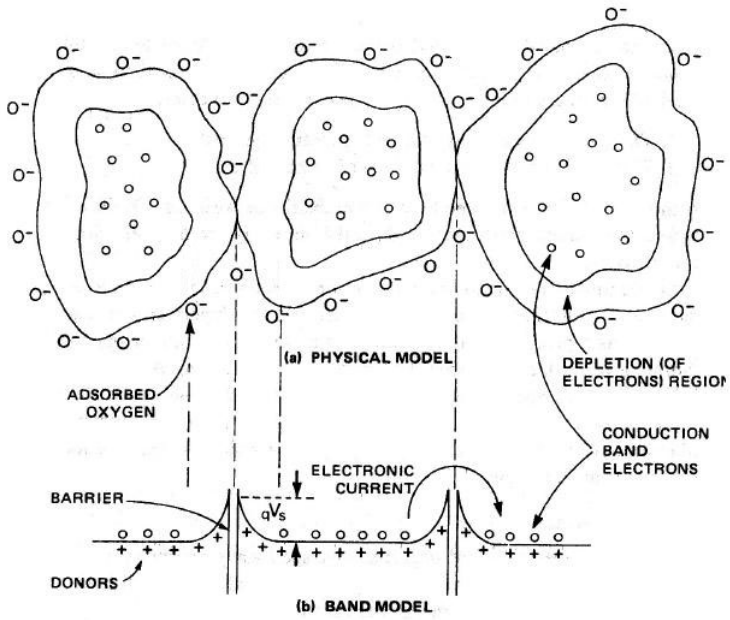

Figure 1.5: On the top grains are schematically represented with their structure composed by a bulk at the center, the depletion layer and the surface occupied by oxygen ions; on the bottom a schematic representation of the potential barriers between grains [1].

Fig. 1.5 represents intuitively the effects of absorption of oxidizing chemical species on the surface of the semiconductor grain: the contribution to the formation of a surface charge layer is responsible for the creation of an intergranular potential barrier that electrons must surpass to cross multiple grains.

1.5 Poisson equation and Depletion Approximation

We consider now an idealization of the actual charge distribution in the depletion region that originates from the fact that the majority carriers have been removed. We say this region is depleted of majority carriers. It facilitates the use of Poisson equation because we can obtain a closed-form solution. When using *depletion approximation* (*DA*), we are assuming that the carrier concentration (n and p) is negligible compared to the net doping concentration (N_a and N_d) in the depletion region. Outside this region, it is assumed that the net charge density is zero.

The monodimensional Poisson equation connects the potential to the charge density. In the case of *DA* it assumes the following form:

$$\frac{d^2\phi}{dx^2} = \frac{qN_i}{\epsilon_r\epsilon_0} \quad , \tag{1.2}$$

where ϕ is the electric potential, depending on the distance x from the surface; N_i is the density of ions in the space charge region; ϵ_r is the relative dielectric constant of the material and ϵ_0 is that of vacuum. If the material is homogeneously doped, the density of donors (or acceptors) is independent of x and N_i is constant in the equation 1.2.

In order to interpret the functional form of the equation 1.2, it is convenient to perform a coordinate transformation to introduce the energy owned by an electron instead of the electric potential. We define the function V as:

$$V(x) = \phi_b - \phi(x) \quad , \tag{1.3}$$

where ϕ_b is the *bulk* potential of the semiconductor. Substituting the function 1.3 in the equation 1.2 and then integrating we obtain:

$$\frac{dV}{dx} = \frac{qN_i(x - x_0)}{\epsilon_r\epsilon_0} \quad , \tag{1.4}$$

where x_0 is the thickness of the space charge region, determined by the need of totally compensating the layer of surface charge. By imposing the boundary condition for the electric field $[\frac{dV}{dx}]_{x=x_0} = 0$ at the equation 1.4, the semiconductor is discharged for $x \geq x_0$. Inside *n-type* materials, the number of electrons per unit surface, extracted from the surface

region of thickness x_0 is given by: $-N_d x_0 = N_i x_0$ (in fact N_d is the density of positive donors, N_a of negative acceptors, therefore $N_i = -N_d$ in a n-type semiconductor, while $N_i = N_a$ in a p-type one). This value should equally be referred to electrons which are migrated towards the surface, so $N_d x_0 = N_s$ (*neutrality condition*), where N_s is the density of the charged surface states. Integrating another time the equation 1.2 and imposing the boundary condition $V = 0$ for $x = x_0$, we obtain:

$$V(x) = \frac{qN_i(x - x_0)^2}{2\epsilon_r\epsilon_0} \quad . \tag{1.5}$$

Calculating the value of equation 1.5 at $x = 0$, it emerges the so called **Schottky relation**, that express the value of the surface barrier V_s (that is the potential V at $x = 0$):

$$V_s = \frac{qN_i x_0^2}{2\epsilon_r\epsilon_0} \quad . \tag{1.6}$$

Electrons must have an energy at least equal to qV_s to be able to migrate towards surface energy levels. Remembering that $N_i x_0 = N_s$, the relation 1.6 can also be written in the following form:

$$V_s = \frac{qN_s^2}{2\epsilon_r\epsilon_0 N_i} \quad . \tag{1.7}$$

The equation 1.7 is of fundamental importance to quantify the potential difference between the surface and the *bulk*: the energy *gap* which separates surface-electrons from bulk-electrons as a function of N_s.

The entire calculation has been done assuming a "clean"[3] surface, but in a more general case V_s can also be related to the density of adsorbed oxygen ions (O_2^- and O^-) and of oxygen atoms still present in the atmosphere in a molecular form (O_2), interesting for sensors operating in air.

1.6 Limits of planar geometry

In the previous section we have talked about the "Schottky barrier"[4], but it is generally contextualized in the field of DA in planar geometry. In the case in which the average radius of the semiconductor grain is comparable to the width of the *depletion layer*, curvature effects start to be relevant.

[3] A "clean" surface is a surface with no adsorbed gas.

[4] The appellative "Schottky barrier" refers to the surface barrier of potential V_S expressed by the Schottky relation 1.6.

In order to describe curvature effects, we start writing the Poisson equation 1.2 in spherical coordinates:

$$\frac{1}{r}\frac{d^2}{dr^2}[r\phi(r)] = -\frac{qN_d}{\epsilon} \quad , \tag{1.8}$$

where N_d is the density of donors (supposed to be totally ionized at the working temperature of the sensor) and ϵ is the absolute dielectric constant of the material.

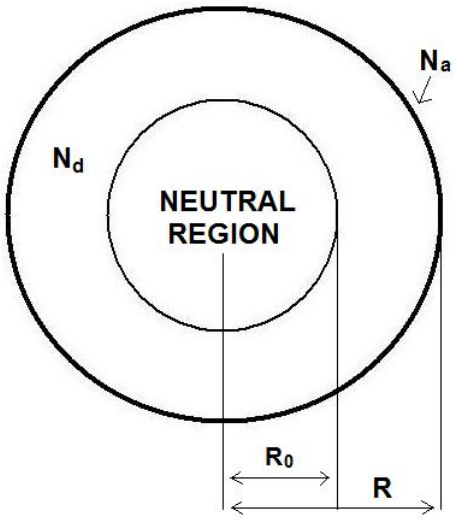

Figure 1.6: Semiconductor grain. N_a is the acceptor density on the surface and N_d donor density in the depletion layer.

Referring to Fig. 1.6, R is the grain radius and R_0 is the radius of the internal neutral region. For the DA, the density of charge is qN_d in the region of thickness $R - R_0$ and zero otherwise. Then, the potential $\phi(r)$ is zero at $r = R_0$ and if $r \leq R_0$ also the electric field is zero. It follows that the width $R - R_0$ represents both the thickness of the *depletion region* and the extinction length of the potential.

The difference between the value of the potential at the center of the grain and the value of the potential at the surface is named **built-in-potential (V)**, while the right boundary conditions to impose at the Poisson equation in spherical geometry 1.8 are:

$$[\phi(r)]_{R_0} = 0 \quad ; \tag{1.9}$$

$$\bigtriangledown\phi(r)|_{R_0} = 0 \quad . \tag{1.10}$$

The analytical solution for the electric potential is:

$$\phi(r) = -\frac{qN_d}{6\epsilon}r^2 - \frac{qN_d}{3\epsilon}\frac{R_0^3}{r} + \frac{qN_d}{2\epsilon}R_0^2 \tag{1.11}$$

for $R_0 \leq r \leq R$ and zero otherwise. The passage to the spherical geometry generates in the solution 1.11, an hyperbolic term of Coulomb nature. This term becomes relevant in the limit $R_0 \to 0$. In fact in the DA for planar geometry, the expression for the potential 1.5 shows only the parabolic term but not the hyperbolic one. If the grain is globally neutral, the density of surface charge qN_a exactly compensates the space charge in the depletion region and the following relation becomes valid:

$$N_a = N_d\left(\frac{R}{3} - \frac{R_0^3}{3R^2}\right) \quad . \tag{1.12}$$

Although the model described is of spherical nature, it is still based on the DA. However, when the dimension of the grain becomes lower than a limit value, this approximation gets inadequate. In this case, the expression which correctly express the density of charge of an n-type semiconductor is:

$$\rho(r) = qN_d - qN_d e^{\frac{q\phi(r)}{kT}} \quad , \tag{1.13}$$

where the exponential term represents the contribution given by mobile charge carriers at a temperature higher than the absolute zero. In particular the charge density qN_d, calculated in the hypothesis of DA, is obtainable from the expression 1.13, considering the energy (and so the potential) to be zero at the value E_{CBB} (*Conduction Band Bottom*) of the *bulk*.

In the case of nanostructured powder, the E_{CBB} level is reachable only in the case in which the grain is sufficiently big, whereas using the DA it is implicitly assumed that the potential has to be zero independently from the dimensions of the grain. In the case of non-applicability of the DA, the Poisson equation in spherical geometry becomes:

$$\frac{1}{r}\frac{d^2}{dr^2}[r\phi(r)] = -\frac{qN_d}{\epsilon} + \frac{qN_d}{\epsilon}e^{\frac{q\phi(r)}{kT}} \quad . \tag{1.14}$$

In this case, the new boundary conditions are different from the constraints (1.9 and 1.10) implied in the DA. In fact, the spherical symmetry requires that, at the center of the grain, the electric field is zero, whereas the potential $\phi(r)$ is zero at the CBB only if the grain is sufficiently big. It is also necessary to modify the definition 1.13 of the charge density ρ. The potential on the surface $\phi(R)$, if referred to that of CBB, assumes a value independent on R and uniquely determined by working conditions (the type of semiconductor, the type of doping, the temperature and environmental conditions).

Defining $\phi(R) = V_s$, the boundary condition obtained for the equation 1.14 is:

$$\phi(R) = -V_s \quad . \tag{1.15}$$

Nevertheless, the comparison between V_s and what we can experimentally measure is difficult. In fact, the most frequently used methods in order to determine the surface potential, measure the *built-in potential* V, defined as the difference $V = \phi(0) - \phi(R)$ between the CBB-potential (at the center of the grain) $\phi(0)$ and the potential on the surface $\phi(R)$. If $R \geq \Lambda$ (where Λ is the extinction length of the potential), $\phi(0)$ is effectively zero and $V = V_s$, on the other hand, if $R < \Lambda$, dimensions of the grain are not sufficient to cancel $\phi(0)$ and the boundary condition 1.15 is incorrect.

Analogously to what happened in the regime of the DA it is necessary to impose the neutrality of the grain: the integral of the density of charge extended to the total volume of the grain must be equal to the integral of the density of surface states N_s, assumed to be uniform over the entire surface:

$$4\pi \int_0^R \left(qN_d - qN_d e^{\frac{q\phi(r)}{kT}} \right) r^2 dr = 4\pi R^2 q N_s \quad . \tag{1.16}$$

Hence, the system of equations that defines the model based on the correct density of charge $\rho(r)$ is:

$$\frac{1}{r}\frac{d^2}{dr^2}[r\phi(r)] = -\frac{qN_d}{\epsilon} + \frac{qN_d}{\epsilon} e^{\frac{q\phi(r)}{kT}} \quad ; \tag{1.17}$$

$$-\left.\frac{d\phi(r)}{dr}\right|_{r=0} = 0 \quad ; \tag{1.18}$$

$$\phi(r)|_{r=R} = -V_s \quad ; \tag{1.19}$$

$$-\left.\frac{d\phi(r)}{dr}\right|_{r=R} = \frac{qN_s}{\epsilon} \quad , \tag{1.20}$$

where the equation 1.20 follows from the neutrality condition 1.16. The model presents the unknown function $\phi(r)$ as dependent on six parameters (T, ϵ, V_s, N_d, N_s, R). N_d and

ϵ are characteristic and measurable values of the semiconductor, while the temperature T is known. Therefore, after setting these three parameters, the value of V_s is influenced only by the working atmosphere of the sensor and it can therefore be determined through a particular procedure of measurement of the conductance, named *Arrhenius plot*. This measure must be performed in conjunction with a slow variation of the working temperature of the sensor itself.

Once established the type of semiconducting material and known the surrounding atmosphere, it becomes possible to calculate the potential $\phi(r)$ and the density of surface states N_s as functions of the grain radius R only.

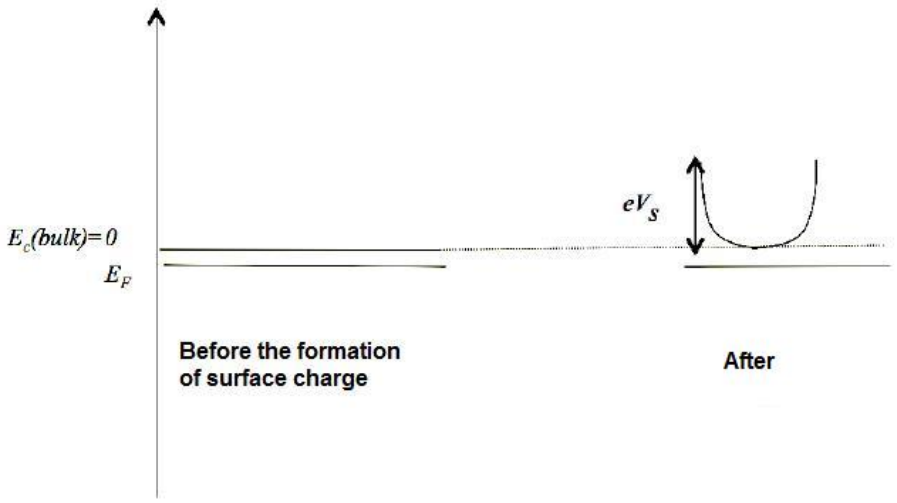

Figure 1.7: Representation of the band bending in the case in which $R > \Lambda$.

For example we can consider experimental data relative to SnO_2 in air ($T = 400°C$, $\epsilon = 10^{-10}\frac{F}{m}$, $N_d = 5 \cdot 10^{18}$ cm^{-3}, $V_s = 0.68V$) and it is so possible to numerically solve the equation 1.17. If generally $R > \Lambda$, the potential $\phi(r)$ becomes zero at a distance $\Lambda \simeq 8\lambda_D \simeq 22$ nm[5] from the surface.

In the figure 1.9 are shown the two numerical solutions of the equation 1.17 for $R = 100$ nm and $R = 30$ nm. In the first case $R \gg \Lambda \gg \lambda_D$ and the DA in planar geometry is sufficient to well describe the situation; in the second case $R \simeq \Lambda \gg \lambda_D$ and the planar approach is no longer valid even if the DA is still useful.

However, as soon as R became less then Λ, the potential would non to be able to cancel, even at the center of the grain: in this case the DA would no longer be valid. Here, the model based on the complete charge density $\rho(r)$ is preferable because it has not intrinsic

[5] $\lambda_D = 2.7$ nm is the *Debye length*.

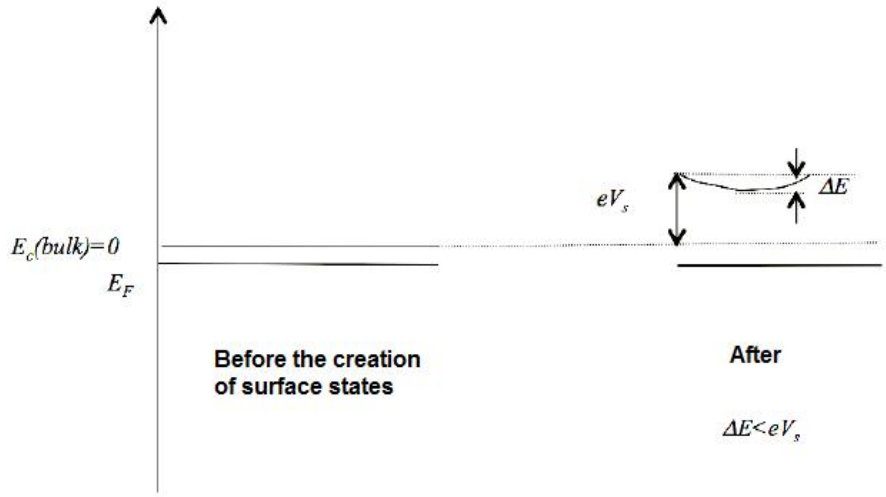

Figure 1.8: Representation of the band bending in the case in which $R < \Lambda$. It is possible to notice from the figure that, after the formation of the surface charge N_s, it follows a substantial flattening of the band bending between the surface and the center of the grain, smaller than the barrier eV_s.

limitations and it can be used for a wide range of values for the grain radius. In figure 1.10 it is shown the limiting case for which $R = 10$ nm and the potential cannot extinguish.

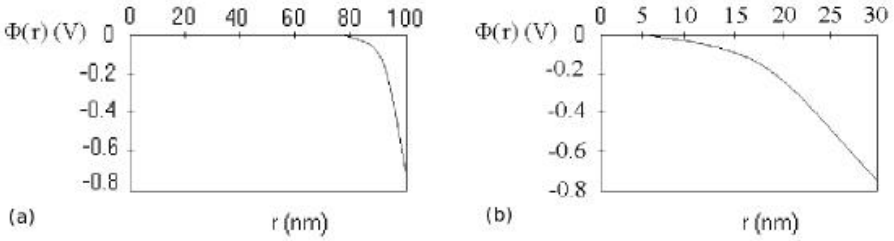

Figure 1.9: Functional form of the potential $\phi(r)$ for $R = 100$ nm (a) and $R = 30$ nm (b). In both the situations the potential becomes zero at a distance $\Xi = 22$ nm from the surface.

1.7 Surface reactions

The interaction between the n-type metal oxide semiconductor and the oxiding gases in general (first of all the oxygen), that acts as surface acceptors, is at the basis of complex chemico-physical mechanisms responsible for the conductivity variation of the material itself. In order to pass from grain to grain, electrons must cross the surface potential barrier at the external shell of all grains of the material.

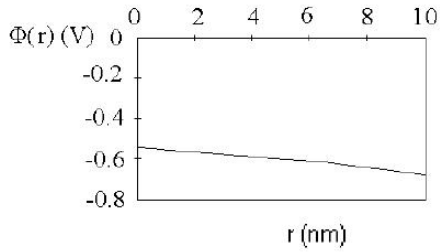

Figure 1.10: Functional form of the potential $\phi(r)$ for $R = 10$ nm. The potential does not vanish even in the center of the grain and the behavior is quite constant, differing from that predicted by DA.

The electrical conductivity of metal-oxide semiconductors is proportional to the density of electrons n_s at the grain surface and close to the superior limit of the potential barrier. Furthermore, n_s exponentially varies, following the surface barrier potential qV_s. In fact:

$$n_s = N_c e^{-\frac{qV_s + E_c - E_F}{kT}} = N_d e^{-\frac{qV_s}{kT}} \quad , \tag{1.21}$$

where N_c is the effective density of energy states near the CBB. Therefore, it is necessary to present a model capable of describing variations of the density n_s, due to the adsorption of the atmospheric oxygen on the surface of the semiconductor. For a complete treatment, we must take on account also other atmospheric (reducing or oxidizing) gases.

Chapter 2

Thick film sensors: production process

The combination of nanocrystalline materials and the serigraphic technology[1] allows the production of nanometric sensing films of ceramic type, electrically stabilized at high temperatures. In order to be employed for gas detection, gas sensors must rely on the following characteristics:

- good sensitivity even at low gas concentration;
- reliability;
- repeatability of the measurement;
- low energy consumption;
- small dimensions;
- good cost-performance ratio;
- ease of automation;
- versatility

In order to obtain these features, it is necessary to adopt a specific production process named *thick film* technology. To understand the preparation process of thick film sensors it is necessary to summarize all the crucial aspects of the fabrication process. Thick film technology is a particular form of serigraphy introduced in technology during the '70s, to build printed hybrid circuits. It was employed in the construction of electronic components used in various sectors. Thick film hybrid circuits are famous for their multiple qualities

[1] Serigraphy is one of the more ancient techniques of reproduction of graphic arts.

as compactness, robustness, low cost. Thick film technology is also relevant because it allows to realize very precise geometries, for this specific reason it is useful in the sensor field. In the last years, the serigraphic technique is highly evolved, even if the application procedures have not substantially changed. However, what makes the thick film technology suitable for the sensors realization is its low cost combined to the capability of operating also in hostile working conditions.

The production process is summarized in Fig. 2.1.

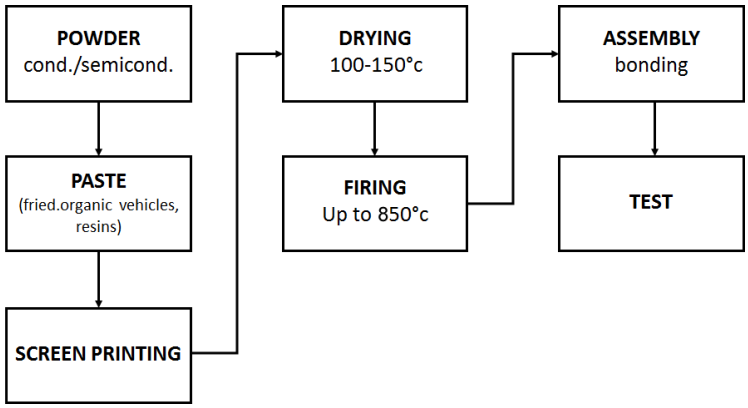

Figure 2.1: Production process scheme for thick film gas sensors.

2.1 Substrate

Substrates used for gas sensors have the dual task of mechanical support for the sensing layer and of electric insulator between the functional part (sensing film) and the circuit elements. The most widely used substrate is Al_2O_3 (alumina), because of its good thermal stability and resistance to corrosion and use, its excellent dielectric properties and low cost. Alumina powder is obtained from bauxite (the principal source of aluminum existent in nature). It is ground together with other oxides (SiO_2, NaO, MgO) in order to obtain a substrate with the desired physico-chemical characteristics. Grinding is obtained through a mill with blades, to ensure a good mixing level. After that, the obtained compound undergoes two treatments at different pressure, depending on the desired thickness (later or less than 1 mm). Then, after imposing a shape to the substrate, it is exposed to firing treatment for 12-24 hours. This thermal treatment is composed by two main steps:

- *pretreatment*, performed at 300-600°C and necessary to eliminate organic additives, employed for grinding;
- *sintering*, performed at 1500-1700°C and serves to promote the adhesion between powder particles by means of two steps, indicated as "densification" and "growth of

grains". Densification is a process that reduces the porosity of the sample, making it denser; the growth of grains, instead, is a process which increases the average dimension of the particles constituting the material. While densification needs high temperatures, the growth of grains occurs naturally during the process itself. The modulation of temperatures and of total firing times is the key to optimize physico-chemical characteristics of materials.

The substrate should not play an active role in the sensing activity, moreover a certain compatibility between the sensitive layer and the support must subsist, in order not to create tensions as a result of thermal expansion. Then, substrates have to be characterized by a smooth and uniform surface and by the lowest number possible of visible surface defects. Furthermore the substrate materials must have a chemical and physical compatibility with the materials with which they are in contact.

2.2 Screen printing

To be interfaced with the control electronics and to be placed onto the substrate, the active material of the semiconductor must be mixed with other substances, obtaining a paste, whose main components are:

- the active material (semiconductor metal-oxide or -sulfide);
- the frit;
- organic vehicles.

The active material consists of a nanometric powder made of semiconducting particles, with an average diameter smaller than 100 nm, which must be chosen depending on the type of gas to be detected. Therefore, the first step consists in the powder preparation in laboratory. The second step consists in the ink preparation, a powder suspension in one or more organic vehicles suitably dosed. Then, the frit must be added to the preparation in small percentages in weight, depending on the powder used. The frit is a powder composed of a mixture of glassy oxides based on silica (SiO_2) charged with alkaline-earth oxides or with oxides of the IV group, to modify its behavior with temperature. Its function is to join particles together and to anchor the paste to the substrate. The first aspect is of fundamental importance in order to form an uniform network of particles and also to obtain intergranular Schottky barriers; the second aspect is practical and is essential to avoid the detachment of the film. Organic vehicles are generally made with organic solvents, in which resins and surfactants are dissolved, in order to optimize the dispersion of solid particles inside the medium and to regulate the viscoelastic behavior for an ideal printing. The organic vehicle is completely removed in the following thermal processes.

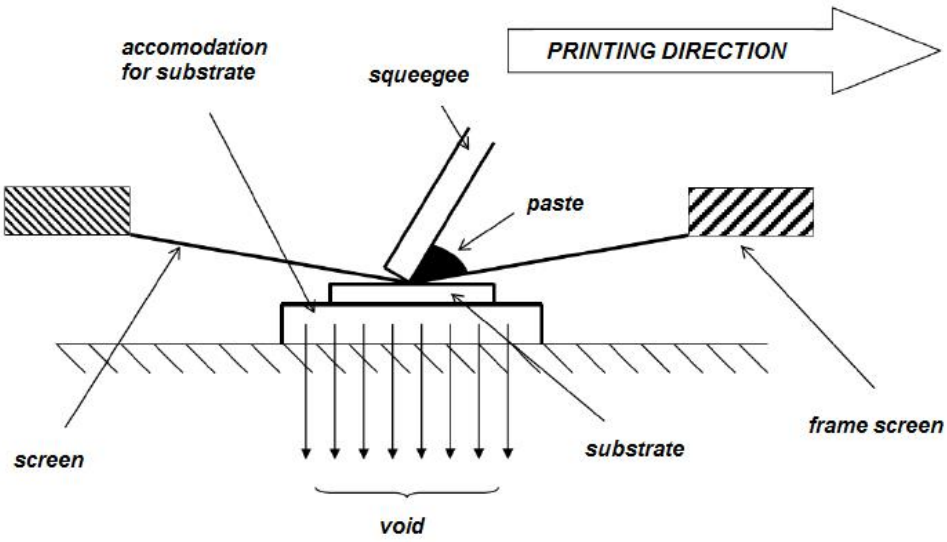

Figure 2.2: Screen printing, lateral simplified section of the machine.

The printing of the paste on the substrate is carried out with a screen printing machine (see Fig.2.2).

The essential components of a screen printing machine are:

- screen, which shows the geometry of the design to be printed;
- squeegee, a spatula which exerts pressure and allows the paste to cross the screen and to settle on the substrate, reproducing the design with high quality.

A typical screen consists of a network of finely twisted steel wires (of 100μm), stretched over a frame of aluminum. As shown in Fig. 2.3, between cables there is an empty space. In order to characterize a printing screen, a specific unit of measure, named *mesh*, should be defined. The mesh number corresponds to the number of wires per linear inch that can be calibrated as a function of the required application. The cables network is covered by an UV-sensitive emulsion, on which the design to be printed is photographically impressed. Moreover, the screen presents some areas in which the emulsion is absent, through which the paste can be printed on the substrate. Therefore the function of the printing screen is to define the design and to calibrate the quantity of paste. The paste must be a pseudo-plastic fluid, which varies its viscosity as a function of the applied stress.

The squeegees must be resistant to solvents involved in the process and present in the paste. Squegees are two: the first one forces the paste through the screen, the second one works in the opposite direction and reports the paste in the initial position for a new print.

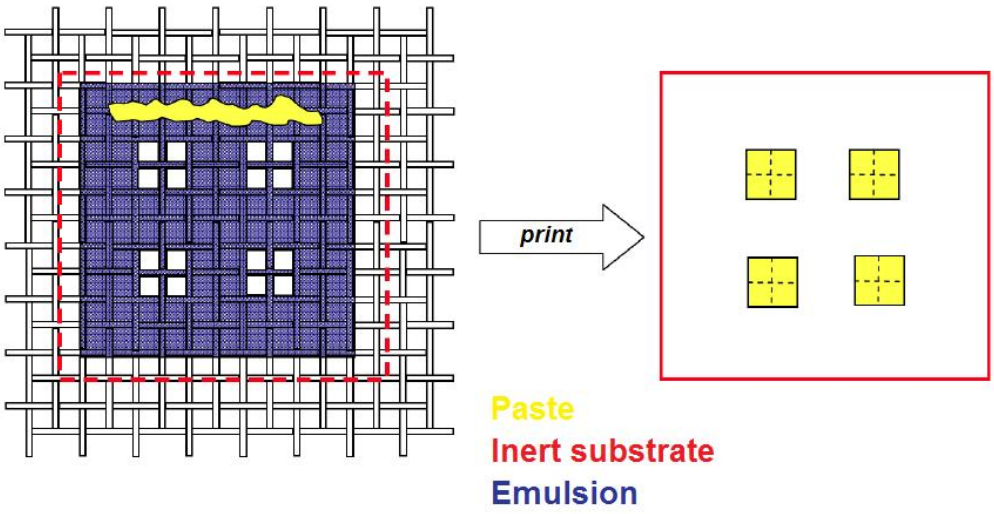

Figure 2.3: Illustration of the squeegee passage on the screen after the application of the photosensitive emulsion and of the paste.

2.3 Drying and Firing

Once printed, the ink undergoes two different treatments: the *drying* and the *firing*. The *drying* is a low-temperature treatment, in the range between $100 - 150°C$ that serves to eliminate the most volatile organic solvents and to avoid the draining of the printed ink. It can be done in a common airy hotplate or in an infrared oven.

The *firing* is a high-temperature process (up to 850°C) made in a muffle furnace or in an infrared oven. It serves to eliminate all organic additives used to obtain the ink and to leave on the substrate only the film composed by the functional material and by the small percentages of frit. During these two processes, the temperature must be rigorously controlled, in order to limit the formation of cracks on the handwork, that may prejudice conductive phenomena through the material.

2.4 Assembly

The sensor must be assembled by means of a technique named *bonding*, which consists in the connection of the sensor to a support, by using four pins (Fig. 2.4). These pins are welded to the heater by thermo-compression and to the contacts of the plate on which the film is deposited.

This connection, powered by gold wires (99.99%) with a diameter of 0.06 mm, is carried out via the apparatus shown in Fig. 2.5, named bonder.

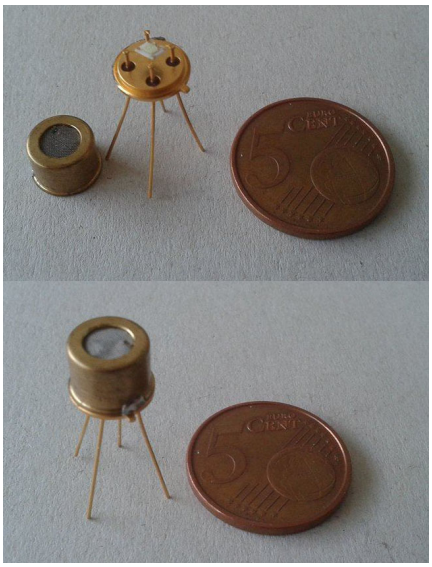

Figure 2.4: Bonded sensors open (up) and closed (down) compared to a five-cent money.

Figure 2.5: Instrument for the assembly (bonder).

2.5 Powder synthesis: *sol-gel* technique

Chemical techniques used to obtain in laboratory polycrystalline semiconductors, are essentially of two types: first the conventional chemical-mechanical techniques as the synthesis for solid state reaction, second the more recent techniques called "wet", that occur in solution. Through wet-techniques, by controlling reaction parameters as temperature, pH and purity of reagents, materials with controlled requirements can be obtained. The mainly used technique at the Sensors and Semiconductors Laboratory consists in the so called *sol-gel* process. It is a chemical treatment performed in solution, responsible for the synthesis of ceramic or glassy materials. It has, in fact, many advantageous features as versatility, relative simplicity, economy and, above all, it allows to obtain spherical nanoparticles with an high degree of purity and with a singlemode distribution of the grains size.

The fundamental steps of the *sol-gel* technique are the following:

- a starting reactive (dissolved in water or alcoholic solutions) is converted in a colloidal suspension (*sol*) of the precursor of the final oxide (*gel*), through processes of *hydrolysis* and *condensation*;
- removal of the solvent, through evaporation;
- execution of an irreversible thermal oxidation of the precursor from which the final oxide, with a well defined crystalline structure, is obtained.

2.6 Humidity effects

The change in the sensors response in *wet* conditions can be interpreted as the negative effect due to the surface adsorption of OH^- groups, competing with the gas molecules in the reaction mechanism involving the film surface. The result of the interaction between H_2O molecules in the wet ambient and the surface of the film, is the deposition of a hydrogen atom (H) which binds to adsorbed oxygens (O^-), producing the hydroxyl group (OH^-). Consequently, the number of available active surface states decreases. On the other hand, by increasing the temperature, an increasing number of OH^- groups leave the reactive sites and the water molecules lesser interfere with the reaction involving the gas.

As an example, an investigation of the humidity effects was made on SnO_2-based sensors in CO detection (Malagù et al., 2006) [3]. The result is the suggestion of an algorithm for compensating water vapor pressure in the gas detection.
From the Clapeyron equation, it is possible to derive the partial water vapor pressure as an analytical function of the relative humidity (RH) and the temperature (T):

$$p_{H_2O} = \frac{RH}{100} \times g \times e^{-\frac{f}{T}}, \tag{2.1}$$

where g and f are parameters obtained by fitting the saturation water vapor pressure tables. If either CO or humidity are let vary in a test chamber, the sensors conductance shows the following dependence on gas concentration: 1) $G(H_2O) = a + bp^{\alpha}_{H_2O}$ and 2) $G(CO) = c + d[CO]^{\gamma}$, where a and b are functions of the CO concentration and c and d are functions of the water vapor pressure. Experimental evidence proves that a and g are nearly constant [3]. By substitution of (2) in (1), under the hypothesis of nearly constancy of the exponents, the result is an analytical surface whose expression contains an interaction term.

$$G(p_{H_2O}, CO) = G_0 + Ap^{\alpha}_{H_2O} + B[CO]^{\gamma} + Cp^{\alpha}_{H_2O}[CO]^{\gamma} \tag{2.2}$$

A 3D fit allows one to determine the parameters (see Fig. 2.6).

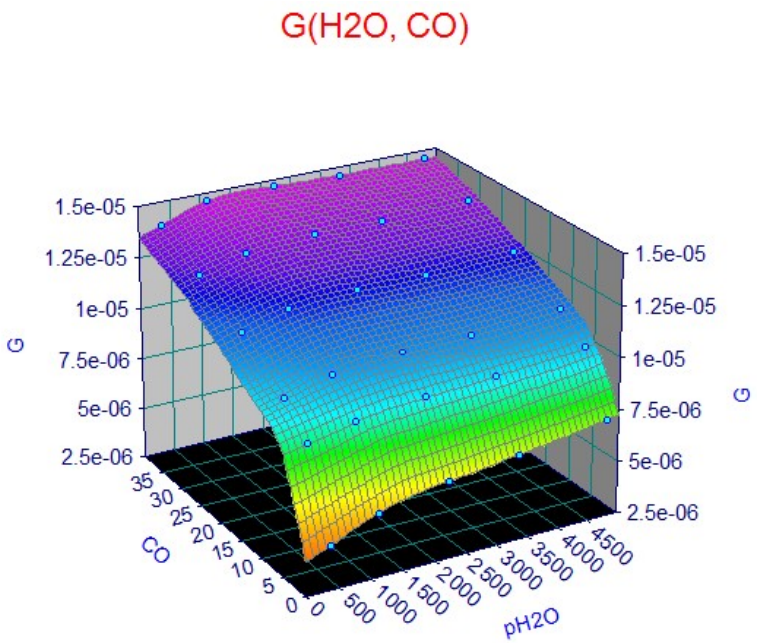

Figure 2.6: Analytic 3D surface that fits the concentration of H_2O and CO [3].

The analytical expression can be inverted to work out unknown CO concentrations once the humidity has been measured (Eq. 2.3). The algorithm keeps working as soon as the sensor signal is stable.

$$[CO] = \left(\frac{G - G_0 - Ap^{\alpha}_{H_2O}}{B + Cp^{\alpha}_{H_2O}} \right)^{\frac{1}{\gamma}} \tag{2.3}$$

Humidity interferes with the sensing mechanism if it was demonstrated that is the vapor partial pressure and not the RH that modifies the sensor behavior.

$$p_{H_2O} = RH(T)ae^{-\frac{b}{T}}, \tag{2.4}$$

Injecting, separately, in the test chamber water vapor and CO, see (1) and (2). In the presence of a mixture of CO and water vapor, c and d become water vapor functions. Experimental evidences prove that α and γ remains constant.

2.7 In-diffusion effects

It is widely accepted that barriers formed between particles or grains have a Schottky-type nature and they govern the electrical behavior of the sensor. Adsorption of gaseous species at the grain boundaries can induce changes in the barrier height and in the donor concentration. Many metal-oxide semiconductors contain a large number of oxygen vacancies conferring their n-type character. Chemisorbed oxygen species (O^{2-} and O^{-}) from the air act as electron acceptors and lead to the formation of a depletion layer extending into the grains and originating the surface barrier. These surface barriers play a key role in the sensing mechanism, as they control electron transfer between grains, affecting the overall resistance [4]. The mechanism at the surface of a metal-oxide sensor is described in Fig. 2.7, where the letters from a to d indicate:

- (a) oxygen exchange equilibrium between the atmosphere and the grain surface;
- (b) diffusion of oxygen in and out of the grain;
- (c) interstitial-vacancy creation and recombination;
- (d) energy band diagram.

At temperatures high enough (higher than about 200°C) oxygen diffusion into the grains can be detected, annihilating oxygen vacancies and thus reducing the donor concentration. Conversely, if oxygen diffuses out of the grains, vacancies are generated. The relevant passages from the gas phase to the bulk of the grain for oxygen are:

$$O_2(gas) \leftrightarrow O_2(ads) \leftrightarrow O^{-}(ads) \leftrightarrow O^{2-}(ads) \leftrightarrow O^{2-}(int) \leftrightarrow O^{2-}(latt) \tag{2.5}$$

where $O_2(gas)$ refers to oxygen in the environment, $O_2(ads)$ to an oxygen molecule adsorbed at the grain surfaces, $O^{-}(ads)$ and $O^{2-}(ads)$ to singly and doubly ionized monatomic oxygen at the grain surface, $O^{2-}(int)$ to interstitial oxygen, and $O^{2-}(latt)$ to oxygen at the metal-oxide lattice. In the last part of the relation 2.5, interstitial oxygen migrates from the surface to the bulk, annihilating oxygen vacancies, V^{++}, i.e., making the equation explicit:

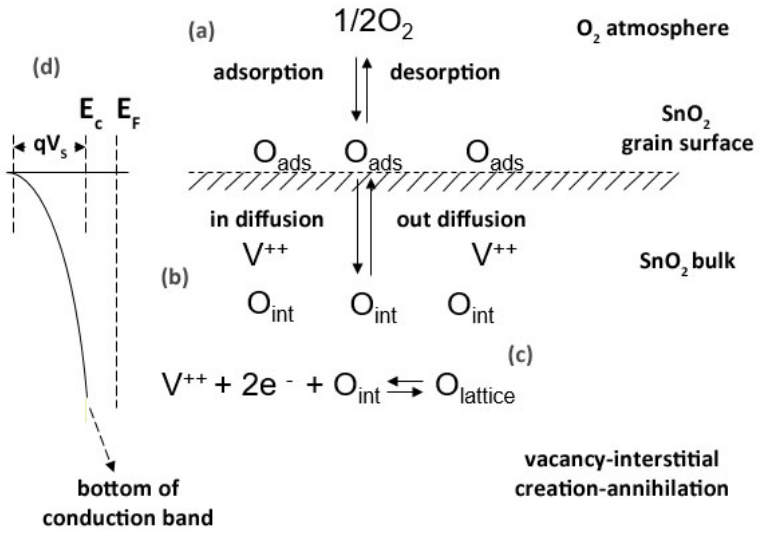

Figure 2.7: Basic mechanism in n-type metal-oxides.

$$V^{++} + O^{2-}(int) \leftrightarrow O(latt) \tag{2.6}$$

Thus, after oxygen treatment, at high enough temperatures, a V^{++} decrease can be expected. Conversely, during vacuum treatments, the oxygen vacancies concentration (V^{++}) is expected to increase.

Let us investigate now on the equation:

$$O_0 \leftrightarrow V^{++} + 2e^- + \frac{1}{2}O_2, \tag{2.7}$$

according to the mass action law, the concentration of oxygen will be:

$$K = [V^{++}]n^2 p(O_2)^{\frac{1}{2}} \tag{2.8}$$

Separating the two steps of this process, the first is the extraction of an oxygen atom from a lattice site inside the crystal and its landing at the surface (see Eq. 2.9, 2.10), the second is the adsorption process at surface, where S is a surface site (see Eq. 2.11, 2.12)

$$O_0 + S \leftrightarrow V + O^0{}_S, \tag{2.9}$$

$$\frac{[V][O^0{}_S]}{[S]} \propto e^{\frac{-E_{sur}}{kT}} \tag{2.10}$$

$$O^0{}_S \leftrightarrow \frac{1}{2}O_2 + S \tag{2.11}$$

$$\frac{p(O_2)^{\frac{1}{2}}[S]}{O^0{}_S} \propto e^{\frac{-E_{ads}}{kT}} \tag{2.12}$$

By combining Eq. 2.10 with Eq. 2.12, the vacancies concentration will be represented by Eq. 2.13:

$$[V] \propto p(O_2)^{\frac{-1}{2}} e^{\frac{-(E_{sur}+E_{ads})}{kT}}. \tag{2.13}$$

Here it is possible to introduce the quantity $E_{for} = E_{sur} + E_{ads}$, which is the total energy required to take an atom from a lattice site inside the crystal to the vapor phase. The Eq. 2.13 can be now rewritten as a function of this new value as:

$$[V] \propto p(O_2)^{\frac{-1}{2}} e^{\frac{-E_{for}}{kT}}. \tag{2.14}$$

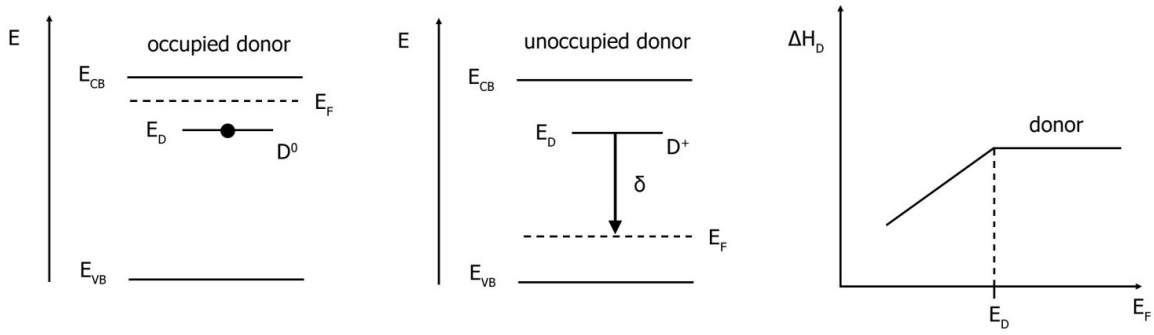

Figure 2.8: Dependence of the defect formation enthalpy ΔH_d on the Fermi energy.

In Fig. 2.8, is shown the dependence of the defect formation enthalpy ΔH_d on the Fermi energy. If $E_F > E_D$ the defect is electrically neutral and ΔH_d is not dependant from E_F; if, instead, $E_F < E_D$, the defect is positively charged and the e^- expelled is transfered to the electron reservoir (E_F), leading to an energy gain δ, lowering the ΔH_d [5]. To obtain $[V^{++}]$ electrons relaxed to the Fermi level lead to an energy gain: $E_{d1} - E_F + E_{d2} - E_F$. Defining $E_0 = E_{for} + 2E_c - E_{d1} - E_{d2}$ the resulting equation appears to be:

$$[V^{++}] = Cp(O_2)^{\frac{-1}{2}} exp - \frac{[E_0] - 2(E_c - E_F)}{kT} \tag{2.15}$$

At a fixed O_2 partial pressure and in equilibrium, the (ionized) oxygen vacancies density increases exponentially as E_F goes down in band gap, which results in the non uniform

doping level along the whole space charge region. Now, normalizing with the doping level in the bulk, N_d, the resulting equation is:

$$[V^{++}] = N_d exp \frac{2(E_c(x) - E_{cb})}{kT}. \tag{2.16}$$

Since $E_c(x) - E_{cb} = eV(x)$, one obtains:

$$[V^{++}] = N_d exp \frac{2eV(x)}{kT} \tag{2.17}$$

and the Poisson equation becomes:

$$\frac{d^2V(x)}{dx^2} = \frac{2e}{\epsilon} N_d exp \frac{2eV(x)}{kT} \tag{2.18}$$

In the case of SnO_2, E_0=2.2 eV [6], [7]. The Eq. 2.18 leads to:

$$V(x) = \frac{kT}{2e} ln \left[1 + tan^2 (\frac{x}{\sqrt{2} L_D}) \right], \tag{2.19}$$

where $L_D = (\epsilon kT/4e^2 N_d)^{1/2}$ is the **Debye length**.

In Fig. 2.9 is shown the the profile of the potential near the surface due to the band bending with the variable $x' = x/(2^{1/2} L_D)$. The inset shows the same potential in a log-log scale to show the abruptness of the potential. The width of the depletion region can be determined resorting to charge neutrality:

$$x_0 = \sqrt{2} L_D arctan \left(\frac{N_s}{2\sqrt{2} N_d L_D} \right) \tag{2.20}$$

and the height of the surface potential energy barrier is finally obtained:

$$V_S = \frac{kT}{2e} ln \left[1 + \frac{{N_s}^2}{8 {N_d}^2 {L_D}^2} \right], \tag{2.21}$$

In order to obtain the equation for the density of chemisorbed oxygen it is necessary to consider the fact that oxygen is adsorbed monatomically (working $T > 150$°C). From equation 2.11 and assuming low coverage, the concentration of surface states [S] can be taken as constant and the resulting relation is:

$$\frac{p(O_2)^{1/2}}{[{O_s}^0]} \propto exp(-E_{ads}/kT). \tag{2.22}$$

The ratio between ionized and neutral oxygen atoms at the surface depends on the Fermi level position as:

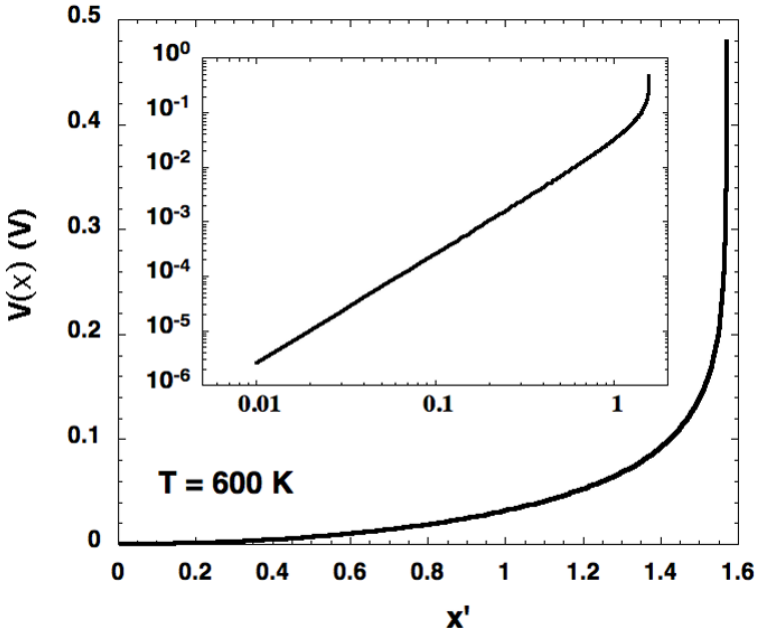

Figure 2.9: Profile of the potential near the surface due to the band bending [8].

$$\frac{[O_S{}^-]}{[O_S{}^0]} \propto exp[-(E_{cs} - E_F)/kT], \tag{2.23}$$

where E_{cs} is the ionization energy, which is the energy of an electron at the top of the surface barrier.

As a result [6]:

$$N_S = Ap(O_2)^{1/2} exp[-(eV_S + E_{cb} - E_F - E_{ads})/kT]. \tag{2.24}$$

To work out the equations through a numerical simulation of the barrier height, it has been assumed, as an example, that for a given oxygen pressure p_0 at $T = 600$K, the values obtained are $N_d = 1020\ 1/m^3$ and $N_s = 1017\ 1/m^2$. These values were chosen because they lead to regularly observed barrier heights. The Schottky barrier height results from the sum of $E_{cb} - E_F$ and eV_S and are reported in Fig. 2.10 [8].

Recently reported results by Barsan et al. [9] show a change in work function of about 53 meV at 300°C after a relative change in pressure of a factor 20.

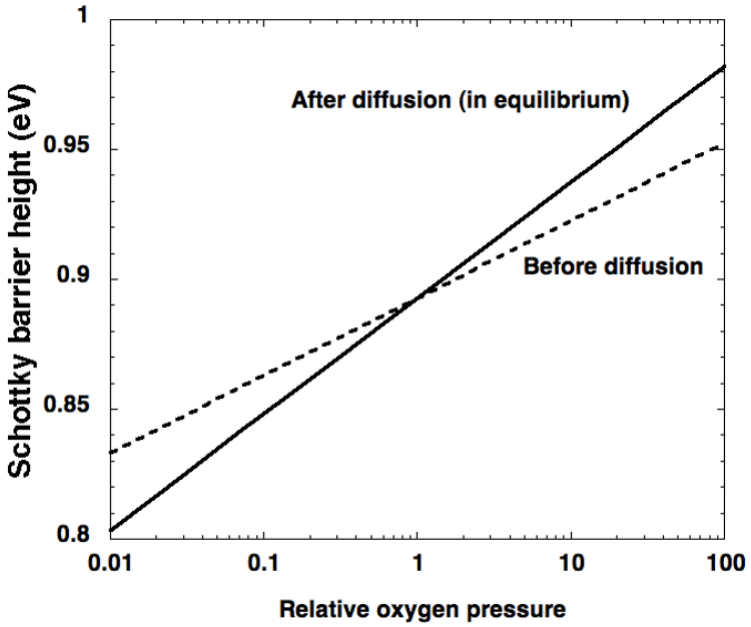

Figure 2.10: Schottky barrier height versus relative oxygen pressure before and after in-diffusion [8].

2.8 Sensor types

Sensors can be differentiated into two categories, depending on the presence or not of oxygen atoms in their chemical structure. The widely used sensing materials are of metal-oxide type, so they are composed of one or more chemical compound that contains at least one oxygen atom and one other element. In order to overcome the problem of in-diffusion (see Sec. 2.7) during the last years, the research on gas sensing has been focused in parallel on another category of materials: metal-sulfides. Due to the presence of sulfur instead of oxygen atoms inside their crystalline structure, these materials show a higher stability of response compared to their metal-oxide counterpart [24].

2.8.1 Metal-oxides

ZnO

ZnO has been a pioneering material in gas sensing (Seiyama et al., 1962 [10]). Zinc oxide has a direct wide band-gap (3.37 eV) semiconductor and exhibits high exciton binding energy (60 meV), which causes an efficient UV emission (∼380 nm). Among the various oxides, ZnO is particularly suitable to be synthesized in such nano-forms (Schmidt-Mende et al., 2007 [12]; Wand, 2004 [13]). ZnO mainly exhibits very good responses towards

oxidizing gases, in particular with ozone. ZnO has been successfully employed also to detect other gases, such as H_2, O_2, H_2S, LPG, $HCHO$ and NH_3. In addition to thermally activated gas sensors, ZnO is particularly suitable to be assisted by UV irradiation. In this operational mode, the sensors work at room temperature overcoming the main technical limitation of the high operating temperature, essential in chemo-resistive gas sensors.

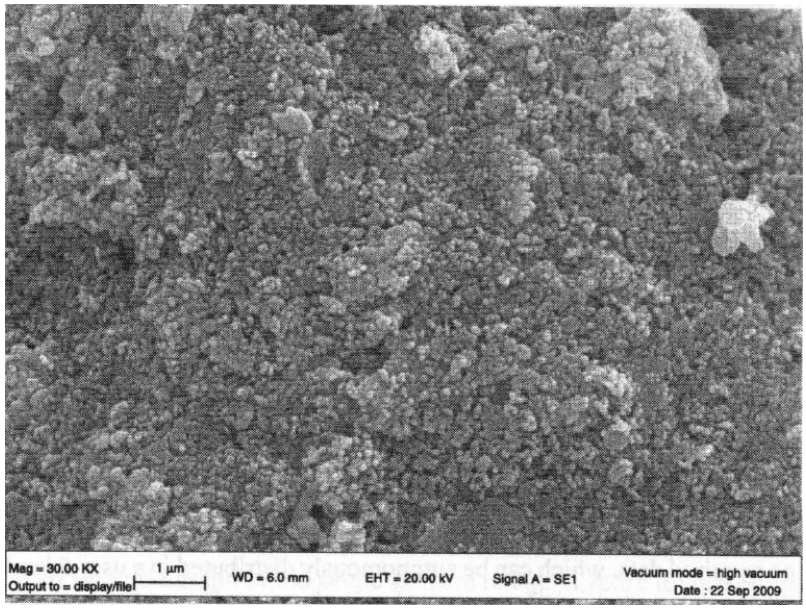

Figure 2.11: SEM micrograph of ZnO thick-film fired at 650°C [11].

SnO_2-based materials

Tin dioxide in the most widely used material for gas sensing. It exhibits n-type semiconductor behavior due to lattice defects, in particular oxygen vacancies acting as electronic donor levels. The typical behavior of SnO_2 energy barrier versus temperature exhibits a minimum and maximum corresponding to the increase of the depletion layer depth with temperature attributed to a negative surface charge accumulation, typically O^- ions. As the first material extensively investigated in gas sensing, many studies have been performed to improve the sensing and selectivity properties of SnO_2, above all by adding small amounts of ions to the crystal lattice. In this thesis are used materials derived from tin oxides in different percentage, doped with titanium as ST20 650, ST25 650, ST25 650+ Au1%, ST30 650, ST50 650 and with titanium and niobium as STN.

WO_3-based materials

Tungsten trioxide has been investigated mainly because of its wide number of crystalline forms. Like SnO_2 it behaves as a n-type semiconductor because of lattice defects in particular, oxygen vacancies acting as electronic donor levels. However it shows a band gap ranging from 2.5 to 2.8 eV (Erbs et al., 1984 [14]) and contemporaneously a conductance value, at low temperature, almost three orders of magnitude higher than SnO_2. Both materials present the same trend versus temperature, but a very low value in the case of WO_3 to detect oxidizing gases. Also the preparation of mixed oxides of tungsten and tin tends to exhibit the same behavior in relation to oxidizing gases. Indeed, as shown in Chiorino et al., (2001) [15], adding 1 or 5% of W in SnO_2 progressively modifies the sensing properties of the sensors from the detection of reducing to the detection of oxidizing gases. In this thesis WS30 is used, which combines tungsten oxide (30%) and tin.

TiTaV

TiTaV is a relatively new material based on *titanium dioxide* (TiO_2) modified by *tantalum* and *vanadium*. When fired between 410 and 850°C, the doped titania powders are in the anatase phase; further heating up to 1050°C is required to obtain the rutile phase. The presence of dopant atoms delays the rate of transformation as compared to pure titania powders. M. Sacerdoti et al. [16], to better understand the role played by dopant atoms in inhibiting bot the phase to rutile and grain growth, performed X-Ray Absorption Spectroscopy measurements at the L_{III}-L_I absorption edges of Ta and Nb K absorption edge. The results from experiment made by Carotta et al. (2004, 2005) [17] [18] showed that Ta addition inhibited the anatase-to-rutile phase transformation and hindered drain growth during heating, keeping TiO_2 grain size in the nanometric range. On the other hand, V addition facilitated the anatase-to-rutile phase transformation. This trend is ultimately determined by the ratio between tantalum and vanadium contents and these sensors showed a good response to benzene (see fig. 2.12, 2.13), in particular with greatest content of Ta.

2.8.2 Metal-sulfides

Metal-sulfides are nanocrystals with great potential for investigation, due to their various types of structures. They are abundant and cheap because they exist in nature as minerals, i.e., heazlewoodite (Ni_3S_2), chalcocite (Cu_2S), pyrite (FeS_2) and others. The morphology of metal-sulfide nanostructures can be controlled by applying general solution methods and thermal evaporations, and their possible applications in energy conversion and storage were demonstrated. In the scientific literature, many papers have been reported to provide an overview of recent research and significant advances, ranging from synthesis to properties and applications, especially in energy conversion and storage, such as solar cells, lithium-ion batteries, piezoelectric nanogenerators and fuel-cells [19] [20] [21]. So far, in the gas sensing field, metal sulfides have been mainly studied in combination with metal oxides

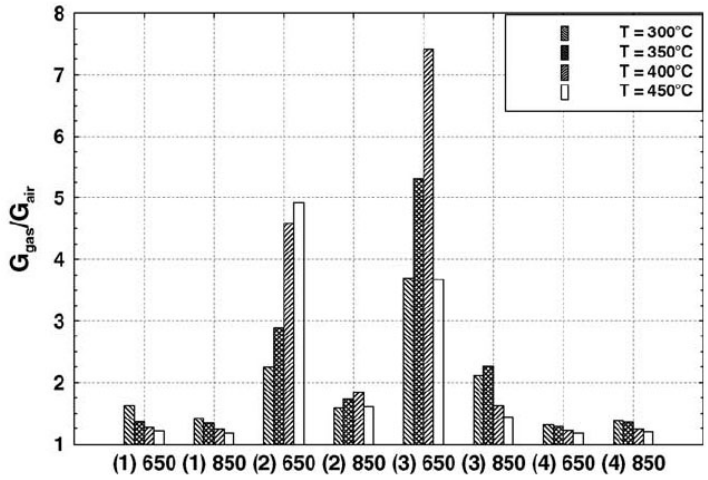

Figure 2.12: Electrical response to benzene (10 ppm) in dry air for four TiTaV samples: (1) Ti:Ta:V=100:5:5, (2) Ti:Ta:V=100:8:2, (3) Ti:Ta:V=100:15:5 and (4) Ti:Ta:V=100:2:8, measured at 300, 350, 400 and 450°C [2].

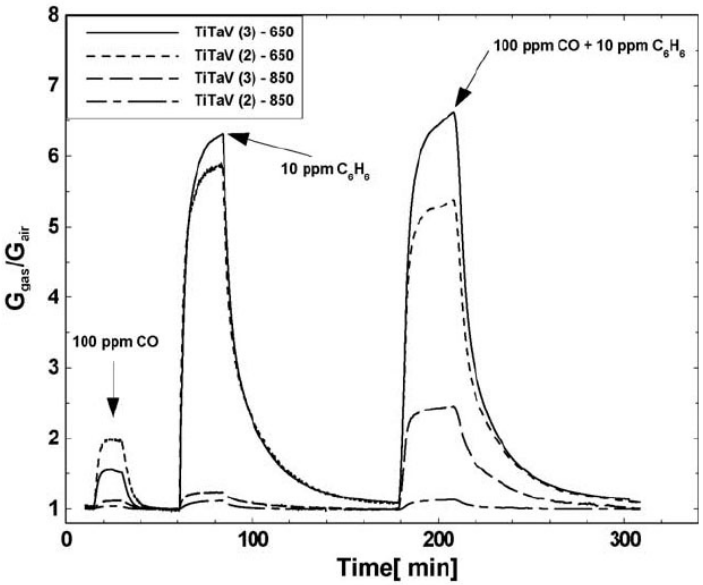

Figure 2.13: Electrical response to 100 ppm of CO, to benzene (10 ppm) and to mixtures of the two gases in dry air for TiTaV (2) and TiTaV (3) fired at 650 and 850°C at the working temperature of 380°C [2].

in order to modify the sensing activity of the latter [22] [23]. By studying physical and chemical properties of nanostructured metal sulfides, it arose that such materials may be very good candidates to be further investigated in the chemoresistive gas sensing field. Indeed, by using these materials, it is expected an improvement from an energy consumption point of view, both in thermal- and photo-activation modes, due to their lower band-gap than for metal-oxide semiconductors. This means that the activation of intrinsic surface reactions occurs at lower working temperatures, then minor power supply is necessary. Due to this advantage, we were motivated in the search for potential improved performance in terms of selectivity and stability. The absence of oxygen in the crystal lattice of metal sulfides leads to a different catalytic mechanism on the surface reaction with respect to metal oxides. In addition, this absence may solve the constant drift of the signal suffered by metal oxides and ascribed to the in/out diffusion of oxygen vacancies, which alters the doping level.

CdS

The powders can be employed as functional materials to obtain thick films, printed through a screen-printing technique. The obtained devices then can be electrically characterized under thermo- and photo-activation modes [24]. CdS show a high selectivity and a sensitivity comparable to the films used for gas sensing based on metal-oxides and show a high repeatability of the performances over six weeks. Through a comparison measurement carried out with their metal-oxides counterparts, in order to further study the gas-sensing properties of these metal sulfide, CdS showed better chemoresistive properties than CdO [24]. The results published in [25], showed the interesting behavior of CdS semiconductor in photo-activation mode. Indeed, CdS films showed under light irradiation at room temperature a fast and reversible response to gases tested. Furthermore, an important result consists of the observation of different surface chemical activity used with different wavelengths of excitation on nanostructured CdS films. In fact, band gap-resonant excitation turned out to maximize not only the photoconductivity, as found in early works about CdS [25], but also the surface chemical activity. This behavior has been observed for all tested gases, and so it could be expected that it is an intrinsic feature of CdS in photo-activation mode. The observed properties are very interesting concerning the use of CdS as low consumption gas sensors [26]. In the study [24], which is an extension of preliminary works on the sensing properties of metal sulfides [27] [28] [29], CdS was tested with 13 gases, which belong to different chemical classes, in thermo-activation mode. The behavior was investigated in dry and humidity conditions. The materials showed high selectivity to carbonyl (aldehydes and ketones compounds) and hydroxyl group (alcoholic compounds).

In the work of our team [24], cadmium sulfide, whose chemical structure is shown in Fig. 2.14, was obtained by precipitation in aqueous solution using as reagents: cadmium acetate dihydrate as source of Cd^{2+} ions, Thioacetamide as source of S^{2-} ions and

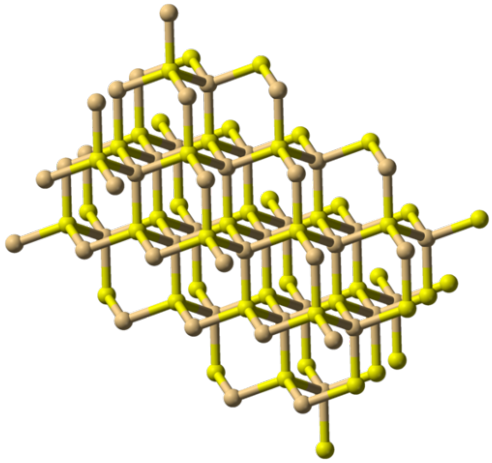

Figure 2.14: Molecular structure of CdS [31].

Figure 2.15: Obtained powder for CdS.

o-diaminobenzene as complexing agent. An image of the obtained powder is shown in Fig. 2.15. Regarding the structural, morphological and chemical characterizations, some consideration can be done by observing the results of SEM-EDX, UV-vis, XRD and TG analysis, respectively shown in Fig. 2.16, 2.17, 2.18 and 2.19. SEM-EDX highlights average grain size around 100 nm and an high purity of the product obtained; UV-vis shows a well defined peak due to the absorption of CdS with a blue-shift compared to the common peak of CdS, due to quantum size effect; XRD shows the presence of only one crystalline phase (cubic, hawleyite) and a medium crystallite size of 2,6 nm; TG analysis shows a thermal stability of CdS up to 450-500°C.

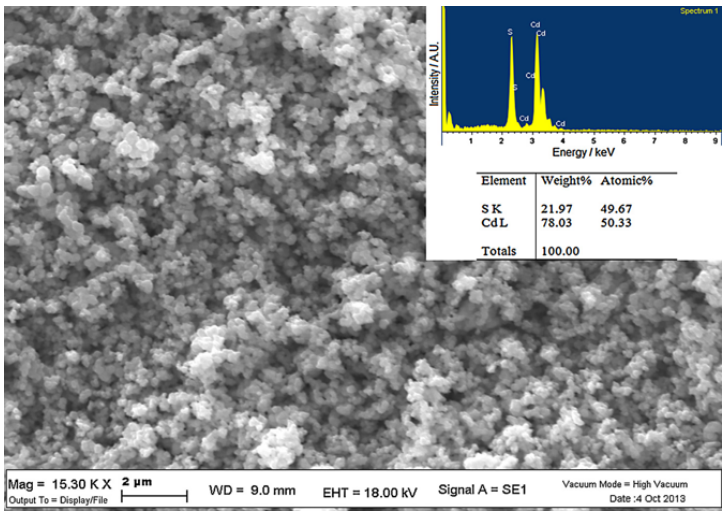

Figure 2.16: SEM-EDX analysis of CdS [29].

As it was already anticipated, CdS is selective to alcoholic chains. Fig. 2.20 shows this property by comparing the response of CdS to diverse gases. Only alcohols (methanol, ethanol and n-butanol) show a significant response. In parallel, it was also observed that the high response to alcohols is proportional to the length of alcoholic chains. In Fig. 2.21 it is proposed a probable explanation of this phenomenon by taking on account the process of dehydrogenation of the alcohol by the adsorbed oxygen ions. The phenomenon is probabily due to the fact that, when a ionized oxygen of the chain reacts with the sensor surface, all the molecule is bound to position itself along the surface, giving thus way to the remaining part of the chain to interact with the sensor. The greater the length of the chain is, the higher the probability of interaction with the CdS surface.

By comparing CdS with its metal-oxide counterpart (CdO), the second shows a very low chemoresistive behavior at 300°C (see Fig. 2.22). The surface barrier height found for CdS is of $\sim$ 1,08 eV at 300°C and it is shown in Fig. 2.23.

An interesting characteristic of CdS, as said before, is represented by its good performances in photoactivation mode. CdS is an inorganic semiconductor with an energy

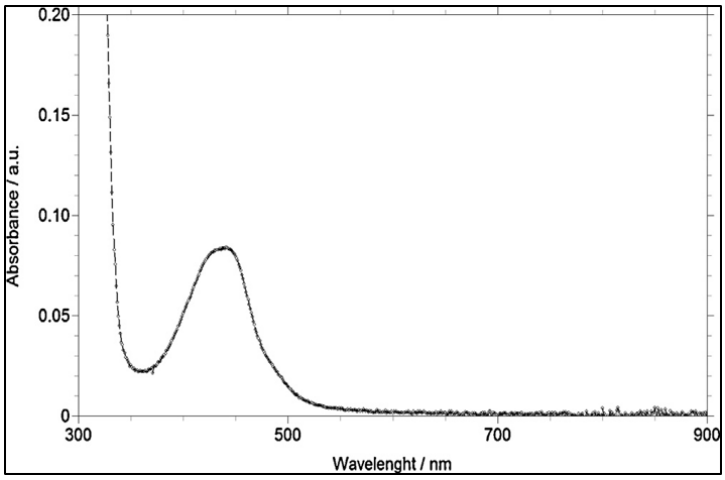

Figure 2.17: UV-vis analysis of CdS [29].

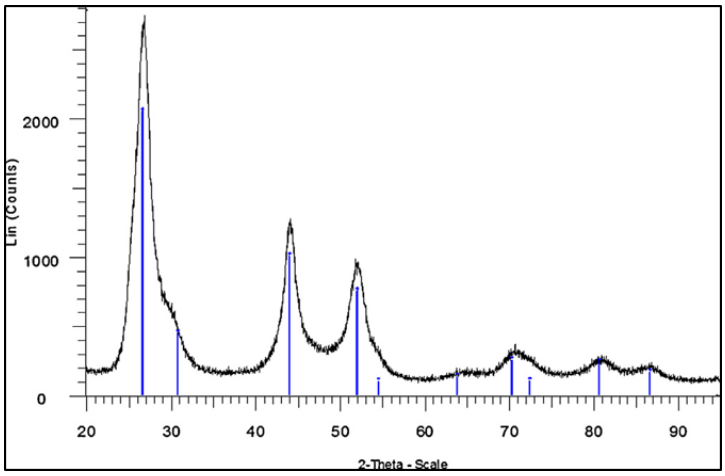

Figure 2.18: XRD analysis of CdS [29].

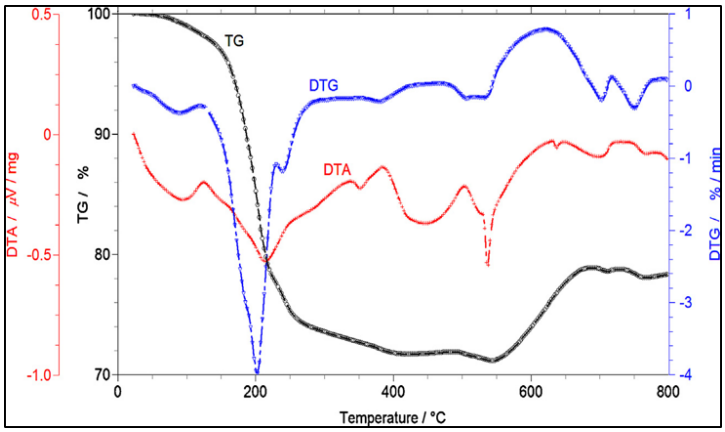

Figure 2.19: TG analysis of CdS [29].

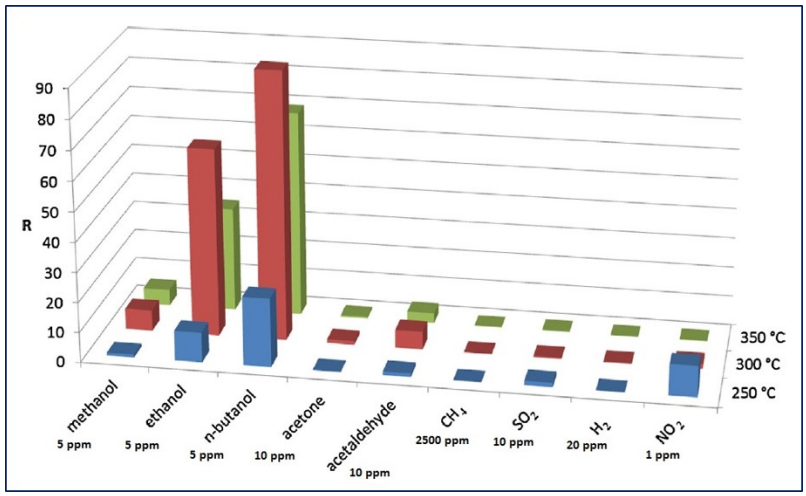

Figure 2.20: Comparison between responses of CdS to diverse gases. It results selective to alcohols [24].

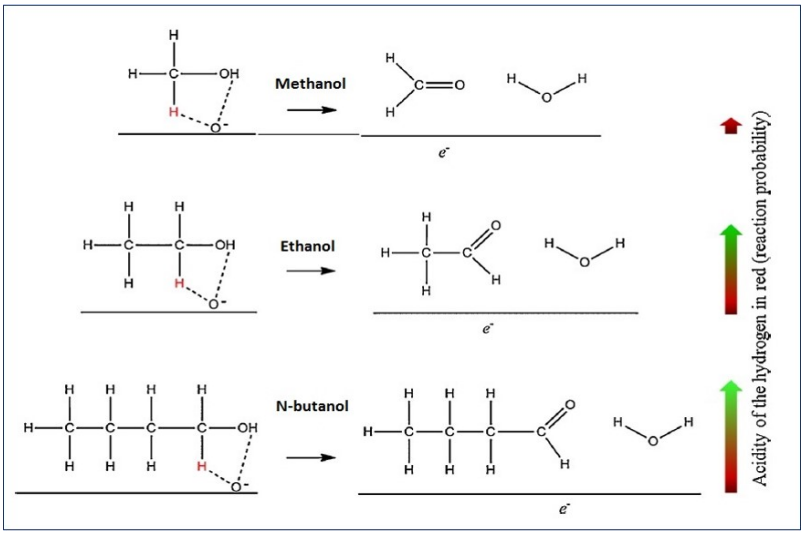

Figure 2.21: Mechanism of dehydrogenation of alcoholic chains [24].

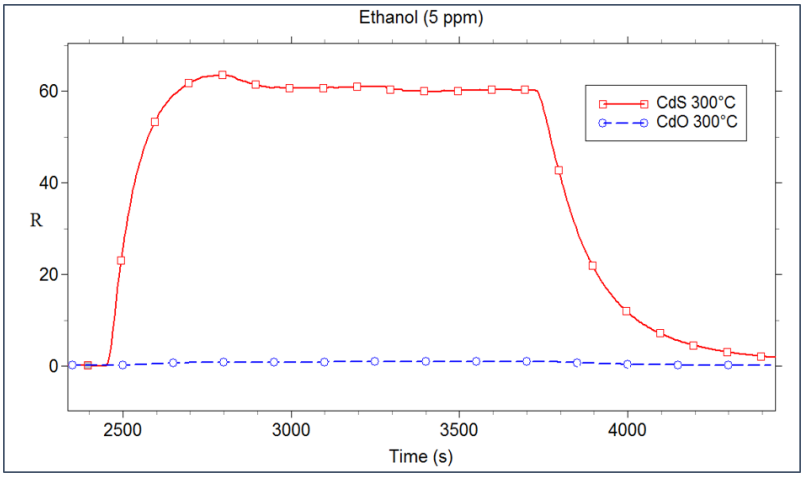

Figure 2.22: Response curve of CdS and CdO to ethanol at 300°C [24].

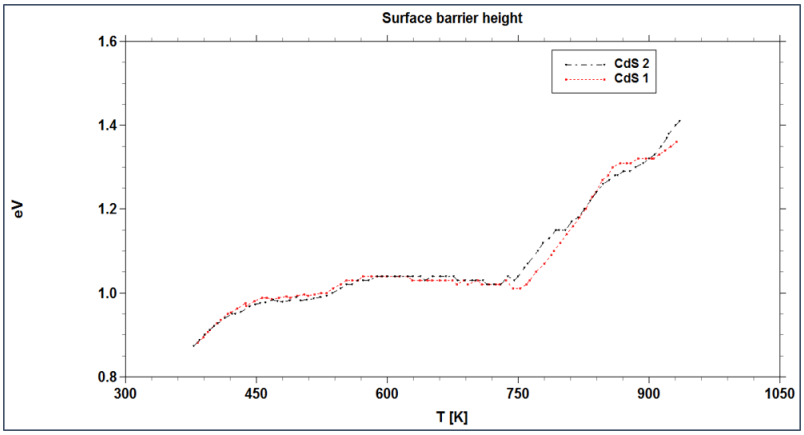

Figure 2.23: Surface barrier height estimated for two CdS sensors [24].

gap E_g of 2,40 eV. It can undergo heterogeneous mechanisms of photocalysis and its main properties are chemoresistivity and chemiluminescence. CdS thick films that were realized show homogeneous spherical grains, with diameter below 100 nm and with thermal stability up to 500°C. The peak of response for green light is at 525 nm, which corresponds to an energy of 2,36 eV.

By means of the bandgap-resonant excitation (Fig. 2.24) it is possible to reach the maximization of surface chemical activity. By observing Fig. 2.25 it is noticeable that the peak of response for all the tested gases is located at the same wavelength/energy, that corresponds to that of the resonant peak for green light.

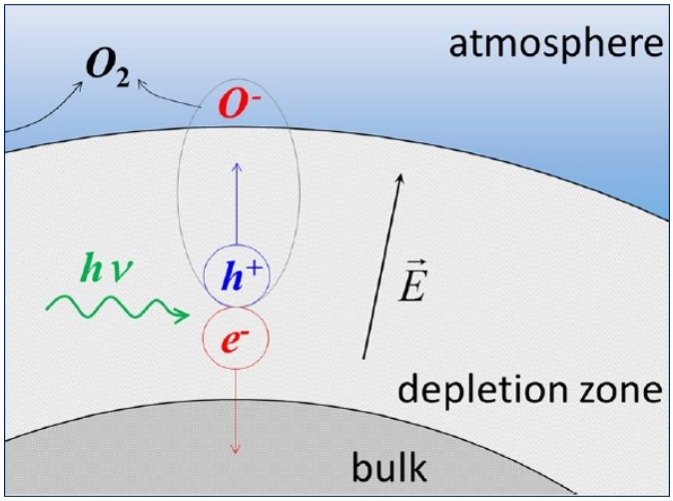

Figure 2.24: Mechanism of bandgap-resonant excitation [24].

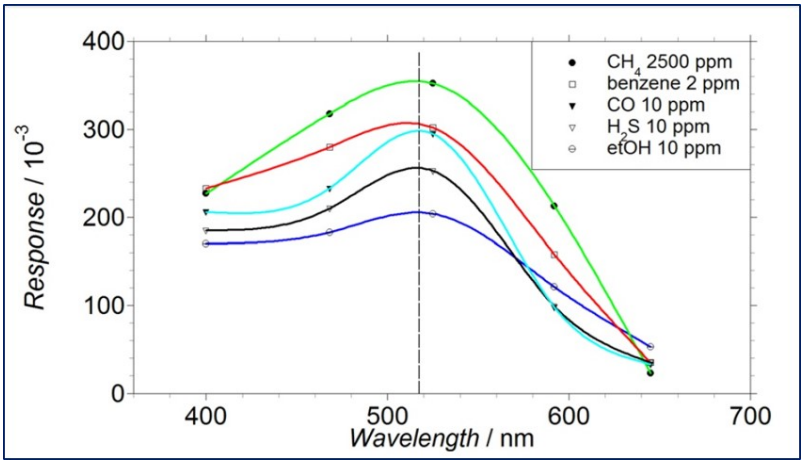

Figure 2.25: Response of CdS to diverse gases. The response peak is always at the excitation energy for green light.

SnS_2

The same tests performed in on CdS in thermo-activation mode, both in dry and wet condition, has been performed in the work [24] for SnS_2. Also SnS_2 showed high selectivity to carbonyl (aldehydes and ketones compounds) and hydroxyl group (alcoholic compounds), is stable over time. In recent literature, Ou et al. [32] have demonstrated the sensitivity of SnS_2 films to NO_2, by exploring the sensing behavior of this material with five target gases (H_2, H_2S, CH_4, NO_2 and CO_2), whereas Shi et al. [33] prepared SnS_2 nanostructure through hydrothermal synthesis and they studied its sensing behavior to ammonia at room temperature. A brief comparison between responses obtained at room temperature with SnO_2, SnS_2 and $SnS_2 - SnO_2$ hybrid materials was carried out vs. ammonia by Xu et al. [23], but the grains of SnO_2 and SnS_2 which composed the films had different morphological features. Concerning SnS_2 thick films, the results obtained in photo-activation mode did not show a significant change of conductivity. Therefore, SnS_2 layers are not suitable as photo-activated chemoresistive gas sensors with light sources having wavelengths ranging from 400 to 645 nm. Moreover in [24], as it has been done for CdS, comparison measurements were carried out for SnS_2 with its metal-oxides counterparts. However, unlike in the case of CdS, SnS_2 presented a lower signal drift than SnO_2.

The principal characteristics of SnS_2 are the following:

- they are IV-VI semiconductors;
- they have direct band gap of 2.2 eV;
- they have a crystalline structure, rhombohedral (berndtite);

- they are used for many applications such as solar cell material, lithium batteries, field-effect transistors and optoelectronics.

In the work of our team [24], tin(IV) sulfide, whose chemical structure is shown in Fig. 2.26, was obtained by precipitation in aqueous solution using as reagents: tin(IV) cloride pentahydrate as source of Sn^{4+} ions, thioacetamide as source of S^{2-} ions and hydrochloric acid to obtain an adapt pH. An image of the obtained powder is shown in Fig. 2.27.

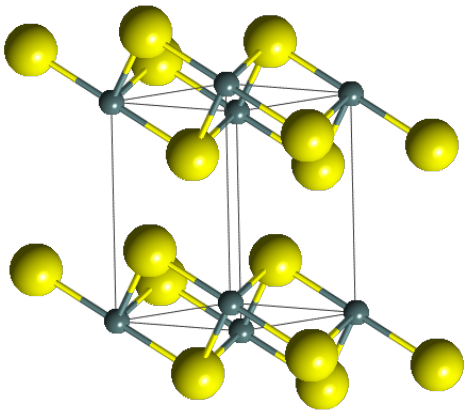

Figure 2.26: Molecular structure of SnS_2.

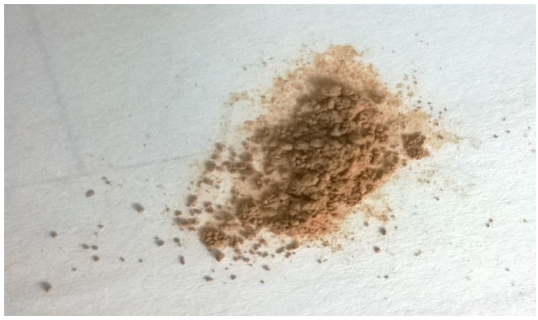

Figure 2.27: Powder of SnS_2.

Regarding the structural, morphological and chemical characterization some consideration can be done by observing the results of SEM-EDX, TEM, XRD and TG analysis, respectively shown in Fig. 2.28, 2.29, 2.30 and 2.31. SEM-EDX analysis highlights a medium grains average around 100 nm and an high purity of the product obtained and TEM measurements show that SnS_2 is featured as nanorods with length around few tens of nm. Then XRD analysis shows the presence of the rhombohedral crystalline phase (called berndtite) and highlights a medium crystallite average of 6,18 nm and TG analysis shows a thermal stability of SnS_2 up to 400°C.

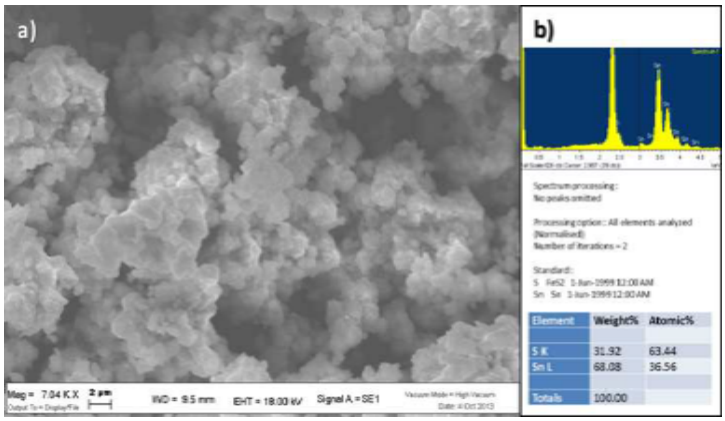

Figure 2.28: SEM-EDX analysis of SnS_2 [28].

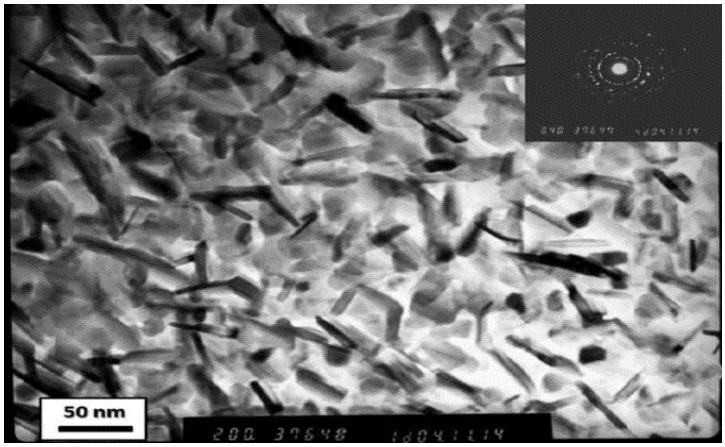

Figure 2.29: TEM analysis of SnS_2 [28].

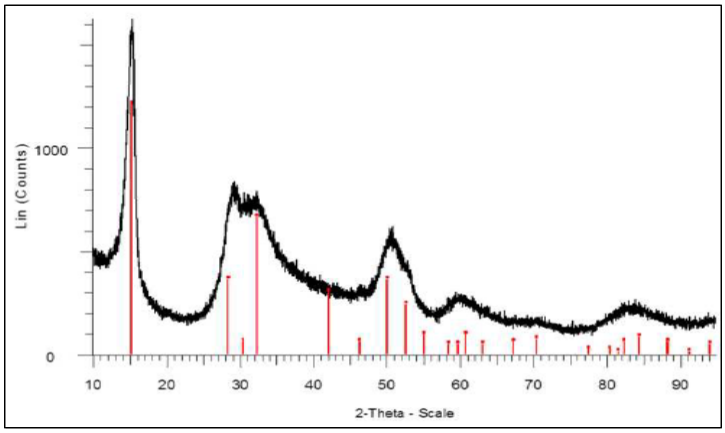

Figure 2.30: XRD analysis of SnS_2 [28].

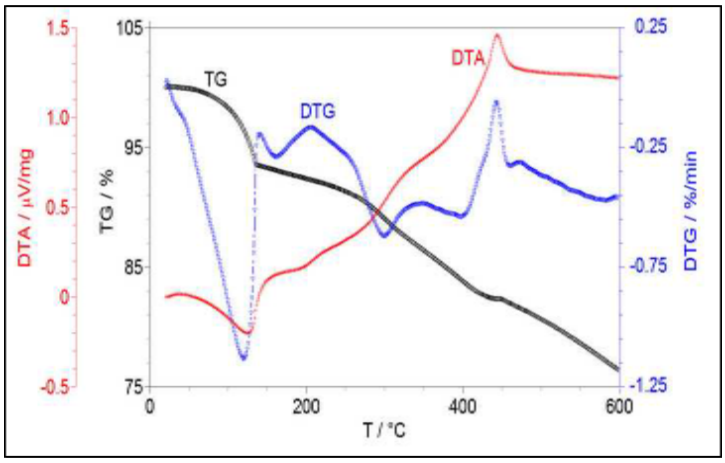

Figure 2.31: TG analysis of SnS_2 [28].

SnS_2 thick films show a selectivity to aldehydes and ketones (carbonyl group) at the best temperature work of 300°C (see Fig. 3.5) and a great response stability as shown in Fig. 2.33 in response to 10 ppm of acetone.

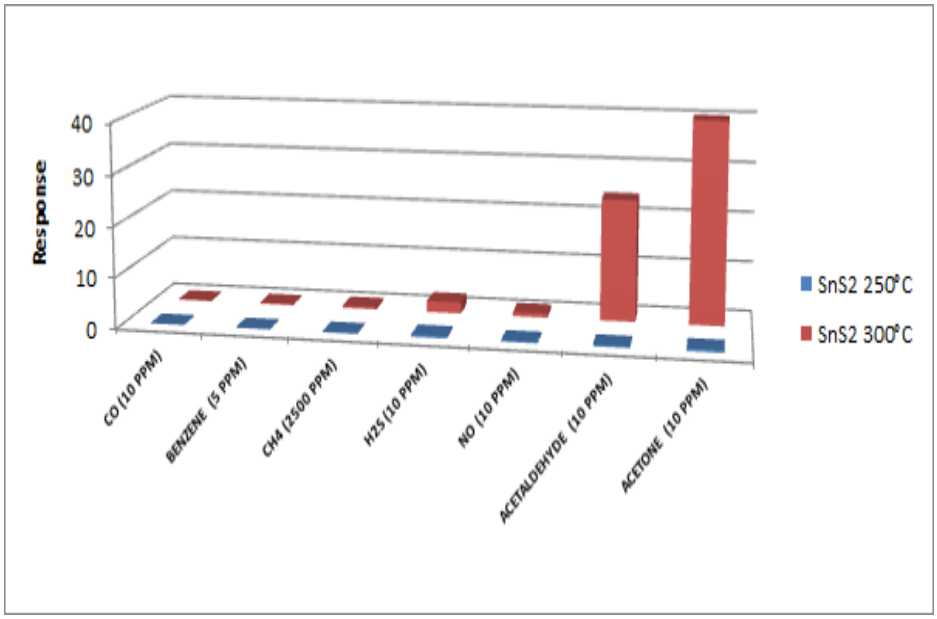

Figure 2.32: Selectivity of SnS_2 thick films to carbonyl group [28].

An interesting comparison should be that between SnS_2 and its metal-oxide counterpart (SnO_2). As shown in Fig. 2.34, the response of SnS_2 to 2500 ppm of methane is higher and with faster recovery time than SnO_2, despite it was obtained at 100°C lower temperature. On the other hand, in Fig. 2.35 is shown the surface barrier height found for SnS_2, that is ~ 0.24 eV, instead for SnO_2 the value found is ~ 0.47 eV. The conductance of SnO_2 and of SnO_2 is shown in Fig. 2.36.

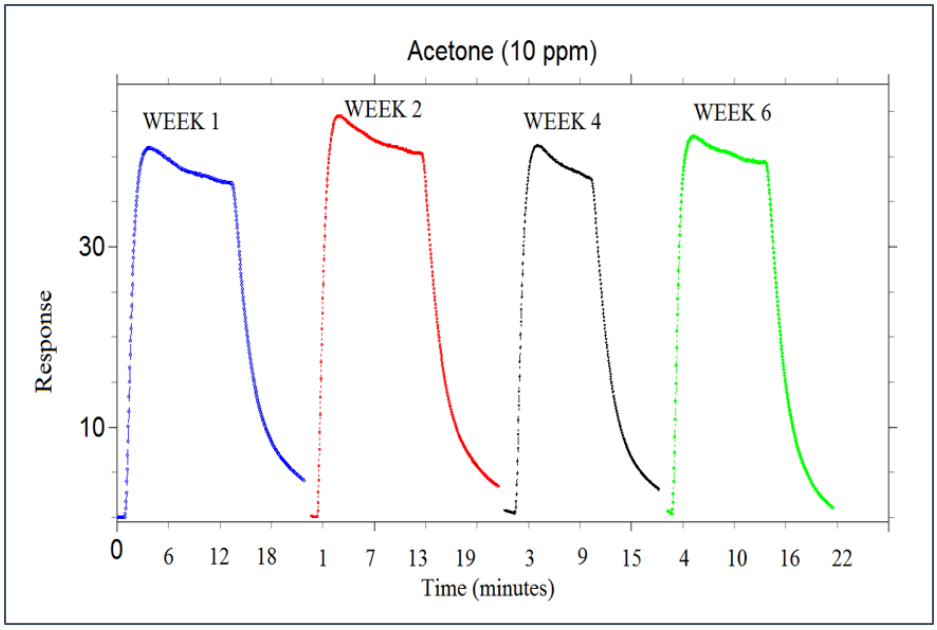

Figure 2.33: Response stability of SnS_2 with 10 ppm of acetone [24].

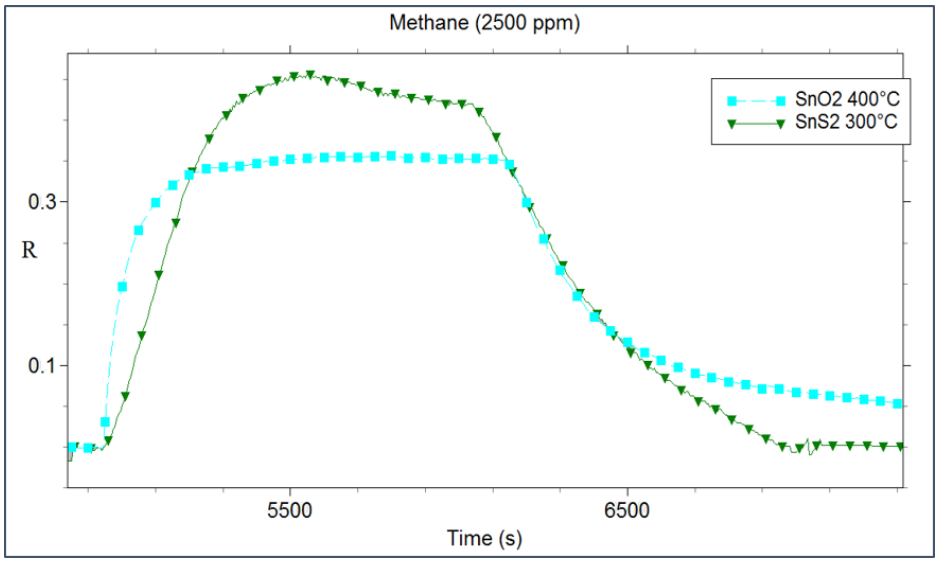

Figure 2.34: Response of SnS_2 and of SnO_2 to 2500 ppm of methane [28].

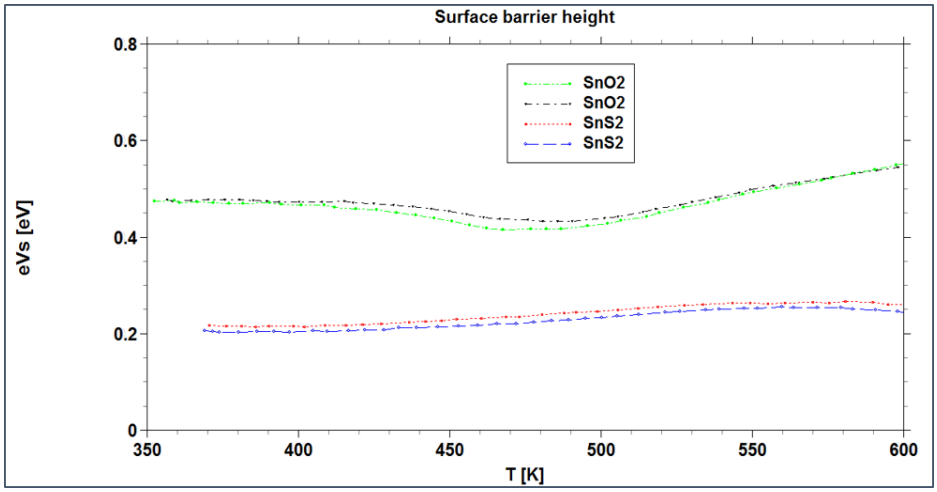

Figure 2.35: Surface barrier height found for SnS_2 and SnO_2 [30].

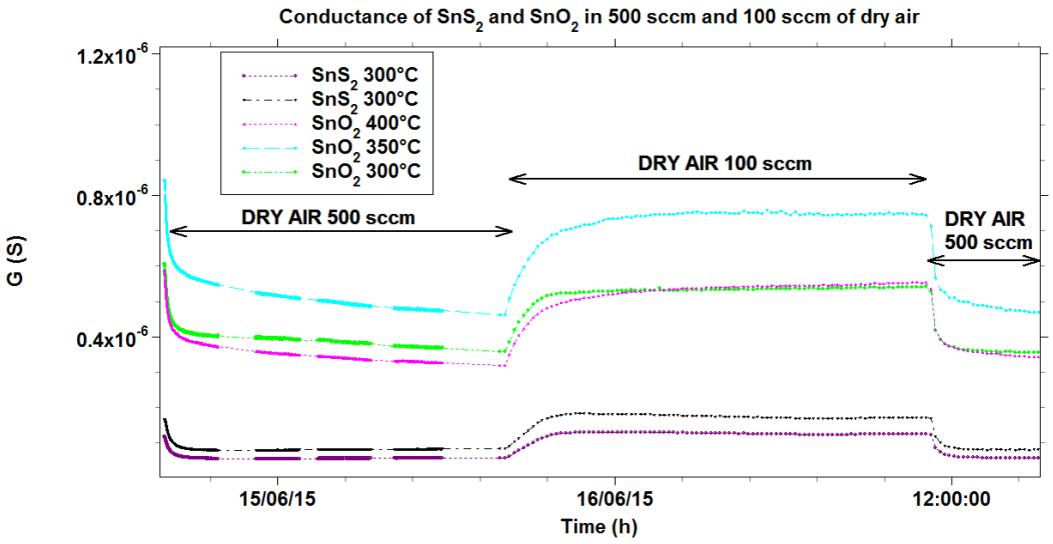

Figure 2.36: Conductance of SnS_2 and SnO_2 in 500 sccm and 100 sccm of synthetic dry air.

Chapter 3

Towards medical applications

Nano-materials can offer promising non-invasive methods to detect and prevent cancer [34]. It is known that VOC emissions, produced by the peroxidation of the cell membrane or by cell metabolic activity, are closely linked to tumor presence and growth and they can be detected both directly from the headspace of cancer cells and through exhaled breath [35], [36]. Indeed, changes in the blood chemistry lead to measurable modifications in the breath composition, due to exchanges inside the lungs, e.g., in the range of 20-100 ppb for several VOCs [37], as well as in feces from normal digestion [38]. The first part of my Ph.D. was a continuation of my Master thesis work, entitled *Detection of low concentrations of 1-iodo-nonane with nanostructured metal-oxide based sensors*. The goal was to study a detection method for VOCs indicators of colorectal cancer (CRC), identifying the most selective sensors for these compounds, in order to develop a method of analysis of intestinal gases, inside which these biomarkers should convey. The most relevant VOCs which may indicate CRC presence include compounds of different nature, e.g., benzene-made compounds, 1-iodo-nonane ($C_9H_{19}I$) and decanal ($C_{10}H_{20}O$) [37], [63]. The main gases that can interfere in this mixture are H_2, CH_4, H_2S, SO_2, N_2, NO_2 and NO, being the main components of the intestinal gaseous environment [40]. This work contributes to the state of the art through the publication of two papers [34], [41]. In this chapter is presented a description of the activities and relative achievements.

3.1 Colorectal cancer (CRC)

CRC is a major worldwide health problem, owing to its high diffusion and mortality rate. The American Cancer Society classifies CRC as the third most commonly diagnosed cancer type in USA and the third leading cause of cancer death, both in men and women. Therefore the lifetime risk of developing CRC is about 1 in 20 (5%) [43]. On the other hand, if promptly diagnosed, CRC is also one of the most curable types of cancer (rate around 90%) and prevention is fundamental to avoid the degeneration into malignant stages

and metastasis. In 2011 about 141,210 people in the USA were diagnosed with CRC and about 49,380 people died of the disease. It is estimated that over 40,000 of the adult UK population are diagnosed with CRC each year [45]. Evidence shows that the majority of CRC cases could be prevented by applying existing knowledge of cancer prevention and by increasing the use of established screening tests. In Fig. 3.1 is shown a chart that represent deaths for CRC every 100.000 subjects around the world considering 2004 data [44].

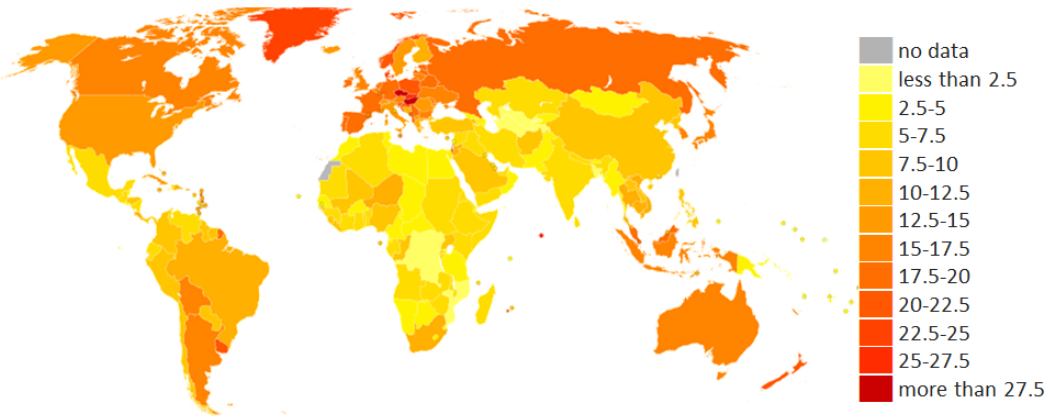

Figure 3.1: Deaths for CRC every 100.000 subjects around the world, 2004 data [44].

What emerges is the major tumor concentration in the more industrialized areas and which have a high consumption of cooked meat. The issue clearly assumes a global reach.

3.1.1 Symptoms

CRC can be identified when it is in the adenoma stage (polyp) or in more degenerate stages (carcinoma or metastasis). In the first case it may manifest in several ways:

- rectal bleeding - people commonly attribute all rectal bleeding to hemorrhoids, thus compromising early diagnosis owing to a lack of concern over "bleeding hemorrhoids";
- chronic rectal bleeding - it may be hidden but may show up as an iron deficiency anemia;
- fatigue and pale skin.

On the other hand, if the tumor gets large enough, it may completely or partially block the colon. The affected subject may notice the following symptoms of bowel obstruction:

- abdominal distension - the belly protrudes more than normal, without weight gain;
- abdominal and rectal pain;

- unexplained, persistent nausea or vomiting;
- unexplained weight loss;
- change in frequency or composition of stool (bowel movements) and sensation of incomplete evacuation after a bowel movement.

Studies suggest that the average duration of symptoms (from onset to diagnosis) is of 14 weeks. There is no association between the overall duration of symptoms and the tumor stage [46].

3.1.2 The management

In the last decade, the management of CRC has been transformed from a routine activity for general surgeons to a specialist activity, in which the multidisciplinary team (MDT) guides increasingly complex investigations and treatments. Most CRC-MDTs stage the disease in three areas [47]:

- *local disease*, assessed in the colon by Computed Tomography (CT) scan, which provides information on the presence of invasion through the bowel wall, direct invasion of adjacent structures or extensive lymph node disease; the common pre-operative planning, before resection, consists in the use of Magnetic Resonance Imaging (MRI). MRI provide detailed images of soft tissues in the body, using radio waves and strong magnets. This technique is uncomfortable, because it takes up to an hour and the patient has to lie inside a narrow tube, which is confining and can upset people with claustrophobia. Another technique consists in transrectal ultrasonography (TRUS), which is considered to be the most accurate tool for the staging of early rectal cancer, making it important in the selection of cases for local excision. With TRUS, a small and lubricated probe placed into the rectum releases sound waves, creating a video image;
- *metastatic disease* in the liver and lungs, is assessed routinely and most centers would be expected to perform abdominal and chest CT. Before the scan, the patient may be asked to drink a contrast solution and/or to get an intravenous (IV) injection of a contrast dye that helps to better outline abnormal areas in the body. Some people are allergic and get hives or, rarely, more serious reactions like trouble breathing and low blood pressure. Another technique is Positron Emission Tomography (PET), a form of radioactive sugar, known as F-18 fluorodeoxyglucose or FDG, that is injected into the blood. Cancer cells in the body grow rapidly, so they absorb large amounts of the radioactive sugar. After about an hour, the subject will be moved onto a table in the PET scanner and lies on the table for about 30 minutes, while a special camera creates a picture of areas of radioactivity in the body. Moreover there are also special machines called PET-CT, which are capable of performing both a PET and CT scan

at the same time. This allows the doctor to compare areas of highest radioactivity on the PET with the more detailed image of that area on the CT. PET-CT is important in those patients in whom, otherwise, occult metastases would be a contraindication to extensive visceral resection, directed at either primary disease or metastases;

- *synchronous disease* should be excluded by complete assessment of the remainder of the colon. Synchronous cancers are present in about 2% of patients with a recent diagnosis of CRC. The optimal investigation is colonoscopy, during which polyps can be removed or the site tattooed, allowing later identification at the time of resection.

Together with barium studies or sigmoidoscopy (a procedure used to investigate the sigmoid colon and rectum), these methods of diagnosis of CRC in its three different stages are invasive and unpleasant for patients, in fact, they have physiologic or psychological contraindications or take a long time [48]. For this reasons, in the last years, the research of non-invasive methods of CRC preventive diagnosis has become very important.

Other non invasive techniques which can be used in order to identify CRC once at the polyp stage, are the following ones [49]:

- *Fecal occult blood tests (FOBT)* - both polyps and colorectal cancers can bleed, and FOBT checks for tiny amounts of blood in feces that cannot be seen. Blood in stool may also indicate the presence of conditions that are not cancer, such as hemorrhoids. Currently, two types of FOBT are approved by the Food and Drug Administration (FDA) to screen for CRC: guaiac FOBT (gFOBT) and the fecal immunochemical test (FIT, also known as iFOBT). With both types of FOBT, stool samples are collected by the patient using a kit, and the samples are returned to the doctor. The gFOBT uses a chemical to detect heme, a component of the blood protein hemoglobin. Due to the fact that gFOBT can also detect heme in some foods (e.g., red meat), people have to avoid certain foods before having this test. On the other hand, FIT uses antibodies to detect human hemoglobin specifically, so, dietary restrictions are typically not required for FIT;

- *Cologuard®* - this test detects tiny amounts of blood in stool (with an immunochemical test similar to FIT) as well as nine DNA biomarkers in three genes that have been found in CRC and precancerous advanced adenomas. The DNA derives from cells of the lining of the colon and rectum that collect in stool as it passes through the large intestine and rectum. As in the case of FOBT, the stool sample for the Cologuard® test is collected by the patient using a kit; the sample is mailed to a laboratory for testing. A computer program analyzes the results of the two tests (blood and DNA biomarkers) and provides a finding of negative or positive. People who have a positive result are advised to undergo a colonoscopy. However, the Cologuard® test also was more likely to identify an abnormality when none was actually present (that is, it had more false-positive results). In August 2014, the FDA approved the Cologuard®

test. At the same time, in a pilot program known as parallel review, the Centers for Medicare & Medicaid Services proposed national coverage for this test. This test is still being evaluated to see where it fits in screening guidelines. To date, it has not been incorporated into clinical practice guidelines or recommended by the U.S. Preventive Services Task Force as a method to screen for CRC. The Task Force is currently updating its guideline and is examining recent evidence on the Cologuard® test;

- *Double-contrast barium enema (DCBE)* - this test is another method of visualizing the colon from outside the body. In DCBE, a series of x-ray images of the entire colon and rectum is taken after the patient is given an enema with a barium solution. The barium helps to outline the colon and the rectum on the images. DCBE is rarely used for screening because it is less sensitive than colonoscopy for detecting small polyps and cancers. However, it may be used for people who cannot undergo standard colonoscopy, for example, because they are at particular risk for complications.

3.1.3 Tumor biomarkers: VOCs

Tumor growth is accompanied by gene and/or protein changes, that may lead to peroxidation [50] of the cell membrane and, hence, to the emission of volatile organic compounds (VOCs), which can be considered as biomarkers for the different cancer typologies. The analysis of the VOCs linked to cancer is a new frontier in medical diagnostics, because it is non-invasive and potentially inexpensive [51] [57]. These VOCs can be detected either directly from the headspace of cancer cells [53] [54] [55] or through exhaled breath [51] [56] [57] [58] [59] [60]) as cancer-related changes into the blood chemistry lead to measurable changes in the breath by exchanges through the lung [59]. Peng et al (2010) [37] reported that a tailor-made array of cross-reactive sensors based on organically functionalized gold nanoparticles (GNPs) discriminates between breath VOCs of healthy controls and of patients suffering from lung, breast, colorectal, and prostate cancers. They reported also the capability of these GNP sensors of distinguishing between the breath patterns of different cancer types in the same pattern analysis, irrespective of age, gender, lifestyle, and other confounding factors. They found also that these results compare favorably with breath testing via a chemical analysis of the constituent compounds by gas chromatography linked with mass spectroscopy (GC-MS). Their study was conducted in three phases. In the first phase exhaled alveolar breath was collected from 177 volunteers aged 20-75 years (lung, colon, breast, and prostate cancer patients and healthy controls) using a method to effectively separate endogenous from exogenous VOCs (endogenous VOCs are those ones generated by cellular biochemical processes in the body, which provide insight into the body functions [61], whereas exogenous VOCs are adsorbed from the environment [62] in the breath, and excluded nasal entrainment. All cancer-affected patients were tested immediately after being diagnosed by conventional clinical means, and before any treatment. In

the second phase an array of 14 cross-reactive nanosensors was designed with different organic functionalities and their ability to detect simultaneously primary, lung, colon, breast, and prostate cancers was tested. Signals collected from the 14-sensor array, after exposure to the breath of the representative subjects, were analyzed using standard Principal Component Analysis (PCA), an effective method to improve human perception of experimental data by reducing the multidimensional data space to its main components (a more detailed description of this method is presented in Section 3.6). In the third phase the purposed method of breath testing using a GNP sensor array was compared with breath test analysis using GC-MS combined with solid-phase microextraction (SPME), which identified 300-400 different VOCs for each sample. In Fig. 3.2 are shown the characteristic odour prints of the studied cancer types. In this work the focus is on the CRC and in Fig. 3.2, the panel (B) shows 6 of the 39 common VOCs for colon cancer compared with healthy subjects. The attention is focused on VOC 6 and VOC 8, respectively 1-1'-(1-butenylidene)bis benzene (m/z=208, CAS:1726-14-3) and 1-iodo-nonane (m/z=43; CAS:4282-42-2) which are present in bigger percentage in patients with colon cancer than in healthy subjects and represent possible markers for colon cancer.

A similar study was conducted by Altomare et al. (2012) [63] at the University of Bari but they focused their interest on the colon cancer in particular. The sampling conditions were the same of that of Peng et al. and volunteers refrained from eating and drinking for 3h before the test. Volunteers were 103: 52 diagnosed with colon cancer (with a mean age of 65 years) and 51 healthy subjects (with a mean age of 60 years). Patients with diabetes or intestinal inflammation were excluded. Patients breathed tidally for 5 min through a mouthpiece connected to a three-way-non-rebreathing valve with an inspiratory VOC filter in order to exclude exogenous VOCs. The analysis of compounds was effectuated throug GC-MS and the discrimination between healthy and cancer subjects was made with a probabilistic neural network (PNN), an implementation of a statistical algorithm. The most probable VOCs emerged from this study which can have an high discriminating power are reported in the Table 3.3 (RT is the retention time[1]).

By comparing these two works, it is noticeable that the presence of benzene compounds is common for CRC, moreover it has also bigger values with respect other compounds. For this reason, the first part of this work is the research on materials particularly sensitive on this gas, because it is reasonable to to expect that the sensitivity to benzene is reflected in sensitivity to its compounds and to similar molecules in general. The second part is instead linked to the analysis of one of the two VOCs highlighted in the work of Peng et al. and Altomare et al., the *1-iodo-nonane*, ($C_9H_{19}I$) and the *decanal* ($C_{10}H_{20}O$). Their chemical structures are shown in Fig. 3.4, 3.5.

[1]In chromatography, the RT, is the amount of time elapsed from the injection of a sample into the chromatographic system to the recording of the peak (band) maximum of the component in the chromatogram.

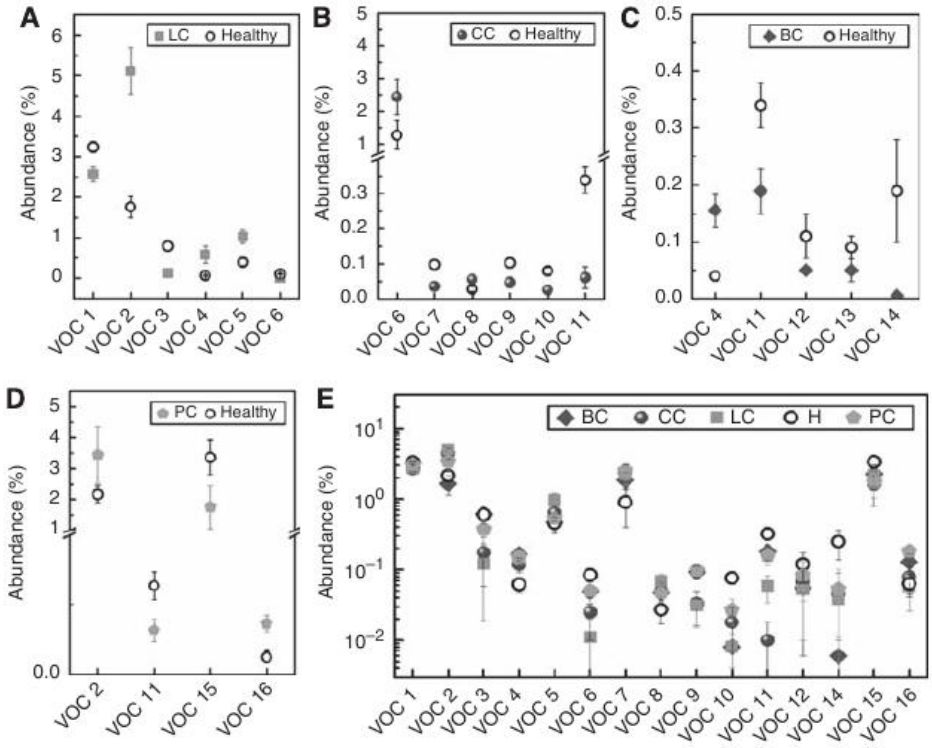

Figure 3.2: Pre selection of the GC-MS input for PCA: the most suitable VOCs were selected for distinguishing between healthy subjects and patients suffering from a specific cancer: (A) 6 of 33 common VOCs for lung cancer; (B) 6 of 39 common VOCs for colon cancer; (C) 5 of 54 common VOCs for breast cancer; (D) 4 of 36 common VOCs for prostate cancer [37].

	Recognition capability (%)
Nonanal	80
4-Methyl-2-pentanone	88
Decanal	92
2-Methylbutane	87
1,2-Pentadiene	95
2-Methylpentane	87
3-Methylpentane	87
Methylcyclopentane	80
Cyclohexane	94
Methylcyclohexane	92
1,3-Dimethylbenzene	96
4-Methyloctane	80
1,4-Dimethylbenzene	80
A (4-methylundecane, RT = 11·3)	59
B (trimethyldecane, RT = 13·2)	72

Figure 3.3: Discriminating variable compounds considered in statistical analysis [63].

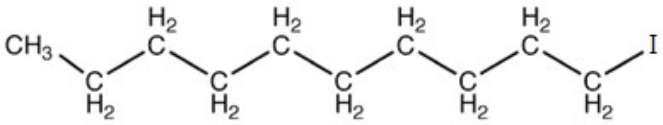

Figure 3.4: 1-iodo-nonane chemical structure.

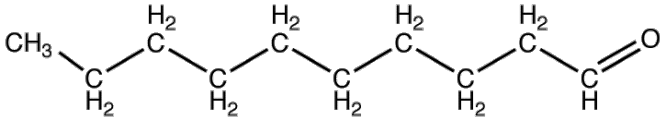

Figure 3.5: decanal chemical structure.

3.1.4 Sampling

Previous works were based on the breath analysis. A large number of other diagnosis methods and research studies concern the analysis of breath. Works of this type are for example that of Gasbarrini et al. (2009) [64], who used H_2-breath test for the diagnosis of gastrointestinal diseases, or that of Hakim et al. (2011) [65] who, through a tailor made NA-NOSE[2], unambiguously identified patients with head-neck cancer in a population that contains healthy subjects and lung cancer patients. Machado et al. (2005) [66] used electronic noses for the discrimination between lung cancer and healthy patients through the detection of specific VOCs. A curious study was conduced by Sonoda et al. (2013) [67] using the acute smell of dogs as "sensors" for tumors biomarkers. In this work exhaled breath and watery stool samples were obtained from patients with CRC and four control samples of healthy controls prior to colonscopy. A Labrador retriever specially trained in scent detection of cancer and a handler cooperated in the test. The dog first smelled a standard breath sample from a patient with CRC, then smelled each sample station and sat down in front of the station in which a cancer scent was detected. This study shows that a specific cancer scent exists and that a cancer-specific chemical compounds may be circulating throughout the body. These odour materials may become effective tools in CRC screening.

Works as that of Buzewski et al. (2012) [68], which analyzed VOCs in breath using GC-MS carried out simultaneously with tests using trained dogs, may then elucidate the question of whether and which VOCs could be markers of the cancer disease that dogs respond to. de Meij et al. (2014) [69] conducted a study on CRC by means of a electronic nose (Cyranose 320 [70]). It was used to measure VOC patterns in fecal gas from patients with histopathologically proven CRC, with advanced adenomas and from controls (no abnormalities seen at colonoscopy).

As already described in the section 3.1.3, VOCs are considered as biomarkers for different types of cancer and disease. They are produced by reactions due to the transformation of cells and they arrive in the lung through blood vessels. There is no reason not to think that VOCs linked to CRC, due to the position of colon inside the body, cannot convey directly inside of intestinal gas. The preliminary idea of this work was to identify sensors capable of discriminating the gas of interest from those of interference in the gut. If it were possible to create very selective sensors or array of sensors capable to perform this discrimination, consequently it would be possible, theoretically, to achieve a non-invasive method for the diagnosis of CRC, based on the collection and analysis of intestinal gases. The reader will see later how, because of the difficulties in the intestinal gas sampling, the original goal has been modified by our group and oriented towards the stoll exhalation analysis. This second activity has become one of the main focal points of my PhD.

However let's focus, at the moment, on the intestinal gas analysis. In order to realize these type of sensors, it is of fundamental importance to take account of all the gas inside

[2]Nanoscale Artificial nose based on array of five gold nanoparticle sensors.

the intestine and their relative amount. These two things vary greatly from individual to individual, as reported in the work of Tomlin, Lowis and Read (1991) [71] and of Probert et al. work [38]. In the first paper, the authors made 24 h collections using a rectal catheter in 10 normal volunteers, taking their normal diet plus 200 g baked beans. It was found that women and men expelled equivalent amounts, the total daily volume ranged from 476 to 1491 ml and a median volume of 705 ml. The produced gases were: hydrogen (361 ml/24 h), carbon dioxide (68 ml/24 h) and three volunteers produced methane (3-26-120 ml/24 h respectively), and the remaining unidentified gas (presumably nitrogen, 213 ml/24 h). Then they showed that the ingestion of a "fibre free" diet for 48 h reduced the carbon dioxide volume and eradicated hydrogen production. In Fig. 3.6 are indicated individual values for the total volume of gas collected in 24 h.

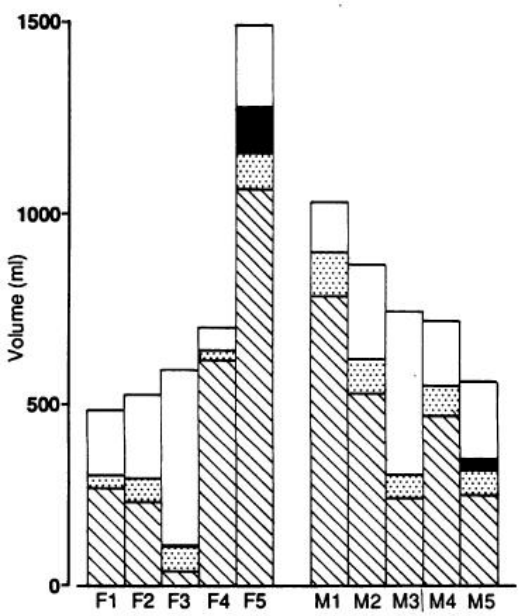

Figure 3.6: Individual values for the total volume of gas collected in 24 hours. Hatched bars indicate the total volume of hydrogen, spotted bars carbon dioxide, dark bars methane in three subjects (F3, F5, M5), and the remaining blank bar represents the volume of unidentified gas (probably nitrogen) [71].

Based on these and other literature results, in the first part of my Ph.D. work in fact I have considered, as interference gases, the fermentation products of our body as methane (CH_4, produced by normal digestion), hydrogen sulfide (H_2S, produced by some vegetables like broccoli, pasta, bread, wheat products, dried fruits and animal proteins from aliments like beef or pork), hydrogen (H_2, produced by meat digestion), nitrogen monoxide and dioxide (NO, NO_2), where the first is a gasotransmitter [72] and both are products of bacteria normally involved in digestion like Coliform bacteria or pathological

intruders like Helicobacter Pilori [73] [74] [75]: These gases has been chosen in order to find appropriate selective sensors which are sensitive to benzene, decanal and 1-iodo-nonane but not too much sensitive to these interferers. Another gas that was tested is sulfur dioxide (SO_2) to verify the occurring of the chemical reaction:

$$2H_2S + 3O_2 \rightarrow 2H_2O + 2SO_2, \tag{3.1}$$

which represents the combustion of H_2S which happens at high temperatures on the surface of the sensing films (H_2S autocombustion occurs at 260°C) [83] [80]. Its signature is visible from the initial peak of response before reaching the plateau, then it gradually reduces with time, due to the increasing relative humidity caused by the surface reaction (Fig. 3.7). Naturally is useful to consider the fact that a percentage of fermentation gases should be reduced or eliminated with the help of specific diets, to facilitate the diagnosis. CO was tested for two reasons: it is normally present in the digestive system, as regulator of the smooth muscles in the intestine [77], and it is produced by some organic processes as hemoglobin degeneration [78]; this process can occur even when hemoglobin is stripped away from the red blood cells (e.g. with denaturation of the proteins), like when the cell itself is destroyed (hemolysis in fact represents a problem in the analysis of feces of patients with CRC, as described below).

3.2 Experimental setup

3.2.1 Measurement apparatus.

In order to evaluate the response of a sensor to a specific gas or to a gas mixture, it is necessary to employ an appropriate instrumentation. These instruments allow to work in ideal conditions, enabling the repeatability of measurements at the same conditions. The apparatus used consists of:

- flow meters for gas mixing;
- sensors and measurement chamber;
- data acquisition system.

Here a description of the instruments.

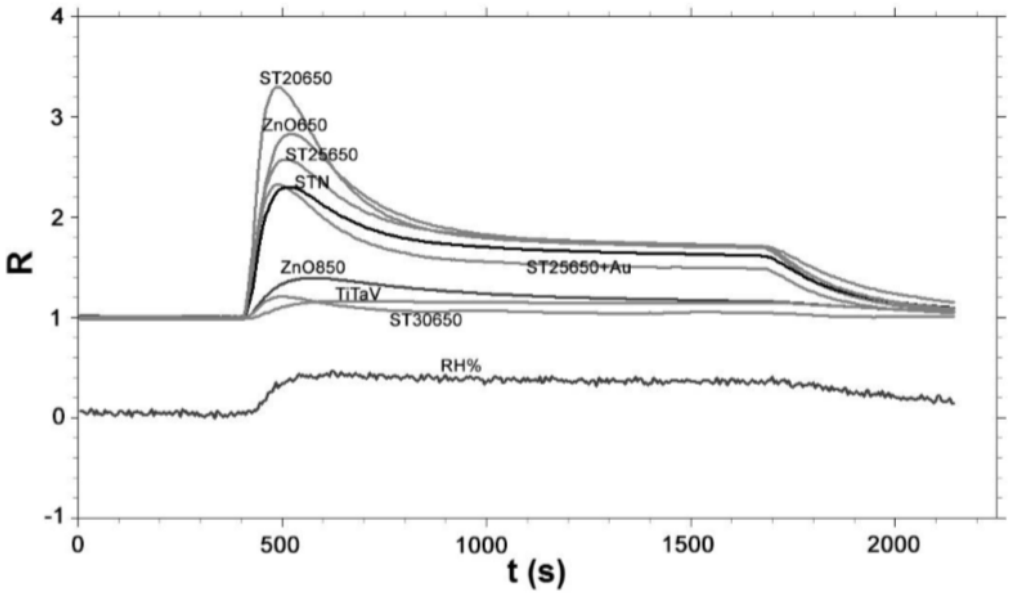

Figure 3.7: Sensors responses (normalized to 1), as a function of time, to H_2S in dry conditions at 450°C. Humidity increases when H_2S is inflated, due to the reaction 3.1, shown in the text. The sensor codes are indicated in the graph for each response curve [2].

Flow meters for gas mixing

The gases to be studied are contained in bottles, connected to flow meters that allow to set the flow. The gas flow is then sent to the measuring chambers, by means of Teflon tubes. To know which flow is to be set, the following equation must be used:

$$F = \frac{F_{tot} \cdot C}{C_{bot}} \quad , \tag{3.2}$$

where F_{tot} is the total flux in the flow meter (in this case 500 sccm[3]), C is the gas concentration to be sent to the chamber and C_{bot} is the gas concentration in the bottle (certified by the supplier).

Measurement chamber

The measurement chamber is the place in which sensors are inserted. It has a cylindrical shape, it is made of aluminum and hermetically sealed. At the center of the chamber is placed a gas diffuser, while sensors are positioned circularly around it. In each chamber it is possible to place up to eight sensors, together with a humidity sensor and a temperature

[3]Standard Cubic Centimeters per Minute.

sensor. Furthermore it is important to specify that the gas is diffused uniformly inside the chamber, in order to solicit sensors at the same time. In Fig. 3.8 two images of the chamber both open and closed.

Figure 3.8: Sensor inside the chamber (left) and chamber hermetically sealed (right).

Electronic circuit

In order to detect the changes in the sensor conductance, it is necessary to insert the sensor inside a circuit, represented in Fig. 3.9.

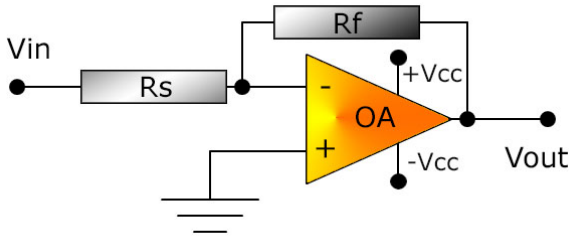

Figure 3.9: Circuit in which the sensor is inserted.

This is an inverting operational amplifier (OA), in fact the input signal is connected to the negative entrance of the amplifier, while the positive one is grounded. At the ends of the resistors R_S and R_f we have respectively the voltage values V_{in} and V_{out}, so:

$$\frac{V_{out}}{R_f} = -\frac{V_{in}}{R_S} \quad . \tag{3.3}$$

The gain is given by:

$$\frac{V_{out}}{V_{in}} = -\frac{R_f}{R_S} \quad . \tag{3.4}$$

Fixing $V_{in} = -5V$, because of the virtual short circuit to the inputs of the OA, the inverting input terminal is at the same potential that the non-inverting input terminal. In this way the sensor is subjected to a constant potential difference of 5V until the OA works far from saturation. Being the values of V_{in} and R_f known and constant, the output voltage V_{out} is then proportional to the conductance:

$$V_{out} = -R_f \cdot V_{in} \frac{1}{R_S} = const \cdot G \quad , \tag{3.5}$$

where G is the conductance in the presence of the gas and G_{air} the conductance measured without the gas. Moreover, the expression of for response assumes a really simple shape, independent from the circuit parameters:

$$\frac{G}{G_{air}} = \frac{V_{out}(gas)}{V_{out}(air)} \quad , \tag{3.6}$$

where the wordings *gas* or *air* indicate the presence or not of the gas to measure. For the *heater*, the circuit is represented in Fig. 3.10.

The heater is a thermal sensor and consists of a platinum coil in which resistance increases linearly with temperature. The relation between temperature and resistance is the following:

$$R_h = R_0(1 + \alpha T + \beta T^2) \tag{3.7}$$

in which R_h is the resistance at room temperature, R_0 is the resistance at $0°C$, T is the temperature at which one wants to set the sensor, while α and β are two characteristic constants of the material. For the specific case of platinum they are:

$$\alpha = 0.003263°C^{-1} \quad , \tag{3.8}$$

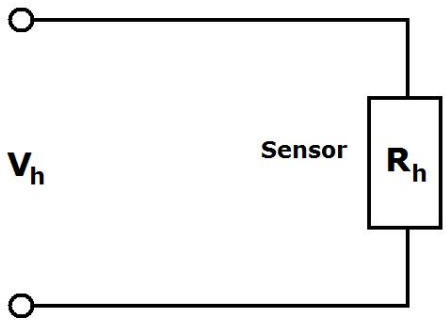

Figure 3.10: Heater circuit.

$$\beta = -6.6668 \cdot 10^{-7} {}^{\circ}C^{-2} \quad . \tag{3.9}$$

Measuring the resistance at room temperature and inverting the relation 3.7 it is possible to determine R_0. At this point, choosing the working temperature it is possible to find the corresponding R_h. Applying a voltage V_h to the circuit the current that circulates, according to Ohm Law, will be:

$$R_h = \frac{V_h}{i} \quad , \tag{3.10}$$

where V_h is established by the user and the current is measured by the feeder. It is so possible to control and directly modify R_h and so the temperature of sensors (by changing V_h).

3.2.2 Data acquisition system

The data acquisition system must manage all phases regarding the sensor electronics (see Fig. 3.11). It is made of:

- multimeter K2000 (Keitheley): it serves to convert all output voltages from analog to digital. Then these values will be sent to the computer. The multimeter is composed by ten input channels and has a sensitivity of ten decimal digits;
- management and acquisition software: it consists of a program, in TestPoint, capable of acquiring all the ten input channels of the multimeter (eight gas sensors, a temperature sensor and a humidity sensor), at regular intervals (one acquisition every five seconds). Through this software it is possible to visualize the response graph of each sensor and to control or modify supply voltage values, to set sensors at the desired temperature.

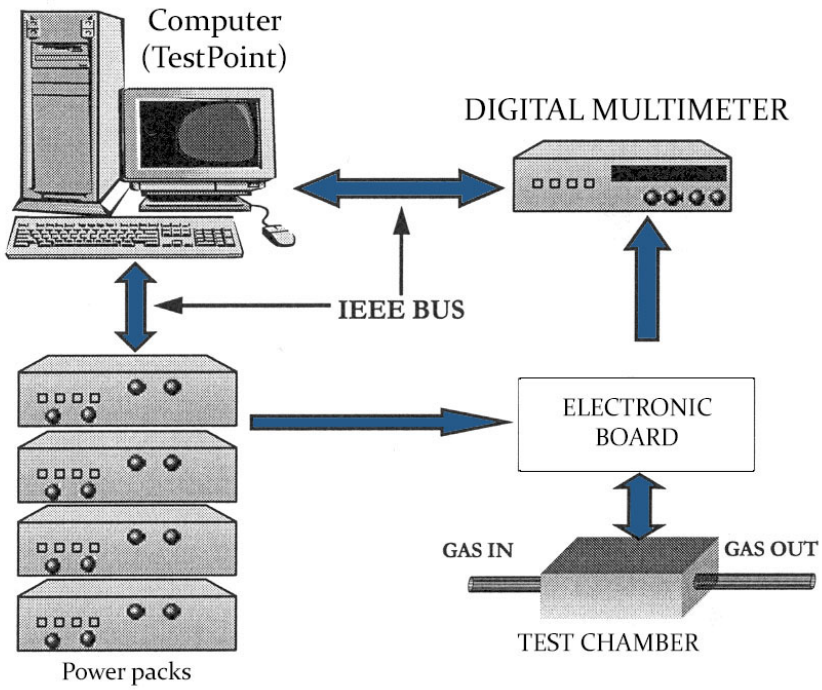

Figure 3.11: Data acquisition system: experimental setup [2].

3.3 Sensors responses to VOCs

For the laboratory set up described before, a single array of 8 sensors was used, placed into the sensor chamber (where T_F is the firing temperature of the sensor):

- **TiTaV**: a sensor based on titanium, tantalum and vanadium oxides;
- **ST25 650**: a sensor based on tin oxides (25%) and titanium, T_F: 650°C;
- **STN**: a sensor based on tin, titanium and niobium oxides;
- **ST20 650**: a sensor based on tin oxides (20%) and titanium, T_F: 650°C;
- **ST25 650+Au(1%)**: the same of ST25 650 but with an addition of Au (1%);
- **ST30 650**: a sensor based on tin oxides (30%) and titanium, T_F: 650°C;
- **ZnO 650**: a sensor based on zinc oxide, T_F: 650°C;
- **ZnO 650**: a sensor based on zinc oxide, T_F: 950°C.

The initial idea is to identify the most selective sensors to CRC-VOCs inside a mixture of intestinal gases that could interfere with them. These sensors were used before to test individually all the compounds from gas bottles, in order to observe their sensitivity to the various chemicals; then they were tested with four gas mixtures: **(1)** $\boldsymbol{H_2S+NO_2+C_6H_6}$, **(2)** $\boldsymbol{SO_2+NO+C_6H_6}$ and **(3)** $\boldsymbol{CH_4+H_2+C_6H_6}$ in both wet and dry conditions, **(4)** $\boldsymbol{C_9H_{19}I+C_{10}H_{20}O}$ on wet conditions, to test their selectivity to the target VOCs (C_6H_6, $C_9H_{19}I$, $C_{10}H_{20}O$). The logic behind the combinations of these chemicals was:

- for the mixture (1), to detect benzene inside an environment of gases produced by digestion or due to pathological states (like bacterial infection) which can cover the presence of a VOC emission. It was tested both in dry and wet conditions. It is important to remember that the presence of H_2S over the sensor surface at 260°C or more, leads to the reaction described previously by the formula 3.1;
- for the mixture (2), to detect benzene inside an environment of gases derived from chemical reactions inside the intestine, due to bacteria or epithelial cells (NO is a product of nitrogen bacteria metabolism, as well as a gasotransmitter from the digestive system to the blood stream [72] [74] [75]). Tests were performed both in dry and wet conditions;
- for the mixture (3), to detect benzene while interfered with the two main products of human digestion, hydrogen (from meat) and methane (from vegetables), both in dry and wet conditions;

- for the mixture (4), in wet conditions only, to detect the two VOCs when emitted together, observing the results of their interaction.

Tests were performed both in dry (standard procedure) and wet conditions, using a gas bubbler, due the fact that inside intestinal environment, the water vapor is a major component.

This step was of fundamental importance for the birth of the following research on feces (see Chapter 4), in fact at the beginning, the working temperatures of the sensors were set to the best ones to detect benzene, decanal and 1-iodo-nonane respectively.

Due to the variety of targets, different measures were taken to obtain the best and most repeatable conditions for every test done, nonetheless to guarantee the safety of the operations.

Responses to the target gases were observed for different working temperatures, both in dry (RH $\sim 0\%$) and in wet conditions ($18\% < \text{RH} < 60\%$). Choosing the most favorable temperatures of each sensor for benzene detection, the intestinal standard gas mixture was approximately reproduced into the sensors chamber. CO_2 was not considered because it is well known that it is hardly detected by chemoresistive sensors [79]. During the experiment, testing measurements were performed in dry and wet airflow, with the purpose of checking the differences in response at the variation of humidity, operating temperature and oxidation state of the films. It is important to state the effects of the oxygen variations on the sensor responses for three main reasons:

- in the intestine there are variations of oxygen production due to the digestive, bacterial and cellular activity;
- there are some chemical reaction that occur between oxygen and other compounds both in the intestine and in the experimental setup;
- some bottles (e.g., H_2) used in the experimental tests cannot contain oxygen for safety reasons but contain N_2.

For these reasons, the total volume of the chamber was filled with N_2 and O_2 in different concentrations. At first, a flow of synthetic dry or wet air (20% O_2 and 80% N_2) was used, then, with the addition of a flow of pure N_2 and the lowering of the synthetic air flow, the ratio between O_2 and N_2 in the chamber was modified (increasing O_2 volume concentration of 1%). This variation lead to a detailed analysis of the disturbance, due to environmental changes and to differences in metal oxide films (Fig. 3.13, 3.14). The symbol Δ was defined as the difference between responses in the two cases described before. It is important to notice that humidity during interference tests gives rise to two different phenomena:

- if injected in the role of interferer in dry conditions, the responses of all sensors raises;

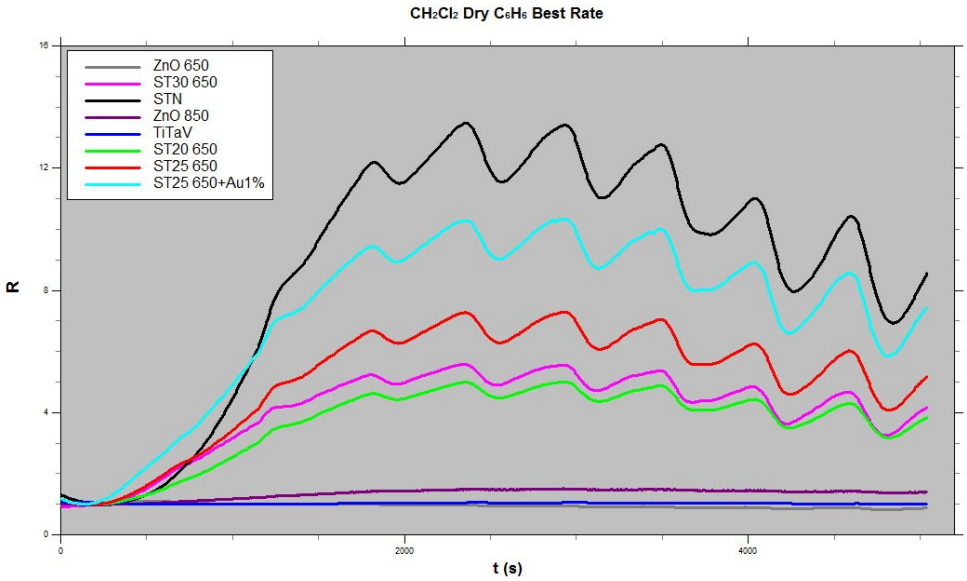

Figure 3.12: Sensor responses, as a function of time, to a drop of CH_2Cl_2 in dry conditions at the best detecting temperatures for C_6H_6 [2].

- if injected before the interference tests and kept stable (so generating a stable wet environment) the response of all sensors lowers.

Methane and hydrogen are inflammable gases, having ignition temperatures (in environmental air and at a pressure of 1 atm) of 540°C, for concentrations between 5 and 15% of volume for CH_4 and of 560°C between 4 and 75% of volume for H_2; thus, these chemicals were never employed in this range of concentrations. Moreover, the interference tests to simulate the intestinal environment were done while keeping the relative concentrations of the two gases on the same scale of their relative amount inside the intestinal environment with clinical diet (60% hydrogen, 10% methane, 2 and 5% benzene, quantities extrapolated from literature [40]), while perfused in a synthetic air filled chamber. Regarding decanal and 1-iodo-nonane, it is important to notice that the reported moles number represents an upper limit, obtained from the subtraction in weight of the drops of compounds from the pipette; due to the uncontrollability of the evaporative process and the non-hermetical lockup of the gas bubbler, part of the dose can be assumed not to have reached the sensors at all. Tests with 1-iodo-nonane were performed in dry conditions, using an empty gas bubbler to evaporate it; no solvents were used to haste the evaporation of $C_9H_{19}I$, due to the high sensitivity of sensors to alcohols and other organic reagents like dichloromethane (CH_2Cl_2); in Fig. 3.12 it is possible to see the effect of the solvent on the response, with the undulation following the refrigerating cycle.

The two tumor markers, as already explained, are in liquid form (Fig. 3.15 shows

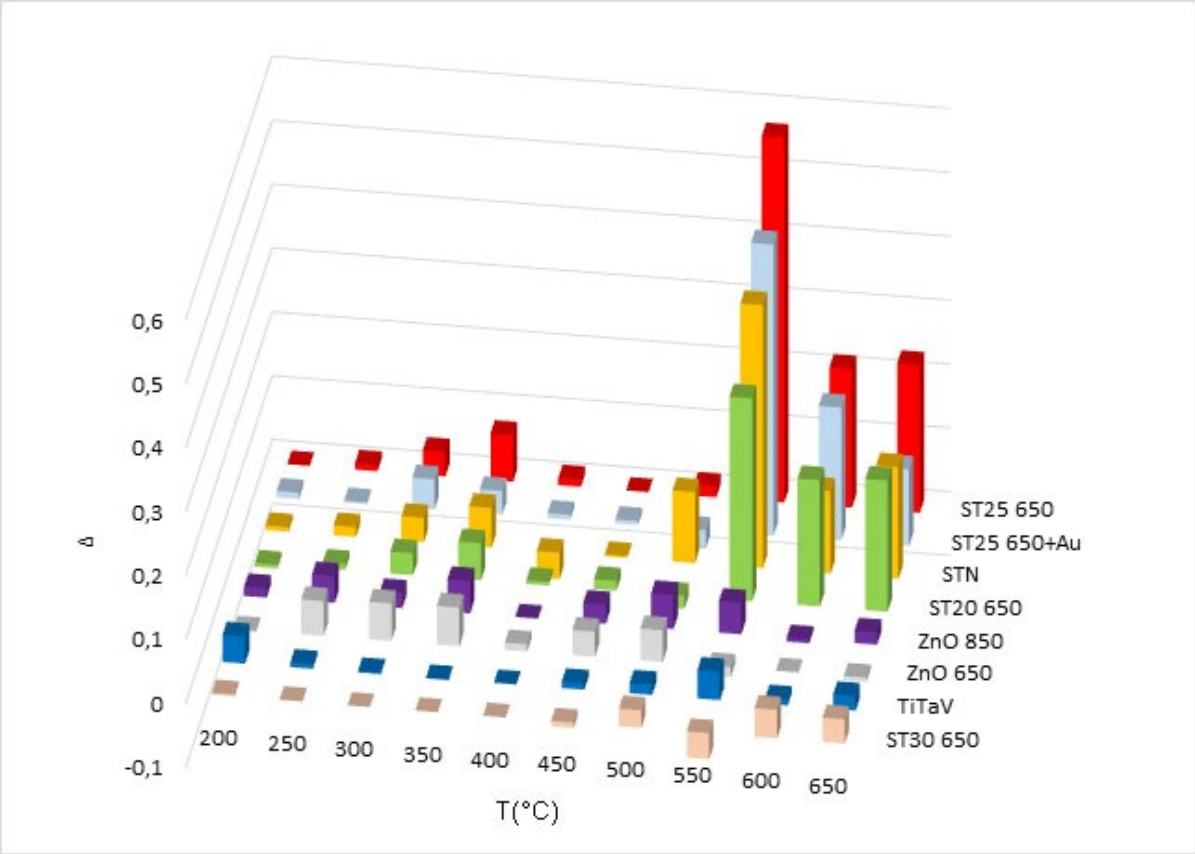

Figure 3.13: Subtraction between successive plateaux of N_2 and dry synthetic air interferences, normalized over their baseline. The symbol Δ shows the difference of responses for that temperature to the variation, for addition, of 5 sccm of O_2 in the 500 sccm of the chamber [2].

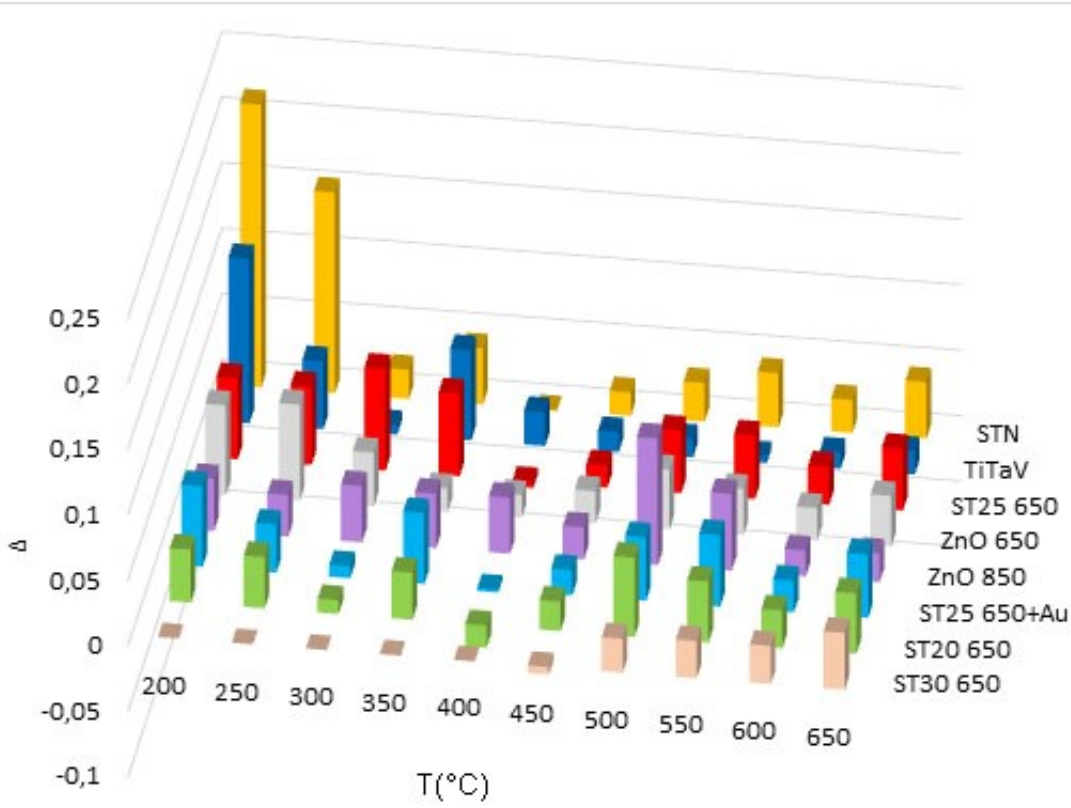

Figure 3.14: Subtraction between successive plateaux of N_2 and dry synthetic air interferences, normalized over their baseline. The symbol Δ shows the difference of responses for that temperature to the variation, for addition, of 5 sccm of O_2 in the 500 sccm of the chamber [2].

Figure 3.15: Bottles containing decanal and 1-iodo-nonane in the liquid state.

the bottles in which they are contained); in the following tables are shown their main characteristics:

NAME	**1-iodo-nonane**
VOC	$C_9H_{19}I$
ASSAY	95 %
CONTAINS	copper as stabilizer
REFRACTIVE INDEX	n20/D 1.487(lit.)
BOILING POINT	107-108°C/8 mmHg(lit.)
DENSITY	1.288 g/ml at 25°C(lit.)
PACKAGING	25 g in glass bottle

NAME	**decanal**
VOC	$C_{10}H_{20}O$
ASSAY	96 %
FORMULA WEIGHT	156.27
MELTING POINT	-5°C
BOILING POINT	207÷209°C
DENSITY	0.828 g/ml at 25°C(lit.)
PACKAGING	100 ml in glass bottle

The weight of the reagent was measured through a precision balance, in order to calculate the moles number and to obtain an average value of the concentration. To identify the best detecting temperature for each type of sensing material, the sensors response was studied at several working temperatures (350, 400, 450, 500, 550, 600°C). 1-iodo-nonane

is sensitive to light, so all the dropping procedures and weight measurements have been done in conditions of darkness, to preserve the original state of the compound [81]. As it has been done with 1-iodo-nonane, the weighing and deposition of the drops of decanal have been done in darkness conditions; $C_{10}H_{20}O$ is, in fact, also air sensitive, but it is still light activating the process of auto-oxidation, leading at first to peroxo-acids production and thus to the alteration on the compound [82]. For most of the interference tests, gases were sent in the chamber at the same moment, to obtain a direct interference. Then, the inflation of the target gas was delayed, letting the chamber environment stabilize. This step is of fundamental importance to see if there are changes in the sensor responses if benzene is sent later into the chamber, as if the VOC would have suddenly appeared in a healthy intestinal environment.

3.4 Working temperatures choice

The procedure starts with the identification of the working temperatures for each sensor. The apparatus consists of a polystyrene box in which sensors are connected to a multimeter with a four-tip output (in order to avoid the noise of about 0,4 Ω introduced by a standard two-tip output) that measures their resistance at ambient temperature. The temperature is measured after some minutes of stabilization by a thermometer put inside the box. Applying the formula 3.7 it is possible to find the resistance to be set at a given temperature. Data are listed in the table of Fig. 3.16,

SENSORS	R_h	T_h	R_0	200	250	300	350	400	450	500	550	600	650
TiTaV	9,291	21,1	8,59	15,02	16,56	18,06	19,54	20,98	22,40	23,79	25,15	26,48	27,78
ST25 650	8,755	20,2	8,12	14,20	15,65	17,07	18,47	19,84	21,18	22,49	23,77	25,03	26,26
STN	8,848	20,1	8,21	14,36	15,82	17,26	18,67	20,06	21,41	22,74	24,04	25,31	26,55
ST20 650	8,896	20,1	8,25	14,43	15,91	17,36	18,77	20,16	21,53	22,86	24,17	25,44	26,69
ST25 650+Au	8,744	20,1	8,11	14,19	15,64	17,06	18,45	19,82	21,16	22,47	23,75	25,01	26,24
ST30 650	10,121	20,1	9,39	16,42	18,10	19,75	21,36	22,94	24,49	26,01	27,49	28,95	30,37
ZnO 650	9,677	20,1	8,98	15,70	17,31	18,88	20,42	21,93	23,42	24,87	26,29	27,68	29,04
ZnO 850	9,489	20,1	8,80	15,40	16,97	18,51	20,03	21,51	22,96	24,38	25,78	27,14	28,47
CdS (2)	9,077	21,8	8,37	14,64	16,13	17,60	19,04	20,45	21,83	23,18	24,51	25,80	27,07
SnO2	9,027	22,8	8,30	14,51	15,99	17,44	18,87	20,27	21,63	22,97	24,29	25,57	26,83
SnS2 (1)	-----	-----	8,905	15,57	17,16	18,72	20,25	21,75	23,22	24,66	26,07	27,45	28,80
W11	10,235	24,3	9,36	16,36	18,03	19,67	21,28	22,86	24,40	25,91	27,39	28,84	30,26
ZnO 850	10,047	24,3	9,18	16,06	17,70	19,31	20,89	22,44	23,95	25,44	26,89	28,31	29,70
WS30 650	10,685	24,5	9,76	17,07	18,81	20,52	22,20	23,84	25,45	27,03	28,58	30,09	31,56
ZnO 950	28,570	20,5	26,47	46,29	51,02	55,66	60,21	64,67	69,03	73,31	77,50	81,59	85,60
LF4	10.155	22.4	9.35	16.34	18.01	19.65	21.26	22.83	24.37	25.88	27.36	28.81	30.22
SmFeO3	9.934	22.4	9.14	15.99	17.62	19.22	20.79	22.33	23.84	25.32	26.77	28.18	29.56

Figure 3.16: Resistances associated to the working temperatures of sensors. R_h is the resistance at ambient temperature and R_0 is the resistance at a temperature of 0°

where R is the resistance at ambient temperature, measured in Ω by the multimeter (with a resolution limit of 0.001 Ω, because the following digits are variable); T is the ambient temperature, indicated by the thermometer in °C (with an error of 0.1°C, given by the sensitivity of the instrument); R_0 is the resistance at 0°C, in Ω, calculated inverting the formula 3.7 and other values are the resistances to be set to obtain temperatures from 300 to 650°C, through the formula 3.10. Errors for these last values should be calculated using the formula for error propagation.

Reversing 3.7, we obtain

$$R_0 = \frac{R_h}{1 + \alpha T + \beta T^2} \quad , \tag{3.11}$$

so, its error should be calculated in the following way:

$$\Delta R_0 = R_0 \left(\frac{\Delta R_h}{R_h} + \frac{\Delta(1 + \alpha T + \beta T^2)}{1 + \alpha T + \beta T^2} \right) = R_0 \left(\frac{\Delta R_h}{R_h} + \frac{\alpha \frac{\Delta T}{T} + 2\beta \frac{\Delta T}{T}}{1 + \alpha T + \beta T^2} \right) \tag{3.12}$$

$$\Delta R_0 = R_0 \left(\frac{\Delta R_h}{R_h} + \frac{\Delta T}{T} \frac{\alpha + 2\beta}{1 + \alpha T + \beta T^2} \right) \tag{3.13}$$

For each measure, considering only three digits, the error is of 0.001 Ω. The error for the resistance to be set to obtain desired temperatures, knowing the relative errors for power packs ($\frac{\Delta V_h}{V_h} = \frac{1}{100}$, $\frac{\Delta i}{i} = \frac{1}{1000}$), is given by the formula $\Delta R_h = \left(\frac{\Delta V_h}{V_h} + \frac{\Delta i}{i} \right) R_h = 0.011 R_h$. This corresponds to a relative error of about 4% on the temperature.

3.5 Sensors response

The following step serves to elaborate a sort of *temperature spectrum*, in order to identify the temperature at which each sensor has the best response. The operation is done via the software **TestPoint**: manually changing input voltages and through the relation 3.10 to each sensor is possible to associate the desired resistance, starting from 650°C down to 300°C (each step is of 50°C and corresponds to a change in the input voltage of about 0.4 V). Sending a flow of 500 sccm of synthetic dry air (N 80%, O_2 20%) to the chamber, sensors are left to stabilize. The stabilization is reached when the response on the desktop appears to be flat, due to the fact that humidity is absent or at least a constant next to zero and do not interfere with the measure. At this point it is possible to send the gas, at the desired concentration. In this case the chosen concentrations are:

- 2 and 5 ppm of C_6H_6, minimum and average concentration alerting the presence of a CRC or polyps;

- 10 and 100 ppm of CH_4. Methane is normally elusive for sensors, thus high quantities are needed to obtain appreciable responses, while the lower concentration is taken to simulate its relative concentration, in human intestine;
- 10 and 60 ppm of H_2. Hydrogen normally is well detectable thorugh sensors, interfering with and covering the effects of other chemicals, therefore it will be our main disturbance for benzene detection. The highest concentration is used to simulate its relative concentration, compared to benzene, in human intestine;
- 20 ppm of H_2S. This gas is tricky to test, because of the low autocombustion temperature (260°C) which leads to the chemical reaction 3.1. The concentration is chosen to simulate its relative concentration, compared to benzene, in human intestine;
- 2 ppm of SO_2, tested with the purpose to verify the chemical reaction 3.1, occurring on heated surfaces;
- 2 ppm of NO, a gasotransmitter and bacterial product. The concentration is chosen to simulate its relative concentration, compared to benzene, in human intestine;
- 10 ppm of CO, a product from hemoglobin degeneration and a vascular regulator of cyclic guanosine monophosphate (cGMP) and intestinal smooth muscles.

1-iodo-nonane and decanal, which are in liquid form, where tested in a range of concentrations of $0.88 \cdot 10^{-4} \div 6.14 \cdot 10^{-4}$ mol and $3.2 \cdot 10^{-4} \div 7.76 \cdot 10^{-4}$ mol respectively, in a temperature range from 350 up to 600°C, again with steps of 50°C each. The flux for these concentrations (in ppm) is derived through the relation 3.2 and shown in the following table:

GAS	$F_{tot}(sccm)$	$C_{vol}(ppm)$	$C_{bot}(ppm)$	$F(sccm)$
C_6H_6	500	2, 5	10	100, 250
CH_4	500	10, 100	5000, 25000	1, 2
H_2	500	2, 4, 10, 60	1000	1, 2, 5, 30
H_2S	500	20	100	100
SO_2	500	2	100	10
NO	500	2	100	10
NO_2	500	2, 5	10	100, 250
CO	500	10	100	50

Here the total flux is indicated with F_{tot} and C_{vol} , C_{bot} are the concentration in volume and the certified concentration of the bottle. Since the total flux arriving to the chamber must be fixed at 500 sccm, in order to send a flux of gas, it is necessary to proportionally decrease that of dry air so that their sum remains equal to 500 sccm. For the gases taken singularly, we had an inflated dry air flux of:

- 400 sccm for C_6H_6;
- 499 sccm for CH_4;
- 495 sccm for H_2;
- 400 sccm for H_2S;
- 490 sccm for SO_2;
- 490 sccm for NO;
- 250 sccm for NO_2;
- 450 sccm for CO.

Then, in the case of interference tests:

- for $H_2S + NO_2 + C_6H_6$, 100 sccm of hydrogen sulfide, 100 sccm of nitrogen dioxide, 100 sccm of benzene and alternatively 200 sccm of dry or wet synthetic air were inflated;
- for $SO_2 + NO + C_6H_6$, 10 sccm of sulfur dioxide, 10 sccm of nitrogen oxide, 100 sccm of benzene and alternatively 380 sccm of dry or wet synthetic air were inflated;
- for $CH_4 + H_2 + C_6H_6$, two different setup of concentrations were taken, one with the inflation of 30 sccm of hydrogen (switched to 1 sccm, corresponding to 2 ppm, to compare the response to that of benzene at the same concentration), 1 sccm of methane, 100 sccm of benzene and alternatively 369 sccm of dry or wet synthetic air, the other with 30 sccm of hydrogen (switched to 2 sccm, corresponding to 4 ppm, to compare the response to that of benzene at nearly the same concentration), 1 sccm of methane, 250 sccm of benzene and alternatively 219 sccm of dry or wet synthetic air.

During interference tests, the working temperatures of the sensors were set at the best ones for the detection of the target gas (benzene) with respect to the two interferers.

Concerning the drop measurements, for both decanal and 1-iodo-nonane, two flows of synthetic dry air were sent into the chamber: one pure of 200 sccm and one of 300 sccm, after passing through the gas bubbler were the drops were left.

Flows were maintained constant during the interference tests, but the gas bubbler was filled with water, to simulate the water vapor present inside the intestine. The working temperature was fixed at 450°C, the best one for the most significant sensors to detect both chemicals.

Once the response reached stability (when the slope of the curve became quite null for each sensor), generally after 10-20 minutes from the beginning of the measurement, it was possible to stop the gas and let sensors stabilize another time. By repeating this process for the two gases of interest at each working temperature, the response was found in the form of an output voltage (V_{out}). To better visualize it in real time, during the mesurement it was useful to change resistances in a circuit connected to the sensors. Increasing or decreasing values of resistors, also output voltages were shifted. For a practical point of view, it was useful to put them at a value next to 1, because the response seen on the desktop increased proportionally to the starting baseline. This discrepancy was removed normalizing the response to 1. As it has been described in the previous chapter, the response is given by the relation 3.3 as a ratio of the conductance in air and in gas, equal to the ratio of output voltages. Using the software EasyPlot, it is obtained the graphic of the output voltages as a function of time. Then response graphics are realized normalizing curves to 1 by equation 3.14:

$$R = \frac{y}{V_{out}(base)}. \tag{3.14}$$

where $V_{out}(base)$ is the voltage value of the baseline of the curve (when sensors were stable in dry air). In the following pages the most significant graphics are shown, corresponding to the temperature spectra of C_6H_6 (Fig. 3.17), H_2S (Fig. 3.18, where it is also evident the characteristic sign of the reaction described by the formula 3.1), the whole $SO_2 + NO + C_6H_6$ dry interference (Fig. 3.19), part of the wet interference $H_2S + NO_2 + C_6H_6$ (Fig. 3.20), the interference $C_6H_6 + H_2 + CH_4$ (Fig. 3.21), $C_9H_{19}I$ (Fig. 3.22), $C_{10}H_{20}O$ (Fig. 3.23), and the wet interference $C_9H_{19}I + C_{10}H_{20}O$ (Fig. 3.24) [41].

After these previous steps it is possible to identify for each sensor the temperature of best response to the considered gas or mixture. Here data are reported, graphically, inside histograms (Fig. 3.25, 3.26, 3.27, 3.28, 3.29, 3.30, 3.31). The accuracy for these data is given by the following formula, typical of the software used: $\pm$(30 ppm$\times$ READING VOLTAGE + 5 ppm$\times$ RANGE VOLTAGE) so, considering an average voltage of 5 V (intermediate value considering the ordinate of the graphic seen on the desktop that covers the interval 0$\div$12 V) and a range of 10 V (given by the settings of the instrument), the accuracy is of $\pm 200\mu V$, about 4 order of magnitudes smaller than the measure. *The error is so small that may be neglected for the scope of this analysis.*

It is important to notice that all the oxidative (negative) responses are normalized so that their baseline corresponds to 0, and not to 1 like reductive (positive) responses. Looking at these results, the most sensitive sensors to benzene, decanal and 1-iodo-nonane have been identified.

From these histograms, some statements regarding tests employing gas bottles can be

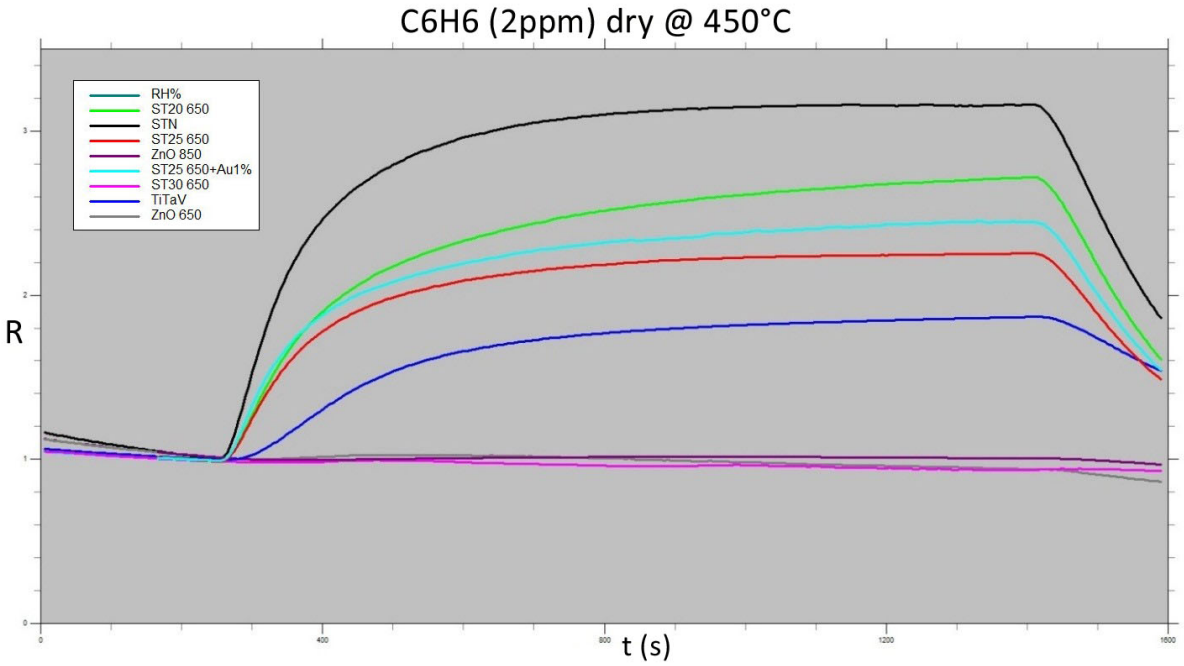

Figure 3.17: Sensor responses (R) as a function of time (t), to 2 ppm of C_6H_6 in dry conditions at 450°C [2].

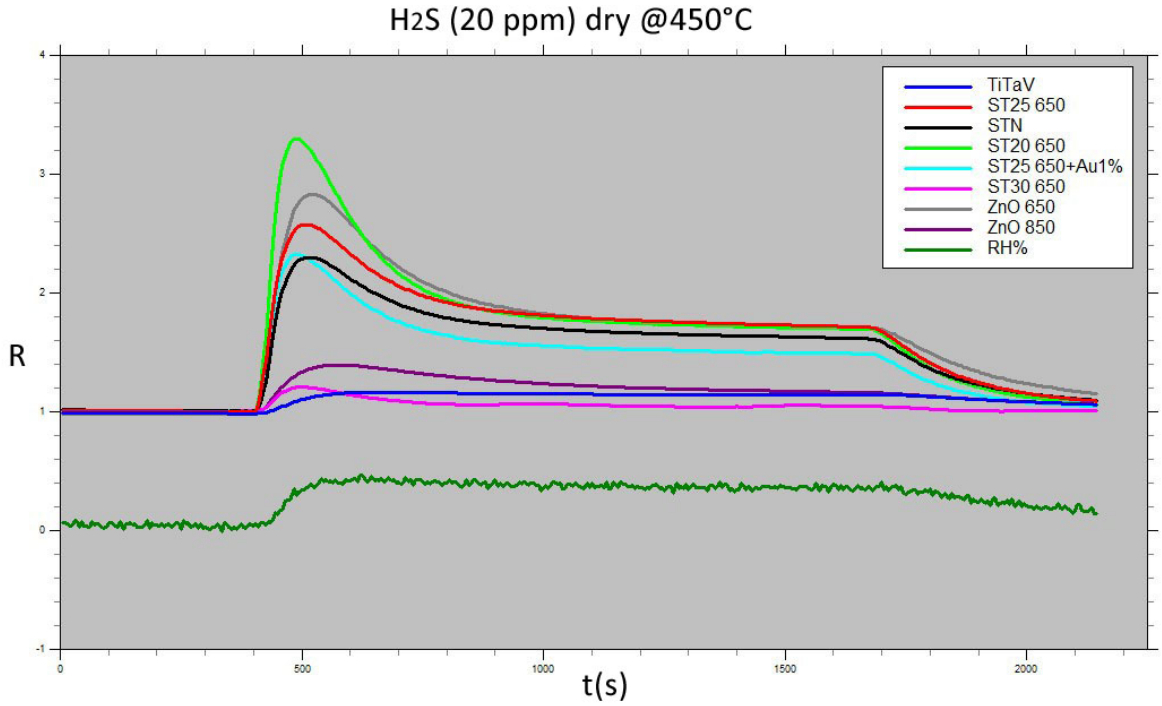

Figure 3.18: Sensor responses, as a function of time (t), to 20 ppm of H_2S in dry conditions at 450°C. Humidity increases when H_2S is inflated, due to the effect of the reaction 3.1 [2].

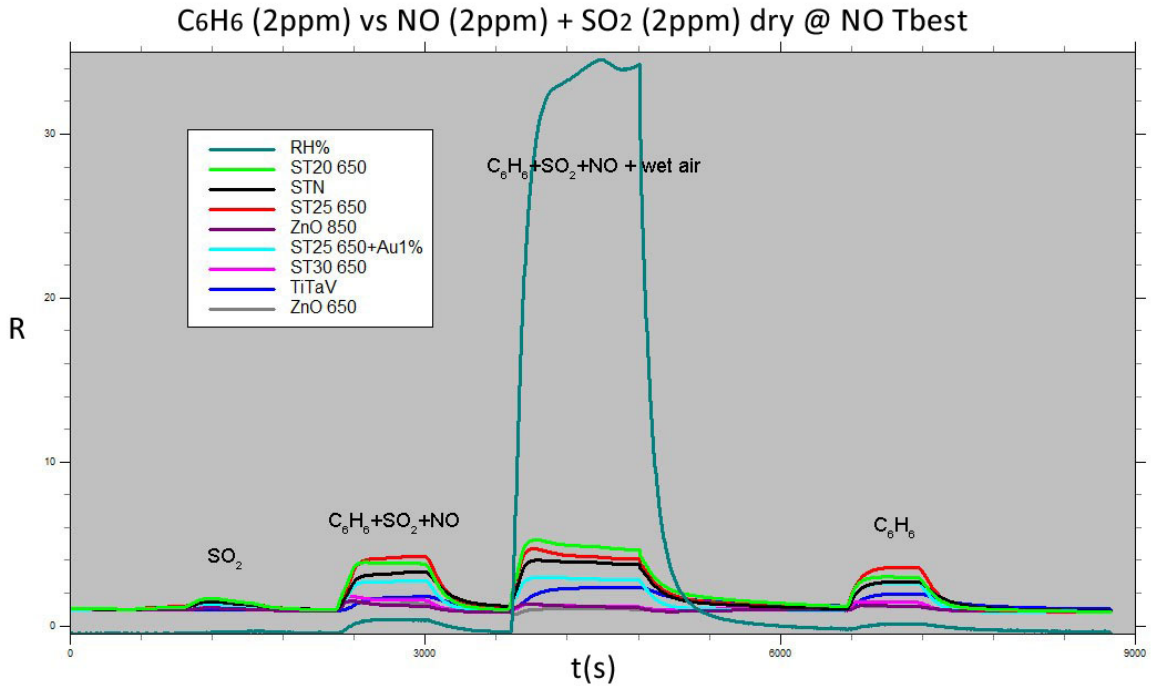

Figure 3.19: Sensor responses (R), as a function of time (t), to SO_2 (1^{st} peak), $C_6H_6 + SO_2 + NO$ (2^{nd} peak), $C_6H_6 + SO_2 + NO$+wet air (3^{rd} peak), C_6H_6 (4^{th} peak) in dry conditions. The gas concentrations are of 2 ppm for all the gases. Temperature chosen are the ones at which the sensor responses to NO become negligible [2].

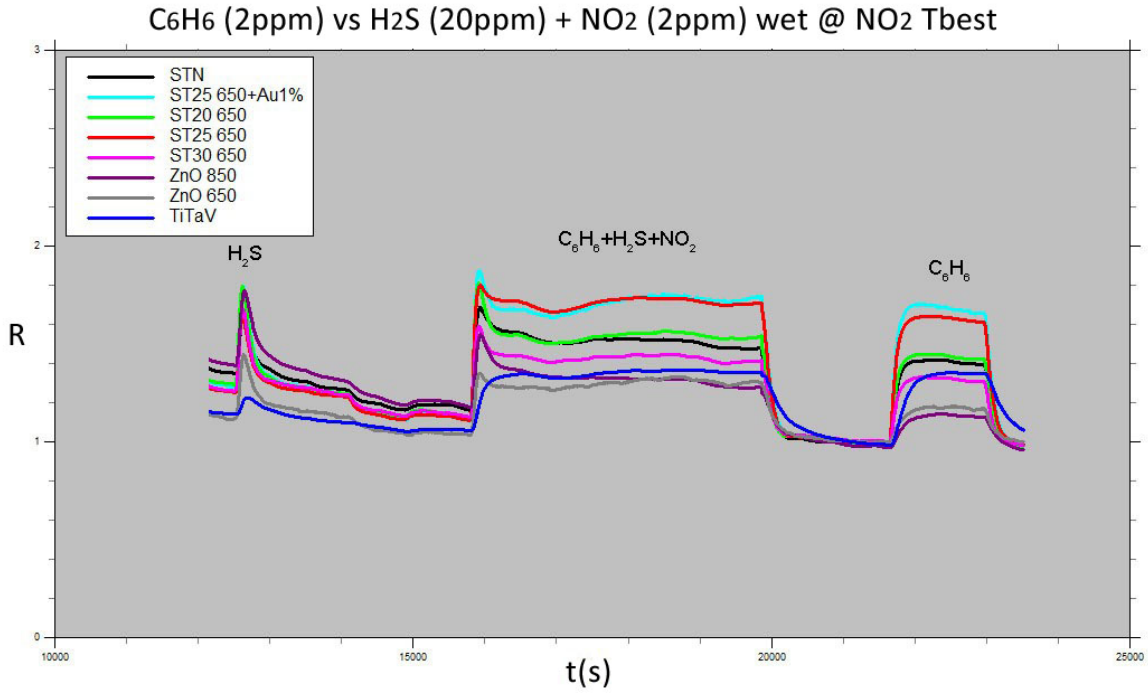

Figure 3.20: Sensor responses (R), as a function of time (t), to H_2S (1^{st} peak), $C_6H_6 + H_2S + NO_2$ (2^{nd} peak), C_6H_6 (3^{rd} peak), in wet conditions. The gas concentrations are of 2 ppm for C_6H_6 and NO_2 and of 20 ppm for H_2S. Temperature chosen are the ones at which the sensor responses to NO_2 become negligible [2].

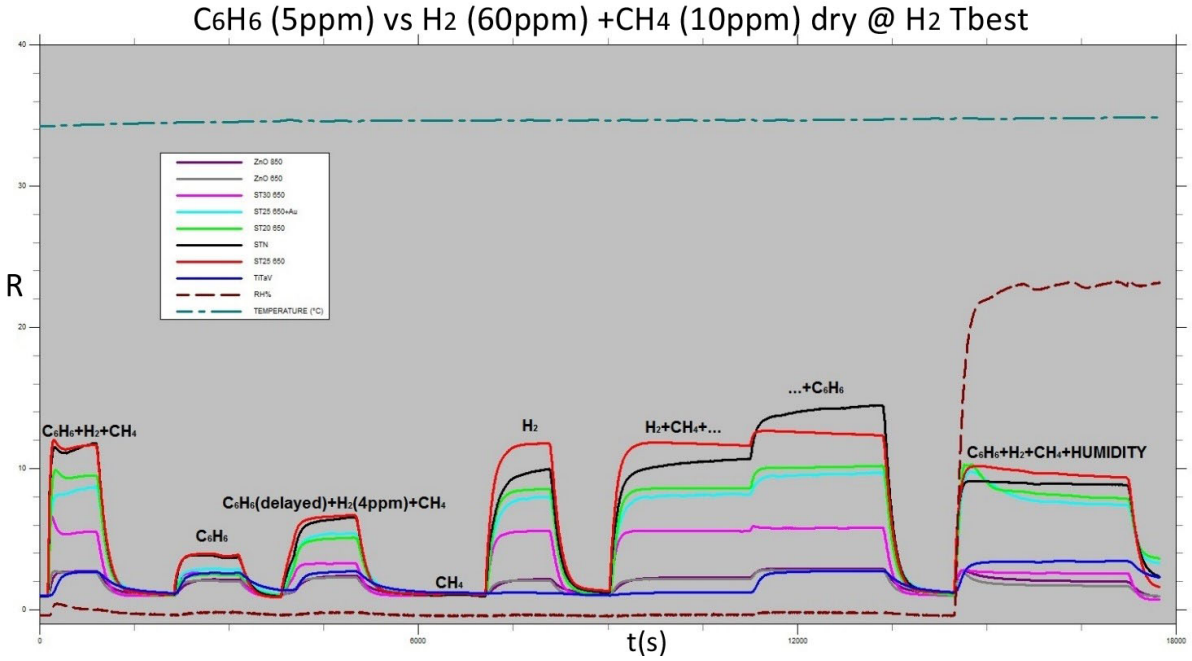

Figure 3.21: Sensor responses (R), as a function of time (t), to $C_6H_6 + H_2 + CH_4$ (1^{st} peak), C_6H_6 (2^{nd} peak), $C_6H_6 + H_2 + CH_4$ with H_2 at a closer concentration to the one of C_6H_6 and the flow of C_6H_6 slightly delayed (3^{rd} peak), CH_4 (4^{th} peak, nearly null), H_2 (5^{th} peak), $H_2 + CH_4$ and delayed addition of C_6H_6 (6^{th} peak), $C_6H_6 + H_2 + CH4_+$ humidity as interferer (RH%: 23.01), in dry conditions (7th peak). Temperature chosen are the ones at which the sensor responses to H_2 are the lower as possible compared to C_6H_6 [2].

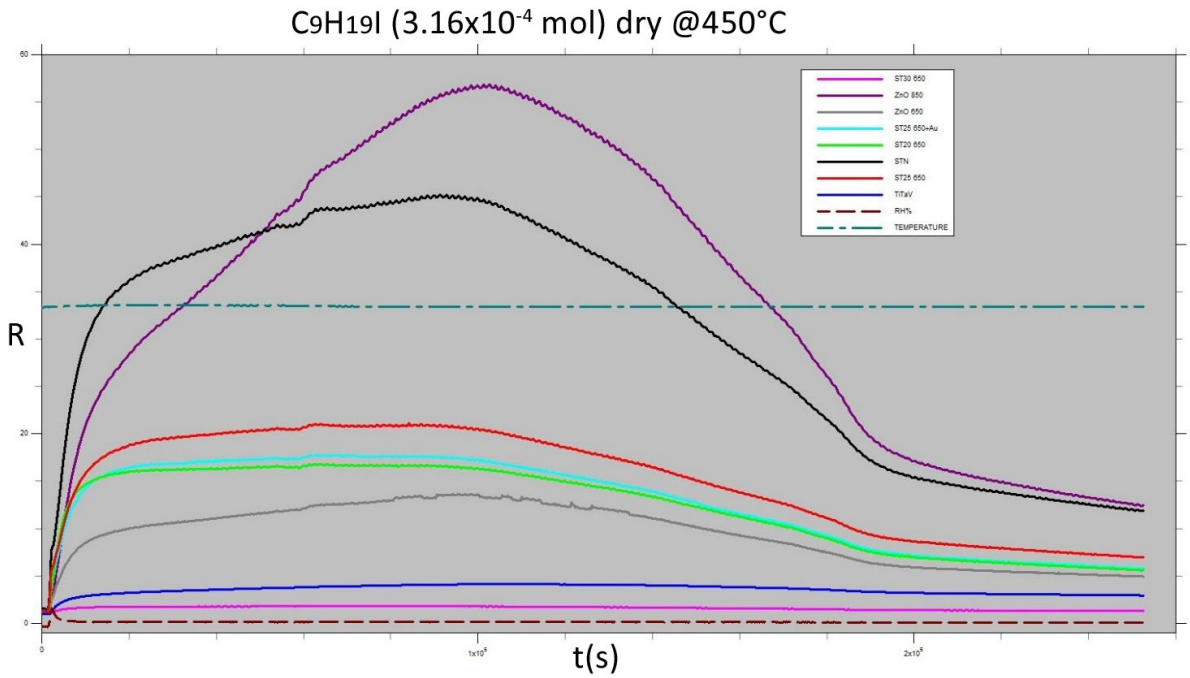

Figure 3.22: Sensor responses (R), as a function of time (t), to $C_9H_{19}I$ in dry conditions at 450°C [2].

deducted :

- the occurrence of reaction 3.1 for hydrogen sulfide on heated surfaces has been verified, as described in literature [83] and expected from the setup, due to the increase of humidity in the chamber during the inflation of hydrogen sulfide. In particular, an interesting behavior can be guessed from Fig. 3.20 (and described also in a the paper of Malagù et al. (2014)[34]). As shown in detail in Fig. 3.32, inside the first circle, the behavior of the curves recalls the signature of hydrogen sulfide (already seen in Fig. 3.18), even in the interference with benzene. In fact, at first benzene increases responses, then they drop under the plateau level (second circle). This phenomenon does not occur for H_2S, whose response is reductive, but a similar effect is given by NO_2 (oxidizing), which then disappears to reach again the original plateau, following the same trend of C_6H_6 (third circle). This effect was recurring for both dry and wet interferences between these gases. These sort of signatures can be used to recognize the presence of a specific gas or reaction, directly observing the behavior of the sensor responses;

- while the working temperatures for the sensor array chosen to identify benzene range from 450 to 650°C, the best working temperature in order to detect the two aldehydes (decanal and 1-iodo-nonane) seems to be of 450°C for all the sensors used, except

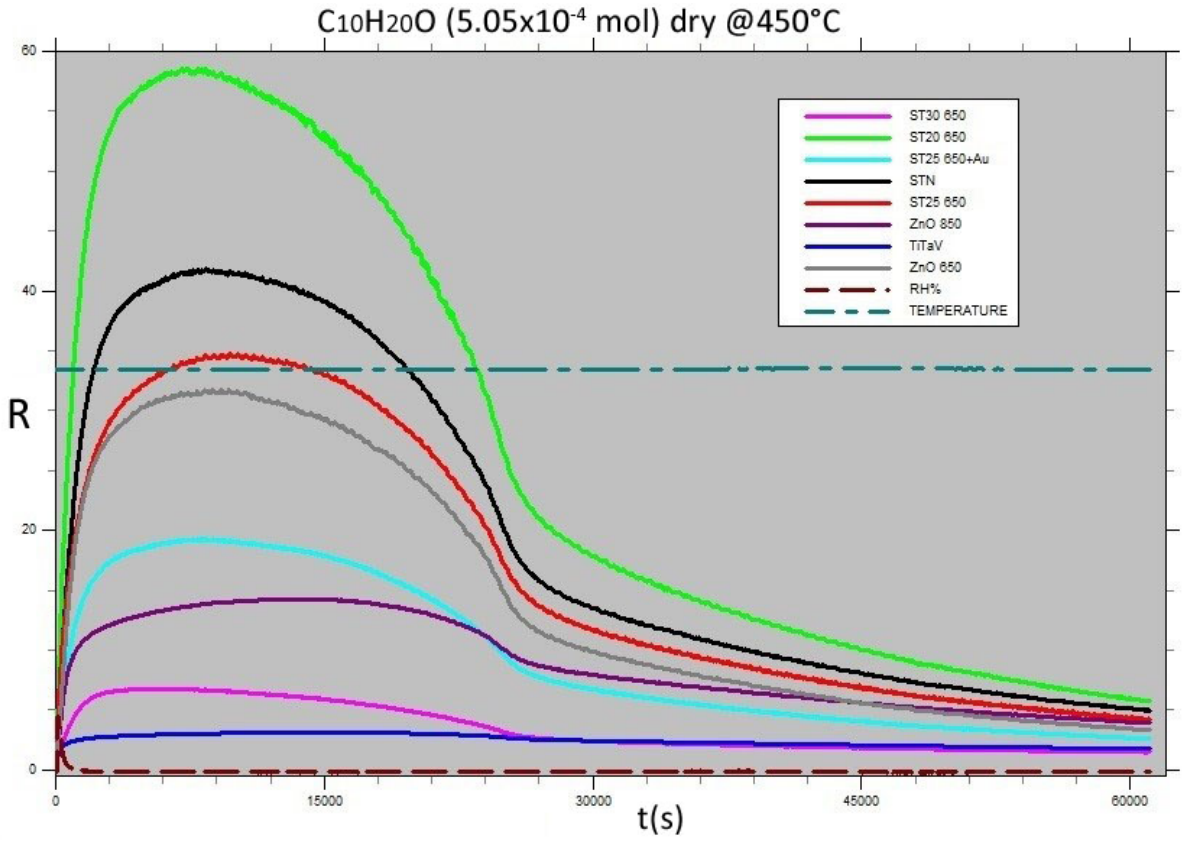

Figure 3.23: Sensor responses, as a function of time (t), to $C_{10}H_{10}O$ in dry conditions at 450°C [2].

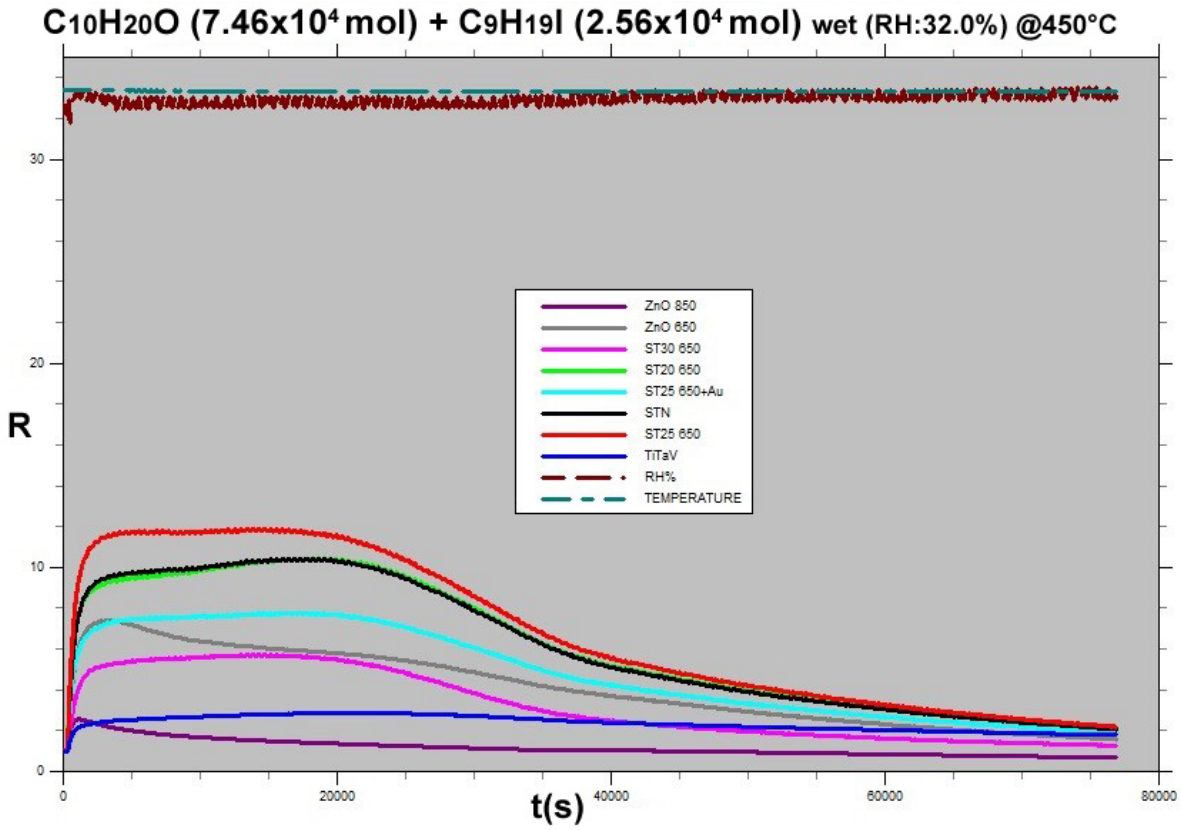

Figure 3.24: Sensor responses, normalized to 1, as a function of time (t), to $C_9H_{19}I + C_{10}H_{10}O$ in wet conditions (RH:32.0%) at 450°C [2].

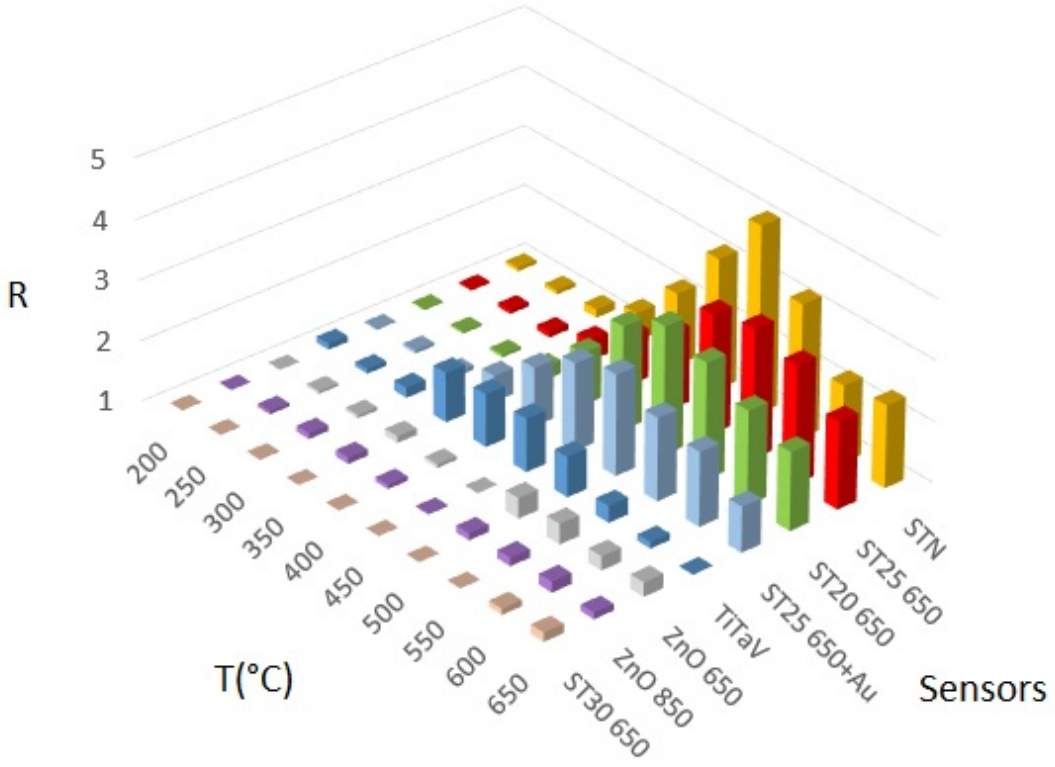

Figure 3.25: Histogram representing the responses of sensors to C_6H_6 as a function of temperature (T) in °C [2].

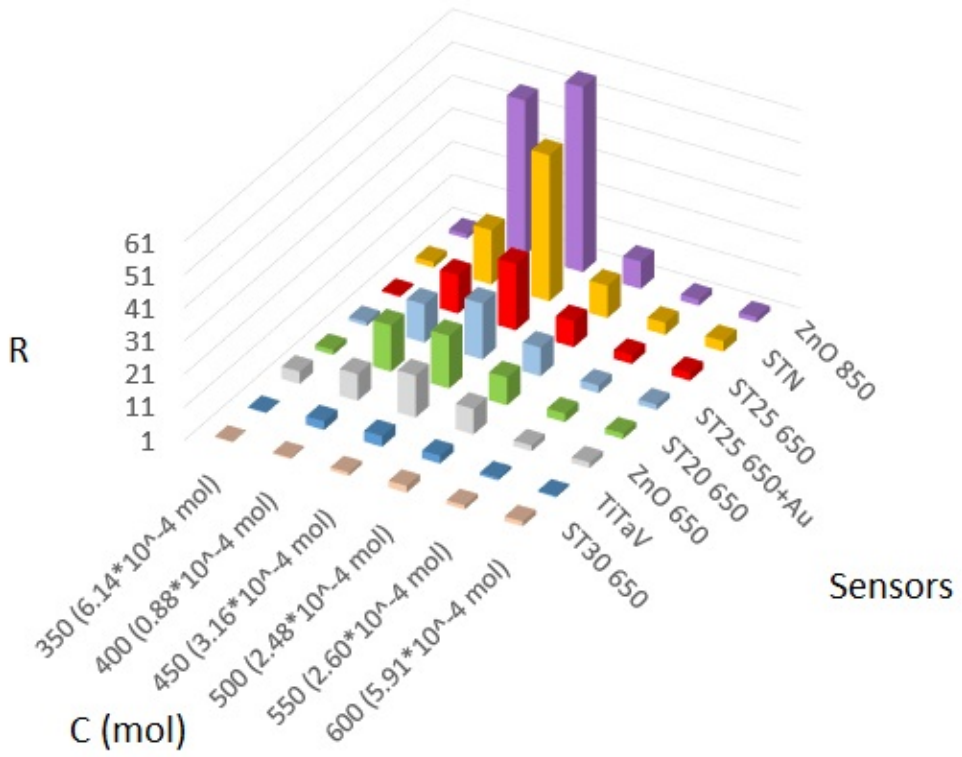

Figure 3.26: Histogram representing the responses of sensors to $C_9H_{19}I$ as a function of the concentration (C) in moles [2].

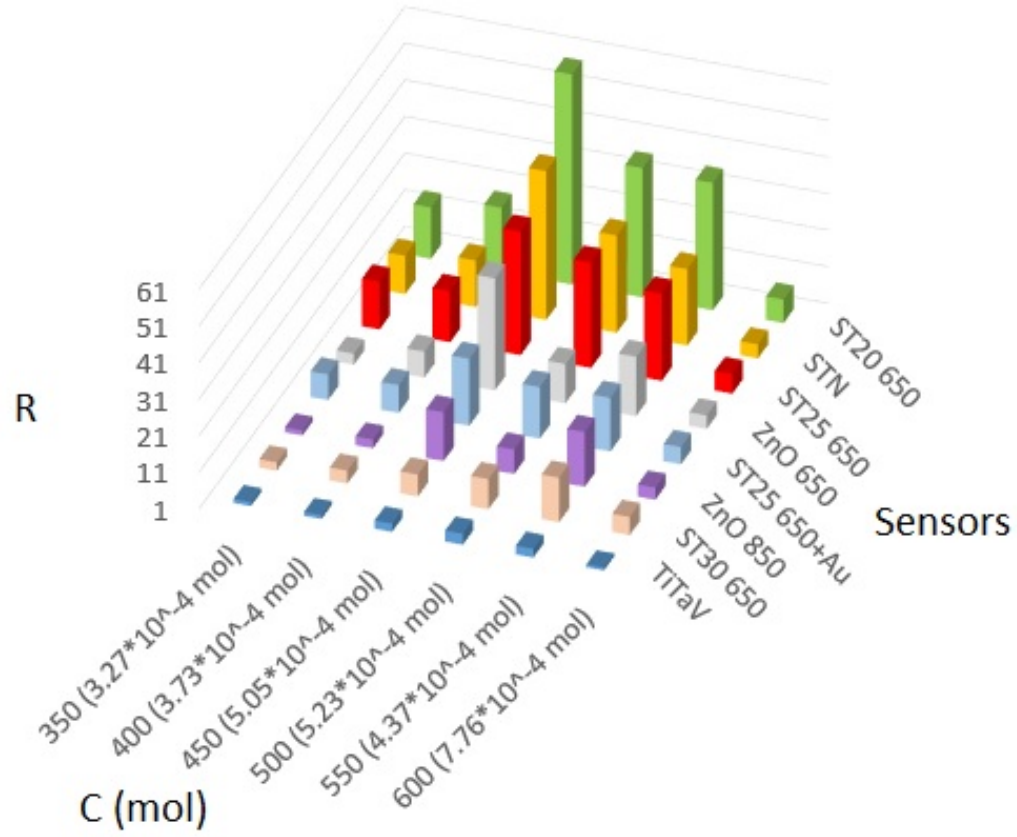

Figure 3.27: Histogram representing the responses of sensors to $C_{10}H_{20}O$ as a function of the concentration (C) in moles [2].

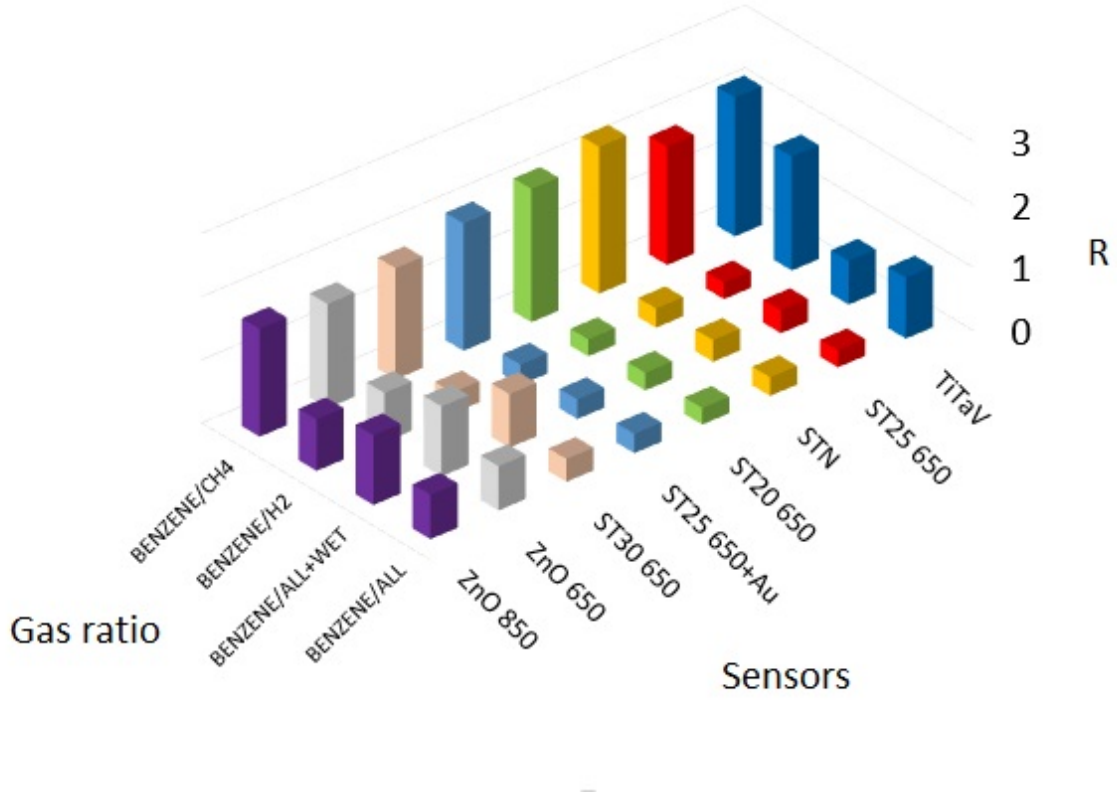

Figure 3.28: Histogram representing the ratios regarding the interference $C_6H_6 + H_2 + CH_4$ (H_2 best rate, dry, 2ppm of C_6H_6 , chamber temperature: 34,8°C) [2].

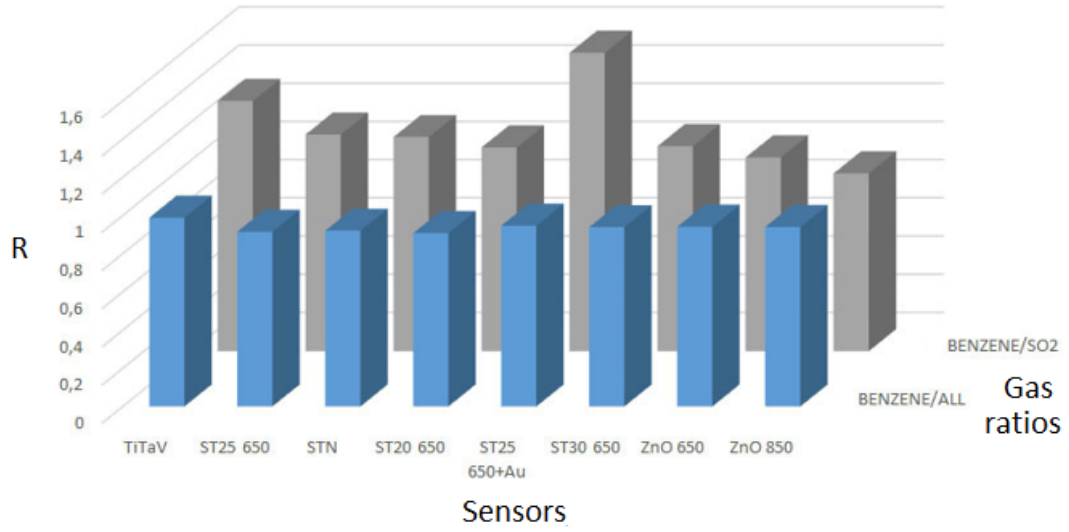

Figure 3.29: Histogram representing the ratios regarding the interference $C_6H_6 + SO_2 + NO$ (NO best rate, RH: 33.81%, 2ppm of C_6H_6 , chamber temperature: 36°C) [2].

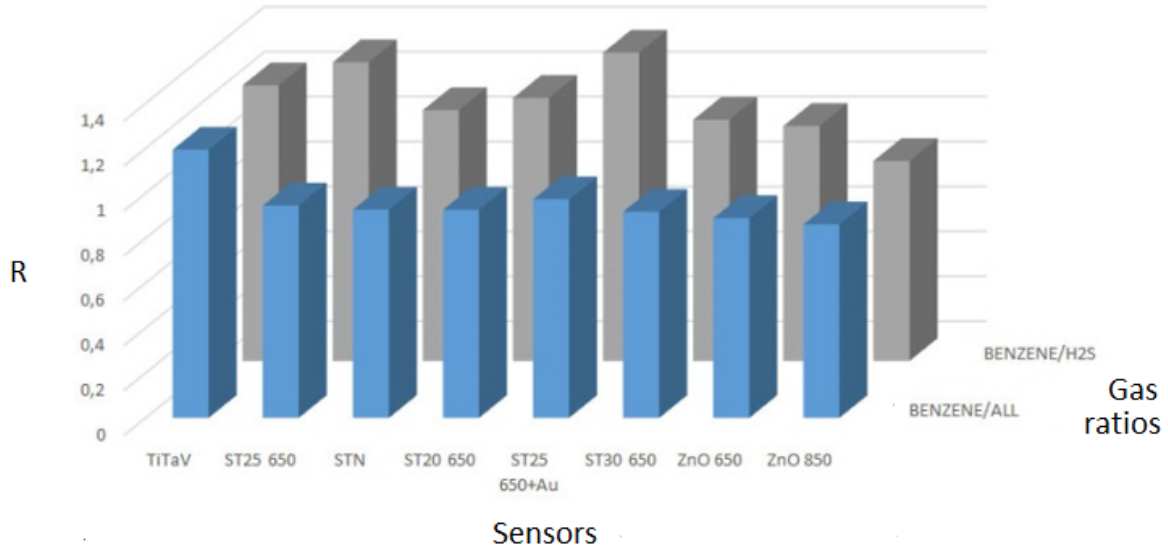

Figure 3.30: Histogram representing the ratios regarding the interference $C_6H_6 + H_2S + NO_2$ (NO_2 best rate, RH: 19.86%, 2ppm of C_6H_6 , chamber temperature: 34.6°C) [2].

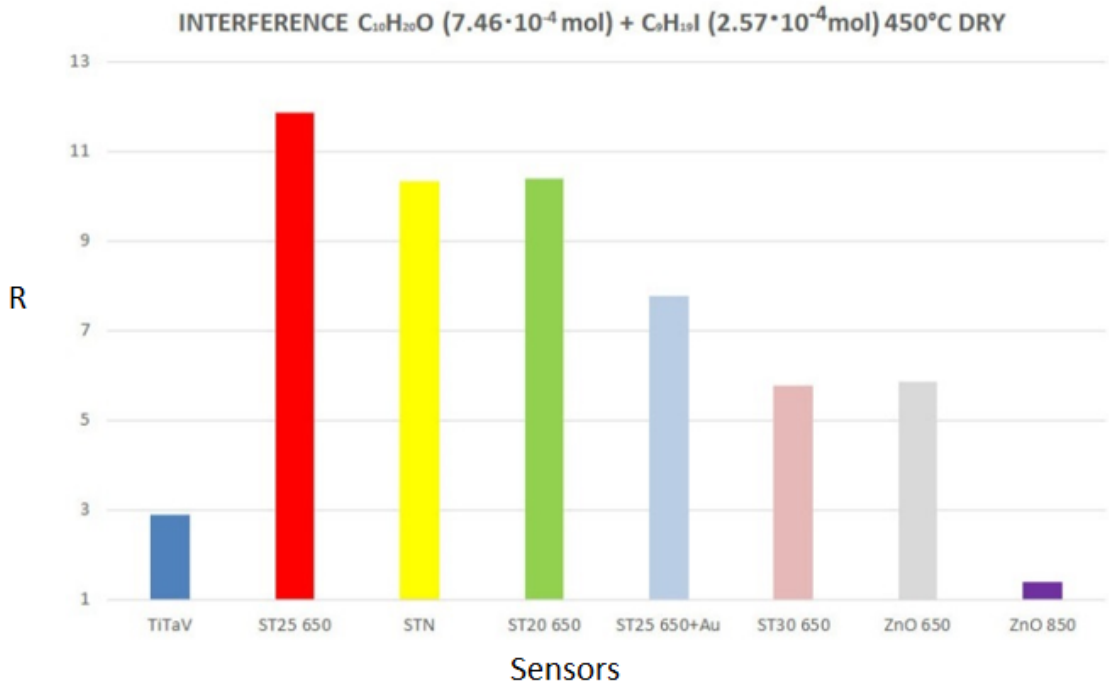

Figure 3.31: Sensor responses to $C_9H_{19}I$ and $C_{10}H_{20}O$ in combination, in wet conditions. The working temperature of all sensors is fixed at 450°C. Under parenthesis is shown the quantity of reagent (moles) taken for each measure [2].

ST30 650, whose best working temperature is of 500°C for both the compounds, and except TiTaV, whose best working temperature to detect decanal is 500°C;

- responses are oxidative in presence of NO_2, and also in presence of benzene for ZnO 650 and ZnO 850 sensors at 200°C;
- ST25 650+Au showed to be the fastest sensor, for both response time and for recovery time.

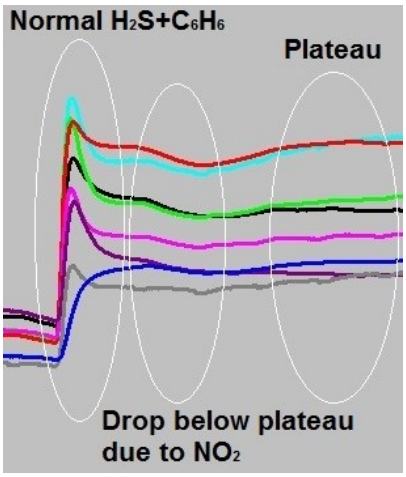

Figure 3.32: Zoom on the sensor response of $C_6H_6 + H_2S + NO_2$ interference, in wet conditions [2].

Ratios between different gas responses can be defined as the ratio between the target gas response and the interferer(s) response, thus identifying the best sensors for different aims (for instance, to detect the target gas mixed to one or more interferers, or to observe the amplitude of the response to a particular interferer inside the mixture).

From graphs in the book *Detection of tumor markers on feces with nanostructured sensors* [2] (a book which contains all details of this work) it is possible to arrive to the following conclusions:

- TiTaV is overall the best sensor to discriminate C_6H_6 inside gas mixtures (two gases or more) of the intestinal gases tested in this thesis, expecially against the major interferers H_2 and CH_4, which do not affect so much the total response. This is due to the fact that TiTaV is really refractory to all the other chemical species tested, but it has good affinity with benzene. So, even if the other sensors show higher responses to benzene (alone or against a particular chemical), the strict selectivity of TiTaV makes it the best choice for benzene detection inside the intestinal environment (i.e., in flatus). The gas combination that seemed to give more problems to TiTaV was $H_2S + NO_2$, due to the reactivity of the two species with oxygen and water vapor;

- for some interference tests in wet conditions, some sensors look to be the best gas detectors, like ST30 650 or ZnO 650. However, taking a closer look to the response graphics, it appears crystal clear that this is only a mathematical effect. The only advantage those sensors had was the higher working temperature of the film, linked to a hastened evaporation of water over their surface;
- in presence of H_2, benzene proved to be the most detectable gas for all tin oxide sensors.

3.6 Principal component analysis

In the previous work, the attempt was to test different sensing materials inside a chamber which can contain up to eight sensors, in order to find the most selective ones to CRC-biomarkers (e.g., benzene, 1-iodo-nonane, decanal). Although the high number of test performed (both with gases taken singularly and gas mixtures), the conclusions were only useful to make a preliminary selection of materials but not sufficient to discriminate single compounds with high precision. In order to obtain more information on sensor responses, the idea was to perform a statistic treatment on data, named **Principal Components Analysis (PCA)**[84].

PCA is a way of identifying patterns in data, and expressing them in such a way as to highlight their similarities and differences. Since patterns can be hardly observable in data of high dimensions, where the luxury of graphical representation is not available, PCA is a powerful tool for analyzing data giving more information otherwise hidden. Another main advantage of PCA is that, once patterns in the data have been found and the data compressed, i.e. by reducing the number of dimensions, there is not significant loss of information.

PCA can be thought of as fitting an n-dimensional ellipsoid to the data, where each axis of the ellipsoid represents a *principal component (PC)*. If some axis of the ellipse is small, then the variance along that axis is also small, and by omitting that axis and its corresponding PC from the representation of the dataset, only a commensurately small amount of information is lost.

To find the axes of the ellipse, it is necessary first to subtract the mean of each variable from the dataset to center the data around the origin. Then, the covariance matrix of the data can be computed, and the eigenvalues and corresponding eigenvectors of this covariance matrix calculated. Then, it follows the orthogonalization of the set of eigenvectors, and the normalization of each to obtain unit vectors. Once this step is done, each of the mutually orthogonal unit eigenvectors can be interpreted as an axis of the ellipsoid fitted to the data. The proportion of the variance that each eigenvector represents can be calculated by dividing the eigenvalue corresponding to that eigenvector by the sum of all eigenvalues.

It is important to note that this procedure is sensitive to the scaling of the data, and that there is no consensus as to how to best scale the data to obtain optimal results.

3.6.1 Example of PCA treatment

As mentioned earlier, the purpose of the PCA is to identify patterns in data samples, in order to perform a reduction of variable sample sizes. This reduction can be achieved through a "compression" of the data, trying not to lose too much information. To better understand the PCA processes, a PCA will be carried out, step by step, using a part of the data obtained by laboratory analysis: the response of two sensors (ST25 650 + Au and 650 ST20) in a screening test for CRC through the analysis of 9 healthy patients stool (see Chapter 4). The data employed are summarized in the Table 3.6.1, where in the first two column are shown the response values of the two sensors, and in the second two columns the variation from the mean of each measurement:

ST25 650+Au	ST20 650	x	y
15,64	11,72	6,35	4,15
5,49	4,08	-3,80	-3,49
8,02	6,46	-1,27	-1,11
6,84	5,26	-2,45	-2,31
5,62	5,22	-3,67	-2,35
9,50	7,93	0,21	0,36
14,31	13,01	5,02	5,44
8,97	7,03	0,32	-0,54
9,26	7,43	-0,03	-0,14

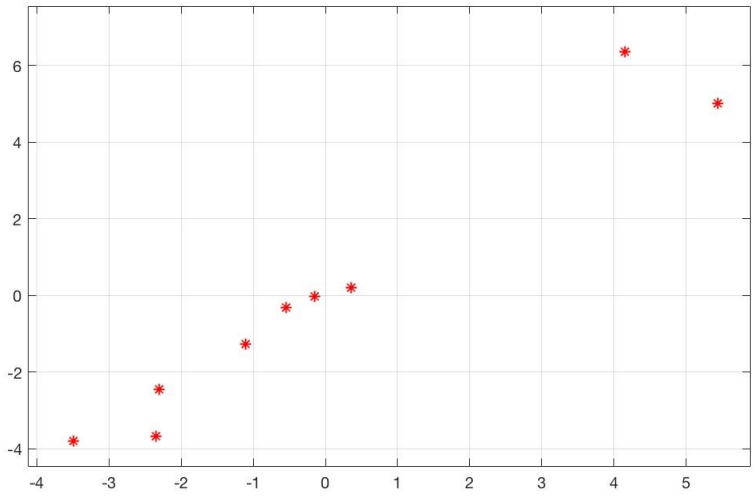

Figure 3.33: Graphic representation of the data.

In Fig. 3.33 a graphic representation of the data. The next step will be to creation of the covariance matrix, in this case will be a 2×2 matrix:

$$Cov = \begin{pmatrix} 12,649 & 10,361 \\ 10,361 & 8,947 \end{pmatrix} \tag{3.15}$$

The resulting eigenvalues (E) and eigenvectors (v) will be, respectively: $E = \begin{pmatrix} 21,323 \\ 0,273 \end{pmatrix}$ and $v = \begin{pmatrix} 0,6419 & -0,7668 \\ -0,7668 & -0,6419 \end{pmatrix}$. In Fig. 3.34, a plot of the two eigenvectors and of dispersions.

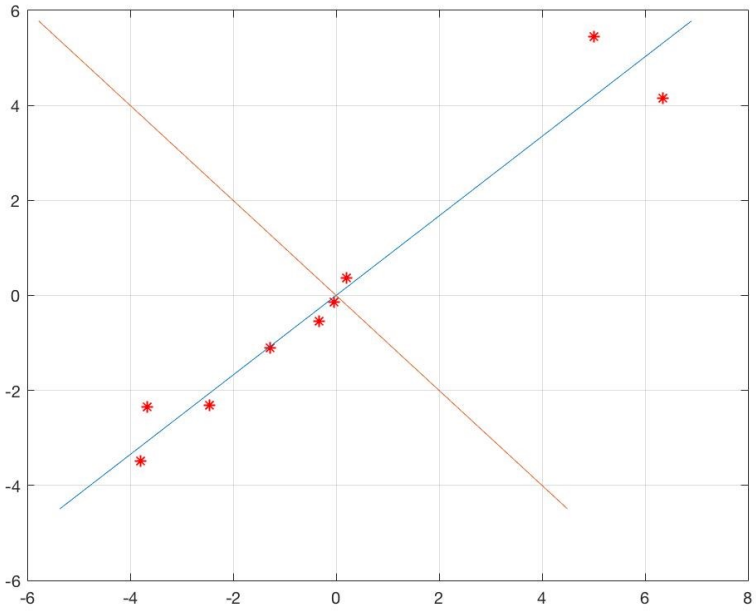

Figure 3.34: Graphic representation of the eigenvectors and of dispersions.

It is noticeable from Fig. 3.34 that one of the two eigenvectors seems to follow accurately the distribution of data. This eigenvector is the PC. The second eigenvector provides little information about the patterns of our data, which seem to be arranged all along the PC, but its contribution is not null and generates a slight shift of the pattern. In this specific case, the PCA studies the patterns of the data as if they were tied to only one main eigenvector. Ignoring the least significant eigenvectors definitely produces a loss of information, however, this information can be considered negligible.

The meaning of the PCA is, therefore, to reduce the degrees of a system of n-dimensions (with n eigenvectors) to a new system of n-dimensions, in which, however, only a reduced number p of the new variables with the largest variance is kept (in which p is the number of principal eigenvectors).

The act of choosing the principal components means to find a compromise between the loss of information and the reduction of system size. Therefore, the eigenvectors that will be chosen will be those generated by progressively smaller eigenvalues. Once such principal eigenvectors are chosen, a characteristic vector (v_c) is then constructed (or a matrix that includes the main eigenvectors):

$$v_c = \begin{pmatrix} v_1 & v_2 & v_3 ... & v_p \end{pmatrix} \tag{3.16}$$

In the specific case presented here: $v_c = \begin{pmatrix} 0,6419 & -0,7668 \end{pmatrix}$

After choosing the components to be conserved (by using the v_c), data can be rewritten in the final form, where the variation in the final shape is given as:

$$V_f = {v_c}^T \times {V_d}^T \tag{3.17}$$

where T is the transposition operator and V_d is the variation of data from the mean (x and y in Table 3.6.1). The new data obtained have components only on the eigenvectors chosen as characteristic vectors.

Imagine to have chosen as v_c both the two found eigenvectors. It is expected to achieve a simple rotation, in which the new axes are the chosen eigenvectors, since there is not lost information. As can be observed in Fig. 3.35, which shows the plot of the data shown in Table 3.6.1, less than a scale factor, the plot of the data written in the final form is no more than a data rotation of the plot in Fig. 3.34.

x	y
-7,528	0,894
5,160	0,237
1,688	0,032
3,362	0,192
4,329	-0,553
-0,388	-0,144
-7,341	-0,955
0,598	0,209
0,119	0,089

Choosing as a PC only the most significant vector $v_c = \begin{pmatrix} 0,6419 & -0,7668 \end{pmatrix}$, as expected, having lowered the data by one degree the size, the obtained system will be one-dimensional and the final variations will result as in Table 3.6.1.

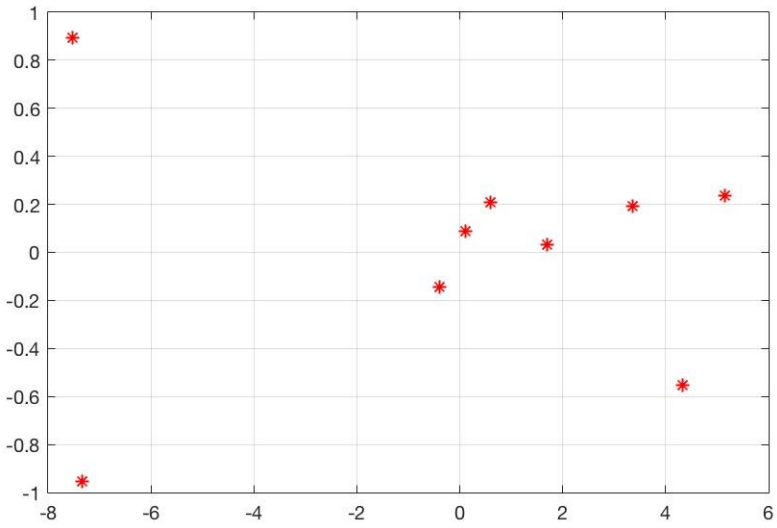

Figure 3.35: Plot of the variation from the mean value in the final form, by using the two eigenvectors.

x
-7,528
5,160
1,688
3,362
4,329
-0,388
-7,341
0,598
0,119

Moreover, by comparing Tables 3.6.1 and 3.6.1, it is noticeable that the x-axis does not undergo variations after the elimination of the second eigenvector.

The inverse problem, which consists in recovering the original data after it is processed, can be faced by inverting the transformation 3.17. However, due to the elimination of the eigenvectors, the "new" original data will have lost the information. The inverse transformation is:

$$V_d = ({v_c}^T)^{-1} \times V_f \tag{3.18}$$

and to obtain the new original data (OD):

$$OD = ((v_c{}^T))^{-1} \times V_f) + OMV \tag{3.19}$$

where OMV is the original mean value.

From the observation of Fig. 3.36, by comparing the variations obtained with the original ones in Fig. 3.34, it is evident that the component along the excluded eigenvector excluded is completely eliminated.

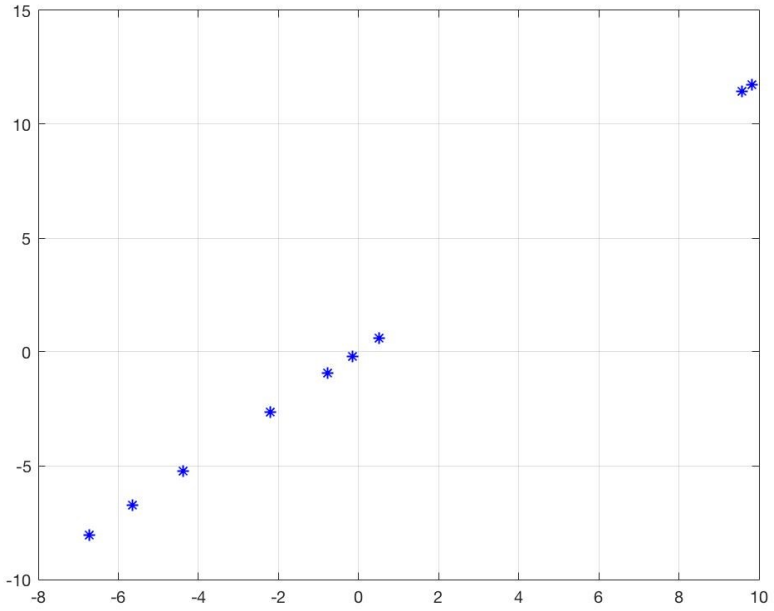

Figure 3.36: The graph represents the superposition of the variations in Fig. 3.34 and new variations obtained via (13).

The methodology just described shows numerous applications and it can be used to search for patterns in any data sample that can be written in matrix form. A very interesting application is the facial recognition, due to the fact that an image can be written as a matrix of pixels. In the following section is proposed the application of PCA to CRC-VOC and interferers recognition.

3.6.2 CRC biomarkers analyzed with PCA

Data obtained with the sensor array employed for the analysis of CRC-biomarkers (1-iodononane, decanal and benzene), already described in Section 3.3, inside a mixture of intestinal gases taken from gas bottles (SO_2, NO_2, NO, H_2S, H_2, CO, CH_4) have been

analyzed by the help of PCA.
Two different approaches have been followed with two different intentions:

- *gases VS array*, where each gas is considered as a single category and the sensors are the starting variables. This approach has been done for six different working temperatures in the range 350-600 °C. The graphs, obtained by reducing the system to three PC, show the best temperature at which the array better discriminates each target gas;

- *gases VS temperature*, where each gas is considered as a single category and the temperatures (in the range 350-600 °C) are the starting variables. This approach has been done for each sensor of the array. The graphs, obtained by reducing the system to three PC, show the sensor that better discriminates each target gas.

Regarding the approach *gases VS array*, I report here, as an example, the optimum temperature for gas discrimination, that resulted to be 600°C. In the table below are shown the starting data, i.e. the responses of each sensor to the gas listed in the first column.

GAS	TiTaV	ZnO 650	ZnO 850	ST20 650	ST25 650+Au	ST25 650	ST30 650	STN
C_6H_6	1,11	1,23	1,18	2,55	2,23	2,95	1,10	2,28
$C_9H_{19}I$	1,43	2,69	2,55	2,63	2,59	3,31	2,46	4,20
SO_2	1,02	1,50	1,23	3,17	2,42	3,38	2,03	2,86
NO_2	1,01	1,30	1,17	1,04	1,00	1,02	1,19	1,03
NO	1,07	1,37	1,40	1,68	1,29	1,54	1,56	1,35
H_2S	1,02	1,02	0,87	1,20	1,07	1,24	0,89	1,23
H_2	1,01	1,04	1,01	2,41	2,35	2,78	1,10	2,37
CO	1,01	1,10	1,23	2,88	2,91	3,51	1,49	3,19
CH_4	1,01	1,44	1,33	4,24	4,38	5,35	1,68	4,33
$C_9H_{19}I$	1,81	4,72	4,28	7,42	5,70	6,34	5,93	4,82

In Fig. 3.37 is shown the projection PC1 vs PC2, where on the left side diagram are reported the variables (sensors) and on the right side diagram the gases analyzed. All the dots are in a different position of the space PC1-PC2 and so they show a good degree of discrimination. The other two projections are reported in Fig. 3.38, 3.39.

The second approach *gases VS temperature* is useful in order to find the most discriminating sensor in the array. I report in the following figures (Fig. 3.40, 3.41, 3.42, 3.43, 3.44, 3.45) the PC1 vs PC2 of the most discriminating sensors of the array (TiTaV, STN, ST30 650, ST25 650+Au and ST25 650). It can be seen from these graphs, that all the five sensors shown have a high discrimination capability for CRC-VOCs (in the range 350-600°C). In fact the dots corresponding to $1-iodo-nonane$, *decanal* and C_6H_6 are far both from

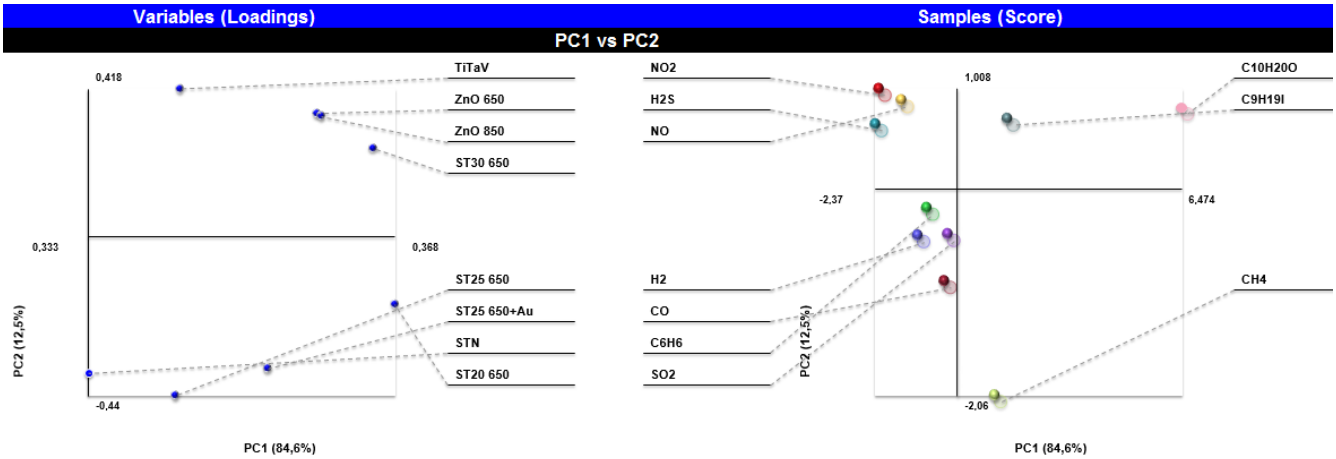

Figure 3.37: PC1 vs PC2 at 600°C, sensors as variables and gases as samples.

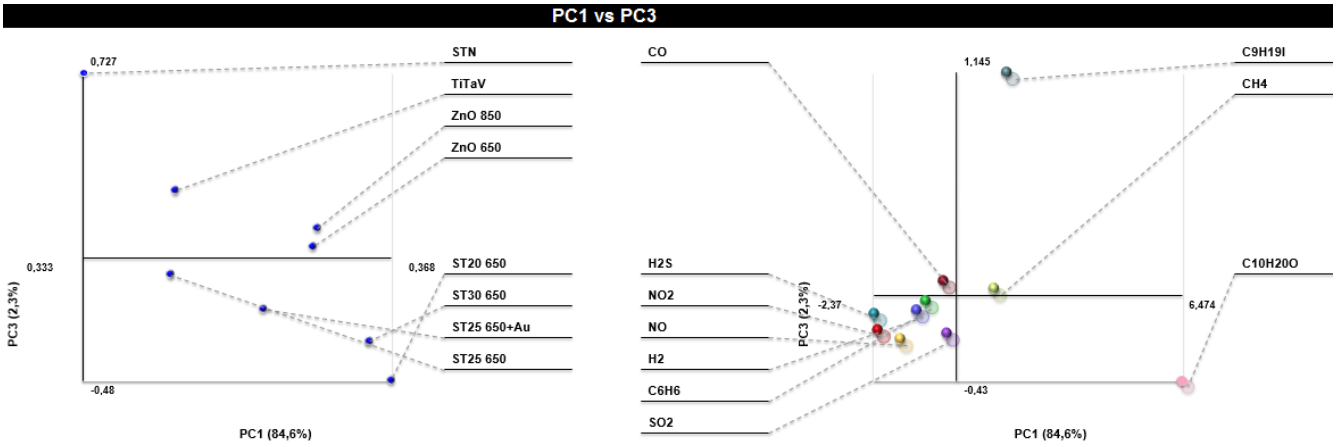

Figure 3.38: PC1 vs PC3 at 600°C, sensors as variables and gases as samples.

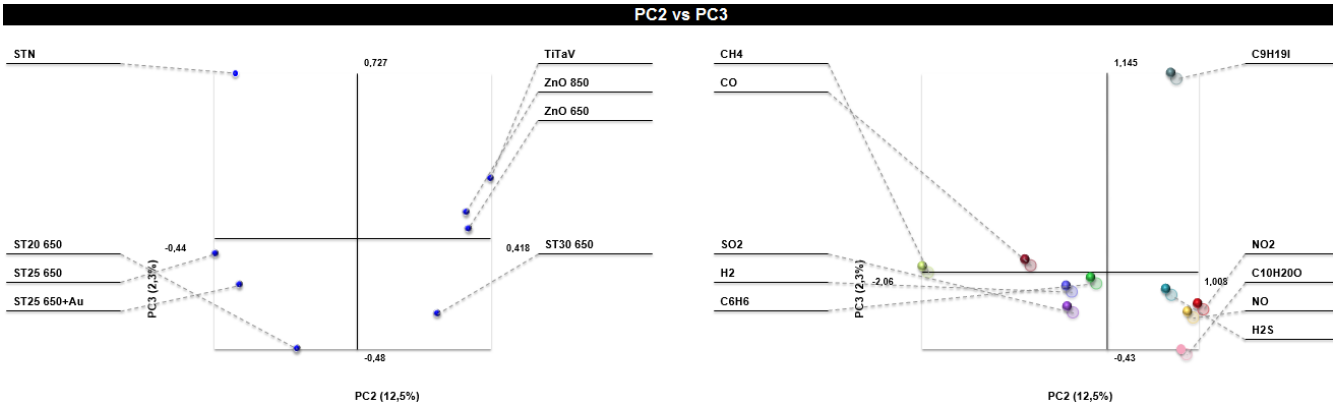

Figure 3.39: PC2 vs PC3 at 600°C, sensors as variables and gases as samples.

each other and from the interferer dots. Furthermore, focusing on ST30 650 (Fig. 3.42), this discrimination capability is still valid but affects also the interferer dots at the chosen temperature range. This sensor can be both useful in CRC-VOC identification and also in the interfering gases discrimination.

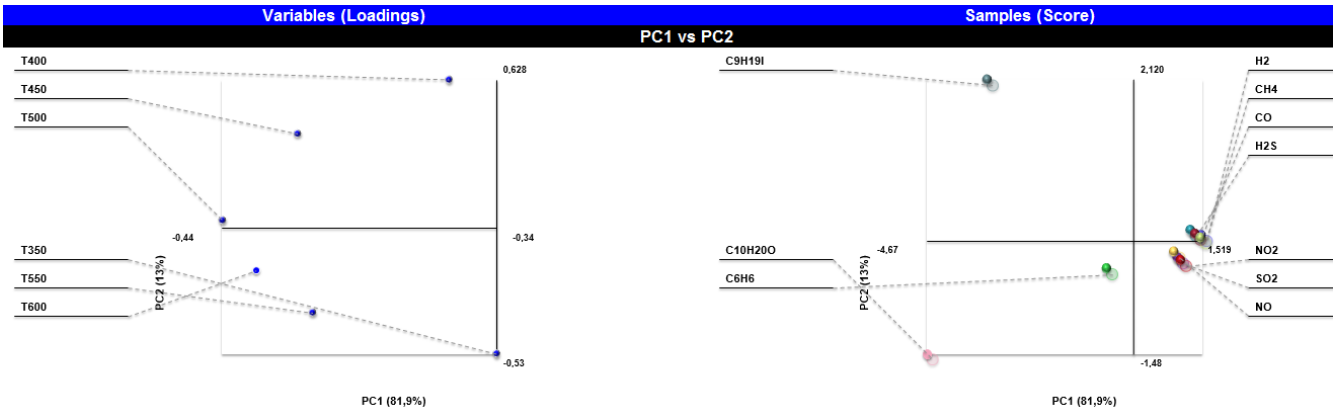

Figure 3.40: PC1 vs PC2 of TiTaV, temperatures (in the range 350-600°C) as variables and gases as samples.

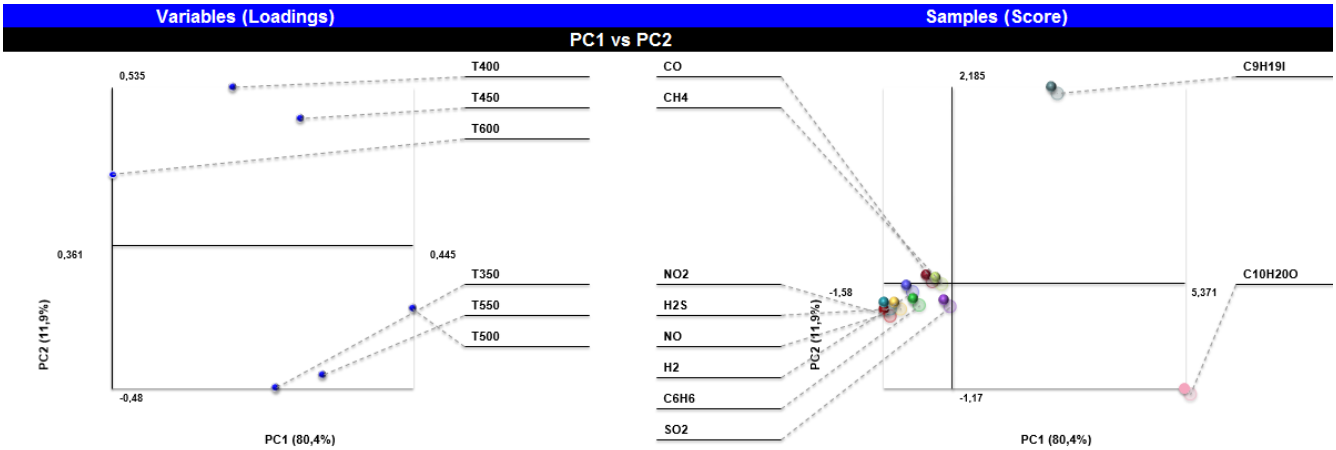

Figure 3.41: PC1 vs PC2 of STN, temperatures (in the range 350-600°C) as variables and gases as samples.

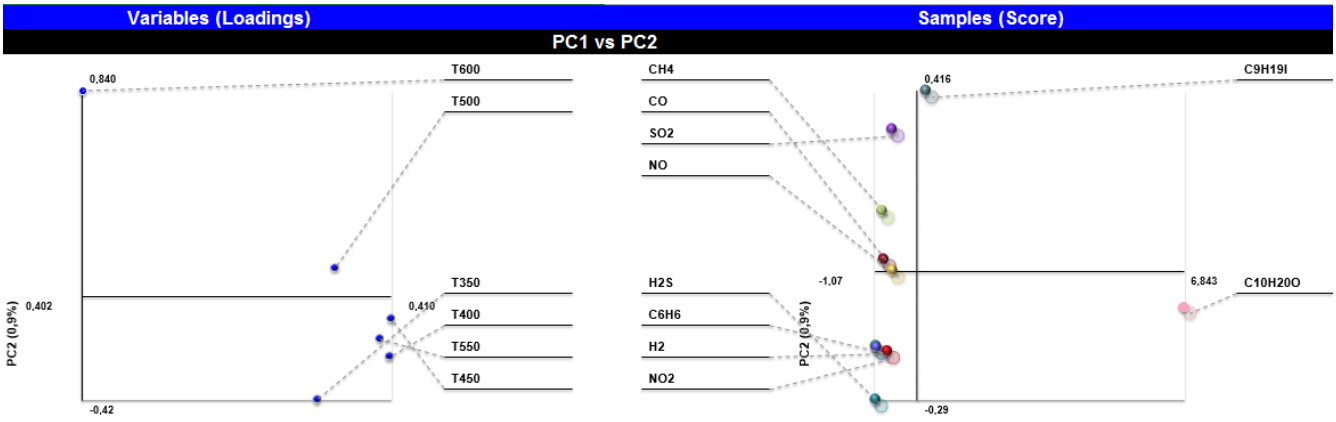

Figure 3.42: PC1 vs PC2 of ST30 650, temperatures (in the range 350-600°C) as variables and gases as samples.

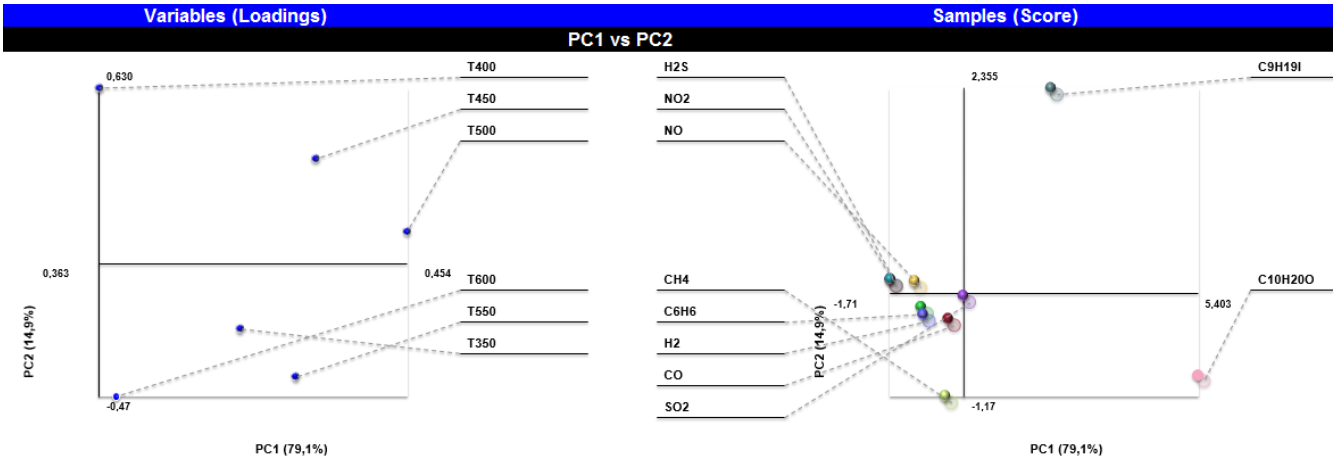

Figure 3.43: PC1 vs PC2 of ST25 650+Au, temperatures (in the range 350-600°C) as variables and gases as samples.

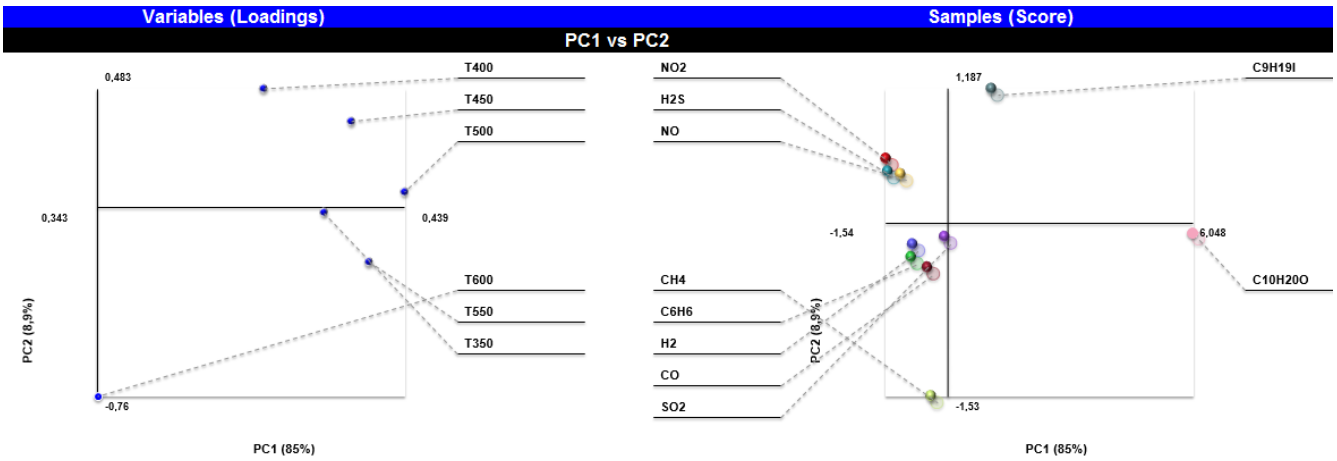

Figure 3.44: PC1 vs PC2 of ST25 650, temperatures (in the range 350-600°C) as variables and gases as samples.

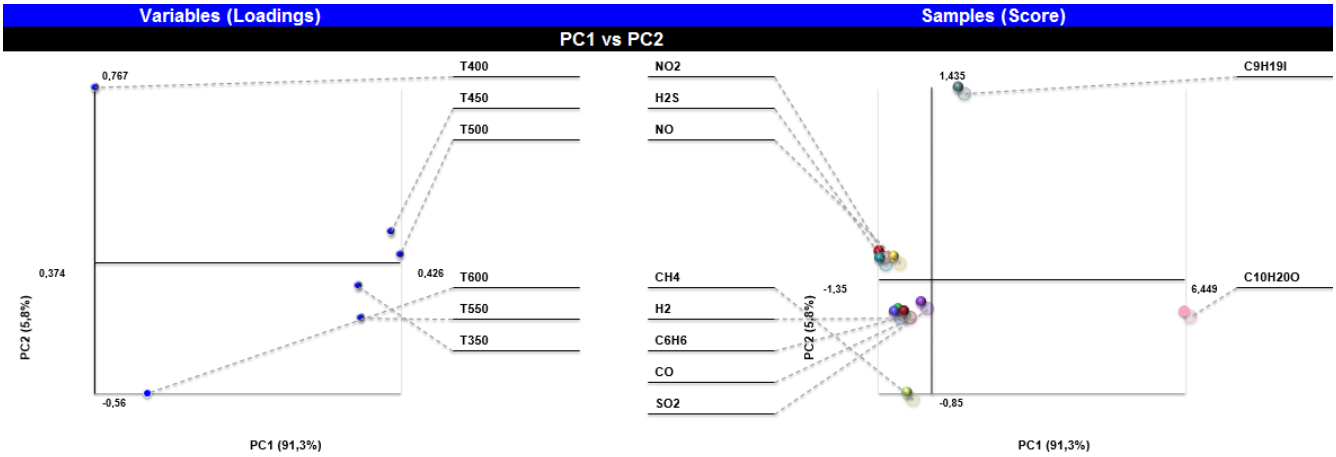

Figure 3.45: PC1 vs PC2 of ST20 650, temperatures (in the range 350-600°C) as variables and gases as samples.

Chapter 4

Prototype for colorectal cancer pre-screening: SCENT A1

The attempt of reproducing the intestinal gaseous environment with the experimental apparatus of Section 3.2.1 by the use of commercial gas bottles, was interesting from the research point of view but not so useful in the real medical application. In fact, if the goal was to obtain a non invasive screening method for colorectal adenomas, this way may encounter two big problems. First, it is impossible to reproduce in a laboratory chamber all the variables present in a real intestine, second, if we imagine to test real samples, the procedure for intestinal gas collection would be invasive, difficult and unpleasant for patients.

Due to the fact that it is fundamental, for a preventive screening, to work with **real samples**, the analysis was shifted towards something of "less evanescent" than pure gas samples and easier to collect: the test can be done by the analysis of fecal exhalations.

The goal was the realization of a device made of a specific array of chemoresistive sensors, capable of acquiring a complete statistic on fecal samples, by performing a sufficient number of tests. The idea was to find differences between the sensor responses to feces of people with CRC or polyps and to healthy control ones. The sample preparation and all the security procedures are listed in Section 4.1.2.

Nowdays, the test accepted by the Italian National Health Service (NHS) and the NHS of other countries (e.g., France, UK), is the FOBT, which generates a huge percentage of false negatives (about 20%) and of false positives (more than 40%). Our idea was to adapt our test as much as possible to the collection protocol of the FOBT, in order to avoid procedural complications and to introduce improvements in the diagnosis. In the following Section a description of the device: SCENT A1.

4.1 The device

The instrument, indicated with the name of SCENT A1, is now the form of a prototype (Italian patent and PCT extension obtained thanks to the funds of the University of Ferrara [85]) and its characteristics are portability, low cost and ease-of-use even by unqualified personnel. The name of the instrument derives from the name of the start-up SCENT S.r.l. [86] (acronym of Semiconductor-based Electronic Network for Tumors), founded by the members of Sensor Laboratory of the Department of Physics and Earth Sciences of UNIFE, which strictly collaborates with the University. SCENT A1 will represent a form of preventive screening in the field of CRC diagnostics, which currently relies on not completely reliable methodologies, e.g., the FOBT, or invasive and expensive such as colonoscopy and sigmoidoscopy, sources of further hardships for patients already debilitated and often old. Colonoscopy, in particular, can lead to serious problems such as bowel perforation. The idea regards the field of preventive medicine. The aim is to promote awareness and a prior investigation by means of a non-invasive method for diagnosing colorectal tumor formations.

SCENT A1 will be a safe and effective method of pre-diagnosis, to support FOBT, already accepted by the Italian NHS. In particular, since 2005, FOBT is performed in Ferrara (Italy) every two years on subjects aging between 50 and 69 years. SCENT A1 will act alongside the latter, in order to reduce the number of false negatives, whose existence is known (above 20%) and is a cause of late intervention and to reduce the number of false positives. In those states where FOBT or other pre-screening tests are not adopted, such as Russia, Poland, Brazil, Argentina and Spain, SCENT A1 will be proposed, after clinical validation, as a method of preventive diagnosis on population at risk. The introduction of SCENT A1 will decrease the number of deaths due to cancers not diagnosed by FOBT, with a significant socio-health impact and it will increase the number of operating colonoscopies than useless ones. The system will also allow to collect a large number of statistical data on the population and to use the positive results to reveal any high risk areas.

The idea comes from reading and studying the medical and scientific literature on the subject, and has been the main object of three thesis in physics (a bachelor's and two master's thesis). A branch in continuous evolution in the diagnosis of cancer is based on the detection of VOCs, compounds that have a high vapor pressure at room temperature. Such compounds have different chemical nature depending on the type of cancer and are originated from diseased cells, due to the modification of the structure of their membrane (peroxidation) and their metabolic activity. VOCs can be identified either directly, in the environment surrounding the cells, and indirectly through the breath, after being conveyed by the bloodstream to the lungs. SCENT A1 focuses on the pre-diagnosis of CRC (since the stage of adenoma) and, being this tumor localized in the intestinal region, it is known in the literature and verified by laboratory tests that VOCs generated from it directly affect the composition of feces, altering their odor. The diagnosis tool proposed by us is therefore able to detect with extreme precision such alterations, so as to provide a criterion

for distinguishing between feces of healthy subjects and subjects suffering from intestinal polyps or carcinomas. The operational idea is based primarily on the application of nano-structures, which are of great current interest for industrial applications, to the medical field. SCENT A1 is made of a core of nano-structured sensors, based on semiconductor powders. These sensors are capable of monitoring small changes in gas concentrations of the order of tens of parts per billion (ppb), in line with VOCs variations inside of the human body. SCENT A1 will provide an effective and non-invasive CRC pre-screening, by analyzing stool samples exalations. SCENT A1 is currently in the form of a patented MVP (Minimum Viable Product). The performance of laboratory tests gave extremely encouraging results about the capability of SCENT A1 of distinguishing between stool samples of healthy subjects and of patients with high risk adenomas and carcinomas, by means of a simple threshold system. Additional double blind tests will be needed for certification of the instrument. Changes in the electronics and packaging will help us to make it user-friendly, less bulky and ready for future market introduction.

4.1.1 Structure of the device

Since SCENT A1 is under bureaucratic secrecy [85], the description will be limited to a simple functioning scheme, as seen in Fig. 4.1 and a photo of the prototype itself (Fig. 4.2). Samples are introduced in the red box and the airflow pumped into the circuit delivers the emitted chemicals to the sensors.

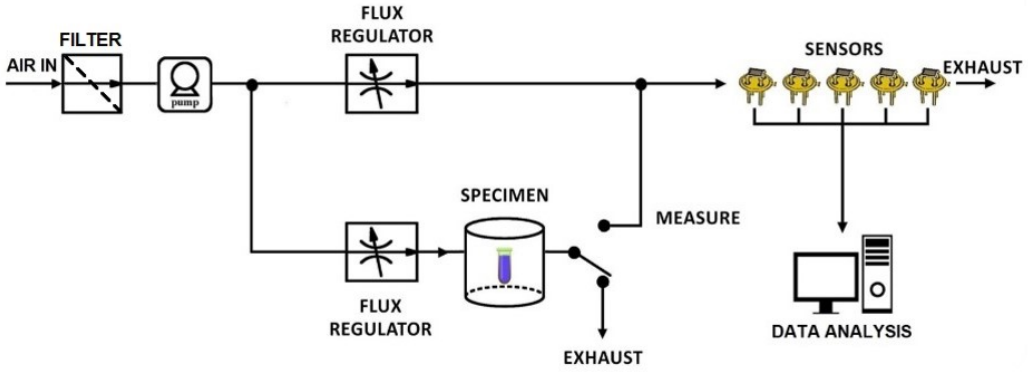

Figure 4.1: Schematic representation of SCENT A1 setup [85].

Sensors were combined into a five slot array (Fig. 4.3), and are invested by an airflow produced by a pump taking the air from the external environment. A carbon filter is put immediately after the pump in order to stabilize humidity. The flow is then divided into two lines, one arriving directly to the sensors, always active in order to set the response baseline, the other which arrives to sensors only when the measurement begins, passing inside the sample box in which feces are inserted with their standard containers.

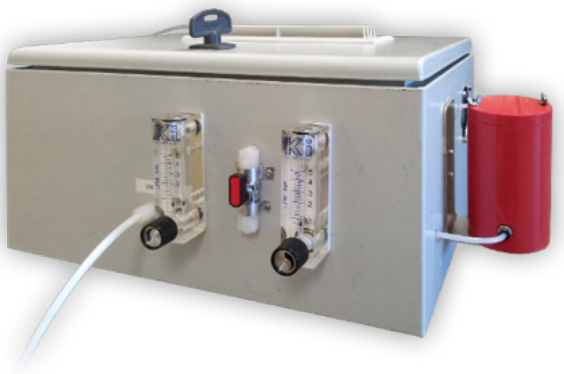

Figure 4.2: The packaging of the device SCENT A1 [85].

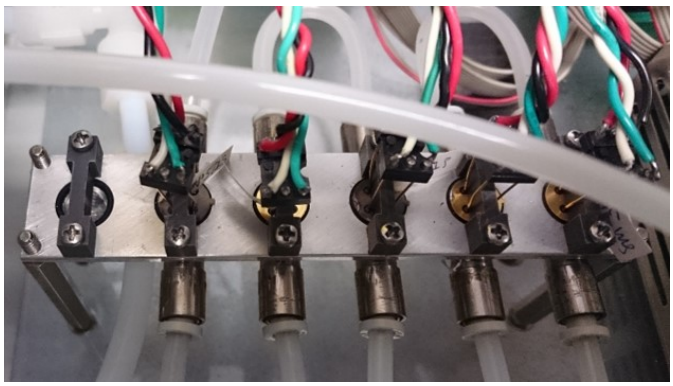

Figure 4.3: The sensor allocations of the sensing core of SCENT A1.

4.1.2 Sample treatment

For a preliminary feasibility study it was relatively easy to find healthy subject samples, but it can be a problem to find samples of tumor affected people. Thanks to a partnership with Dr. Giorgio Benea (Department of Radiology) and Dr. Gabriele Anania (Section of General and Thoracic Surgery) of S. Anna Hospital [42], the harvesting of tumor-affected-people feces has become possible, with the direct extraction during the surgical operation. Since those samples mainly come from people with expanded neoplasia, that cannot be removed with normal polypectomy, it is reasonable to assume that metabolic production [36] and membrane peroxidation produced enough VOCs to alter the feces exhalations composition. Feces are samples difficult to be treated. First of all, their geometry is not similar to any regular figure. Since the flux of air inside the box carries compounds exhaled from the surface of the feces, it is important that samples are distributed on the largest surface possible, to let more air flow pass over them and to carry them to the sensors. Changing the amount of fecal mass do not changes neither the responses nor the behavior of sensors if the exposed surface is fixed. Since all feces were put inside standard sample holders all with the same volume, this problem of irregular geometry is easy to avoid for healthy or ill patients which were able to recover their own sample. This problem becomes more tricky when the feces are directly extracted from the intestine of a patient under surgery. In fact, people waiting for a surgical operation have to drink a laxative that forces their intestine to empty, so the remaining fecal material inside the gut, extracted for laboratory tests, it is not abundant enough to cover the same surface that is took from patient recovered samples.

Another problem with fecal samples is their chemical instability, given by different factors:

- *bacterial activity* - about the 7,5% in weight of the feces is composed by bacteria, many of them belonging to fecal coliform type, a family of non-sporulating bacteria like Escherichia Coli, normally present in human and warm blooded animal intestine. These bacteria, similarly to all the cells, have their own metabolism and produce their own metabolites, on a faster rate than normal cells. In addition to this factors, it is necessary to consider also the foreign species contained the air or in the external environment which can pollute the sample during the insertion in the sample container. Considering the huge number of microorganisms present, their activity hugely affects fecal composition. Therefore, it is important to conserve feces frozen, immediately after the extraction, in order to force bacteria slowing down their metabolism and reducing their activity. This allows to clean the fecal emission and even to kill the species that cannot turn into spore. if a freezer is not employed, after 24 hours feces produce so much microbiological activity to saturate all sensors responses (Fig. 4.4);

- *red blood cells hemolysis* - hemolysis occurs due to various factors: (i) chemical (difference of osmotic pressure which leads to the explosion or implosion of the cell), (ii)

thermal (the freezing temperature make water content to expand due to ice increase of volume, breaking the cell; also, fast gradients of temperature may lead to the break of the cell membrane), (iii) mechanical (the membrane of red blood cells is resistant to compressions and higher pressures in respect to atmospheric one, but they are susceptible to tractions and shear stress T, and break easily under this kind of stimulus). Remains of red blood cells increase the response of sensors as a reductive effect, covering interferers and VOCs in some case. Nonetheless, this interference can be used as substantial data, due to the fact that being able to detect red blood cells remains in feces equalize the test to the FOBT one, which is the actual standard for CRC pre-screening;

- *chemical reactions* - fats, fibers, not absorbed proteins, water and other waste materials are all enclosed in feces. Therefore, the more time passes, the more reactions, catalyzed from outer chemicals in the air or due to microorganisms, can occur, changing the composition of the fecal exhalations. However, all those compounds, once carried into the sensors allocations, get exposed to heat and denature into simpler chemicals. Since the working temperature lingers in the range of 300 - 650°C, these reactions products are considered integral part of the signal.

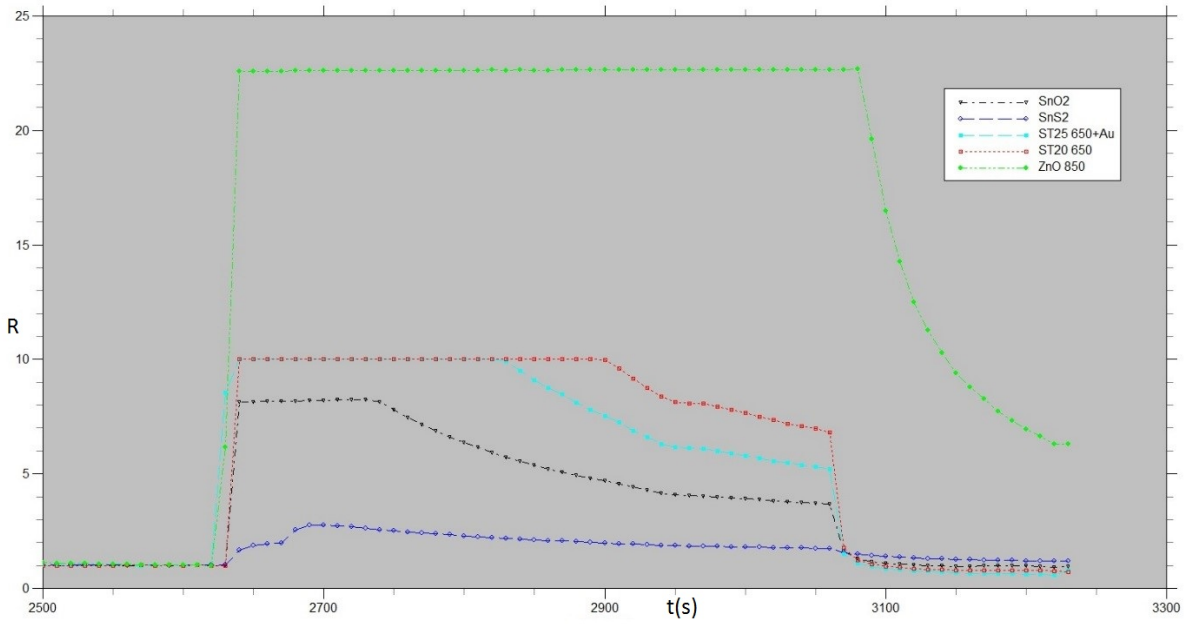

Figure 4.4: This image shows the saturated responses of a feces sample left under laboratory fume hood for one night, without any cooling treatment. It is not possible to get relevant data from this measurement [2].

The composition of feces changes a little also depending on the personal diet (conversely intestinal gas compositions changes a lot with diet). For a clinically consistent result, future medical tests should be done by prescribing a common diet to the patients, 1-2 days before taking the sample. On this phase, this step was avoided, with the precise scope of verifying how much different diets affect the response of sensors. Multiple tests were performed for each sample, during different days, with the aim of verifying the repeatability of the measurements and the time evolution of the fecal emissions. Normally, the second and the third response to each sample were taken as relevant data, but often also the first measure is reliable (with a repeatability ratio of more than 90%).

Fig. 4.5, 4.6, 4.7, show the trend of sensor responses during fecal tests.

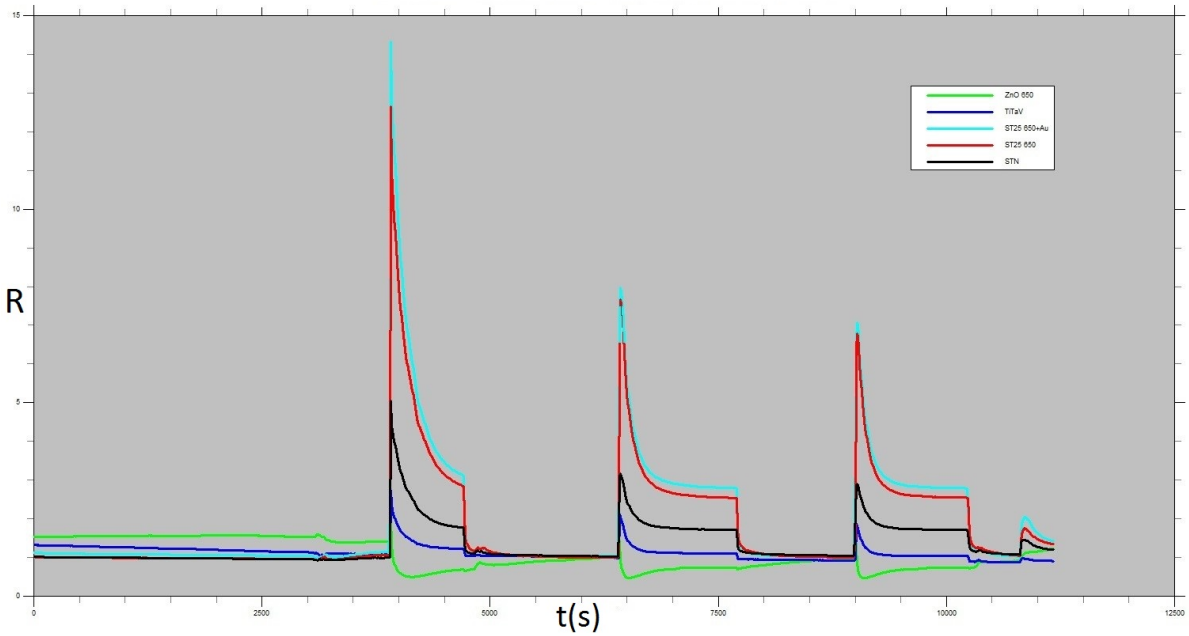

Figure 4.5: example of tumor affected feces, tested with a sensor array, the same day of the extraction from the intestine of the patient. The response of ZnO 850 is slightly oxidative. The first peaks are due to the effect of pressure, humidity and surface reactions. The final tiny peak is produced by the flow cleaning the sample chamber after the removal of the sample [2].

4.1.3 The sensing core

Due to the amplitude of targets and the use of two different measuring set-ups, various sensor arrays were tested, depending on the aim of the analysis. The sensors used for this gas analysis are listed in the following table (T_F is the firing temperature):

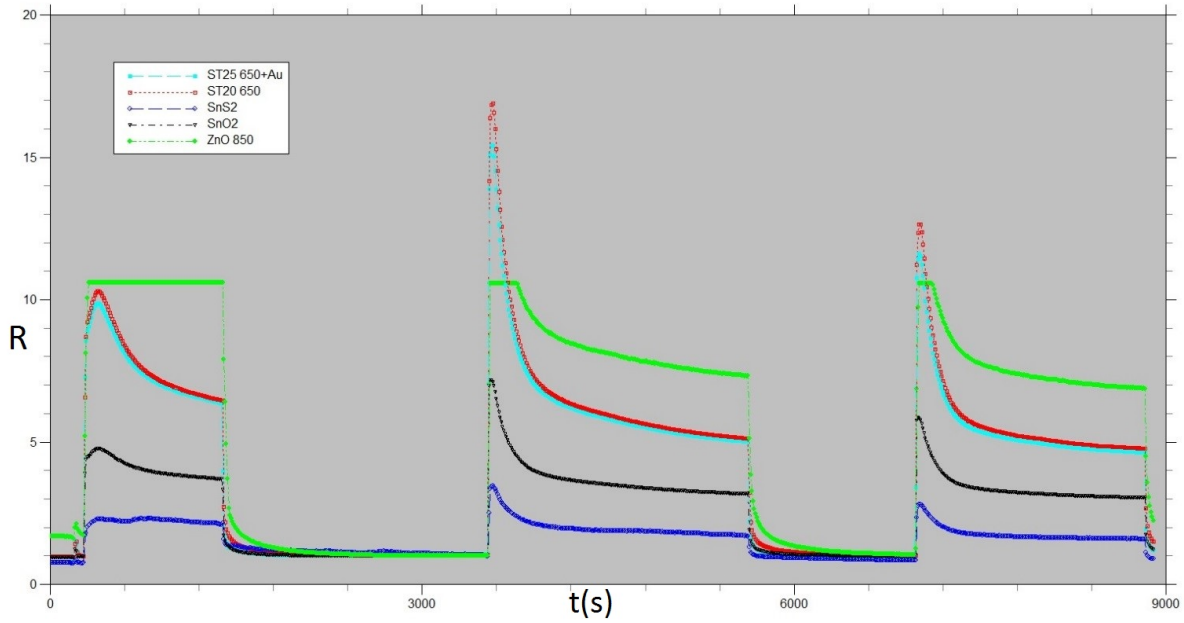

Figure 4.6: example of tumor affected feces, tested with a sensor array, 23 days after the extraction from the intestine of the patient. The oxidative response of ZnO 850 turned into a strong reductive response, and all the responses are higher than the ones in Fig. 4.5. The first ZnO response saturated [2].

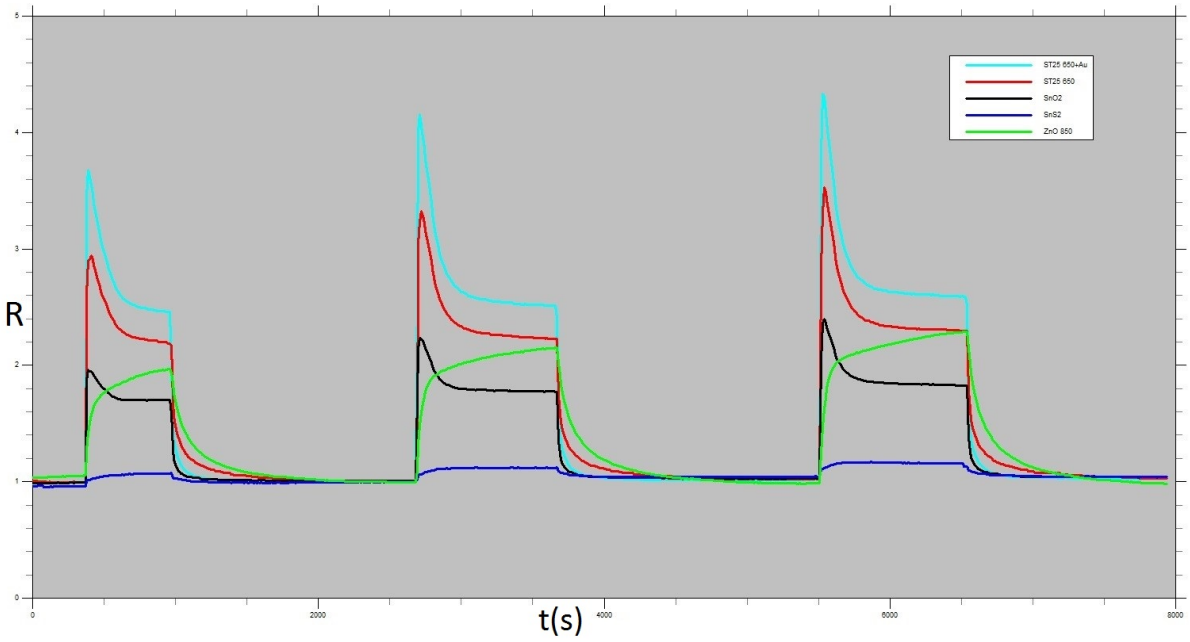

Figure 4.7: example of tumor affected feces, tested with a sensor array, the first day after the deposition. It is evident that all responses are reductive [2].

NAME	MATERIALS	T_F
TiTaV	a sensor based on titanium, tantalum and vanadium oxides	650°C
ST25 650	a sensor based on tin oxides and titanium (25%)	650°C
STN	a sensor based on tin, titanium and niobium oxides	650°C
ST20 650	a sensor based on tin oxides and titanium (20%)	650°C
ST25 650+Au	a sensor based on tin oxides and titanium (25%) and gold (1%)	650°C
ST30 650	a sensor based on tin oxides and titanium (30%)	650°C
ZnO 650	a sensor based on zinc oxide	650°C
ZnO 850	sensors based on zinc oxide	850°C
CdS	a sensor based on cadmium sulfide	180°C
SnO2	a sensor based on pure tin oxide	650°C
SnS2	a sensor based on tin sulfide	180°C
W11	a sensor based on tungsten oxide	650°C
WS30 650	a sensor based on tungsten oxide and tin (30%)	650°C
ZnO 950	a sensor based on zinc oxide	950°C
LF4	a sensor based on lanthanum and iron oxide	750°C
SmFeO3	a sensor based on samarium and iron oxide	750°C
NiT	a sensor based on TiO_2 and Niobium	750°C
W Mn	a sensor based on WO_3 and MnO_2	750°C
LF4	a sensor based on lanthanum and iron oxide	750°C
S11+Pd 0.4	a sensor based on SnO_2 + Palladium	750°C
Indium	a sensor based on Indium	650°C

The sensor names are internal to the laboratory and do not refer strictly to the chemical names of powders. Six different combinations of five sensors were employed for SCENT A1 fecal tests. The sensors working temperatures were set according to the selectivity parameters to detect benzene, decanal and 1-iodo-nonane respectively, derived from the consideration made on gas tests. Here a list of the array employed:

I) First Sensors Array (SA1)

NAME	WORKING T(°C)
TiTaV	450 (previously set to 350)
ST25 650	450
STN	500
ZnO 650	400
ST25 650+Au	450

II) Second Sensors Array (SA2)

NAME	WORKING T(°C)
TiTaV	500
ST25 650	450
STN	450
ZnO 650	450
ST25 650+Au	450

III) Third Sensors Array (SA3)

NAME	WORKING T(°C)
CdS (SnS2)	350 (300)
ST20 650	450
SnO_2	450
ZnO 850	450
ST25 650+Au	450

IV) Fourth Sensors Array (SA4)

NAME	WORKING T(°C)
ZnO 850	450
W11	350
WS30 650	350
ZnO 850	450
ST25 650+Au	450

V) Fifth Sensors Array (SA5)

NAME	WORKING T(°C)
ZnO 950	450
W11	350
WS30 650	350
ZnO 850	450
ST25 650+Au	450

VI) Sixth Sensors Array (SA6)

NAME	WORKING T(°C)
SmFeO3	350
ST20 650	450
LF4	350
ZnO 850	450
ST25 650+Au	450

VII) Seventh Sensors Array (SA7)

NAME	WORKING T(°C)
SmFeO3	350
ST20 650	450
SmFeO3	350
NiT 850	350
ST25 650+Au	450

VIII) Eigth Sensors Array (SA8)

NAME	WORKING T(°C)
SmFeO3	350
ST20 650	450
SmFeO3	450
NiT 850	500
ST25 650+Au	450

IX) Ninth Sensors Array (SA9)

NAME	WORKING T(°C)
SmFeO3	350
ST20 650	450
SmFeO3	350
W Mn	350
ST25 650+Au	450

X) Tenth Sensors Array (SA10)

NAME	WORKING T(°C)
SmFeO3	350
TiTaV	450
S11 + Pd.04	450
W Mn	350
ST25 650+Au	450

XI) Eleventh Sensors Array (SA11)

NAME	WORKING T(°C)
SmFeO3	350
TiTaV	450
ST20 650	450
Indium	350
ST25 650+Au	450

It is noticeable that some sensors were kept in most of the arrays. The reasons for this are as follows:

- ST25 650+Au was kept for all the sensor arrays because of its high sensitivity and fast response (the best between all the sensors tested by now) changing the composition of the environment;
- ZnO 850 was kept starting from the second array and also compared to another ZnO 850 in the fourth array, because it was the sensor recording the highest difference between healthy and tumor patient feces;
- ST20 650 was reintroduced in the sixth array because of his good discriminating behavior together with the previous two sensors, as in SA3.

The most discriminating sensors listed before are not exactly the same found in the previous part of the work (see section 3.5 and subsection 3.6.2). This is due both to the fact that the examined mixture are different in the two approaches (single VOCs in a simplified intestinal gas environment reproduced in laboratory and all the VOCs together with gases emitted by real stool samples) and to the different samples analyzed (VOCs and interferers from bottles and real fecal samples). The approach presented here is the most reliable for the development of a real screening tool for CRC.

4.2 SCENT A1 results

A total of 170 samples have been tested by the chosen sensors, combined in the 11 arrays. Healthy samples were provided by the University Hospital S. Anna of Ferrara and extracted during surgery, while the healthy ones were normally defecated by healthy volunteers. Different method of analysis have been tried in order to obtain the most efficient method possible to be implemented in a threshold system identification software for subjects with CRC. In this chapter the various analysis methods are shown: *radar diagram plots*, *PCA analysis*, *quadratic discriminant analysis (QDA)* and *ROC curve* [2] [42].

4.2.1 Preliminary tests

The sensor responses of the arrays SA1-SA6 have been plotted in radar diagrams, in which each vertex corresponds to a sensor, to show the differences between feces and to better distinguish tumor samples from healthy ones. These results are shown in Fig. 4.8 - 4.22. In order to simplify the graphics, responses of healthy people samples are coloured in blue, while those of diseased patients are in red. The letter *D*, preceeded by a number, in the legend of graphs stands for the number of days after wich the measure was performed.

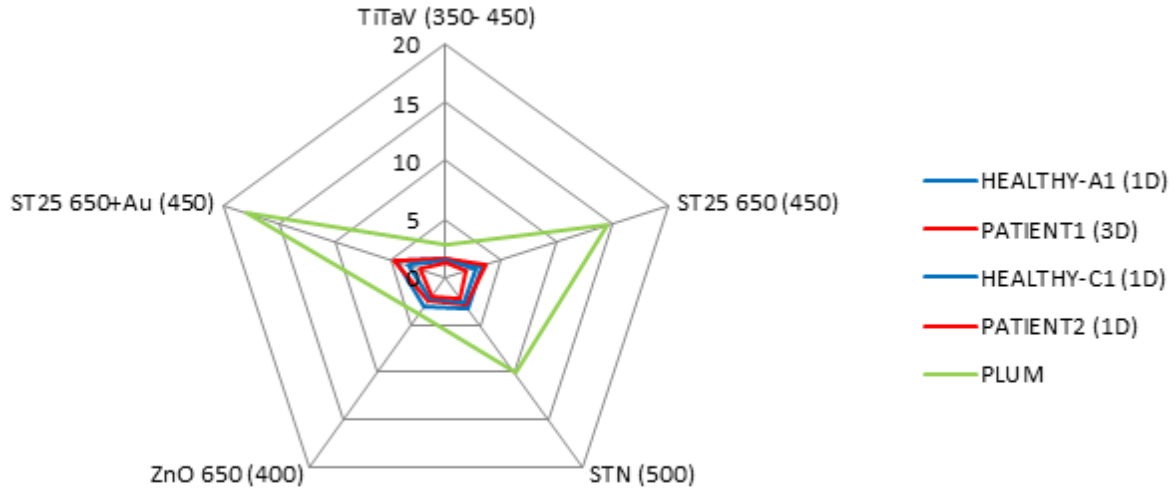

Figure 4.8: Radar diagram of SA1 responses. Mature plum responses, tested in order to verify the functioning of the airflow system of SCENT A1 for the first time was included [2].

From these results it is possible to extrapolate the following observations:

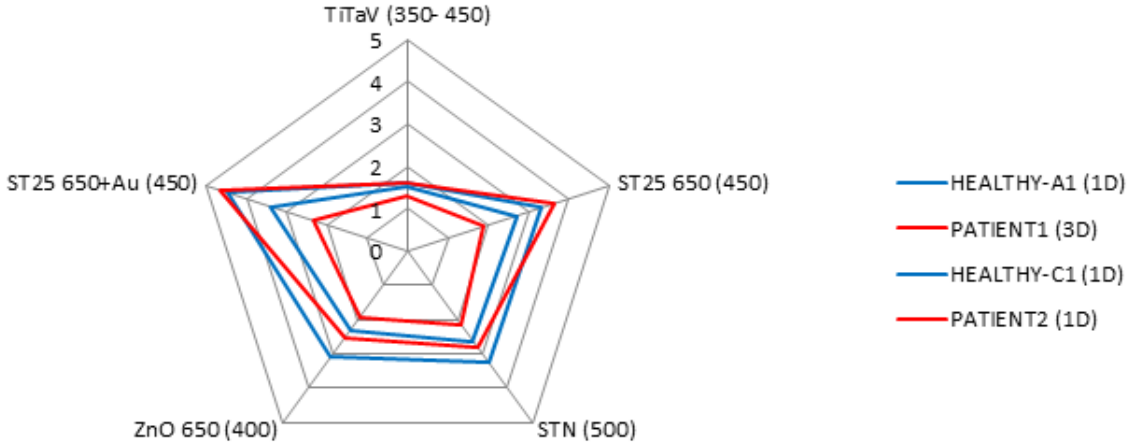

Figure 4.9: Radar diagram of all SA1 responses, only feces included [2].

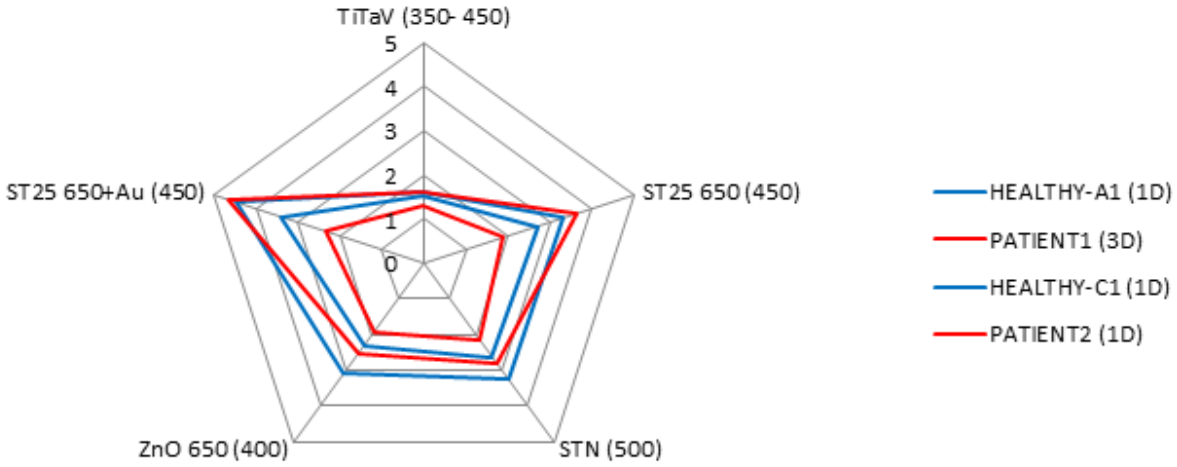

Figure 4.10: Radar diagram of all SA2 responses [2].

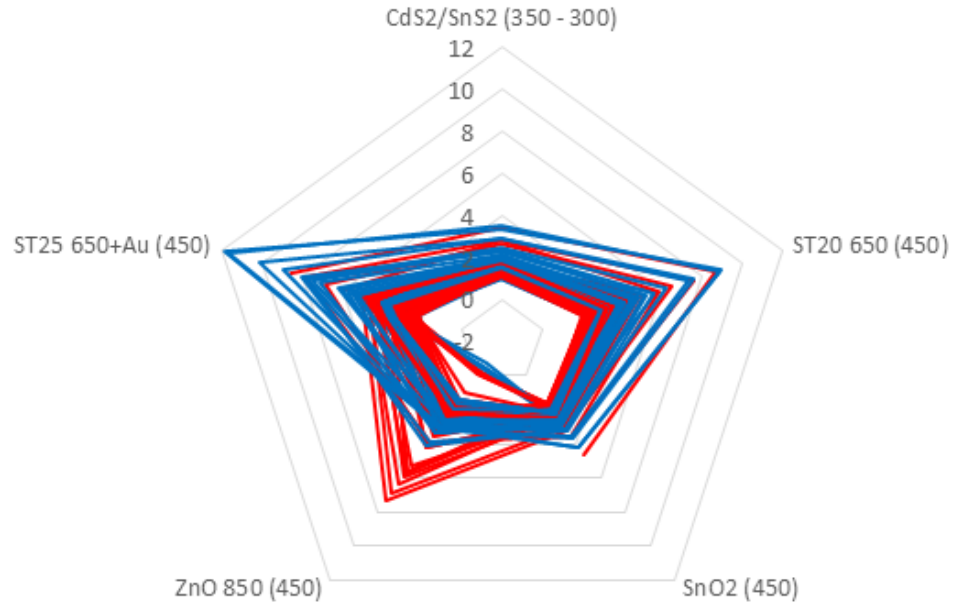

Figure 4.11: Radar diagram of all SA3 responses [2].

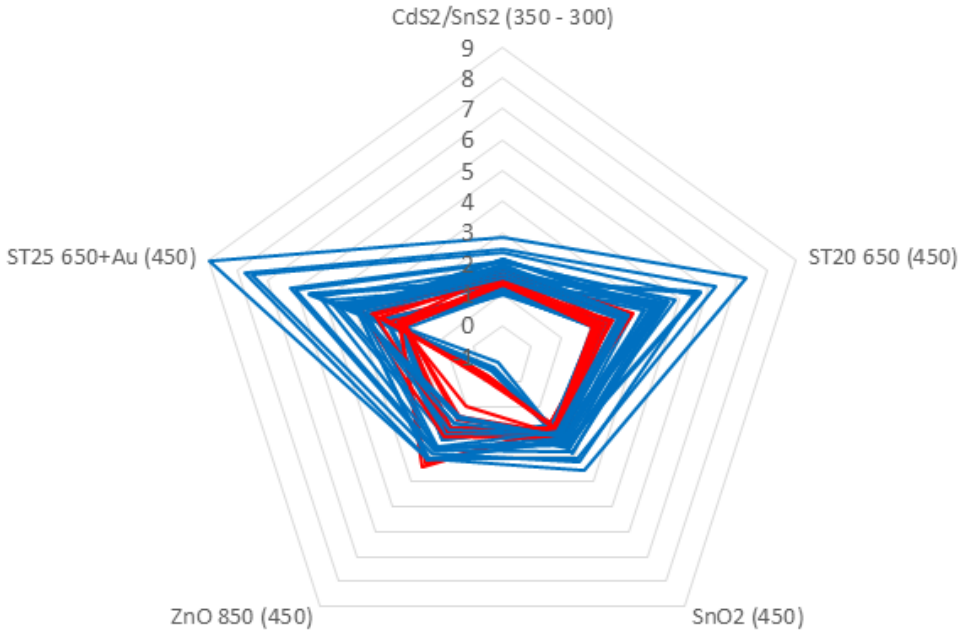

Figure 4.12: Radar diagram of SA3 responses, all measures were made during the first two days after extraction/deposition [2].

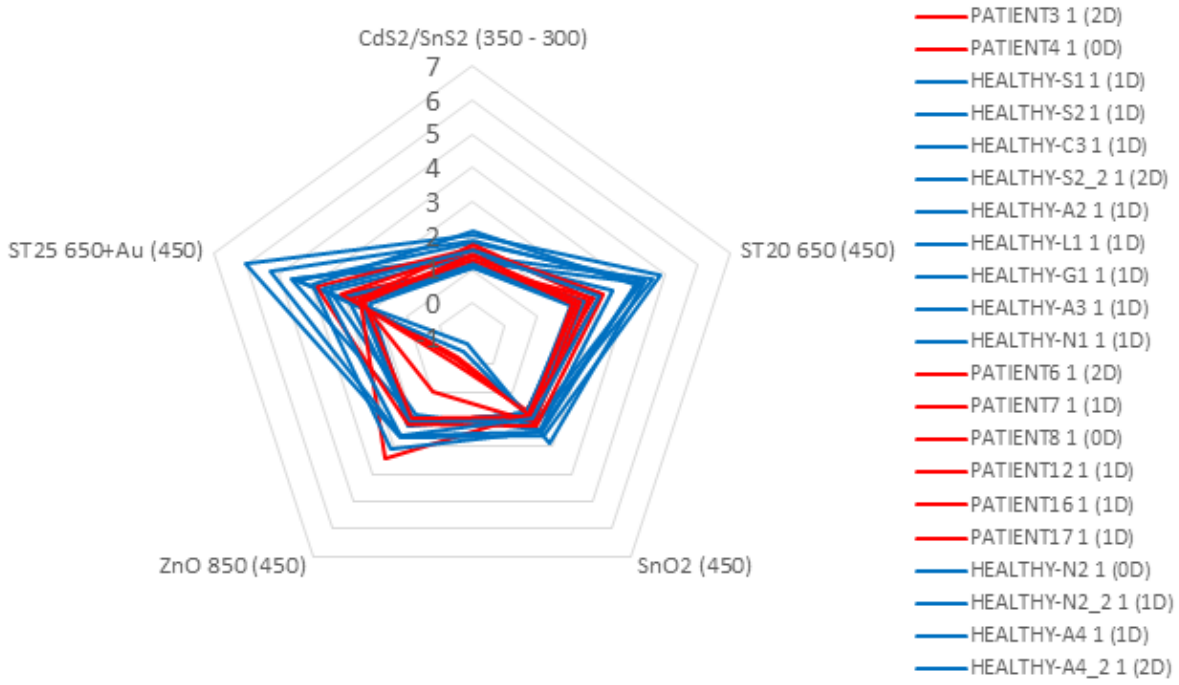

Figure 4.13: Radar diagram of SA3 responses, all measures were made during the first two days after extraction/deposition [2].

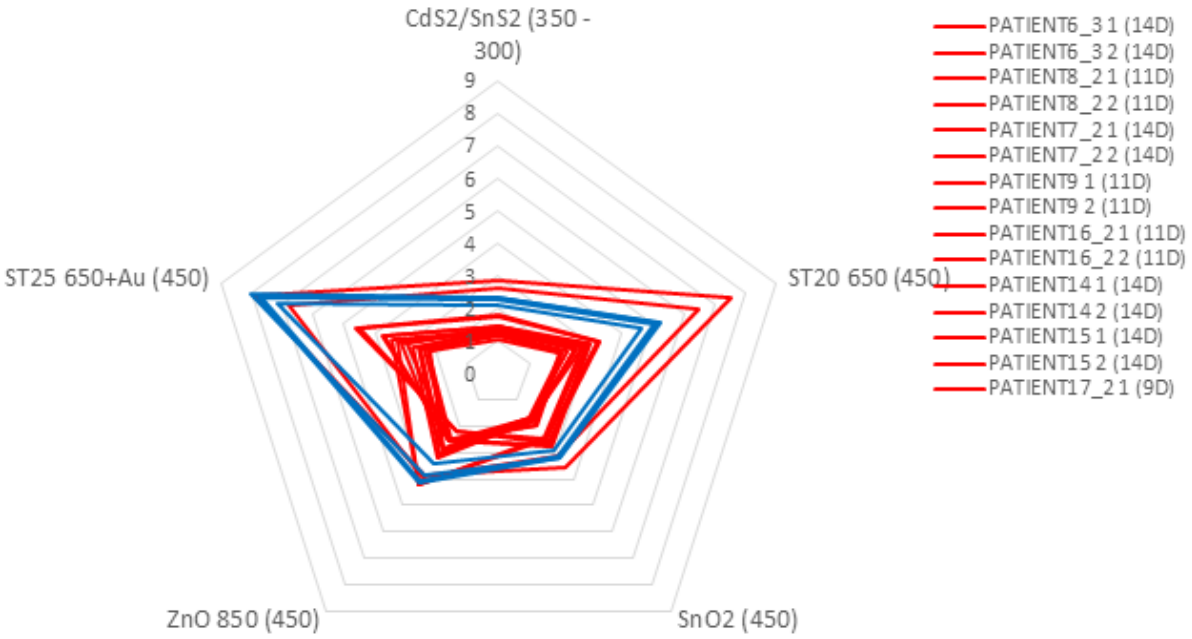

Figure 4.14: Radar diagram of SA3 responses, all measures from the eighth to the fourteenth day after deposition/extraction [2].

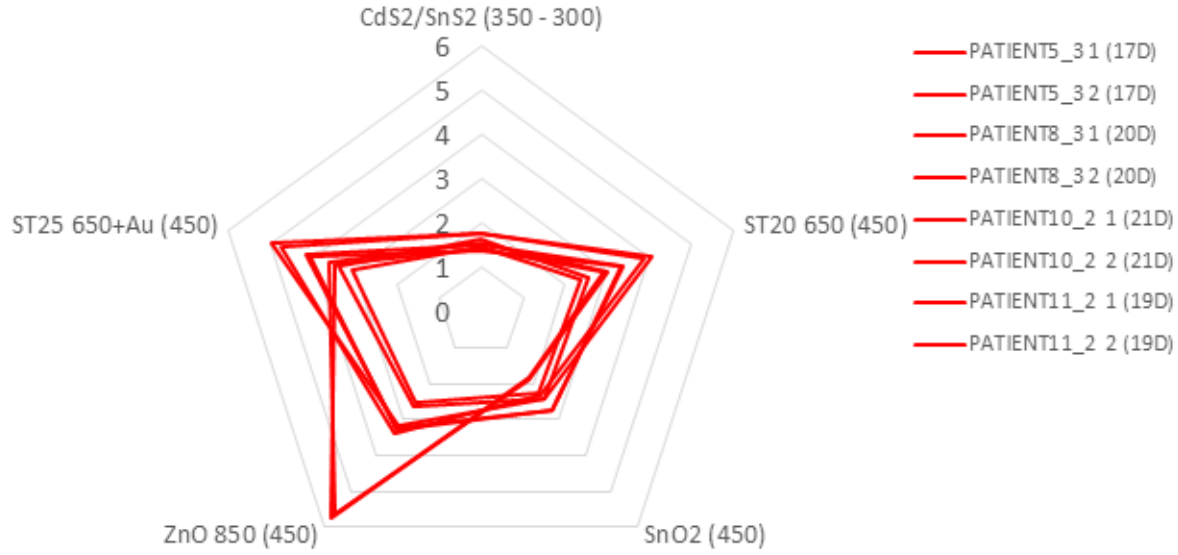

Figure 4.15: Radar diagram of SA3 responses, all measures from the fifteenth to the twenty-first day after deposition/extraction [2].

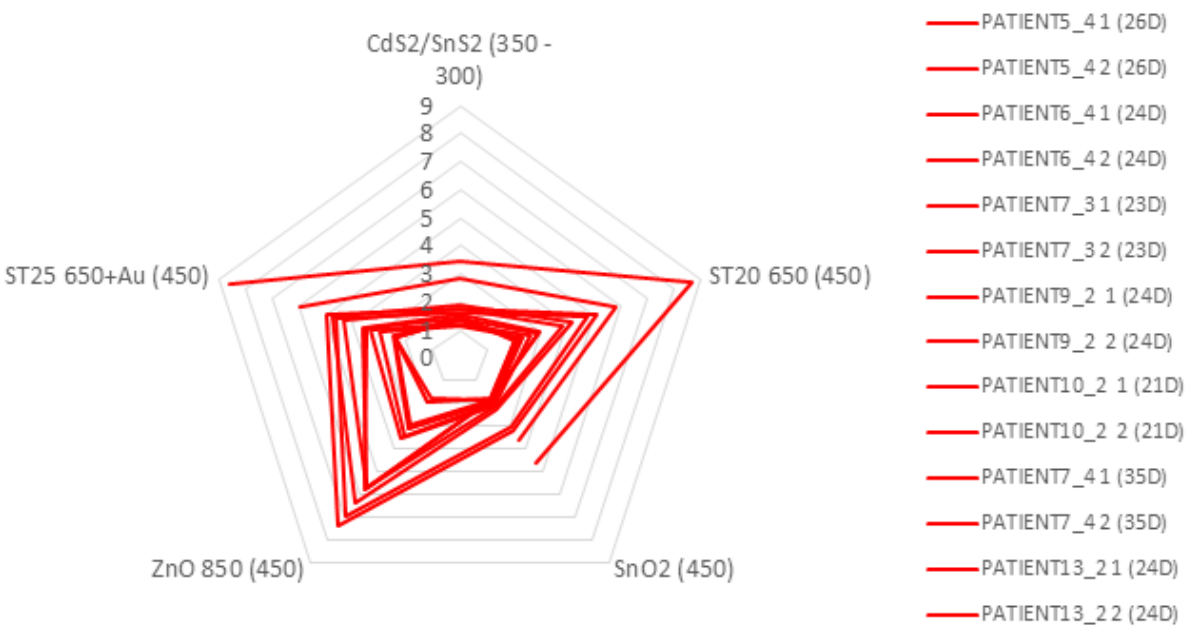

Figure 4.16: Radar diagram of SA3 responses, all measures were made starting from the twenty-second day after deposition/extraction [2].

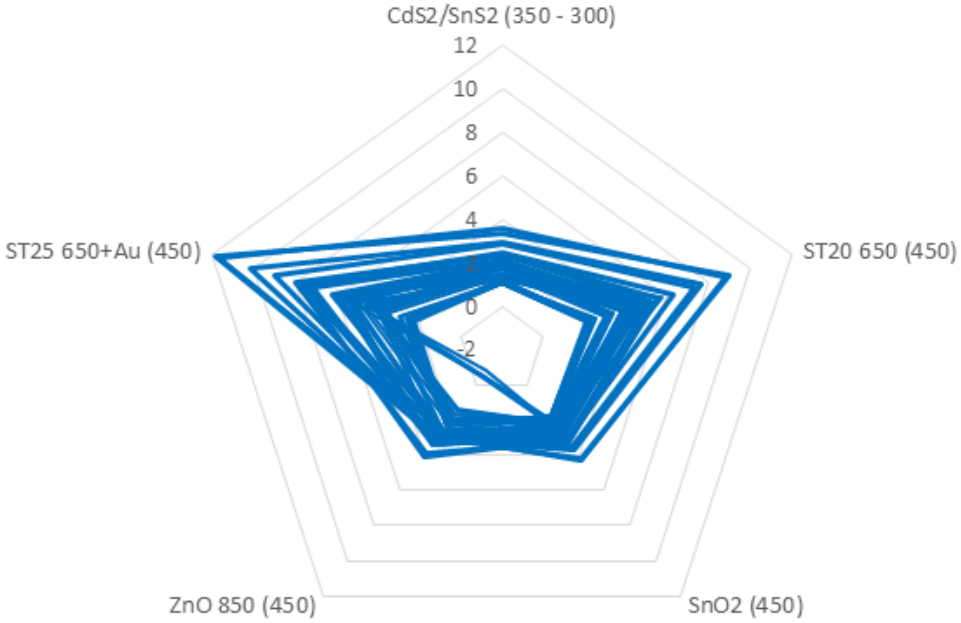

Figure 4.17: Radar diagram of SA3 responses, all healthy subject feces responses [2].

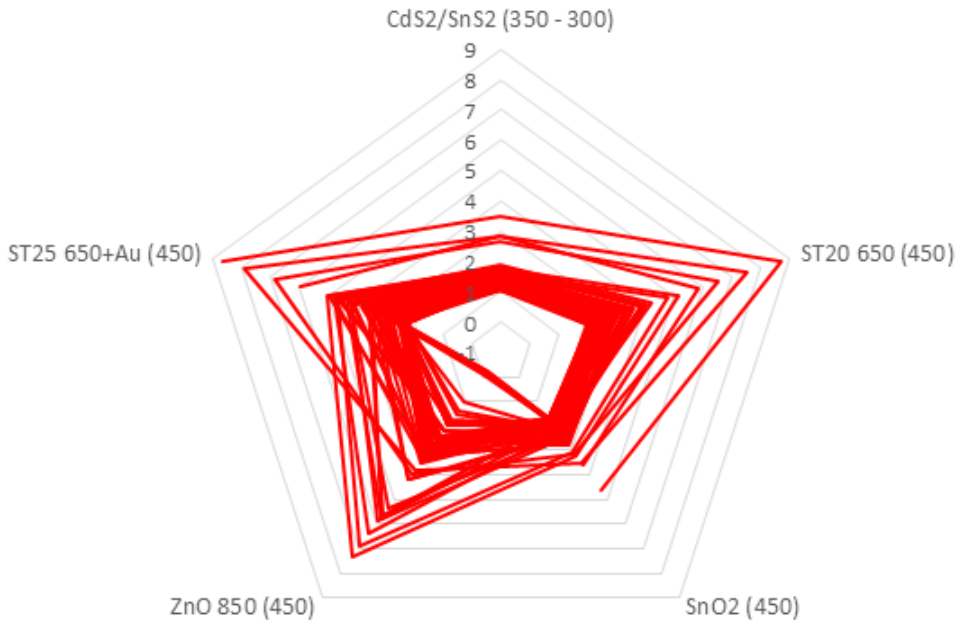

Figure 4.18: Radar diagram of SA3 responses, all tumor affected patient feces responses [2].

- mature plum responses, with SA1, were higher than fresh fecal material responses. This was expected because of the ethylene production by the fruit fermentation and the huge amount of water composing feces;
- observing SA3 responses, the responses of ST-type sensors increased with time for the healthy subject feces, while the responses of ZnO 850 remained on a closer range; on the opposite, with tumor affected patient feces, ZnO 850 response increased exponentially while ST-type responses remained on a closer range between them;
- some tumor affected patient feces (e.g., patient 3, 4, 8 and 16) show an oxidative (p-type) response (for all their initial peaks, and 3,4 and 16 also on their plateaux) on their first tests up to 2 days before the measure. Since this behavior is not observed for all tumor affected patient feces, probably it is connected to some reactions due to a volatile/unstable/low concentrated chemical, whose response is covered by microorganism activity or other reactions. It is still a good discriminant (for just a couple of healthy tests in which ZnO 850 showed oxidative responses) while from patient 8 and 16 it was possible to see the oxidative response turning into a reductive one with time;
- ZnO 850 sensors suffered of bulk drifting, depending on oxygen density defects of the crystal which get filled from O_2 present in the air, and consequently on the

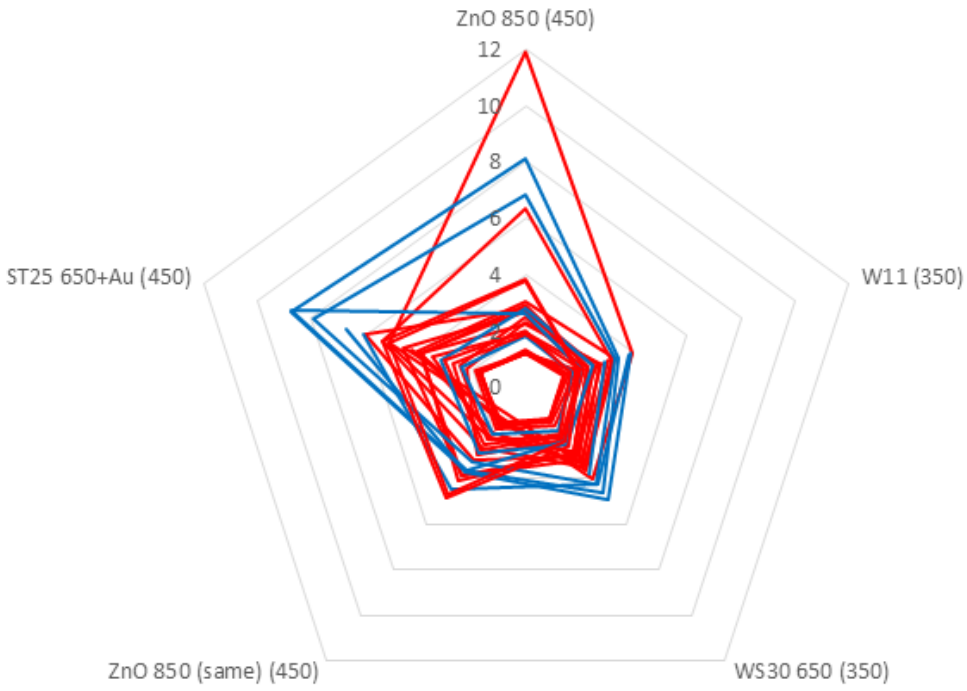

Figure 4.19: Radar diagram of all SA4 responses. First responses of the new ZnO 850 are erratic, because the sensor was still stabilizing; after few days, his behavior followed that of the original Zno 850 (labeled with the word *same* under parenthesis) [2].

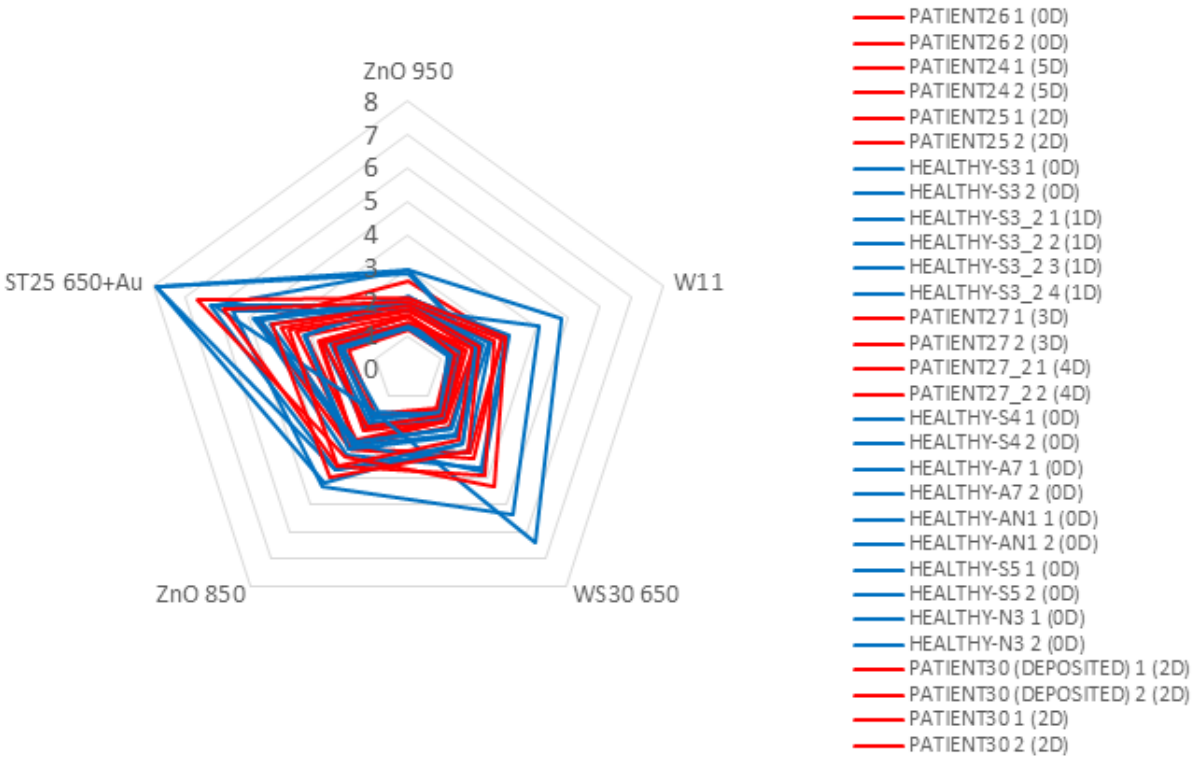

Figure 4.20: Radar diagram of all SA5 responses. Some of the first responses are lower than the others due to the freezing of the samples and to drilled bottle cap tests [2].

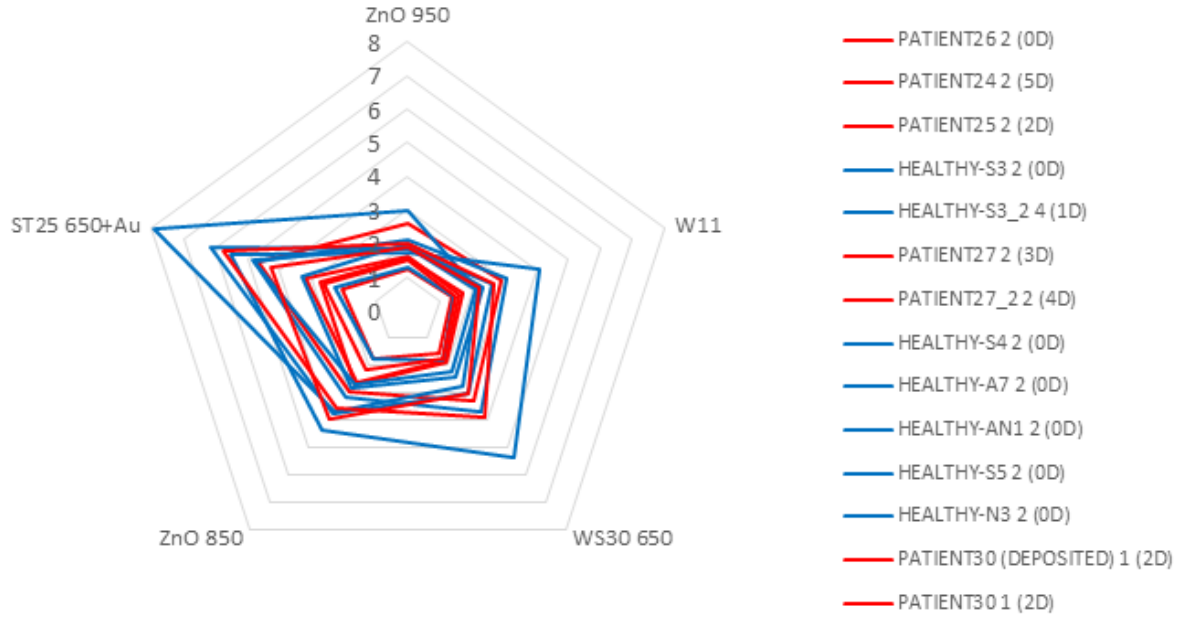

Figure 4.21: Radar diagram of SA5 responses, only one response for each sample (not frozen) [2].

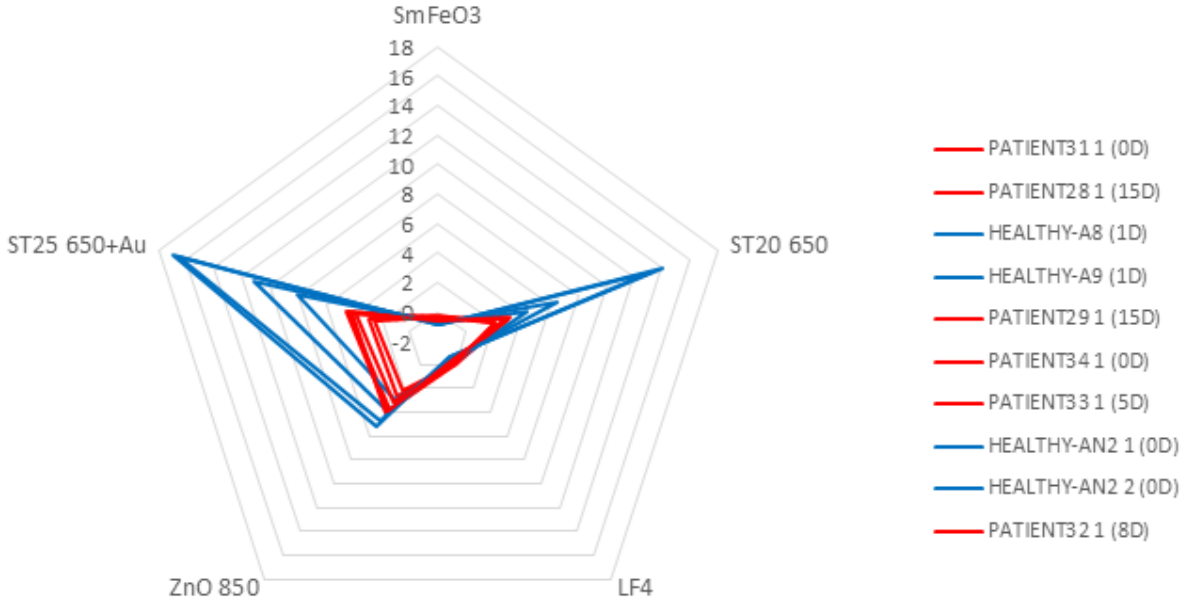

Figure 4.22: Radar diagram of all SA5 responses. Healthy and tumor affected subject feces responses are clearly distinguishable [2].

possible loss of O_2 from the crystal structure (see in Fig. 4.23). This problem, which leads to baseline modifications between different measurements, can be avoided by letting sensors stabilize and by repeating the measure after some time. Tests on ZnO 950 were made, in order to verify if the bulk dimension (internal structure of nanoparticles) depends on the firing temperature at which a sensor is produced; no match in SA5 appeared evident, due to the fact that no drift occurred in the responses of ZnO 950. Further studies on this sensor will be done, because of the erratic nature of the phenomena;

- the sensor W11 showed, especially after long relaxation times, with synthetic air, a double phase activation (see Fig. 4.24). This fact seems not to be connected with the patient health status, but it is still interesting for the study of W11 properties;

- during SA5 measures, tests were made to verify differences in flow given by open bottle cap and by drilled, closed bottle cap. As shown in Fig. 4.25, the differences in responses are substantial. Further tests were done, as in the previous case, by opening the bottle caps, instead of drilling them.

- with SA6, it is possible to observe the discrimination power, even if with low amplitude, of $SmFeO_3$ between healthy and tumor affected subject feces. The same consideration can be done for LF4 in minor entity. Another important goal reached with these sensors is the insensitivity to red blood cells residuals, which were instead detected by ZnO 850; in fact, while the zinc oxide showed a turn of responses from oxidant to reductive, both Fe-based sensors were not affected by hemolysis products, keeping distinction between healthy and tumor affected feces behaviors. The combination of these two sensors with the previously affirmed ST20 650, ZnO 850 and ST25 650+Au, looked to be a promising array for CRC detection;

- freezing feces and fully open their bottle cap proved to be the best standardization possible of the sampling/measurement. This lead to tests, as seen with SA6, stable even after 8 days of retention for tumor affected subject feces;

- overall, with the radar diagram response analysis, the best sensor arrays to discriminate tumor affected from healthy people feces were the SA3 and the SA6. Further statistics and measurements are needed to refine the model, but the differentiation of response appeared evident. In the following section is introduced a new method of response analysis and plot with the arrays SA7-SA11.

4.2.2 SCENT A1 results with PCA analysis

The method of PCA, already described in Section 3.6, is useful for the discrimination of different classes of elements. PCA is a statistical procedure capable of reducing the

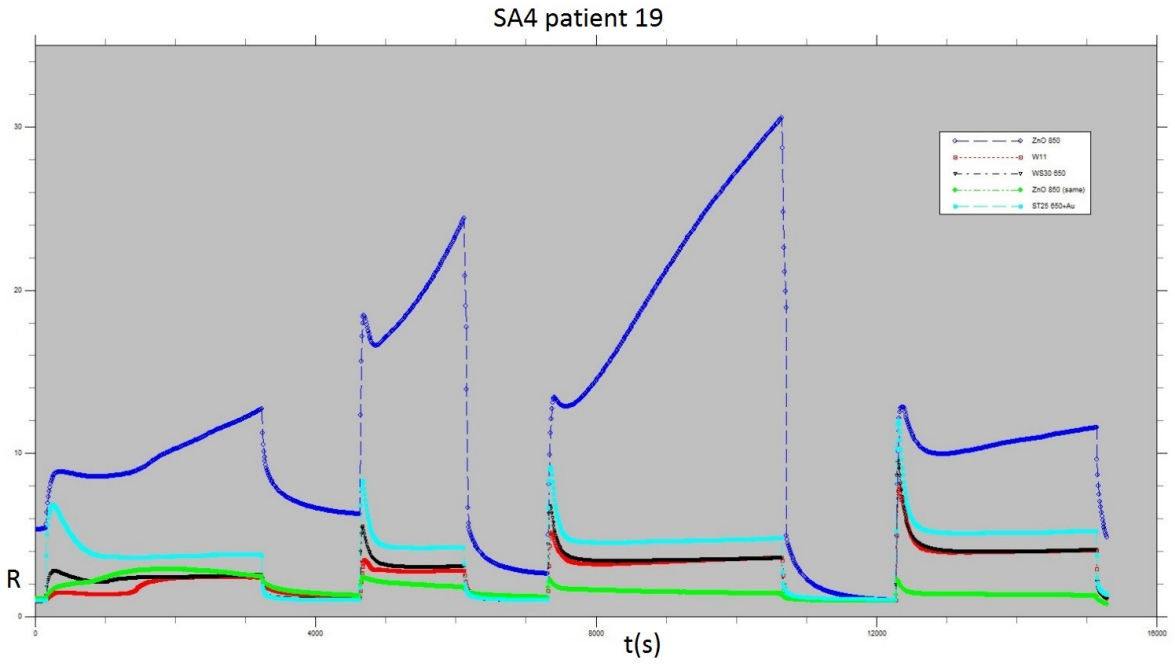

Figure 4.23: Bulk drifting phenomenon, visible in the trend of ZnO 850 response [2].

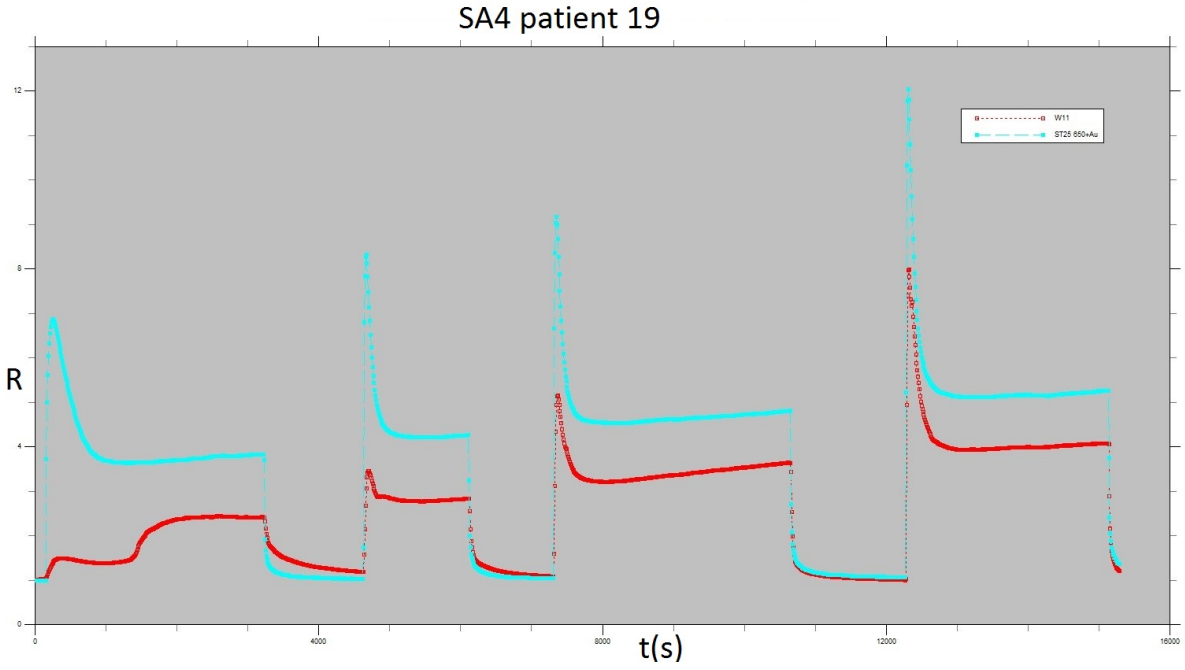

Figure 4.24: Double phase activation of the W11 sensor, compared to ST25 650+Au trend [2].

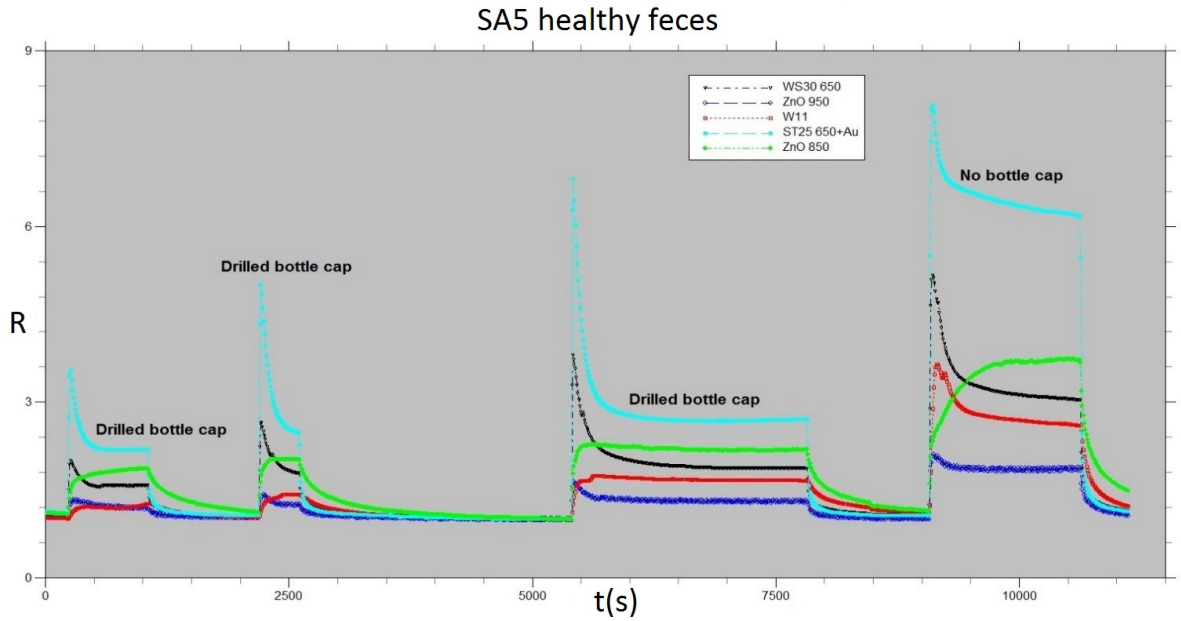

Figure 4.25: Variation of the flux (and so of the responses) between drilled bottle cap tests (from first to third peak) and open bottle cap measures (fourth peak) [2].

dimensionality of a data set by means of orthogonal transformations. The application of PCA technique to the responses of an array of sensors might help the process of identification of the most discriminating combination of sensing materials for CRC identifications. Here the principal component selected are three (PC1, PC2 and PC3) and the two areas correspond to normally defecated healthy control samples (CS) and tumor affected (TA) ones, both cancers and adenomas, surgically extracted during intervention.

The capability of a specific array of sensors of identifying samples of ill patients (dark grey responses in Fig. 4.26 represent TA feces, while light grey ones represent CS feces) has been demonstrated by data analysis. In particular, the array SA9 proved to be the most reliable for single responses. Moreover tin and titanium oxides sensors and $SmFeO_3$ show appreciable difference in the responses and distant mean values between different states of health (Fig. 4.26).

Even if single sensors proved to be (sometime slightly sometime more definitely) capable of identifying differences between TA and CS feces samples, five-sensor arrays showed greater selectivity in the detection of heavy discrimination between the two sample types. This is evident thanks to the post-processing of the single responses PCA. The variance is being decomposed into its principal components, where the first one represents the direction (in the reduced data space) responsible for the largest fraction of the variance, the second principal component the direction (orthogonal to the first one) responsible for the second largest fraction of the variance, and so on. The data points in the transformed space

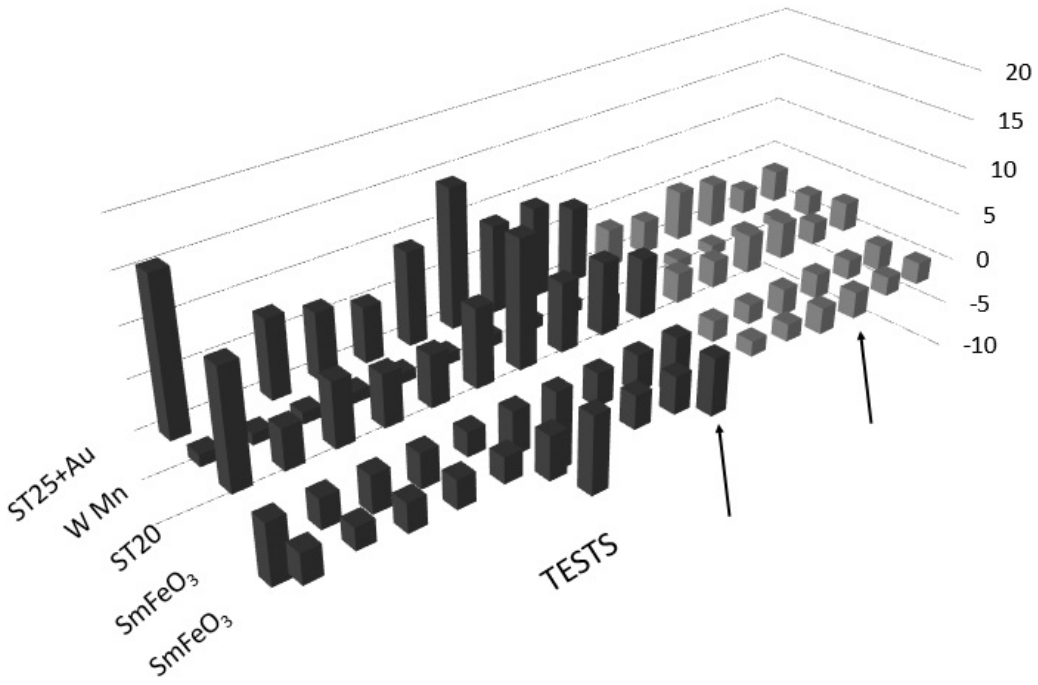

Figure 4.26: Single sensor responses of array SA9. On the vertical axis there is the value of response, indicated with R. R = Single sensor responses of array IX. On the vertical axis there is the value of response, indicated with R. $R = \frac{\Delta G}{G}$ (where ΔG is the change of the conductance in air contaminated by fecal exhalations and the conductance in environmental air and G is the conductance in air) for all sensors, except for $SmFeO_3$ for which R is the reciprocal negative of the previous quantity. Dark grey responses represent TA feces, while light grey ones represent CS feces [42].

identify two different areas: the first one corresponding to the area of healthy subjects and the second one of CRC-subjects. A test results as positive if it falls into the area of ill subjects and negative if it falls into the other area. Fig. 4.27 and 4.28, representing the PCA of arrays SA9 and SA10, show how the areas defining CS (grey dots) and TA (white dots) samples are well defined, with the second one-way being more compact and dense as compared to the first. Moreover, it is possible to verify the lack of intersection between the two areas, or some moderate overlapping. This gives an early but strong proof of the capability of nanostructured gas sensors of detecting differences between samples of stools given from volatile tumor markers, and thus allowing the identification of CRC subjects.

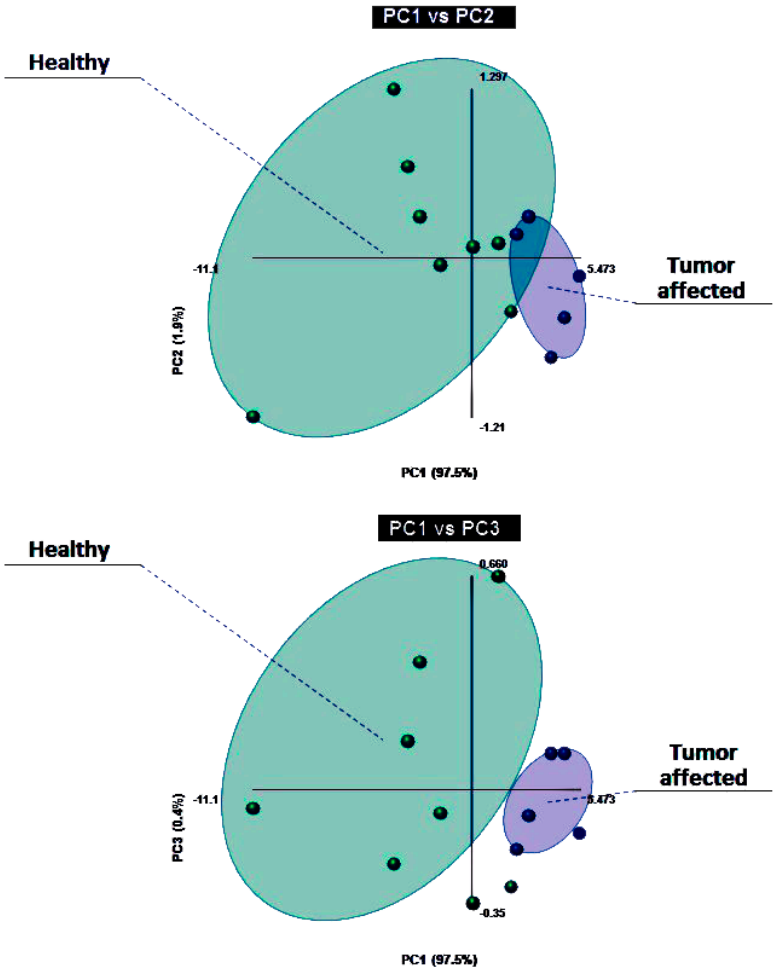

Figure 4.27: PCA analysis with array SA9. Green dots represent CS samples while blue dots represent TA samples, for a total of 13 tests. On the top there is the projection PC1 vs PC2, on the bottom the projection PC1 vs PC3. In both projections the green area represents the region identified by HS samples, while the blue area represents the region identified by TA samples.

4.2.3 QDA analysis

In addition to PCA, for the array X it was also performed the Quadratic Discriminant Analysis (QDA), a statistical method aimed to find a combination of features that characterizes or separates two or more classes of data [87]. The method addresses the problem by the development of a classification algorithm based on the input data. In QDA there is no assumption that the covariance of each of the classes is identical. Fig. 4.29 shows the data used for QDA, 10 CS and 6 TA samples for a total of 16 tests. In this case, the method results in only one classification variable (called *canonical variable*), therefore the classification zones are on a straight line. The Gaussian functions, representing the distribution of the data in this 1-D space, for healthy and CRC-affected groups are reported in Fig. 4.30 (mean and standard deviation were estimated as the mean and standard deviation of experimental data). The classification algorithm calculates no false negatives and only one false positive. It can also be noticed that the Gaussian curves show very modest overlap (Fig. 4.30); the error rate on the classification of the input data evaluates as 5%. Single values of the canonical variable obtained by the QDA are reported in Fig. 4.31 and the line shows that the separation of the two classes (TA and CS) is evident [42].

4.2.4 ROC curve

In statistics, a *Receiver Operating Characteristic (ROC)*, or *ROC curve*, is a graphical plot that illustrates the performance of a binary classifier system as its discrimination threshold is varied. The curve is created by plotting the true positive rate (TPR) against the false positive rate (FPR) at various threshold settings. To better understand this analysis is useful to define the following quantities:

True positive rate

The number of true positives (TP) over the total number of positives (P), which is the sum of the true positives (TP) and the false negatives (FN). The TPR is also defined as *sensitivity* of a test.

$$TPR = \frac{TP}{TP + FN} = \frac{TP}{P} \tag{4.1}$$

True negative rate

The number of true negatives (TN) over all the P. The TNR is also defined as *specificity* of a test.

$$TNR = \frac{TN}{TP + FN} = \frac{TN}{N} \tag{4.2}$$

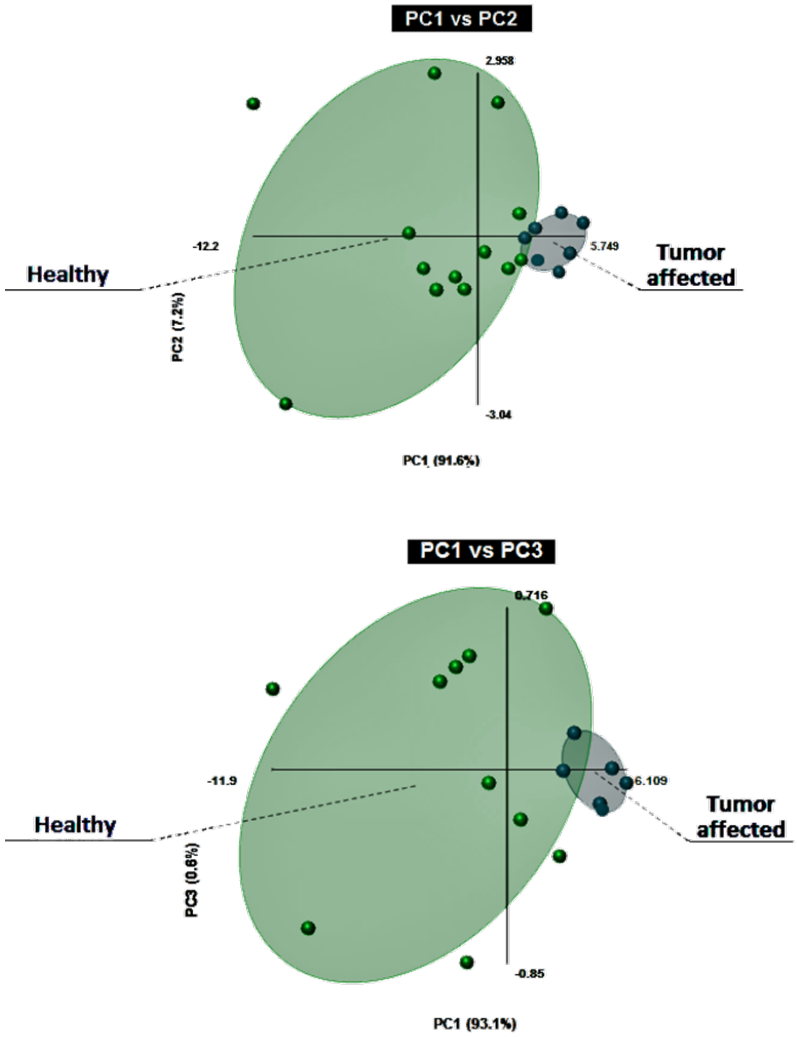

Figure 4.28: PCA analysis with array SA11. Green dots represent CS samples while blue dots represent TA samples for a total of 16 tests. On the top there is the projection PC1 vs PC2, on the bottom the projection PC1 vs PC3. In both projections the green area represents the region identified by HS samples, while the blue area represents the region identified by TA samples.

CLASSIFICATION COUNT

	PREDICTED GROUP		
	HS	**TA**	**TOTAL**
HS	9 (90%)	1 (10%)	10 (100%)
TA	0 (0%)	6 (100%)	6 (100%)
TOTAL	9 (56.25%)	7 (43.75%)	16 (100%)

ERROR RATE

PRIOR	0.5	0.5	
RATE	10%	0%	**5%**

Figure 4.29: Data used for QDA and their results. The error estimated starting from 16 (9 CS and 7 TA) samples is of about 5% [42].

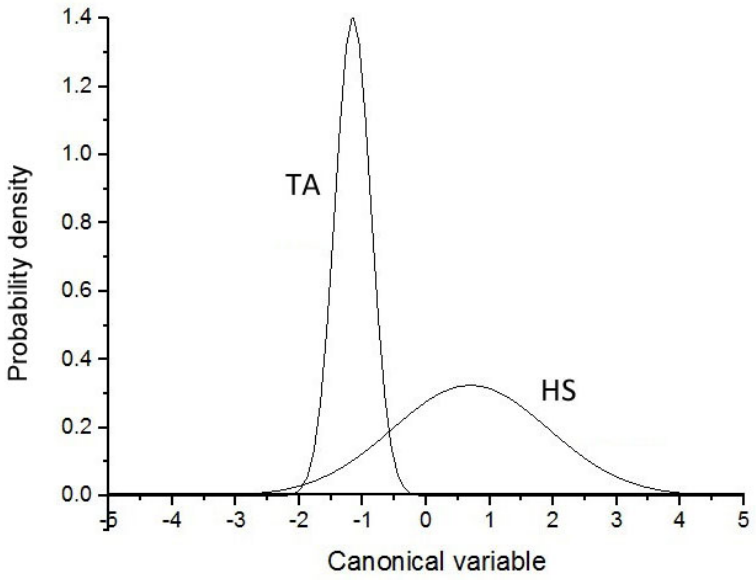

Figure 4.30: Gaussian curves obtained with QDA analysis. The *canonical variable* represents the only classification variable that results from the analysis starting from PCA data. The mean and the standard deviation has been obtained starting from the experimental data. The two Gaussian curves show very modest overlapping due to the fact that the classification algorithm calculates no false negatives and only one false positive [42].

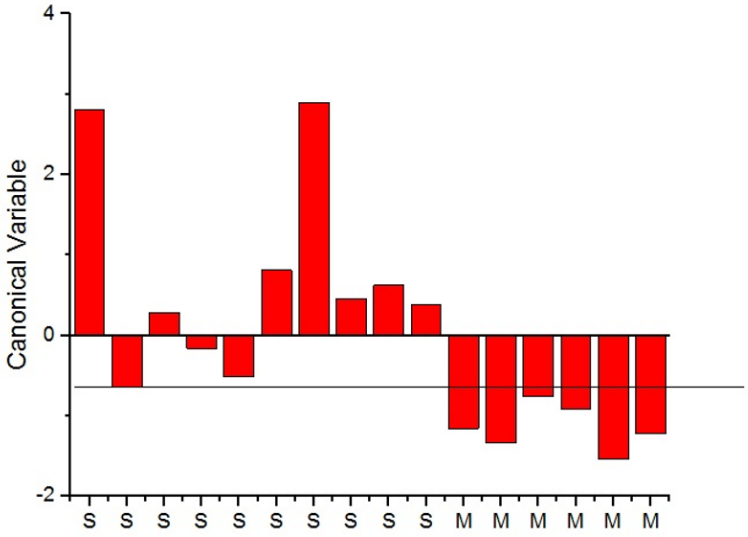

Figure 4.31: Single values of the *canonical variable* obtained by the QDA (S=CS and M=TA) [42].

False negative rate

The number of false negatives (FN) over all the positives (P).

$$FNR = \frac{FN}{FN + TP} = \frac{FN}{P} = 1 - TPR \tag{4.3}$$

False positive rate

The number of false positives (FP) over all the negatives (N).

$$FPR = \frac{FP}{FP + TN} = \frac{FP}{N} = 1 - TNR \tag{4.4}$$

ROC analysis provides tools to select possibly optimal models and to discard suboptimal ones regardless of (and prior of specifying) the cost context or the class distribution. ROC analysis is related in a direct and natural way to cost/benefit analysis of diagnostic decision making.

The accuracy of the ROC curve test is defined as:

$$ACC = \frac{TP + TN}{P + N} \tag{4.5}$$

and depends on how well the test separates the group being tested into those with and without the disease in question. Accuracy is measured by the area under the ROC curve. An area of 1 represents a perfect test; an area of 0.5 represents a worthless test. A rough guide for classifying the accuracy of a diagnostic test is the traditional academic point system:

RANGE	SENTENCE
0.90 - 1	excellent
0.80 - 0.90	good
0.70 - 0.80	fair
0.60 - 0.70	poor
0.50 - 0.60	fail

The area measures discrimination, that is, the ability of the test to correctly classify those with and without the disease.
All the test made with the eleven sensor arrays where analyzed by PCA techniques (all the three projections of each array have been taken into account). Observing the areas and their intersections, the specificity and the sensitivity have been extimated and tabulated in the *confusion matrix* (see Fig. 4.32):

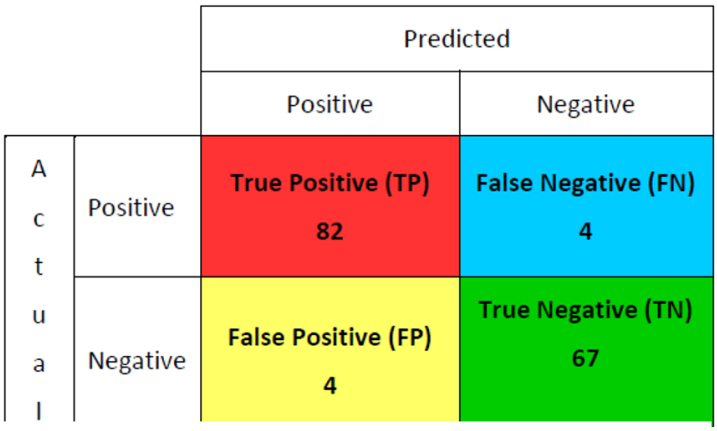

Figure 4.32: Confusion matrix that express all the parameters derived from the data of the eleven sensor arrays.

The ROC curve plotted with this data is shown in Fig. 4.33 whit a specificity and a sensitivity both of 95%, leading to an encouraging result also with this feasibility test.

4.3 Clinical validation protocol

Since May 2016, a clinical validation protocol of the device SCENT A1 has been launched, in collaboration with gastroenterologists of the *University Hospital S. Anna of*

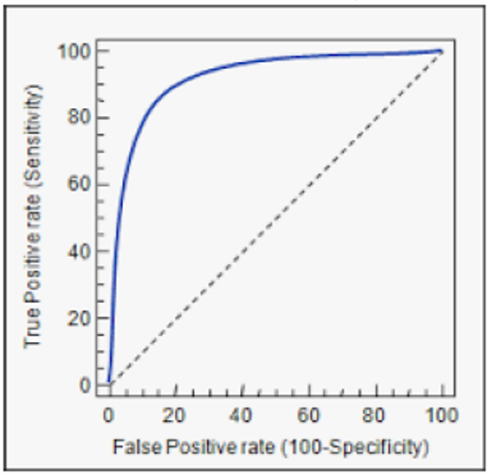

Figure 4.33: ROC curve.

Ferrara (UNIFE) and the *Unitá Igiene Pubblica, Department of Public Health (AUSL).*

A second prototype, similar to SCENT A1 (named SCENT A2, by analogy with the previous one, and shown in Fig. 4.34), was built in order to try new sensor materials in series and to increase statistical results. After the approval of the protocol by the Ethics Committee, all subjects resulted positive to FOBT at the Screening Center of Emilia Romagna (located in Ferrara) are invited to undergo the SCENT A1 test before colonoscopy, which is strongly suggested to verify the diagnosis. Patients will receive a special container that they must return frozen with the sample inside. The test result will then be compared both with the result of FOBT and with colonoscopy, elected as the gold standard (see Fig. 4.35).

The test will continue for at least one year in order to calibrate and clinically validate the device. The statistics on the real positives is in fact very low, owing to the fact that FOBT gives more than 60% of false positives, and this data reflects perfectly the results of the first analysis performed during the course of the Protocol. The first month of tests was fundamental to test the validity of the collection and measurement procedure and to identify any issues.

After having received a positive FOBT result, each patient has to to undergo an interview prior to the colonoscopy. In this session, the figure of a volunteer doctor (Dr. Luciano Ricci) has been integrated. He invites the patient to undergo in addition the experimental test of SCENT A1. The patient receives all the required informations on the collection and conservation method of the sample. During the month of May we realized that the leaflet must be improved, as many samples exceeded the limit amount of fecal material or were badly conserved by the patient. A better description was implemented on the leaflet comprehensive of an explanatory drawing (Fig. 4.36).

Figure 4.34: The prototype SCENT A2, located at the Sensor Laboratory of UNIFE.

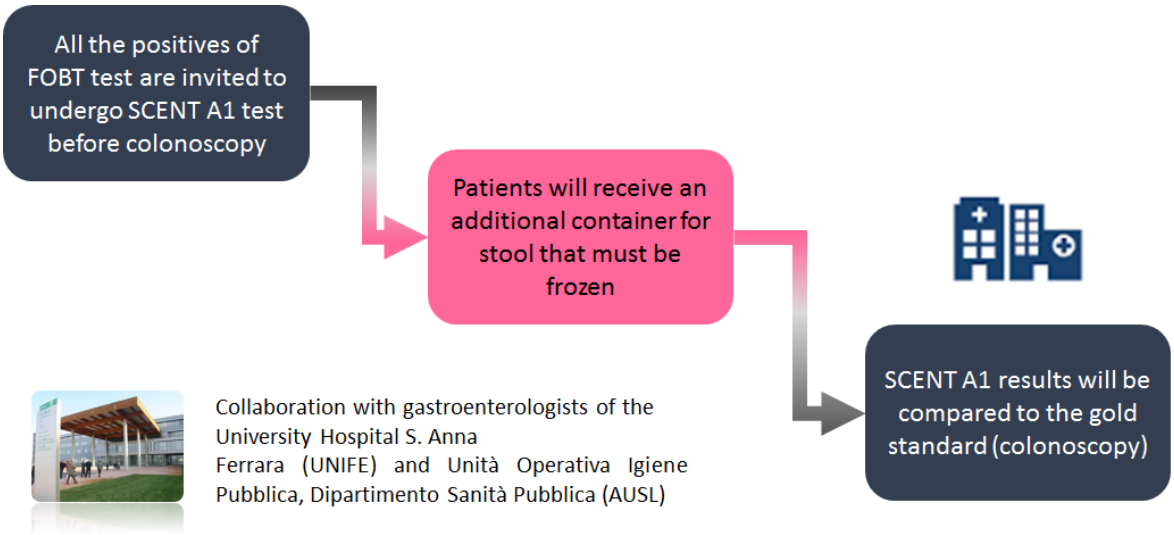

Figure 4.35: Graphical representation of the main steps of the protocol.

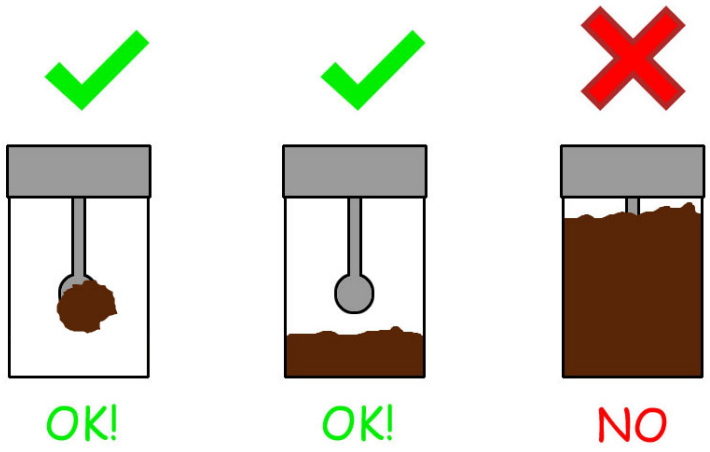

Figure 4.36: Explanatory drawing for the collection procedure of fecal material.

This arrangement has allowed us to further standardize the analysis procedure. The idea of the protocol described in this section is to obtain, after clinical validation, a reliable screening method with great advantages if compared with the methods already employed (i.e., FOBT, virtual colonoscopy) and with the experimental methodologies proposed in the last years (e.g., electronic noses, capsular endoscopy).

In Fig. 4.37 is shown a list of some of the main screening methods proposed in the last years with the advantages and disadvantages with respect to our solution with SCENT A1.

4.3.1 Results of May-June 2016

The first approach chosen for the analysis of SCENT A1 results was the application of PCA technique (already described in Section 3.6), through the software *Multibase (Excel)*. The first classification was based only on known positive FOBTs and healthy volunteers (controls), without any information on colonoscopy results and so on the number of real positives. Every sample was tabulated with the personal details of the subject (no info made public), code (FOBT number) and condition of the sample before the test (e.g., amount, visible characteristics of the fecal material, odor). In Fig. 4.38 is shown a projection of two principal components obtained with PCA technique applied to healthy controls (green dots) and all positive FOBTs (blue dots) tested in the first three weeks without having the colonoscopy results. The FOBT indicated in Fig. 4.38 with the number **1** has been removed due to an error in the sample preservation before the measurement.

In Fig. 4.39 are shown the preliminary results after about one month of tests. Now the blue dots correspond not to all positive FOBTs but only to the ones resulted positive also after colonoscopy. It is important to specify that a *positive* for colonoscopy, is a subject that show an adenoma, whatever its degree of risk. In this regard, it is important to

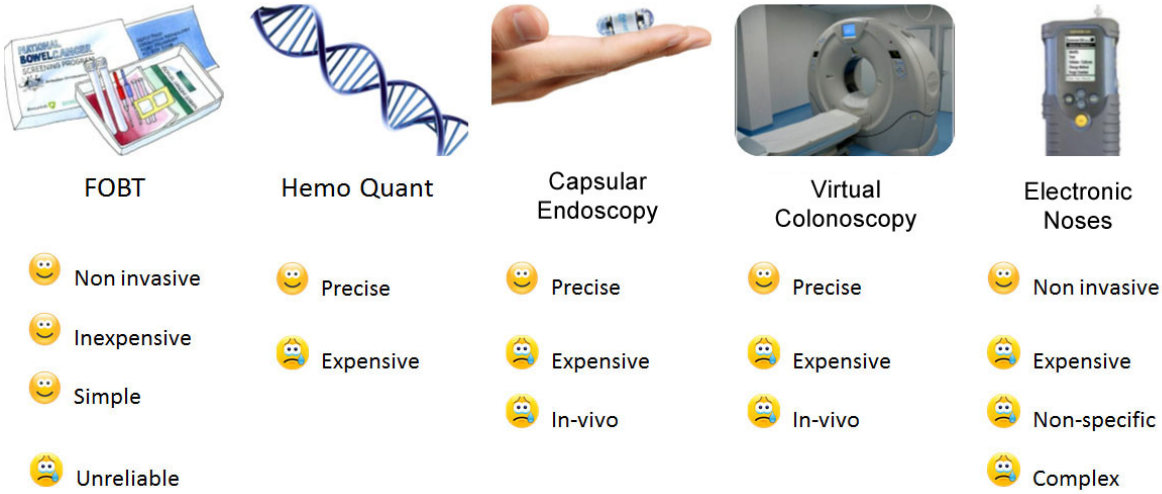

Figure 4.37: List of some of the main screening method proposed in the last years with the advantages and disadvantages with respect to our solution with SCENT A1.

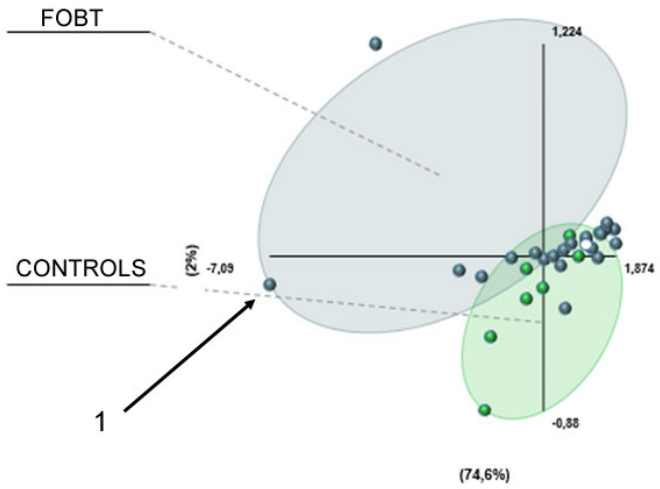

Figure 4.38: Projection of two principal components obtained with PCA technique applied to healthy controls (green dots) and all FOBT positives (blue dots) tested in the first three weeks. The FOBT indicated with the number **1** has been removed due to an error in the sample preservation before the measurement

anticipate that, in the following subsection 4.3.2, this issue will be reviewed in a different light. The positive FOBTs now are indicated as white dots. Therefore, as we receive the results of colonoscopy, white dots are considered as belonging to one of the two populations (control cases, in green, or subjects with adenomas, in blue). In Fig. 4.39 (A) lets focus on FOBT **6** and **25**, which fall in the common area of intersection between healthy and adenoma affected subjects. After having obtained the colonoscopy outcomes, Fig. 4.39 (B), the FOBT **6** has been found as a positive subject by our prediction, while the number **25** is healthy. This is the first true positive identified by SCENT A1 test despite the very low statistics. Moreover, let us observe the FOBT **23** and **28** in Fig. 4.39 (C) and (D). Before colonoscopy they appear ad white dots in the healthy area and after colonoscopy they are confirmed as healthy subjects. This is a second proof of the potentialities of PCA analysis on SCENT A1.

Clearly, the statistics is very low, especially for the fact that the number of true positives is very low compared to the number of true negatives. Moreover, due to the poorness of data, the areas are continuously affected by distortions due to the insertion of new data form that modify the original matrix employed for their determination (see Section 3.6). It will take at least one year of constant work before getting two stable and defined areas to be employed in the determination of healthy and adenoma affected subject.

4.3.2 Results of September-December 2016

After the break during the summer months (june, july and august) the tests are restarted full-time in september with the support of 9 out of 10 patients tested positive for FOBT. However, patients aged 50 to 69 years participating in the test do not represent the prevalence, since FOBT screening was introduced in 2005 in Ferrara. Therefore the number of adenomas actually at risk is very low and the colonoscopies have given mainly negative outcomes. Often the FOBT also identifies low-risk or intermediate risk adenomas, which have a probability of about 1‰ of degenerating into malignant cancers. These polyps are removed during colonoscopy but people who present such benign formations are comparable to healthy ones and the risk of perforation during colonoscopy is higher than the risk of these adenomas degeneration. The idea is now to shift the goal of SCENT A1 test in the identification of high risk adenomas only, so of those polyps that have a good chance of becoming carcinomas if not surgically removed. In Fig. 4.40, 4.41 and 4.42 are reported the PCA projections that collect the tests done from may to december 2016 with the colonoscopy result known (70 samples), obtained by means of the software *Past3*. Positive FOBTs analized with SCENT A1 but with colonoscopy result unknown have been temporarily excluded from the statistics not to complicate the analysis. Here the subjects resulted negative to colonoscopy are indicated as light blue dots, the ones with low/intermediate-risk and hyperplastic adenomas (16 samples) are indicated as grey dots. The patients indicated with fuchsia and red filled squares are respectively a patient with diverse tumor formations and a patient with multiple polyposis. It is noteworthy that in

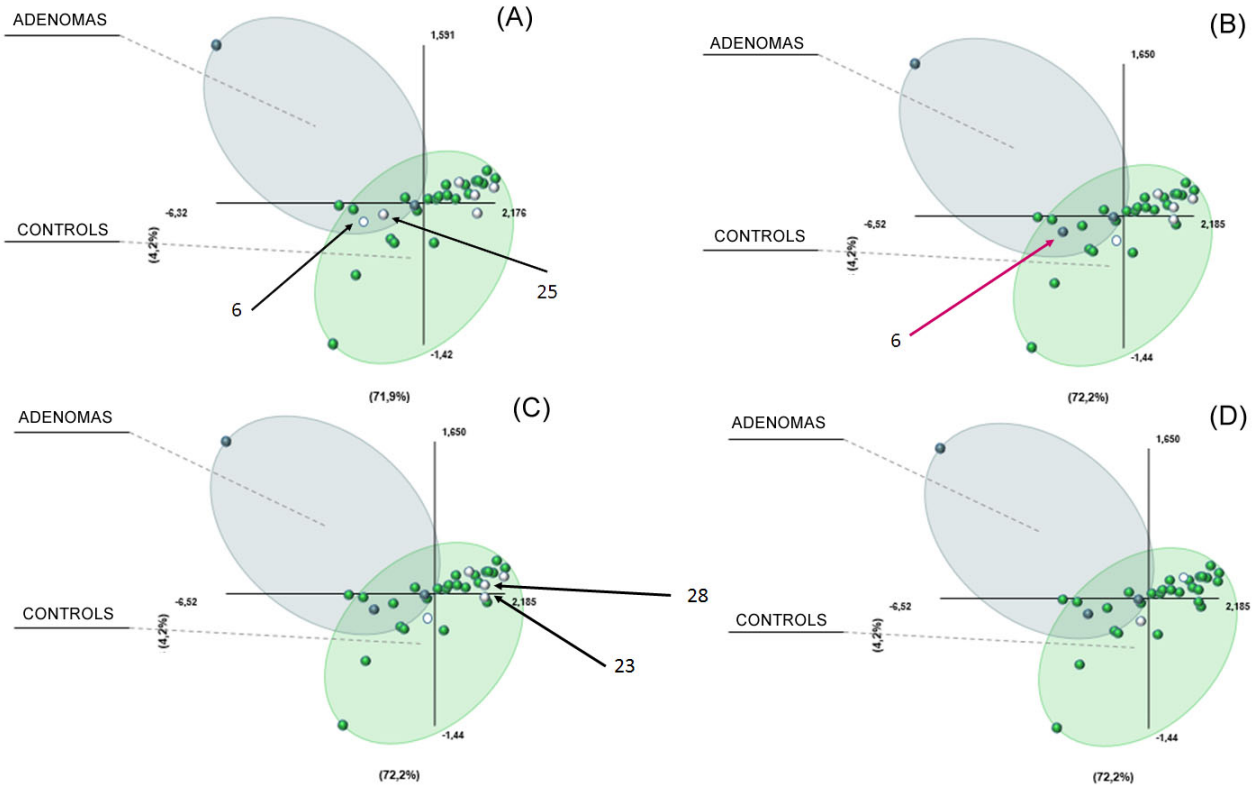

Figure 4.39: Preliminary results after about one month of tests. Projection of two principal components obtained with PCA technique applied to healthy controls and subjects resulted positive to FOBT and negative to colonoscopy (green dots) and subjects positive to both FOBT and colonoscopy (blue dots). White dots correspond to positives to FOBT with unknown colonoscopy result. (A) FOBT **6** and **25** fall in the common area of intersection between healthy and adenoma affected subjects; (B) FOBT **6** has been found as a positive subject by our prediction; (C) FOBT **23** and **28** fall in the healthy area; (D) FOBT **23** and **28** resulted negatives as in our previous prediction.

PC1 vs PC2 and PC1 vs PC3, so in the projections of the three-dimensional PC system that contains the highest degree of information, the two tumor affected tests are at the two sides of the imaginary elliptical area that contains all of the healthy subjects (both individuals negative to colonoscopy and low-risk adenomas) except for a healthy point on the right hand side that can be considered at first sight as a false positive. In the future an area could be defined, within which the subjects can be considered healthy for SCENT A1 test (i.e., without any kind of tumor formation that has a real degenerative risk). It will take a greater statistic to be able to define this boundaries.

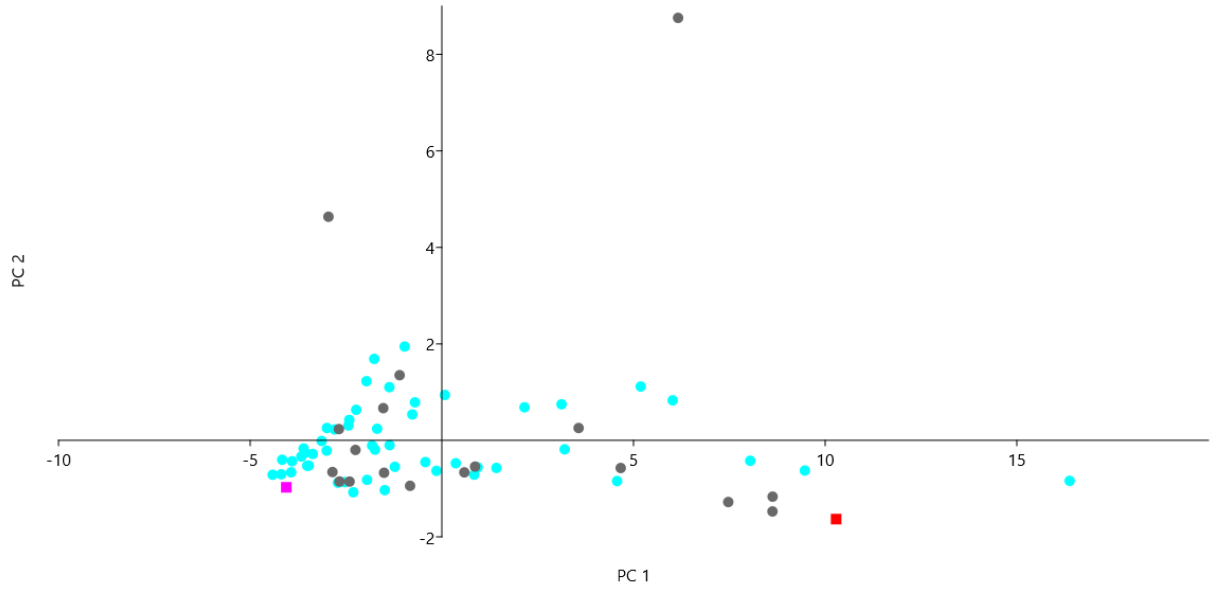

Figure 4.40: PC1 vs PC2 projection of all the tests with colonoscopy resultm upgraded to december 2016. The subjects resulted negative to colonoscopy are indicated as light blue dots, the ones with low/intermediate-risk adenomas are indicated as grey dots. The patients indicated with fuchsia and red filled squares are respectively a patient with diverse tumor formations and a patient with multiple polyposis.

Another PCA similar to the previous one has been performed by changing some of the sample labels. The concept of positive has now been revised. All low-risk adenomas have been now considered as healthy subjects (light blue dots), except than two samples, the first of a subject with a hyperplastic polyp and the second of a subject with a low-risk plus an intermediate-risk polyp (gold filled squares into Fig. 4.43, 4.44, 4.45, indicated respectively with H and IR). It is noticeable that both the intermediate-risk and the hyperplastic polyp are identified from within the healthy zone. The first is slightly further out, as one might expect as it has a quite greater risk of degenerating. To better analize these results it is

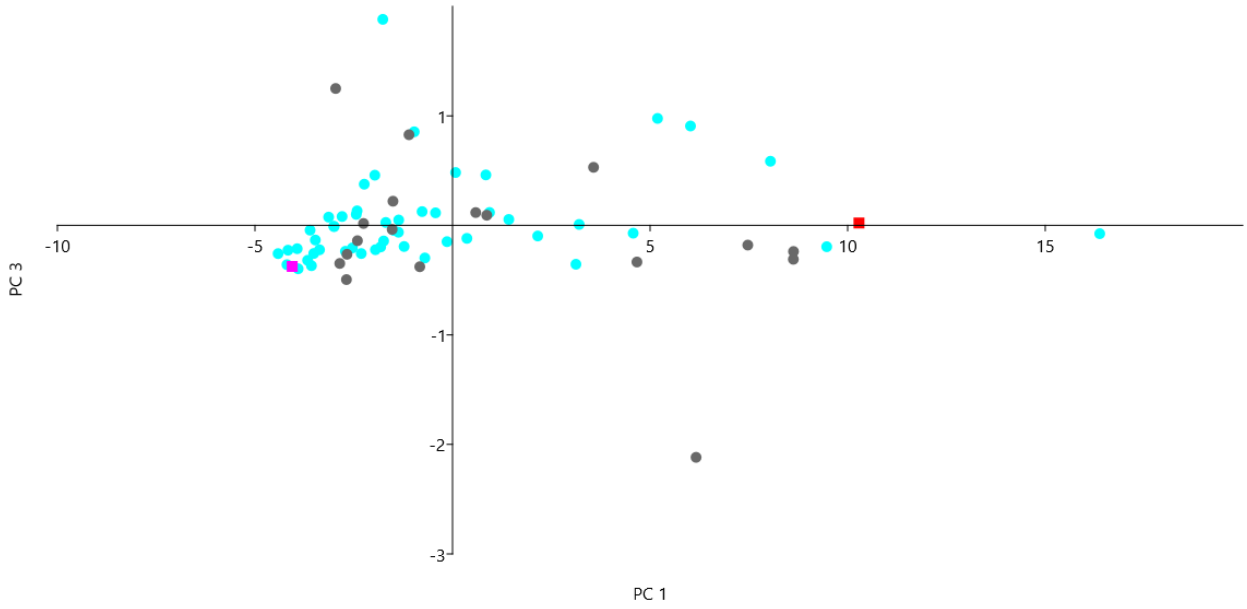

Figure 4.41: PC1 vs PC3 projection of all the tests with colonoscopy resultm upgraded to december 2016. The subjects resulted negative to colonoscopy are indicated as light blue dots, the ones with low/intermediate-risk adenomas are indicated as grey dots. The patients indicated with fuchsia and red filled squares are respectively a patient with diverse tumor formations and a patient with multiple polyposis.

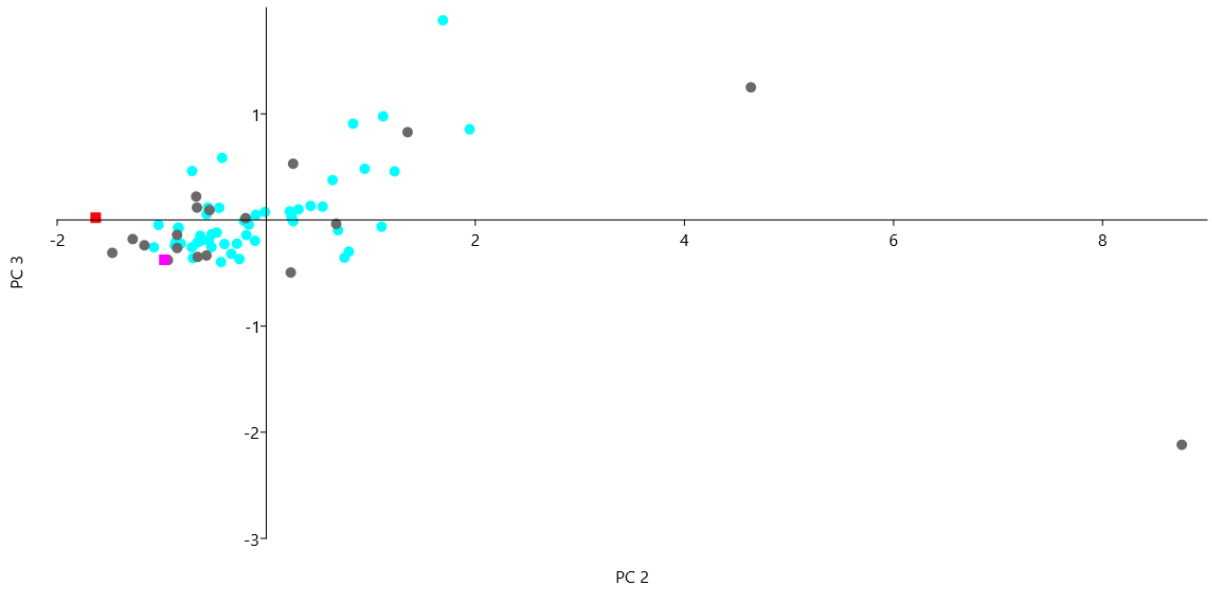

Figure 4.42: PC2 vs PC3 projection of all the tests with colonoscopy resultm upgraded to december 2016. The subjects resulted negative to colonoscopy are indicated as light blue dots, the ones with low/intermediate-risk adenomas are indicated as grey dots. The patients indicated with fuchsia and red filled squares are respectively a patient with diverse tumor formations and a patient with multiple polyposis.

important to focus onto the different types of polyps [88].

Classification of intestinal polyps

- *Pedunculated polyps*: they protrude from the intestinal wall like a mushroom and can be removed easily;
- *Sessile polyps*: without stem dishes, so completely coated on the wall of the bowel and surgical removal is more difficult;
- *Single polyp* (single), *multiple polyps* (1-100), *polyposis* (> 100). Polyposis can be sporadic or familial origin (related to a transmissible genetic defect); in the latter case the risk of degeneration in a CRC is rather high;
- *Hyperplastic polyps and inflammatory*: they are both benign (not present increased risks of tumor development). Inflammatory polyps are often associated with ulcerative colitis, Crohn disease, diverticulosis, and infectious colitis;
- *Hamartomatous polyps*: they are often non-neoplastic lesions;
- *Cancer or adenomatous polyps*: based on the macroscopic and histological features may be in a more or less advanced stage. They are divided into tubular polyps, villous polyps (at greatest risk of cancer) and tubulo-villous polyps mixed;
- Dimensions: varying from a few mm to 3,00 to 4,00 cm. The degeneration risk of a polyp is directly proportional to its size, but that does not mean that even small polyps can be potentially malignant. Statistically speaking, the incidence of mutation in cancer it is of 1% for polyps with less than 1 cm diameter, 10% for those between 2 and 3 cm, and 30% for those with a diameter greater than 2 cm.

What emerges is that, even if low-risk adenomas are labeled as *positive* both for FOBT and colonoscopy, their risk degree of cancer degeneration is quite comparable to the risk of a healthy subject without polyps of contracting cancer. The number of unnecessary colonoscopies is really high and this increases the risk for patients of contracting side effects (e.g., bowel perforation). The SCENT A1 test, which had previously shown to distinguish cancers from healthy subjects (subsection 4.2.2), appears now to show no obvious distinguishing capacity between healthy and low-risk adenomas, although it sounded able to differentiate them in the first analysis (subsection 4.3.2). However, the two true positives (high-risk polyps) in the graphs show a different response from the low-risk adenomas. This method can therefore be employed for the identification of TRUE subjects at risk, reducing unnecessary colonoscopies. A *positive* for SCENT A1 now is not a low-risk adenoma but only an adenoma with the real possibility of degeneration. Once the healthy region will be defined in the PCA graph, although there will still be some false positive, the number of

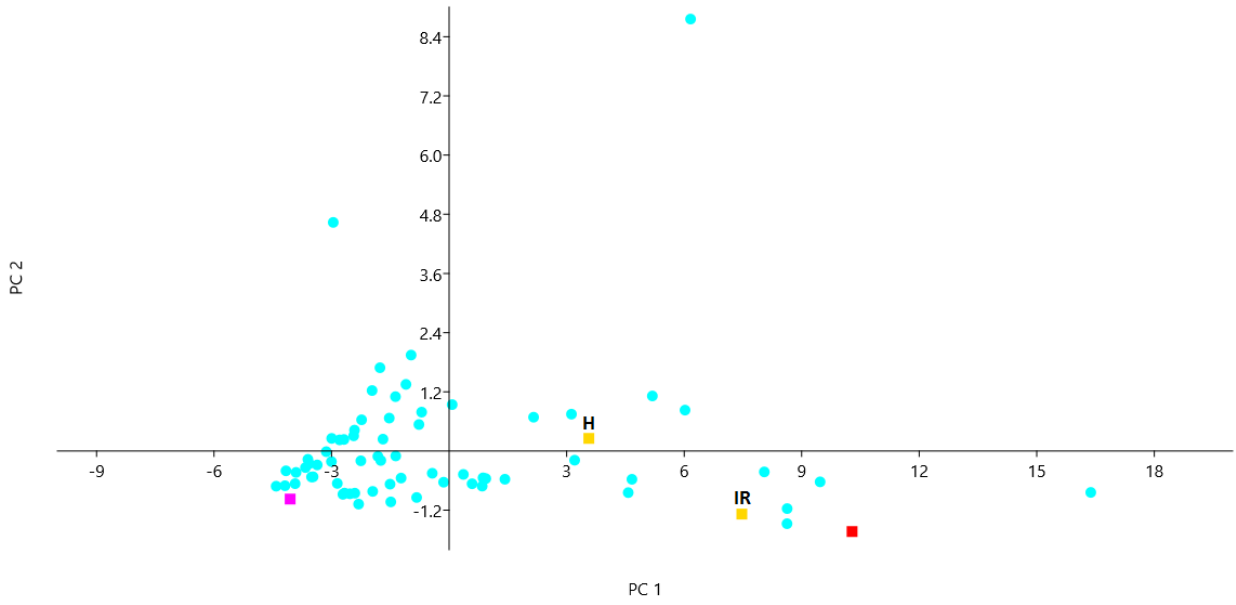

Figure 4.43: PC1 vs PC2 projection of all the tests with colonoscopy resultm upgraded to december 2016. The subjects resulted negative to colonoscopy and low-risk adenomas are indicated as light blue dots. A subject with hyperplastic polyp and a subject with a low-risk plus an intermediate-risk polyp are indicated with gold filled squares. The patients indicated with fuchsia and red filled squares are respectively a patient with diverse tumor formations and a patient with multiple polyposis.

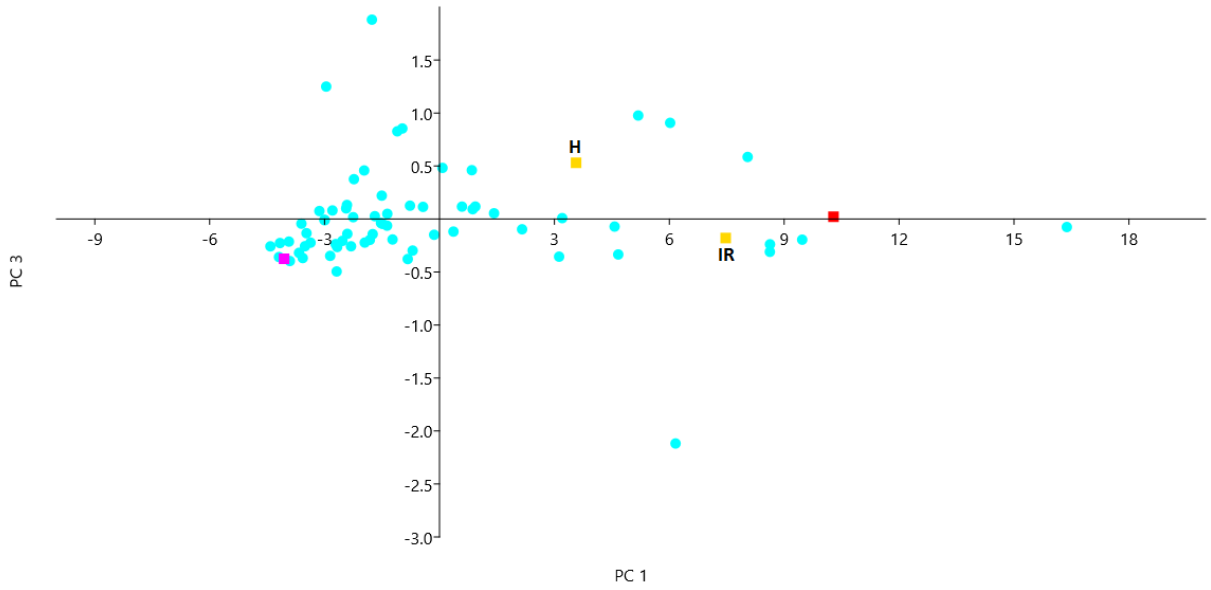

Figure 4.44: PC1 vs PC3 projection of all the tests with colonoscopy resultm upgraded to december 2016. The subjects resulted negative to colonoscopy and low-risk adenomas are indicated as light blue dots. A subject with hyperplastic polyp and a subject with a low-risk plus an intermediate-risk polyp are indicated with gold filled squares. The patients indicated with fuchsia and red filled squares are respectively a patient with diverse tumor formations and a patient with multiple polyposis.

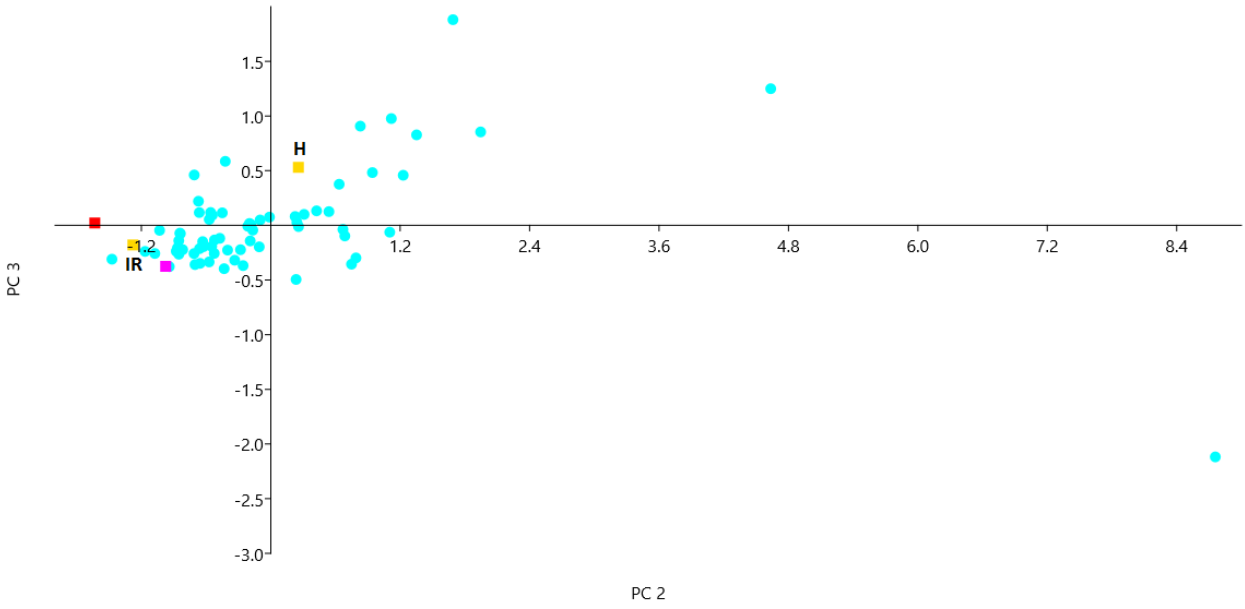

Figure 4.45: PC2 vs PC3 projection of all the tests with colonoscopy resultm upgraded to december 2016. The subjects resulted negative to colonoscopy and low-risk adenomas are indicated as light blue dots. A subject with hyperplastic polyp and a subject with a low-risk plus an intermediate-risk polyp are indicated with gold filled squares. The patients indicated with fuchsia and red filled squares are respectively a patient with diverse tumor formations and a patient with multiple polyposis.

unnecessary colonoscopies will be reduced. The goal is the optimization of the screening system by balancing the risks and benefits.

As laboratory tests are continuing, they are updated with the results of the colonoscopy. The data analysis itself is evolving, adapting step by step to the statistics and the information received. A higher number of high risk adenomas will be critical to better define the regions in the PCA plane.

Chapter 5

The potential power of Gas Chromatography

Gas chromatography (GC) is a common type of chromatography used in analytical chemistry for separating and analyzing compounds that can be vaporized without decomposition. Typically, GC can be employed to test the purity of a particular substance or to separate the different components of a mixture (the relative amounts of such components can also be determined). In some situations, GC may help in identifying a compound. In preparative chromatography, GC can be used to prepare pure compounds from a mixture [89] [90].

In GC, the *mobile phase* (or *moving phase*) is a carrier gas, usually an inert gas such as helium or an unreactive gas such as nitrogen. Helium remains the most commonly used carrier gas in about 90% of instruments although hydrogen is preferred for improved separations [91]. The *stationary phase* is a microscopic layer of liquid or polymer on an inert solid support, inside a piece of glass or metal tubing called a column (an homage to the fractionating column used in distillation). This flexible tube is coiled many times inside a thermostatically-controlled oven to keep it at a constant temperature [92]. The instrument used to perform gas chromatography is called a gas chromatograph (indicated with the same achronym GC).

The gaseous compounds being analyzed interact with the walls of the column, coated with the stationary phase. This causes each compound to elute at a different time, known as the *retention time* of the compound. The comparison of retention times is what gives GC its analytical usefulness.

GC is used to separate complex mixtures, better than thin-layer or paper chromatography. This is because it is more sensitive, allowing the determination not only of what chemicals are present inside the mixture, but also of their amount. The mixture to be analyzed is injected into the stream of carrier gas. As it passes along the column (long thin tube) it separates into the different substances.

Substances with a greater affinity (attraction) for the mobile phase reach the detector at the end of the column more quickly. Substances with a greater affinity for the stationary phase move more slowly through the column.

5.1 GC main components

A schematic representation of a GC is reported in Fig. 5.1.

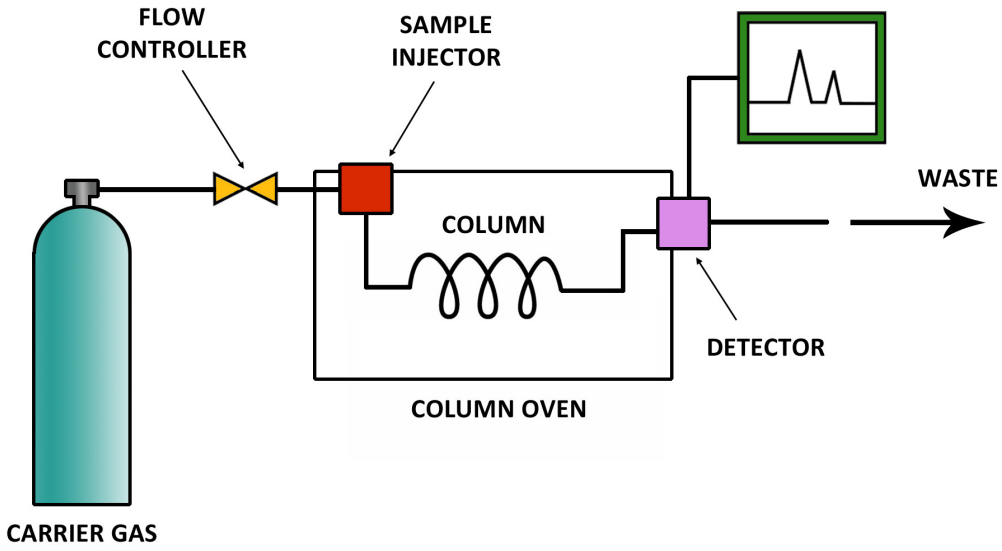

Figure 5.1: Schematic representation of a GC and its main constituents.

The main components of a GC are the following ones:

- the **carrier gas**, which must be chemically inert. Commonly used gases include nitrogen, helium, argon, hydrogen and carbon dioxide. The choice of carrier gas is often dependent upon the type of detector used. The carrier gas system also contains a molecular sieve to remove water and other impurities;

- the **sample injector**. For optimum column efficiency, the sample should not be too large, and should be introduced onto the column as a "plug" of vapor. In fact slow injection of large samples causes band broadening and loss of resolution. The most common injection method consists of microsyringe used to inject the sample through a rubber septum into a flash vaporizer port at the head of the column. The temperature of the sample port is usually about 50°C higher than the boiling point of the least volatile component of the sample. For packed columns, sample size ranges

from tenths of a microliter up to 20 microliters. Capillary columns, on the other hand, need much less sample, typically around 10^{-3} mL. For capillary GC, split/splitless injection is used. Have a look at the diagram of a split/splitless injector in Fig. 5.2. The injector can be used in one of two modes: split or splitless. It contains a heated chamber with a glass liner inside it, into which the sample is injected through the septum. The carrier gas enters the chamber and can leave by three routes (when the injector is in split mode). The sample vapourises to form a mixture of carrier gas, vapourised solvent and vapourised solutes. A proportion of this mixture passes onto the column, but most exits through the split outlet. The septum purge outlet prevents septum bleed components from entering the column;

- the **columns** are generally of two types, *packed* and *capillary* (also known as open tubular). Packed columns contain a finely divided, inert, solid support material (commonly based on diatomaceous earth) coated with liquid stationary phase. Most packed columns are 1.5 - 10 m in length and have an internal diameter of 2 - 4 mm. Capillary columns have an internal diameter of a few tenths of a millimeter. They can be one of two types; wall-coated open tubular (WCOT) or support-coated open tubular (SCOT). Wall-coated columns consist of a capillary tube whose walls are coated with liquid stationary phase. In support-coated columns, the inner wall of the capillary is lined with a thin layer of support material such as diatomaceous earth, onto which the stationary phase has been adsorbed. SCOT columns are generally less efficient than WCOT columns. Both types of capillary column are more efficient than packed columns. In 1979, a new type of WCOT column was devised - the Fused Silica Open Tubular (FSOT) column. These have much thinner walls than the glass capillary columns, and are given strength by the polyimide coating. These columns are flexible and can be wound into coils. They have the advantages of physical strength, flexibility and low reactivity;

- the **column oven** to control the temperature of the column. For precise work, column temperature must be controlled to within tenths of a degree. The optimum column temperature is dependent upon the boiling point of the sample. As a rule of thumb, a temperature slightly above the average boiling point of the sample results in an elution time of 2 - 30 min. Minimal temperatures give good resolution, but increase elution times. If a sample has a wide boiling range, then temperature programming can be useful. The column temperature is increased (either continuously or in steps) as separation proceeds;

- the **detector**. There are many detectors which can be used in gas chromatography. Different detectors will give different types of selectivity. A non-selective detector responds to all compounds except the carrier gas, a selective detector responds to a range of compounds with a common physical or chemical property and a specific detector responds to a single chemical compound. Detectors can also be grouped into

concentration dependent detectors and mass flow dependent detectors. The signal from a concentration dependent detector is related to the concentration of solute in the detector, and the make-up gas does not usually destroy the sample. Dilution of gas will lower the detectors response. Mass flow dependent detectors usually destroy the sample, and the signal is related to the rate at which solute molecules enter the detector. The response of a mass flow dependent detector is unaffected by make-up gas. Have a look at this tabular summary of common GC detectors:

DETECTOR	**SELECTIVITY**
Flame ionization (FID)	Most organic cpds
Thermal conductivity (TCD)	Halides, nitrates, nitriles, peroxides, anhydrides, organometallics
Electron capture (ECD)	Universal
Nitrogen-phosphorus	N, P
Flame photometric (FPD)	S, P, Sn, B, As, Ge, Se, Cr
Photo-ionization (PID)	Aliphatics, aromatics, ketones, esters, aldehydes, amines, etc-
Hall electrolytic conductivity	Halide, N , nitrosamine, S

Some gas chromatographs are connected to a mass spectrometer (MS) which acts as a detector. The combination is known as GC-MS. Some GC-MS are connected to an NMR spectrometer which acts as a backup detector. This combination is known as GC-MS-NMR. Some GC-MS-NMR are connected to an infrared spectrophotometer which acts as a backup detector. This combination is known as GC-MS-NMR-IR. It must, however, be stressed that this is very rare as most analyses needed can be concluded via purely GC-MS.

5.2 Analysis with a GC

In order to perform an analysis it is necessary to set a **method**. The method is the collection of conditions in which the GC operates for a given analysis. Method development is the process of determining what conditions are adequate and/or ideal for the analysis required. Conditions which can be varied to accommodate a required analysis include:

- inlet temperature;
- detector temperature;
- column temperature;
- temperature program;
- carrier gas and carrier gas flow rates;

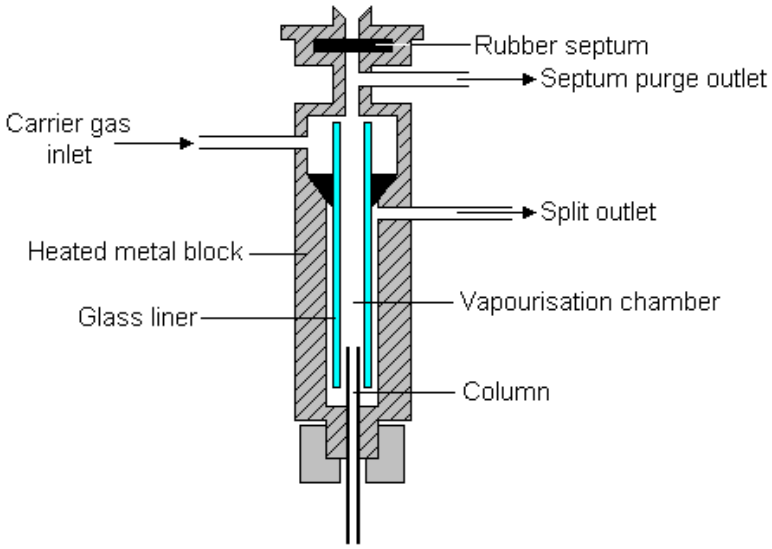

Figure 5.2: Schematic representation of a split/splitless injector [93].

- column stationary phase, diameter and length;
- inlet type and flow rates;
- sample size;
- injection technique.

Depending on the detector/s installed on the GC, there may be a number of detector conditions that can also be varied. Some GCs also include valves which can change the route of sample and carrier flow. The timing of the opening and closing of these valves can be important to method development.

Two types of analysis can be done with a GC: *qualitative* or *quantitative*.

Qualitative analysis

Generally chromatographic data is presented as a graph of detector response (y-axis) against retention time (x-axis), which is called a *chromatogram*. This provides a spectrum of peaks for a sample representing the analytes present in a sample eluting from the column at different times. Retention time can be used to identify analytes if the method conditions are constant. Also, the pattern of peaks will be constant for a sample under constant conditions and can identify complex mixtures of analytes. However, in most modern applications, the GC is connected to a MS or similar detector that is capable of identifying the analytes represented by the peaks.

Quantitative analysis

The area under a peak is proportional to the amount of analyte present in the chromatogram. By calculating the area of the peak using the mathematical function of integration, the concentration of an analyte in the original sample can be determined. Concentration can be calculated using a calibration curve created by finding the response for a series of concentrations of analyte, or by determining the relative response factor of an analyte. The relative response factor is the expected ratio of an analyte to an internal standard (or external standard) and is calculated by finding the response of a known amount of analyte and a constant amount of internal standard (a chemical added to the sample at a constant concentration, with a distinct retention time to the analyte). In most modern GC-MS systems, computer software is used to draw and integrate peaks, and match MS spectra to library spectra.

5.3 GC applications

Gas chromatography is used for different types of analysis (e.g., to detect banned substances in urine samples from athletes or to analyze the gas emitted by organic solutions in general). It is so possible to imagine, in the next future, to employ the GC with a MS as a detector, for the identification and the quantification of the VOCs present inside fecal samples, in order to study the real composition of each sample that is tested with SCENT A1. This will be an interesting study that would provide some information on the chemical reactions occurring on the sensor surfaces, by knowing the gas involved in the response processes. A similar study has been done by the team of de Meij et al. [69], who hypothesized that fecal VOCs may serve as a diagnostic biomarker of CRC and adenomas. Fecal samples of patients who were scheduled to undergo an elective colonoscopy were collected and an electronic nose (Cyranose 320 [70]) was used to measure VOC patterns in fecal gas from patients with histopathologically proven CRC, with advanced adenomas and from controls (no abnormalities seen at colonoscopy). ROC curves and corresponding sensitivity and specificity for detection of CRC and advanced adenomas were calculated. A total of 157 stool samples (40 patients with CRC, 60 patients with advanced adenomas, and 57 healthy controls) were analyzed by electronic nose, then they where also analyzed through GC-MS technique in order to validate the test.

At the Sensor and Semiconductor Laboratory of UNIFE, I am responsible for a GC (described in Section 5.4). This GC is now equipped with TCD detectors but the idea is to connect it with a MS (Cirrus LM99, MKS) in order to enhance the sensitivity to VOCs.

5.4 Micro GC Agilent description

The Micro GC employed for analysis is a Micro GC Agilent 490 (see Fig. 5.3). The 490 Micro GC compact gas analyzer offers between one to four user installable, plug and play analytical GC channels. Each channel is essentially a complete, miniaturized GC with electronic gas control, injector, narrow-bore column and detector, for fast, high efficiency separations. Each is independently controlled, including injection volume, column oven temperature, carrier gas and gas pressure. With micro-electronic gas control and time-programmable optional backflush, is it possible to analyze sample components of interest while eliminating less volatile components and undesired contaminants such as moisture, allowing faster analysis time and extending column and component lifetimes. User exchangeable GC channels or modules provide quick and easy reconfiguration for any application [94].
The columns installed on the Micro GC are two:

- **Molecular Sieve 5A (MS5A)** is referred to as zeolite molecular sieve. These crystalline materials are synthetically produced and have very uniform internal cavities. MS5A has an effective pore size of 5 angstroms and, in order for a compound to be able to pass through these pores, it must be smaller. Compounds like He, H_2, Ar, O_2, N_2, CH_4, and CO are able to pass through pores. The primary advantage of this column is the baseline separation between O_2 and N_2 with a relatively short column and at room temperature. Another is the separation of CO from air and CH_4 (a difficult separation for any non-molecular sieve packed column). The primary disadvantage is that these packings will trap CO_2 and H_2O, which is why these columns are typically used with a pre-column (stripper column) and valve switching. However, if CO_2 and H_2O do get trapped in these columns, the effects are reversible. Finally, one needs to be cautious when using any carrier gas other than nitrogen to dry/condition these columns. Because these materials contain surface metals that cannot be easily removed, it is believed that other carrier gases like hydrogen, argon and helium (at high temperatures) can remove the oxidation layer on the metal surface, which can lead to activity (especially for CO) [95];

- **Porous Layer Open Tubular (PLOT U)**, or PoraPLOT U, provides symmetrical peaks with polar volatiles. Water has no effect on retention times and elutes as a sharp and quantifiable peak. PoraPLOT U is the most polar porous polymer PLOT column and is designed for halogenated compounds, hydrocarbons C1-C6, ketones and solvents. Water has no effect on retention times and elutes as a sharp quantifiable peak. Reliable retention time repeatability [96] [97].

In Fig. 5.4 is reported a view of the Micro GC connected to the computer in which has been installed the software *Soprane 3.5.7* employed for GC analysis. The carrier gas used for both the columns is Helium and represents a good compromise between the two

Figure 5.3: Photo of the Mirco GC Agilent 490.

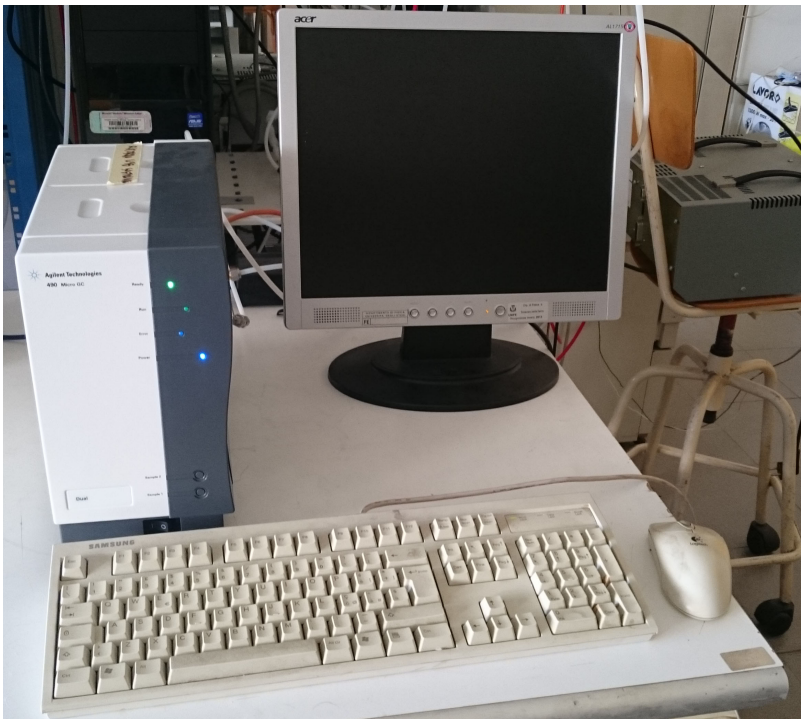

Figure 5.4: Photo of the Micro GC connected to the computer in which the software Soprane 3.5.7 is installed.

in order to have a good gas separation with the TCD detectors inserted in the Micro GC. The choice has been done after some preliminary tests with Nitrogen that have led to unsatisfactory results.

The TCD detector is a universal detector and can detect air, hydrogen, carbon monoxide, nitrogen, sulfur oxide, inorganic gases and many other compounds. TCD works by means of two parallel tubes containing both gas and heating coils. The gases are examined by comparing the heat loss rate from the heating coils into the gas. Normally one tube holds a reference gas and the sample to be tested passes inside the other one. Through this functioning principle, a TCD detects the changes in the thermal conductivity of the column effluent and compares it to a reference flow of carrier gas. Most compounds have a thermal conductivity much smaller than that of the common carrier gases (hydrogen or helium). Therefore, when an analyte elutes from the column, the thermal conductivity of the effluent is reduced and a detectable signal is produced. Helium has traditionally been elected as the favored carrier gas.

The Micro GC is built for the analysis of gases and vapors only. Sample pressure should be between 0 and 100 kPa (0 to 15 psi[1]), the temperature between 0 and (110 ± 5)°C of the analyzer ambient temperature, and it must be filtered, preferably through a 5-mm filter.

The Micro GC is configured for use with either He and H_2 or N_2 and Ar as a carrier gas. The carrier must have a minimum purity of 99.999 %. Since the injection valve is operated pneumatically, there is a limit of 550 kPa ± 10 % (80 psi ± 10 %) to the main gas supply. The gas flow diagram of MicroGC 490 Agilent is shown in Fig. 5.5 [98].

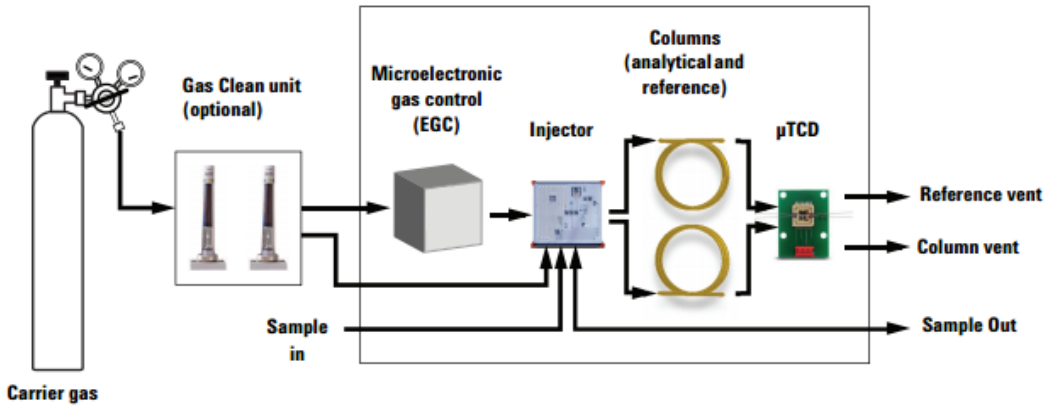

Figure 5.5: Gas flow diagram of MicroGC 490 Agilent [94].

[1] 1 psi = 6,895 kPa = 6,895x10^{-2} atm

5.5 Instrument calibration

The calibration of a Micro GC system is a a fundamental step to be able of identifying the components of interest inside a unknown gas mixture. The procedure consists in sending to the GC diverse known gases, in two or more known concentrations each, so as to be able to associate to each peak the gas that generates it and to obtain a calibration curve for each compound. Gases can be sent by means of gas bottles (taking on account their purity degree) and mass flow controllers or by the help of standard gas mixtures available in bottles. The procedure that I have used is the first one and I will describe it in the following sections.

5.5.1 First calibration attempt

The first attempt of calibration has not been successful, since some difficulties of operation of the instrument have been encountered. The difficulties have been attributed to a problem with the conditioning mode. In fact, to be operative, the GC has to be conditioned for at least 24 hours or more with the carrier gas, so that the columns are impregnated with it. The conditioning should be done with the detectors off and bringing the columns and the injectors at high temperatures (respectively 180°C and 110°C). In the following table are summarized the principal parameters of the conditioning method named **Condizionamento**:

Column type	**MS5A**	**Plot U**
Module	A	B
Column T (°C)	180	180
Injector T (°C)	110	110
Injection time (ms)	100	100
Backflush (s)	10	10
Run time (s)	60	60
Pressure (psi)	30	30

Between each analysis the Micro GC is maintained in a condition of stand-by (method: **Standby**), in order not to damage the modules with too much high temperatures, with the following parameters:

Column type	**MS5A**	**Plot U**
Module	A	B
Column T (°C)	55	65
Injector T (°C)	100	100
Injection time (ms)	40	40
Run time (s)	120	120
Pressure (psi)	28	28

Before each test with a gas or a mixture, the associated method must be charged and the analysis can be started only when the GC is ready, so when the temperature values of columns and injectors recorded in the method are reached.

A wide range of gases mixed with synthetic dry air (80% N_2 and 20% O_2) has been sent to the GC (e.g., CO, CO_2, H_2S, SO_2, CH_4, propane, ethene) in order to identify their peaks. However, after having observed the output peaks, the nitrogen and oxygen peak in MS5A, instead be separate and distinguishable showed a wide margin of overlap, probably due to excessive hydration of the column. In order to understand the reason of this excess of moisture inside the column, three hypotheses have been advanced:

- error in the parameters entered into the acquisition Method;
- loss in the helium line;
- manufacturing defect of the module MS5A.

At the aim of excluding two of them, several tests with modified parameters have been tried and the helium line has been controlled, then the helium bottles has been attached directly to the Micro GC to exclude any kind of gas loss in the line. Despite these precautions, the conditioning period continued to be too short and the rehydration too rapid. A problem in the module has so been identified and it has been replaced with a working module. The addition of a membrane, a pressure reducer and a sintered filter has been done in order to optimize the results and to avoid future damages to the instrument due to the entry in the columns of particles coming from the environmental air.

The calibration has so been performed only with the gases that are detectable by the Plot U module. Here a description of the calibration method of calibration of propane, CO_2 and ethene. Also an attempt of calibrating H_2S was done but the concentration in the gas bottle was too much small to be detected by the GC (100 ppm). Moreover, a characteristic of H_2S is the high degree of adhesion to a lot of surfaces, despite materials as glass or Teflon. The line was not completely realized in Teflon so this should be another reason that brought to a decrease in the concentration of H_2S arriving to the GC.

5.5.2 Propane calibration

Propane (Fig. 5.6) is a colorless, non-polar, flammable gas, C_3H_8, of the alkane series, occurring in petroleum and natural gas: used chiefly as a fuel and in organic synthesis.

Propane is separated in large quantities from natural gas, light crude oil, and oil-refinery gases and is commercially available as liquefied propane or as a major constituent of liquefied petroleum gas (LPG). As with ethane and other paraffin hydrocarbons, propane is an important raw material for the ethylene petrochemical industry. The decomposition of propane in hot tubes to form ethylene also yields another important product, propylene.

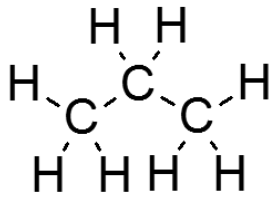

Figure 5.6: Chemical structure of propane (C_3H_8).

From propylene such organic chemicals as acetone and propylene glycol are derived. The oxidation of propane to such compounds of carbon, hydrogen, and oxygen as acetaldehyde is also of commercial interest.
Although a gas at ordinary atmospheric pressure, propane has a boiling point of -42.1°C (-43.8° F) and thus is readily liquefied under elevated pressures. It therefore is transported and handled as a liquid in cylinders and tanks. In this form, alone or mixed with liquid butane, it has great importance as a fuel for domestic and industrial uses and for internal-combustion engines [99].

Propane is separated in the Plot U, so identified by the detector of the corresponding module. The Method employed for propane (named **Giulia 1**) is obtained by setting the column temperature at 90°C and the injector at 100°C and it appears far from the nitrogen peak, at its right-hand side. Inside the bottle, propane is diluted with synthetic dry air, therefore, to set the desired concentration, also a bottle of synthetic air has been employed. The parameters of the method are summarized in the following table:

Column T (°C)	90
Injector T (°C)	100
Injection time (ms)	500
Backflush (s)	10
Run time (s)	70
Pressure (psi)	25

The chosen concentrations for the analysis were: 500, 200, 100 and 50 ppm. The tests were carried out with this four concentration values with three analysis for each concentration in order to take the average value between peaks. This methodology allows to obtain a good correlation degree in the final calibration straight line. In Fig. 5.7 and 5.8 two images of the calibration curves for propane in the four concentrations indicated before. The propane peak appears at 34.08 s from the beginning of the analysis.

In Fig. 5.9 and 5.10 all the parameters related to propane calibration for each concentration level are shown, i.e., the area under the integrated curve and the ratio between the area and the amount of gas sent to the column. Then the calibration curve is shown with its related correlation coefficient r=0.999846.

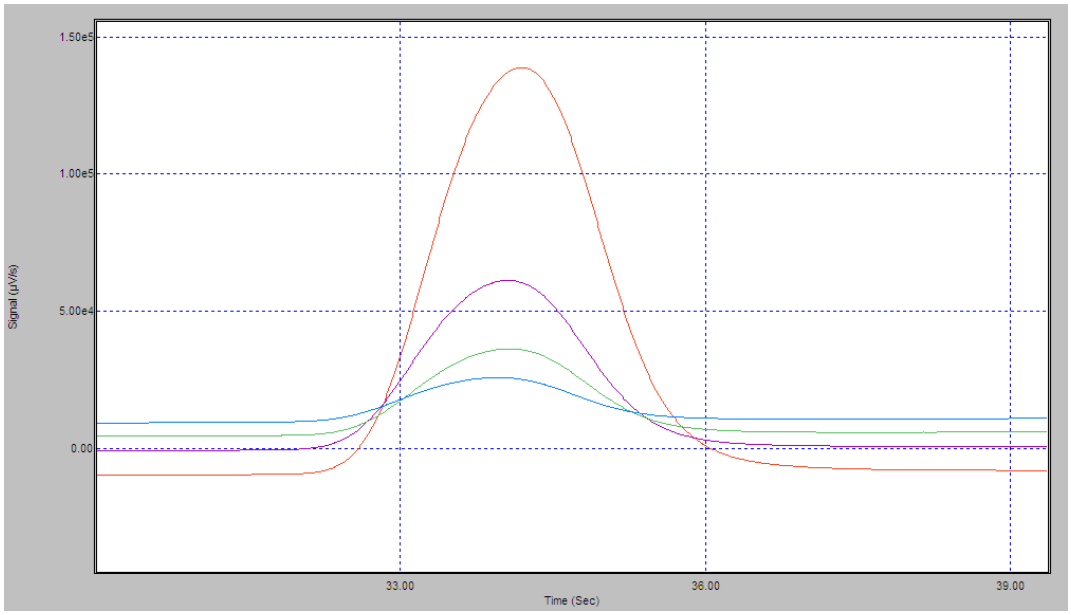

Figure 5.7: Zoom of propane 500 (red), 200 (violet), 100 (green) and 50 (blue) ppm peaks.

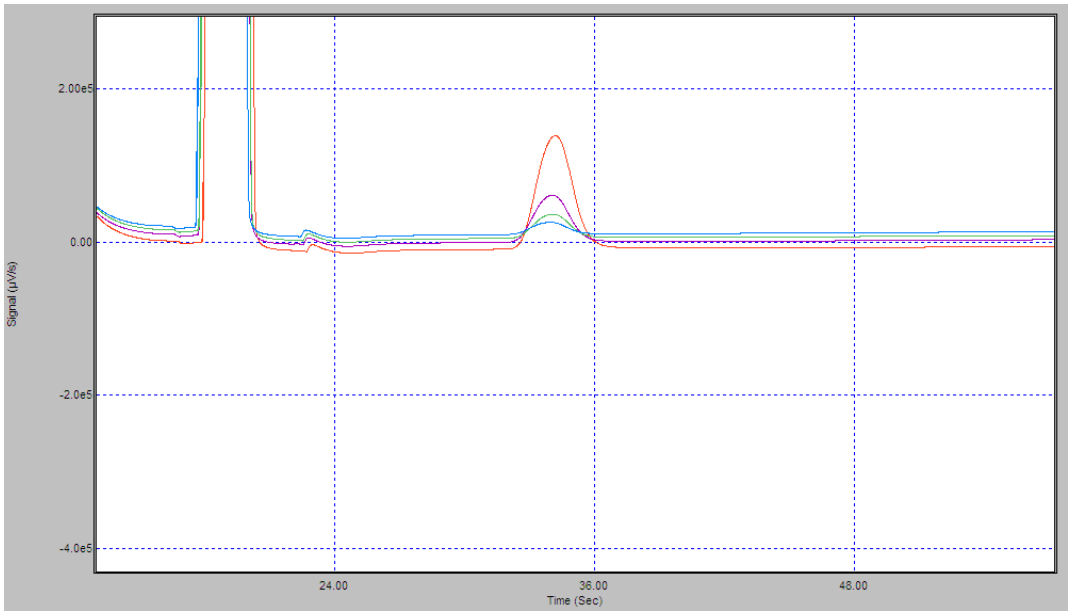

Figure 5.8: Zoom of propane 500 (red), 200 (violet), 100 (green) and 50 (blue) ppm peaks. Here is noticeable the position of the peak at the right-hand side of N_2.

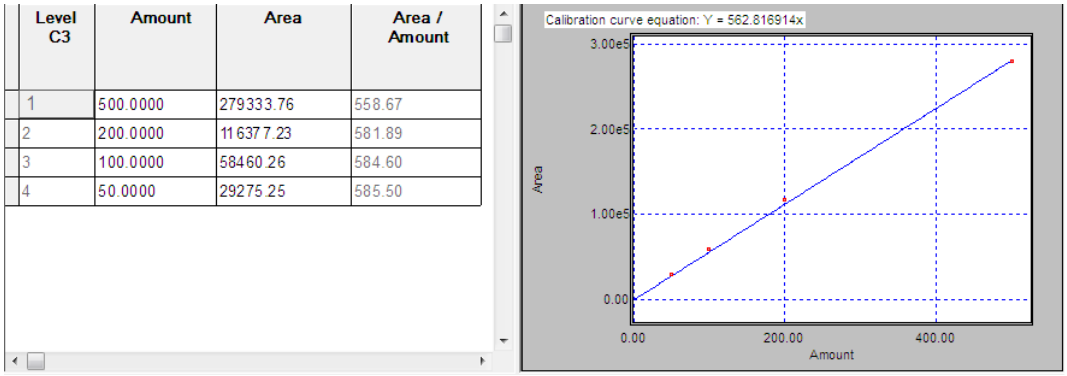

Level C3	Amount	Area	Area / Amount
1	500.0000	279333.76	558.67
2	200.0000	116377.23	581.89
3	100.0000	58460.26	584.60
4	50.0000	29275.25	585.50

Figure 5.9: Calibration curve of propane (C3). The concentration employed are four: 500, 200, 100 and 50 ppm.

Component Name	Time retention (Sec)	Quantity Level 1	Units of report	Curve Type	Correlation Coefficient
C3	34.08	500.000	ppmVol	Linear Through Zero	0.999846

Figure 5.10: Correlation parameter of propane and detection time.

5.5.3 Carbon dioxide (CO_2) calibration

Carbon dioxide (CO_2), whose molecular structure is reported in Fig. 5.11, is a colorless, odorless, incombustible gas, present in the atmosphere and formed during respiration, usually obtained from coal, coke, or natural gas by combustion, from carbohydrates by fermentation, by reaction of acid with limestone or other carbonates, or naturally from springs: used extensively in industry as dry ice, or carbon dioxide snow, in carbonated beverages, fire extinguishers, etc.

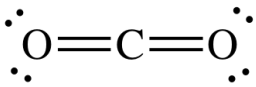

Figure 5.11: CO_2 molecular structure.

The measurement of the CO_2 can be important for various reasons, e.g., air environmental monitoring, soil analysis or biological samples analysis. In particular, regarding the indoor environments, when many people divide the same space, air can soon become heavy and this fact can be attributed to the exhaled CO_2. This can lead to a drop in concentration, productive capacity and wellbeing.

The average concentration of atmospheric CO_2 in the air is approximately 700 mg/m^3 (390 ppm) (NOAA Earth System Research Laboratory Global Monitoring Division, 2011).

Usually the CO_2 concentrations in the residential indoor atmosphere are higher than the outside concentration and they depend on the number of occupants of an environment, which require continuous oxygen and that produce it as a by-product of the respiratory system. Consequently a substantial increase of CO_2 leads to a corresponding decrease in the concentration of O_2 and therefore to a risk for human health. The Joint Research Centre (JCR) of the EU has conducted a study which showed that in the internal ambients there are greater amounts of harmful substances than outdoors. A study of Max von Pettenkofer [100] has proven that people who are in rooms with a CO_2 concentration below 0.1% (1000 ppm) feel at ease while they clearly feel uncomfortable in rooms with concentrations above 0.2% (2000 ppm). With his research he laid over 140 years ago, the basis on which today methods for assessing air quality rely. This directive foresees a CO_2 limit value up to 1500 ppm and in Fig. 5.12 is shown a table with the effects of CO_2 on humans [101].

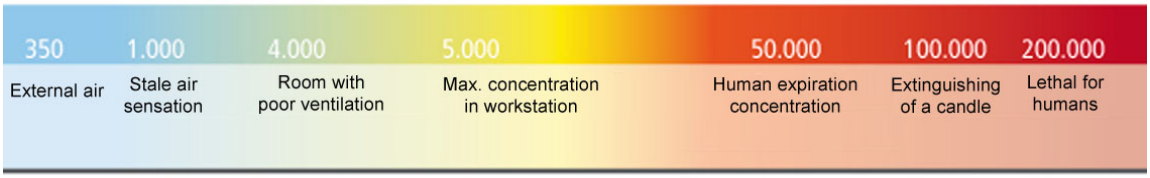

Figure 5.12: Typical CO_2 concentration (in ppm) and their effects on humans [101].

Chemoresistive sensors are not capable of detecting CO_2 so the idea is to observe this gas with the help of the Micro GC.

As in the case of propane, also carbon dioxide is separated in the Plot U. The Method employed for this gas (named **Giulia 2(B50)**) is obtained by setting the column temperature at 50°C and the injector at 60°C and the corresponding peak appears at the right-hand side of the nitrogen one. Inside the bottle, carbon dioxide is diluted with synthetic dry air, therefore, to set the desired concentration, also a bottle of synthetic air has been employed. The parameters of the method are summarized in the following table:

Column T (°C)	50
Injector T (°C)	60
Injection time (ms)	100
Backflush (s)	10
Run time (s)	70
Pressure (psi)	25

The chosen concentrations for the analysis were: 500, 200, 100 and 50 ppm. The tests were carried out with this four concentration values with three analysis for each value in

order to take the average value between peaks. This methodology allows to obtain a good correlation degree in the final calibration straight line. In Fig. 5.13 and 5.14 two images of the calibration curves for propane in the four concentrations indicated before. The CO_2 peak appears at 23.73 s from the beginning of the analysis.

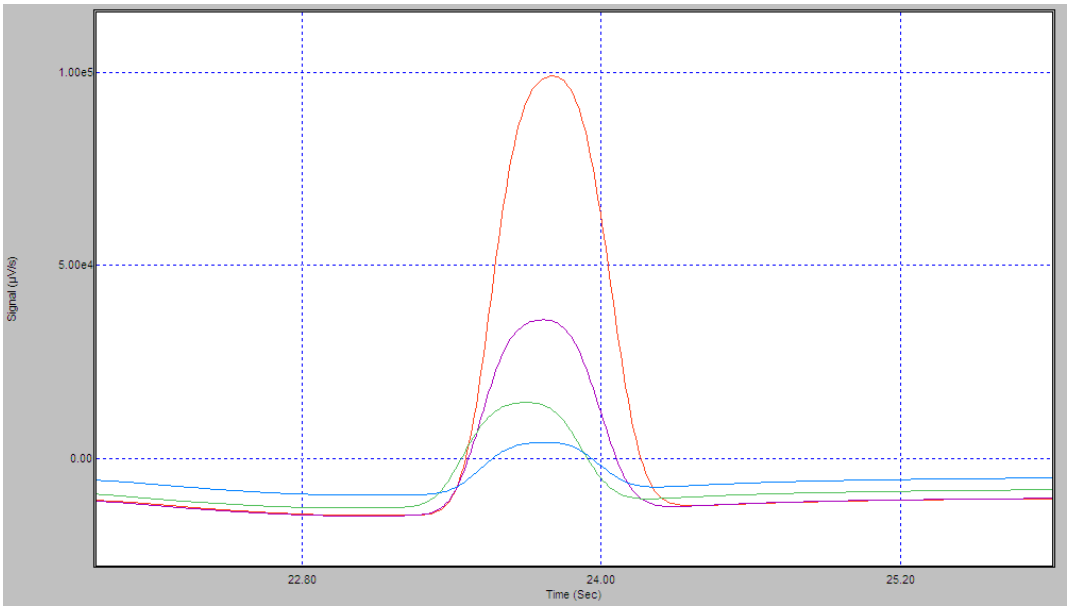

Figure 5.13: Zoom of carbon dioxide 500 (red), 200 (violet), 100 (green) and 50 (blue) ppm peaks.

In Fig. 5.15 and 5.16 all the parameters related to carbon dioxide calibration for each concentration level are shown, i.e., the area under the integrated curve and the ratio between the area and the amount of gas sent to the column. Then the calibration curve is shown with its related correlation coefficient r=0.999051.

Analysis of the CO_2 concentration in laboratory

After having completed the calibration of CO_2, a test was performed in order to evaluate the concentration level of carbon dioxide in the laboratory atmosphere. The first test was performed the 24^{th} October 2016 during in a time interval between the 10:10 and the 18:47 for a total of eighteen sets of measurement. In the following table are registered information on about the number of people present in the laboratory before each measurement and the ppm concentration (C) of CO_2 found by the Micro GC. My presence as operator is not marked when I entered the laboratory only to start the measurement. The histogram representing concentration as a function of time is shown in Fig. 5.17.

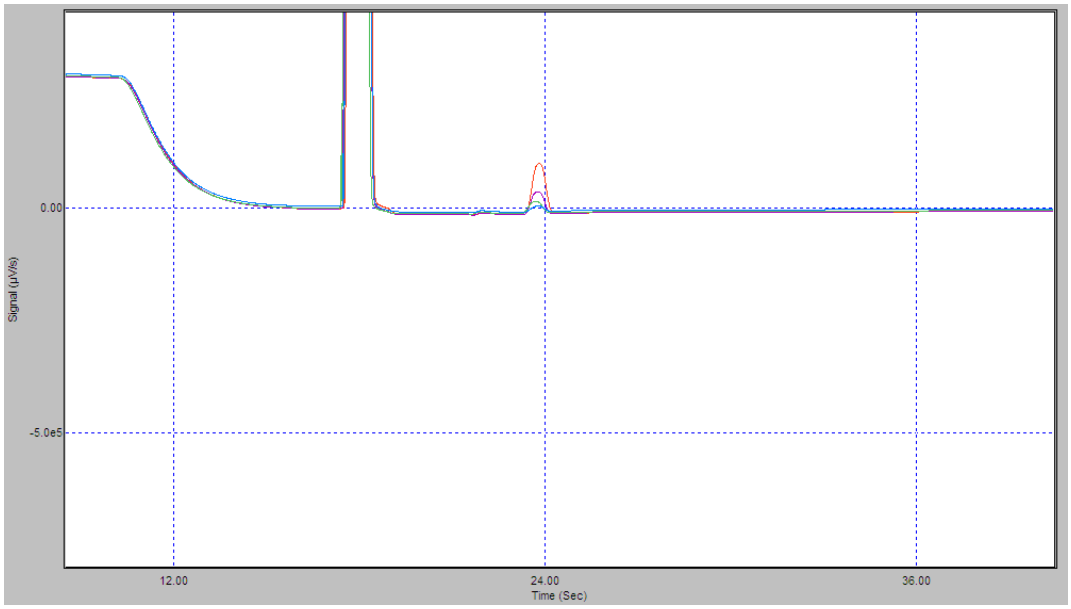

Figure 5.14: Zoom of carbon dioxide 500 (red), 200 (violet), 100 (green) and 50 (blue) ppm peaks. Here is noticeable the position of the peak at the right-hand side of N_2.

Component Name	Time retention (Sec)	Quantity Level 1	Units of report	Curve Type	Correlation Coefficient
CO2	23.73	500.000	ppmVol	Linear Through Zero	0.999051

Figure 5.15: Correlation parameter of carbon dioxide and detection time.

	Level CO2	Amount	Area	Area / Amount
	1	500.0000	52327.00	104.65
	2	200.0000	22844.30	114.22
	3	100.0000	12106.56	121.07
	4	50.0000	5716.37	114.33

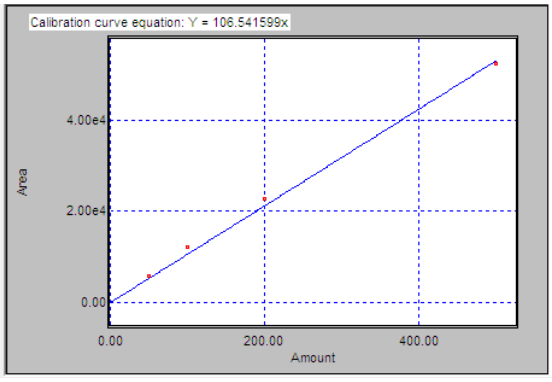

Figure 5.16: Calibration curve of CO_2. The concentration employed are four: 500, 200, 100 and 50 ppm.

Time (h)	C (ppm)	People (n°)
10:10	580	0
10:56	609	2
11:28	626	2
11:41	645	3
12:18	710	3
12:35	715	1
12:53	715	1
14:24	648	0
14:34	663	2
15:18	731	2
15:34	759	4
15:50	755	3
16:36	707	3
17:10	686	2
17:32	689	2
17:42	683	1
17:54	678	1
18:47	660	1

It is is noteworthy that the chart pattern follows the accumulation of carbon dioxide produced by respiration of the people working in the lab during the day. In the morning, there is a low level of carbon dioxide, which grows until lunchtime. After lunch there is a drop and new growth until mid-afternoon, when the presence of people is progressively reduced.

5.5.4 Ethene calibration

Ethene (or ethylene) is the most important organic chemical, by tonnage, that is manufactured. It is the building block for a vast range of chemicals C_2H_4 from plastics to antifreeze solutions and solvents. The chemical formula of ethene is reported in Fig. 5.18.

Ethene is produced from the cracking of fractions obtained from distillation of natural gas and oil. The processes are:

- the steam cracking of ethane and propane (from natural gas and from crude oil);
- the steam cracking of naphtha from crude oil;
- the catalytic cracking of gas oil from crude oil. The choice of feedstock depends on availability, price (which can vary considerably), and what other products from cracking are needed.

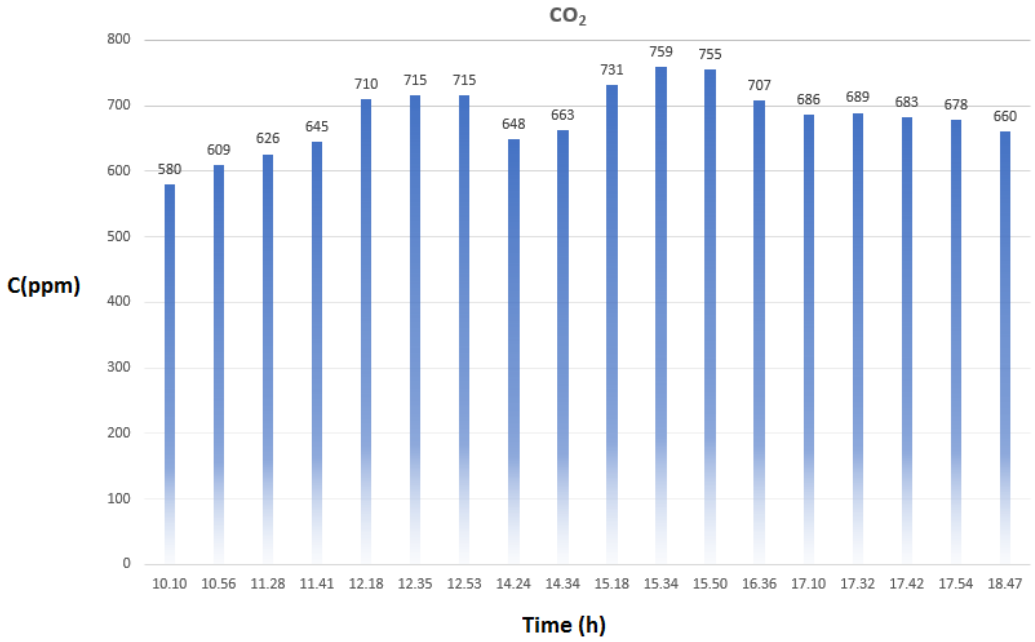

Figure 5.17: Histogram of CO_2 concentration in the laboratory air during the day (24/10/2016). the separation line indicates the lunch time, when the laboratory is empty.

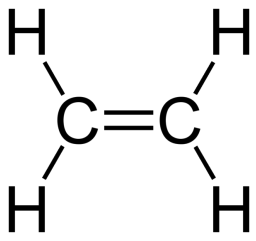

Figure 5.18: Chemical formula of ethene.

The vast majoriy of ethene is produced by steam cracking. Some crackers are capable of producing 3600 tonnes of ethene a day [102].

The same process employed for carbon dioxide has been followed for ethene, that is separated in the Plot U. The Method employed for this gas is **Giulia 2(B50)** and the corresponding peak appears at the right-hand side of the nitrogen one. Inside the bottle, ethene is diluted with synthetic dry air, therefore, to set the desired concentration, also a bottle of synthetic air has been employed.

The chosen concentrations for the analysis were: 500, 200, 100 and 50 ppm. The tests were carried out with this four concentration values with three analysis for each value in order to take the average value between peaks. This methodology allows to obtain a good degree of correlation in the final calibration straight line. In Fig. 5.19 and 5.20 two images of the calibration curves for propane in the four concentrations indicated before. The ethene peak appears at 25.70 s from the beginning of the analysis.

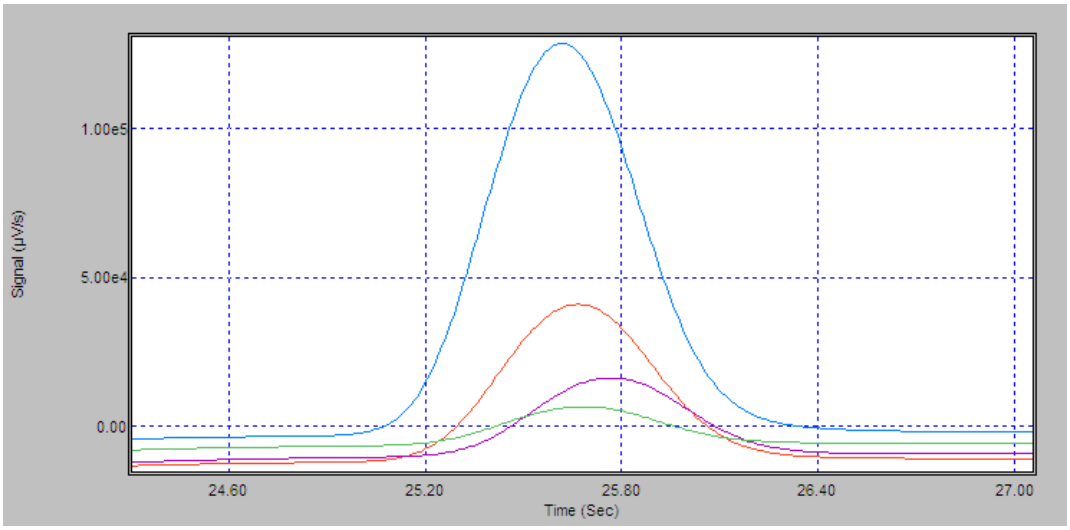

Figure 5.19: Zoom of ethene 500 (blue), 200 (red), 100 (violet) and 50 (green) ppm peaks.

In Fig. 5.21 and 5.22 all the parameters related to ethene calibration for each concentration level are shown, i.e., the area under the integrated curve and the ratio between the area and the amount of gas sent to the column. Then the calibration curve is shown with its related correlation coefficient r=0.999030.

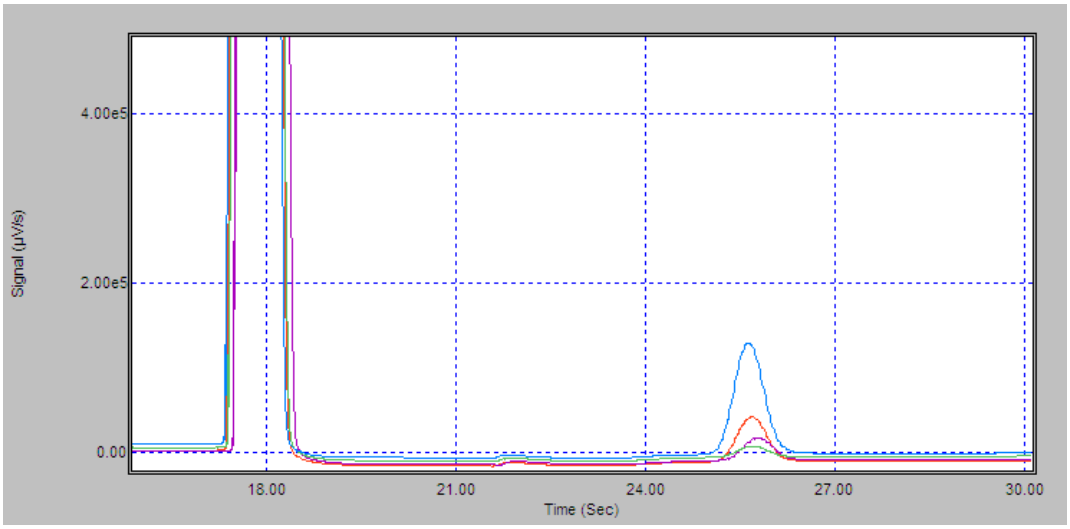

Figure 5.20: Zoom of ethene 500 (blue), 200 (red), 100 (violet) and 50 (green) ppm peaks. Here is noticeable the position of the peak at the right-hand side of N_2.

Component Name	Time retention (Sec)	Quantity Level 1	Units of report	Curve Type	Correlation Coefficient
Etene	25.70	500.000	ppmVol	Linear Through Zero	0.999030

Figure 5.21: Correlation parameter of ethene and detection time.

Level Etene	Amount	Area	Area / Amount
1	500.0000	78734.80	157.47
2	200.0000	33507.54	167.54
3	100.0000	18472.26	184.72
4	50.0000	11016.59	220.33

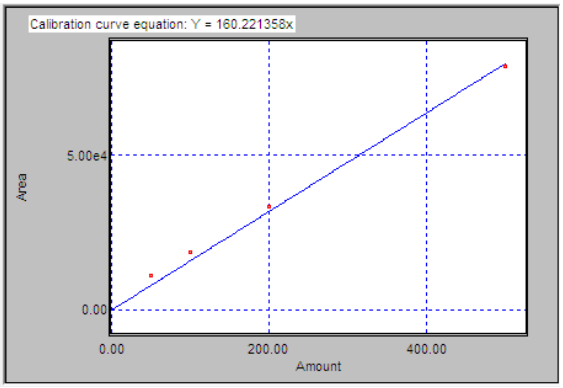

Figure 5.22: Calibration curve of ethene. The concentration employed are four: 500, 200, 100 and 50 ppm.

Conclusions

This thesis focuses on the study of chemoresistive nanostructured sensors starting from a theoretical insight on their functioning to their applications in the medical field. The understanding of the physico-chemical mechanisms that regulate the sensor response is useful to better see how to leverage this technology in the detection of compounds of medical interest. On the other hand, the employment of a wide range of semiconductor materials (both metal-oxides and metal-sulfides), which constitute the sensitive layers of this devices, adds value to the purpose, because each material show very different electrochemical properties and reacts differently to gases. One of the main characteristics of chemoresistive sensors is their high sensitivity (up to tenths of ppb). On the other hand they are un-selective, because each material can react with more than one gas type, even if in a different way. For this specific reason it is of fundamental importance to combine different sensors into arrays, in order to identify specific compounds into gas mixtures by the analysis of the responses in combination. This data treatment can be performed via statistical analysis techniques as principal component analysis or quadratic discriminant analysis.

The goals reached in this three year work of my Ph.D. are reported in this thesis. The first target was the identification of the most selective materials for CRC-biomarkers (e.g., 1-iodo-nonane, decanal and benzene as representative of those CRC-VOCs composed by a benzene ring in their structure) inside a mixture of intestinal gas interferers. The intestinal gas atmosphere of an average human individuals was reproduced into a laboratory setup and an array of eight sensors was employed for the analysis. This analysis was a first step in the identification of useful sensing materials for CRC-VOCs detection but this technique was not applicable for a real screening method in human subjects for three main reasons: i) sample collection of intestinal gases would be invasive and difficult; ii) the intestinal gas mixture varies from individual to individual (due to the diversity of the microbiota); iii) VOCs are too many to be individually identified and it is possible that the molecular chains are broken during the measurement. For that reason, the research has been oriented to a different and more practical approach: the analysis of fecal exhalations of healthy and CRC-affected subjects.

In this second slot of my PhD work, the target was the identification of the differences between fecal samples. Here the focus was not on the single VOC but on the mixture itself. The approach now is a posteriori and thanks to the collaboration of Dr. Gabriele Anania

of the General Section of General and Thoracic Surgery of UNIFE. This feasibility study consisted in the analysis through the patented device SCENT A1, realized by the team of the Sensor Laboratory of UNIFE (to which I belong), of fecal samples of healthy controls and of CRC affected subjects, extracted during colonoscopy. The PCA, QDA and ROC analysis technique provided good discrimination degree between the two populations (the error rate on the classification of the input data evaluates as 5% with QDA).

After obtaining approval from the Ethics Committee a clinical validation study began in collaboration with the gastroenterologists of the University Hospital St. Anna in Ferrara (UNIFE) and the Public Health Research Unit, Department of Public Health (AUSL). Fecal samples of people resulted positive to FOBT are analyzed with SCENT A1 before colonoscopy. A statistics is still under construction thanks to the PCA in order to reach a sufficient number of true positives to obtain the certification of the instrument. These tests began in May 2016 and will last for at least a year. Partial results and considerations on them were presented in this thesis.

Finally a new research on gas chromatographic analysis of gaseous compounds has been started. A Micro GC Agilent 490 has been partially calibrated for compounds as carbon dioxide, ethene and propane. A measurement on the internal CO_2 concentration in laboratory during a day has been done. This will be the starting point for environmental gases and biological samples analysis both with sensors and GC and other future applications.

Bibliography

[1] M.J. Madou, S.R., *Chemical sensing with solid state devices*, Academic Press, New York (1989);

[2] N. Landini, G. Zonta, C. Malagù, Detection of tumor markers on feces with nanostructured sensors, Scholars Press (2015), ISBN-13: 978-3-639-76538-0

[3] C. Malagù, M. Benetti, M. C. Carotta, A. Giberti, V. Guidi, L. Milano, G. Martinelli, *Investigation of the humidity effects on SNO_2-based sensors in CO detection*, Mater. Res. Soc. Symp. Proc. Vol. 915, (2006) Materials Research Society

[4] M. A. Ponce, C. Malagù, M. C. Carotta, G. Martinelli, C. M. Aldao, *Gas indiffusion contribution to impedance in tin oxide thick films*, Journal of Applied Physics. Vol. 104, 054907, (2008)

[5] F. Oba et al J. Phys.: Condens. Matter 22 (2010) 384211

[6] From J. Maier and W. Gopel, J. Sol. Stat. Chem. 72, 293 (1988)

[7] P. Romppainen and V. Lantto, J. Appl. Phys. 63, 5159 (1988)

[8] C.M. Aldao and C. Malagù, Journal of applied Physics 112 (2012) p. 024518-1

[9] N. Barsan, M. HÃ¼bner, and U. Weimar, Sens. and Actuators B 157, 510 (2011)

[10] T. Seiyama, A. Kato, K. Fulishi, M. Nagatani, *A new detector for gaseous components using semiconductive thin films*, Anal Chem, 34, 1502-1503 (1962)

[11] V. Guidi, C. Malagù, M. C. Carotta, B. Vendemiati, *Printed semiconducting gas sensors*, Woodhead Publishing Limited (2012)

[12] L. Schmidt-Mende, J. L. MacManus-Driscoll, *ZnO-nanostructures, defects, and devices*, Mater Today, 10 (5), 40-48 (2007)

[13] Z. L. Wang, *Zinc oxide nanostructures: growth, properties and applications*, J Phys: Condens Matter, 16, R829-R858 (2004)

[14] W. Erbs, J. Desilvestro, E. Borgarello, M. Gratzel, *Visible-light-induced O_2 generation from aqueous dispersions of WO*, J Phys Chem, 88, 4001-4006 (1984)

[15] A. Chiorino, F. Prinetto, M. C. Carotta, C. Malaguù, *Preparation and characterization of SnO_2 and WO_x-SnO_2 nano-sized powders and thick-films for gas sensing*, Sensors and Actuators VB, 78, 89-97 (2001)

[16] M. Sacerdoti, M. C. Dalconi, M. C. Carotta, B. Cavicchi, M. Ferroni, S. Colonna, M. L. Di Vona, *XAS investigation of tantalum and nuobium in nanostructured TiO_2 anatase*, Journal of Solid State Chemistry 177 (2004) 1781-1788

[17] M. C. Carotta, M. Ferroni, S. Gherardi, V. Guidi, C. Malagù, G. Martinelli, M. Sacerdoti, M. L. Di Vona, S. Licoccia, E. Traversa, *Thick-film gas sensors based on vanadium titanium oxide powders prepared by sol-gel synthesis*, Journal of European Ceramic Society 24 (2004) 1409-1413

[18] M. C. Carotta, V. Guidi, C- Malaù, B. Vendemiati, A. Zanni, G. Martinelli, M. Sacerdoti, S. Licoccia, M. L. Di Vona, E. Traversa, *Vanadium and tantalum-doped titanium oxide (TiTaV): a novel material for gas sensing*, Sensors and Actuators B 108 (2005) 89-96

[19] Y. Wu, C. Wadia, W. L. Ma, B. Sadtler, A. P. Alivisatos, *Synthesis and Photovoltaic Application of Copper(I) Sulfide Nanocrystals*, Nano Lett. 8, 2551-2555 (2008)

[20] T.L. Li, Y. L. Lee, H. Teng, *$CuInS_2$ Quantum Dots Coated with CdS as High-Performance Sensitizers for TiO_2 Electrodes in Photoelectrochemical*, Cells. J. Mater. Chem., 21, 5089-5098 (2011)

[21] M. J. Bierman, S. Jin, *Potential applications of hierarchical branching nanowires in solar energy conversion*, Energy Environ. Sci., 2, 1050-1059 (2009)

[22] Z. Zou, Y. Qiu, C. Xie, J. Xu, Y. Luo, C. Wang, H. Yan, *CdS/TiO2 nanocomposite film and its enhanced photoelectric responses to dry air and formaldehyde induced by visible light at room temperature*, ACS Appl. Mater. Interfaces, 7, 11359-11368 (2015)

[23] K. Xu, N. Li, D. Zeng, S. Tian, S. Zhang, D. Hu, C. Xie, *Interface bonds determined gas-sensing of SnO2-SnS2 hybrids to ammonia at room temperature*, ACS Appl. Mater. Interfaces, 7, 11359-11368 (2015)

[24] A. Gaiardo, B. Fabbri, V.Guidi, P. Bellutti, A. Giberti, S. Gherardi, L. Vanzetti, C. Malagù and G. Zonta, *Metal Sulfides as Sensing Materials for Chemoresistive Gas Sensors*, Sensors, 16(3), 296; doi:10.3390/s16030296 (2016)

[25] A. Giberti, B. Fabbri, A. Gaiardo, V. Guidi, C. Malagù, *Resonant photoactivation of cadmium sulfide and its effect on the surface chemical activity*, Appl. Phys., 104 (2014)

[26] B. Fabbri, A. Gaiardo, A. Giberti, V. Guidi, C. Malagù, A. Martucci, M. Sturaro, G. Zonta, S. Gherardi, P. Bernardoni, *Chemoresistive properties of photo-activated thin and thick ZnO films*, Sens. Actuators B, 222, 1251-1256 (2016)

[27] A. Gaiardo, P. Bellutti, S. Gherardi, G. Zonta, B. Fabbri, A. Giberti, V. Guidi, C. Malagù, *Tin (IV) Sulfide chemoresistivity: A possible new gas sensing material*, In Proceeding of AISEM, Trento, Italy, 2-5 February 2015

[28] A. Giberti, A. Gaiardo, B. Fabbri, S. Gherardi, V. Guidi, C. Malagù, P. Bellutti, G. Zonta, D. Casotti, G. Cruciani, G. *Tin(IV) sulfide nanorods as a new gas sensing material*, Sens. Actuators, B: Chem., 223, 827-833 (2016)

[29] A.Giberti, D. Casotti, G. Cruciani, B. Fabbri, A. Gaiardo, V. Guidi, C. Malagù, G. Zonta, S. Gherardi, *Electrical conductivity of CdS films for gas sensing: Selectivity properties to alcoholic chains*, Sens. Actuators B, 207, 504-510 (2015)

[30] V. Guidi, B. Fabbri, A. Gaiardo, S. Gherardi, A. Giberti, C. Malagù, G. Zonta, P. Bellutti, *Metal sulfides as a new class of sensing materials*, Procedia Engineering 120 (2015) 138 - 141

[31] $https://duckduckgo.com/c/Inorganic_compounds?ia=list$

[32] J. Z. Ou, W. Ge, B. Carey, T. Daeneke, A. Rotbart, W. Shan, Y. Wang, Z. Fu, A. F. Chrimes, W. Wlodarski, *Physisorption-Based Charge Transfer in Two-Dimensional SnS2 for Selective and Reversible NO2 Gas Sensing*, ACS Nano, 9, 10313-10323 (2015)

[33] W. Shi, L. Huo, H. Wang, H. Zhang, J. Yang, P. Wei, *Hydrothermal growth and gas sensing property of flower-shaped SnS2 nanostructures*n Nanotechnology, 17, 2918-2924 (2006)

[34] C. Malagù, B. Fabbri, S. Gherardi, A. Giberti, V. Guidi, N. Landini, G. Zonta, Chemoresistive gas sensors for detection of colorectal cancer biomarkers, Sensors, 18982-18992 (2014)

[35] H. Haick, Y. Y. Broza, P. Mochalsky, V. Ruzsanyi and A. Amann, Assessment, origin and implementation of breath volatile cancer markers, Chem. Soc. Rev., 43, 1423-1449 (2014)

[36] B. Tan, Y. Qi, X. Zou, T. Chen, G. Xie, Y. Cheng, T. Dong, L. Zhao, B. Feng, X. Hu, L.X. Xu, A. Zhao, M. Zhang, G. Cai, S. Cai, Z. Zhou, M. Zheng, Y. Zhang, W. Jia, Metabonomics identifies serum metabolite markers of colorectal cancer, J Proteome Res. , 12(6):3000-9, (2013)

[37] G. Peng and M. Hakim, Detection of lung, breast, colorectal, and prostate cancers from exhaled breath using a single array of nanosensors, British Journal of Cancer, 103, 542-551 (2010)

[38] C. SJ. Probert, I. Ahmed, T. Khalid, E. Johnson, S. Smith, N. Ratcliffe, Volatile Organic Compounds as Diagnostic Biomarkers in Gastrointestinal and Liver Diseases, J Gastrointestin Liver Dis., 18(3):337-43, (2009)

[39] D. F. Altomare and M. Di Lena, Exhaled volatile organic compounds identify patients with colorectal cancer, Wiley Online Library (2013)

[40] J. Tomlin, C. Lowis, N. W. Read, *Investigation of normal flatus production in healthy volunteers*, Gut, 32, 665-669 (1991)

[41] G. Zonta, G. Anania, B. Fabbri, A. Gaiardo, S. Gherardi, A. Giberti, V. Guidi, N. Landini, C. Malagù, Detection of colorectal

cancer biomarkers in the presence of interfering gases , Sensors and Actuators B: chemical, 218, 289-295 (2015)

[42] G. Zonta, G. Anania, B. Fabbri, A. Gaiardo, S. Gherardi, A. Giberti, N. Landini, C. Malagù, L. Scagliarini, V. Guidi *Preventive screening of colorectal cancer with a device based on chemoresistive sensors*, Sensors and Actuators B: chemical, 238, 1098-1101 (2017)

[43] http://www.cancer.org/cancer/colonandrectumcancer/detailedguide/colorectal-cancer-key-statistics

[44] Death and DALY estimates for 2004 by cause for WHO Member States (Persons, all ages) (2009-11-12)

[45] G. Wilkes, K. Hartshorn, Colon, Rectal, and Anal Cancers, Seminars in Oncology Nursing, Vol 25, No 1 (February, 2009) pp 32-47), 12 Nature reviews Clinical Oncology.

[46] http://www.emedicinehealth.com.

[47] R. Hompes, C. Cunningham, Colorectal cancer: management (2011)

[48] J. W. Berlin, R. M. Gore, V. Yaghmai, G. M. Newmark, F. H. Miller, Staging of colorectal cancer, Seminars in Roentgenology, Vol XXXV, No. 4 (October, 2000), pp. 370-284

[49] http://www.cancer.gov/types/colorectal/screening-fact-sheet#q2

[50] N. Udilova, D. Jurek, B. Marian, L. Gille, R. Schulte-Hermann, H. Nohl, *Induction of lipid peroxidation in biomembrane by dietary oil components*, Food and chemical toxicology 41, 1481-1489 (2004)

[51] A. Amann, P. Spanel, D. Smith, *Breath analysis: the approach towards clinical applications*, Mini Rev Med Chem 7: 115-129 (2007)

[52] P. J. Mazzone, *Analysis of volatile organic compounds in the exhaled breath for the diagnosis of lung cancer*, J Thorac Oncol 3: 774-780 (2008)

[53] A. Bajaj, O. R. Miranda, I. B. Kim, R. L. Phillips, D. J. Jerry, U. H. F. Bunz, V. M. Rotello, *Detection and differentiation of normal, cancerous, and metastatic cells using nanoparticle-polymer sensor arrays*, Proc Natl Acad Sci USA 106: 10912-10916 (2009)

[54] O. Barash, N. Peled, F. R. Hirsh, H. Haick, *Sniffing the unique 'odor print' of non-small-call lung cancer with gold nanoparticles*, Small 5: 2618-2624 (2009)

[55] W. Filipiak, A. Sponring, A. Filipiak, C. Ager, J. Shubert, W. Miekisch, A. Amann, J. Troppmair, *TD-GC-MS analysis of volatile metabolites of human lung cancer and normal cells in-vitro*, Cancer Epidiemiol Biomarkers PRev 19: 182-195 (2010)

[56] T. Ligor, M. Ligor, A. Amann, C. B. Ager, M. Pienz, A. Dzien, B. Buszewski, The analysis of healthy volunteers' exhaled breath by the use of solid-phase microextraction and GC-MS, J Breath Res 2: 046006/1-046006/8 (2008)

[57] P. J. Mazzone, *Analysis of volatile organic compounds in the exhaled breath for the diagnosis of lung cancer*, J Thorac Oncol 3: 774-780 (2008)

[58] A. Bajtarevich, C. Ager, M. Pienz, M. Klieber, K. Schwarx, M. Ligor, T. Ligor, W. Filipiak, H. Denz, W. Hilbe, W. Weiss, P. Lukas, H. Jamnig, M. Hackl, A. Haidenberger, B. Buzewski, W. Miekisch, J. Schubert, A. Amann, *Noninvasive detection of lung cancer by analysis of exhaled breath*, BMC Cancer 9: 348 (2009)

[59] L. Horvath, Z. Lazar, N. Gyulai, M. Kollai, G. Losonczy, *Exhaled biomarkers in lung cancer*, Eur Respir J 34; 261-275 (2009)

[60] M. Ligor, T. Ligor, A. Bajtarevic, C. Ager, M. Pienz, M. Klieberm H. Denz, M. Fiegl, W. Hilbe, W. Weiss, P.Lukas, H. Jamnig, M. Hackl, W. Miekish, J. Schubert, A. Amann, *Determination of volatile organic compounds in exhaled breath of patients with lung cancer using solid phase microextraction and gas chromatography mass spectrometry*, Clin Chem Lab Med 47: 550-560 (2009)

[61] C. M. F. Kneepkens, G. Lepage, C. C. Roy, *The potential of the hydrocarbon breath test as a measure of lipid peroxidation*, Free Rad Biol Med 17: 127-160 (1994)

[62] J. I. Baubach, V. Vautz, V. Ruzsanyi, *Metabolites in Human Breath: Ion Mobility Spectrometers as Diagnostic Tools for Lung Diseases. Breath Analysis for Clinical Diagnosis and Therapeutic Monitoring*, World Scientific Publishing Co. Pte. Ltd: Toh Tuck Link, Singapore (2005)

[63] D. F. Altomare, M. Di Lena, F. Porcelli, L. Trizio, E. Travaglio, M. Tutino, S. Dragonieri, V. Memeo, G. de Gennaro, *Exhaled volatile organic compounds identify patients with colorectal cancer*, Wiley Online Library, DOI: 10.1002/bjs.8942

[64] A. Gasbarrini, S. R. Corazza, G. Gasbarrini, M. Montalto, M. Di Srefano, G. Basilisco, A. Parodi, P. U. Satta, P. Verniam C. Anania, M. Astegiano, G. Barbara, L. Benini, P. Bonazzi, G. Capurso, M. Certo, A. Colecchia, L. Cuoco, A. di Sario, D. Festi, C. Lauritao, E. Miceli, G. Nardone, F. Perri, P. Portincasa, R. Risicato, M. Sorge, A. Tursi, *Methodology and indications of H_2-breath testing in gastrointestinal diseases: the Rome Consensus Conference*

[65] M. Hakim, S. Billan, U. Tisch, G. Peng, I. Dvrokind, O. Marom, R. Abdah-Bortnyak, A. Kuten, H. Haick, *Diagnosis of head-and-neck cancer from exhaled breath*, British Journal of Cancer (2011) 104, 1649-1655

[66] R. F. Machado, D. Laskowski, O. Deffenderfer, T. Burch, S. Zheng, P. J. Mazzone, T. Makhail, C. Jennings, J. K. Stoller, J. Pyle, J. Duncan, R. A. Dweik, S. Erzurum, *Detection of lung cancer by sensor array analyses of exhaled breath*, Am J Respir Crit Care Med (2005) Vol. 171, pp. 1286-1291

[67] H. Sonoda, S. Kohnoe, T. Yamazato, Y. Satoh, G. Morizono, K. Shikata, M. Morita, A. Watanabe, M. Morita, Y. Kakeji, F. Ionue, Y. Maheara, *Colorectal cancer screening with odour material by canine scent detection*, Gut (2011) 60, 814-819

[68] B. Buzewski, J. Rudnicka, T. Ligor, M. Walczak, T. Jezierski, A. Amann, *Analytical and unconventional methods of cancer detection using odor*, Trends in Analytical Chemistry (2012), Vol. 38

[69] T. G. de Meij, I. B. Larbi, M. P. van der Schee, Y. E. Lentferink, T. Paff, J. S. Terhaar sive Droste, C. J. Mulder, Ad. A. van

Bodegraven and N. K. de Boer, Electronic nose can discriminate colorectal carcinoma and advanced adenomas by fecal volatile biomarker analysis: proof of principle study, International Journal of Cancer: 134, 1132-1138 (2014)

[70] http://www.sensigent.com/products/cyranose.html

[71] J. Tomlin, C. Lowis, N. W. Read, *Investigation of normal flatus production in healthy volunteers*, Gut, 1991, 32, 665-669

[72] J. Vermeiren, T. Van deWiele, W. Verstraete, P. Boeckx, N. Boon, Nitric Oxide Production by the Human IntestinalMicrobiota by Dissimilatory Nitrate Reduction to Ammonium, Journal of Biomedicine and Biotechnology Volume 2009 (2009)

[73] J. Vermeiren, T. Van deWiele, W. Verstraete, P. Boeckx, N. Boon, Nitric Oxide Production by the Human IntestinalMicrobiota by Dissimilatory Nitrate Reduction to Ammonium, Journal of Biomedicine and Biotechnology (2009)

[74] A. Tari, K. Kodama, K. Kurihara, M. Fujihara, K. Sumii, G. Kajiyama, Does serum nitrite concentration reflect gastric carcinogenesis in Japanese Helicobacter pylori-infected patients, Dig Dis Sci., 47(1):100-6 (2002)

[75] T. Kondo, T. Mitsui, M. Kitagawa, Y. Nakae, Association of fasting breath nitrous oxide concentration with gastric juice nitrate and nitrite concentrations and Helicobacter pylori infection, Dig Dis Sci., 45(10):2054-7 (2000)

[76] J. A. Rodriguez, S. Chaturvedi, M. Kuhn, J. Hrbek, Reaction of H2S and S2 with Metal Oxide Surfaces: Band Gap Size and Chemical Reactivity, J. Phys. Chem. B, 102 (28), pp 5511-5519 (1998)

[77] T. Morita, M. A. Perella, M.-E. Lee, S. Kourembanas, Smooth muscle cell-derived carbon monoxide is a regulator of vascular cGMP, Proc. Natl. Acad. Sci. USA Vol. 92, pp. 1475-1479, Cell Biology (1995)

[78] G. Kikuchi, T. Yoshida, M. Noguchi, "Heme oxygenase and heme degradation". Biochemical and Biophysical Research Communications 338 (1): 558-567 (2005)

[79] V. Guidi, C. Malagu', M.C. Carotta, B. Vendemiati, Printed films: Materials science and applications in sensors, electronics and photonics in Woodhead publishing series in electronic and optical materials, pp.278-334 (2012)

[80] http://www.inchem.org/documents/icsc/icsc/eics0165.htm

[81] http://www.chemspider.com/Chemical-Structure.19101.html

[82] http://www.chemicalbook.com/ChemicalProductProperty-0EN-CB2208008.htm

[83] J. A. Rodriguez, S. Chaturvedi, M. Kuhn, J. Hrbek, Reaction of H2S and S2 with Metal/Oxide Surfaces: Band Gap Size and Chemical Reactivity, J. Phys. Chem. B, 102 (28), pp. 5511-5519, (1998)

[84] L. I. Smith, A tutorial on Principal Components Analysis, (2002)

[85] Italian patent number: RM20144000595

[86] http://www.scent-srl.it/

[87] J. Izenman, Modern Multivariate Statistical Techniques, Springer-Verlag New York (2008), ISSN 1431-875X, ISBN 978-0-387-78188-4, DOI 10.1007.978-0-387-78189-1

[88] http://www.airc.it/tumori/tumore-al-colon-retto.asp

[89] Pavia, L. Donald, G. M. Lampman, S. G. Kritz, R. G. Engel, Introduction to Organic Laboratory Techniques (4th Ed.), Thomson Brooks/Cole (2006), pp. 797-17, ISBN 978-0-495-28069-9

[90] A. G. Linde, Gas Chromatography, Retrieved 11 March 2012.

[91] Grob, Konrad, Carrier Gases for GC, Restek Advantage, Restek Corporation $http://www.restek.com/Technical-Resources/Technical-Library/Editorial/editorial\_A017$ (1997), Retrieved 09 March 2016

[92] $http://www.bbc.co.uk/schools/gcsebitesize/science/triple\_ocr\_21c/further\_chemistry/chromatography/revision/5/$

[93] $http://lab-training.com/2014/02/06/benefits-of-split-splitless-injection-in-capillary-gas-chromatography/$

[94] https://www.agilent.com/en-us/products/gas-chromatography/micro-gc-systems/channel-cabinets

[95] http://blog.restek.com/?p=10643

[96] https://www.agilent.com/en-us/products/gas-chromatography/gc-columns/capillary/hp-plot-u

[97] http://www.swisslabs.eu/uploads/files/HPPlot_U_Latest_Innovations_for_Light_Hydrocarbon_and_Polar_Compound_Analysis.pdf

[98] http://cn.agilent.com/cs/library/usermanuals/public/G3581-90001.pdf

[99] https://www.britannica.com/science/propane

[100] DIN 1946-2 (1994)

[101] https://www.theben.it/Sensori-di-CO2

[102] http://www.essentialchemicalindustry.org/chemicals/ethene.html

Acknowledgements

I wish to thank all the people who helped me in my PhD path. First, I thank my tutor, Prof. Cesare Malagú, who always supported and helped me in these years of research and also because he has made me closer to Asimov's books. I thank all the Sensors Group: Nicoló Landini, Sandro Gherardi, Andrea Gaiardo, Alessio Giberti, Barbara Fabbri, Matteo Valt, without which it would not be possible to get the results of these three years. Moreover, they have also helped to make the work environment a pleasant place. I thank Prof. Vincenzo Guidi for his teachings and the coordination of activities. I thank all the people who have contributed to this research including: Prof. Gabriele Anania, Prof. Giorgio Rispoli, Lucia Scagliarini, Caterina Palmonari, Dr. Aldo de Togni, Dr. Luciano Ricci and the doctors of St. Anna Hospital of UNIFE and the Unitá Operativa Igiene Pubblica, Department of Public Health (AUSL). I thank the members and supporters of the startup SCENT S.r.l., without whose support we would never have been able to take this project forward. I thank the reviewers of this thesis for the time spent in reading and correction. I also thank my parents who have financed my studies, without which there would not even be able to graduate (so let alone the Ph.D.). Last but not least, I thank my brother, Andrea, my friends and all the people I have been close in recent years, although they have not contributed directly, they have always believed in me.